U.PORTO

FEUP FACULDADE DE ENGENHARIA
UNIVERSIDADE DO PORTO

Beam characterization and guiding for optical/infrared interferometry

Narsireddy Anugu

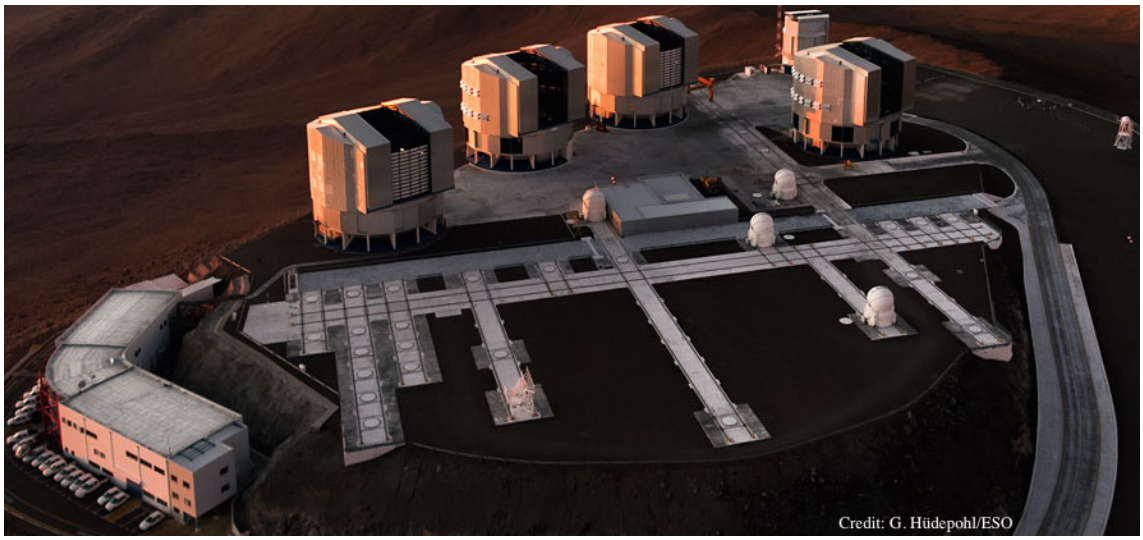

Supervisor: Prof. Paulo Garcia

Co-Supervisor: Prof. António Amorim

Programa Doutoral em Engenharia Física

August, 2016

© Narsireddy Anugu: August, 2016

Faculdade de Engenharia da Universidade do Porto

Beam characterization and guiding for optical/infrared interferometry

Narsireddy Anugu

Dissertation submitted to Faculdade de Engenharia da Universidade do Porto
to obtain the degree of

Doctor in Engineering Physics

President: Dr. Adriano da Silva Carvalho
Member: Dr. Andreas Glindemann
Member: Dr. Jean-Baptiste Le Bouquin
Member: Dr. André Maria da Silva Dias Moitinho de Almeida
Member: Dr. Alexandre Pereira Cabral
Member: Dr. Manuel Joaquim Bastos Marques
Member: Dr. Paulo Jorge Valente Garcia

August, 2016

To my parents and my wife.

Resumo

O instrumento GRAVITY foi construído tendo como objectivo científico o estudo do buraco negro supermassivo no centro da Via Láctea, estando instalado no *Very Large Telescope Interferometer* (VLTI) do Observatório do Paranal do Observatório Europeu do Sul (ESO). É um dos instrumentos para telescópios mais avançado alguma vez construído, permitindo obter imagens por referência e fecho de fase (com uma resolução de 4 milissegundos de arco) e astrometria relativa (com uma precisão de 10 microssegundos de arco). Implementar um modo astrométrico e atingir a precisão referida põe várias dificuldades práticas. A turbulência atmosférica e a erros na medição das linhas de base do interferómetro são os desafios práticos mais importantes que degradam a performance do GRAVITY em dois aspectos: a) sensibilidade do instrumento – a injecção da luz dos objectos nas fibras monomodo é afectada pela presença de *tip-tilts* atmosféricos aleatórios; b) erros astrométricos – causados por *tip-tilts* residuais e erros de linha de base. A câmara de aquisição do GRAVITY é um dos subsistemas que contribui para ultrapassar estes desafios.

O GRAVITY foi construído por um consórcio de institutos na Alemanha, França e Portugal. A responsabilidade pela construção da câmara de aquisição é do grupo SIM da unidade CENTRA, onde esta tese foi desenvolvida. No manuscrito a câmara de aquisição é apresentada, desde a fase de desenho à de *commissioning*, focando as *work-packages* do projecto da responsabilidade do autor ou onde este teve uma contribuição importante.

Em primeiro lugar, o desenho que implementa as quatro funções que permitem a estabilização dos feixes ópticos é apresentado: a) *pupil tracking* – obtendo imagens de quatro lasers de referência de pupila montados nas aranhas de cada espelho secundário dos telescópios; b) *field traking* – obtendo imagens de objectos astrofísicos; c) sensor de aberrações – obtendo imagens com um sensor de Shack-Hartmann; d) monitor de pupila.

Em segundo, as simulações *end-to-end* da câmara de aquisição são realizadas para validar e verificar a precisão dos conceitos implementados no seu desenho. São desenvolvidos algoritmos dedicados de análise de dados para medir as distorções de feixe óptico: a) *pupil-tracking* – medição da posição lateral e longitudinal a pupila; b) *field-tracking* – medição dos *tip-tilts* (erros de camp) do objecto astrofísico; c) sensor de aberrações – medição das aberrações quase-estáticas da frente de onda.

Em terceiro lugar, usando estes algoritmos, uma *pipeline* de análise de dados é implementada segundo os standards de programação e o *framework* do ESO. Os parâmetros medidos (com um tempo de amostragem de 0.7 s) são utilizados no/a: a) alinhamento do GRAVITY no VLTI; b) estabilização activa do campo e pupila; c) correcção de foco para os telescópios auxiliares; d) correcção das aberrações dos diferentes caminhos ópticos entre o sistema de óptica adaptativa do GRAVITY e o recombinador interferométrico.

Finalmente, depois do teste dos componentes ópticos, a câmara foi construída, alinhada opticamente, testada e integrada no instrumento GRAVITY. Este foi enviado para o Observatório do Paranal onde obteve a primeira luz no final de 2015. Os resultados da caracterização confirmam

que ao estabilizar os feixes dos telescópios o erro astrométrico induzido pelos erros de campo e pupila é minimizado para menos de alguns microssegundos de arco.

Abstract

The GRAVITY instrument has been built with the goal of studying the Milky Way Galactic Center super-massive black hole. It is a powerful phase-referenced and closure phase interferometric imaging (4 milli-arcseconds) and high precise narrow-angle astrometric instrument (10 micro-arcseconds) and has been installed at the Very Large Telescope Interferometer (VLTI) of the ESO. There are several practical difficulties in implementing narrow-angle astrometry. The atmospheric turbulence and the error in measuring accurate baseline lengths between any two telescopes are among the major challenges. Due to these, the performance of GRAVITY can be severely degraded in two ways: a) instrument sensitivity – the efficient star's light injection in the single mode fibers is affected in the presence of random atmospheric tip-tilts; b) astrometric errors – caused due to unwanted tip-tilts and baseline errors. As one of the subsystems required to overcome these challenges, the GRAVITY acquisition camera was built.

The acquisition camera was the responsibility of the Portuguese CENTRA-SIM group where my thesis took place. In this manuscript the acquisition camera is presented from the design phase to the commissioning, focusing on the project work packages that were lead by the author or had a major contribution by him.

First, the design implementing four optical functions to enable the required beam stabilization is presented : a) pupil tracking–by imaging (with a 2×2 lenslet) four pupil reference lasers which are mounted on the spiders of each telescope secondary mirror; b) field tracking – by imaging astrophysical targets; c) aberration sensing – by imaging 9×9 lenslet Shack-Hartmanns; d) pupil monitoring by imaging telescope pupil.

Second, the end-to-end simulations of the acquisition camera are performed to verify the validity and the accuracy of the acquisition camera concepts. Dedicated data reduction algorithms are developed to track the beam distortions: a) pupil tracking – lateral and longitudinal pupil positions are measured by analyzing the 2×2 lenslet images; b) field tracker: the image tip-tilts are tracked from the astrophysical targets; d) aberration tracker: quasi-static wavefront aberrations are measured using 9×9 lenselet Shack-Hartmann images. It is demonstrated that the algorithms are robust and have the accuracy to measure the beam parameters within design specifications.

Third, using these algorithms, the acquisition camera data reduction pipeline is developed using the ESO standard software framework. The measured parameters (with sampling of 0.7 s) are used in the : a) alignment of GRAVITY with the VLTI; b) active pupil and field stabilization; c) focus correction for the auxiliary telescopes; d) non-common path error correction between the GRAVITY-Coudé infrared adaptive optics system and GRAVITY four unit telescopes.

Finally, after testing the optical components which are procured, the camera is optically aligned, assembled, tested and integrated within GRAVITY. GRAVITY was shipped to Paranal Observatory, Chile and it had its first light at the end of 2015. The characterization results confirm that by stabilizing the telescope beams, the astrometric error induced by the field and the pupil errors is minimized to less than few micro-arcseconds. Currently, the observations of the black hole environment are ongoing.

Acknowledgments

I would like to express my gratitude to all the people who supported and inspired me during my thesis work and without whom this thesis would not have been possible.

First of all, I would like to thank my supervisor Paulo Garcia and co-supervisor Antonio Amorim for the opportunity, all the advice, mentorship and support during my thesis period. Besides their continuous encouragement, I am grateful for the financial support, which allowed me to work at the University of Lisbon, MPE and to attend numerous conferences. None of this would have been possible if it wasn't the inspiration, the vision of the GRAVITY PI, Frank Eisenhauer.

Special thanks go to Andreas Glindemann and Jean-Baptiste Le Bouquin, who agree to be examiners on my Ph.D. thesis. I am also very grateful to André Maria da Silva Dias Moitinho de Almeida, Alexandre Pereira Cabral and Manuel Joaquim Bastos Marques who agreed to join the examination committee.

Fundação para a Ciência e a Tecnologia (FCT) and IDPASC-Portugal have funded my thesis research. OPTICON Fizeau Programme, European Commission Seventh Framework Programme has funded my work travels to the University of Lisbon, MPE, and the Paranal Observatory.

It has been a pleasure to spend long instrument engineering and commissioning runs at MPE and at the Paranal Observatory, Chile because of the amazingly dedicated GRAVITY consortium staff. I thank all of them for making this work possible.

I would like to thank CENTRA colleagues Paulo Gordo, Jorge Abreu, Joao Castanheira and Jorge Lima for their support on the acquisition camera hardware work starting from the assembly, optical and cryogenics testing and integration into GRAVITY.

I sincerely appreciate the teamwork with MPE colleagues Ekkehard Wieprecht, Erich Wiezorrek, Thomas Ott and Leonard Burtscher for all their support in developing the real-time control software for the beam guiding and for all the interesting discussions.

I also thank Carlos Correia for the productive collaboration concerning the peak-locking algorithms for the Shack-Hartmann wavefront sensing.

It has been a joy to work at FEUP, Porto because of Sandra Regina, Paulo Sá, Vitor Marinho, Joana Ascenso, Paulo Andrade and Nuno Gomes. I have the greatest fun of discussing everything with a wonderful group of colleagues over the past four and half years.

I would like to thank my master thesis colleagues Lancelot Chellaraj Thangadurai, Sivarani Thirupathi and Swapan Saha, who encouraged me to apply for this Ph.D. position and for supporting my application.

Last but not least, I want to thank my parents, brother, and sister for their unconditional love and support. I would like to thank my wife for supporting during the stressful writing-up period.

Contents

List of Abbreviations **xii**

1 Introduction **1**
1.1 The Milky Way super-massive black hole 1
1.2 Observational techniques 4
1.3 Outline of this thesis 9
1.4 Thesis context: my participation in the GRAVITY instrument project 9

2 The GRAVITY instrument and its subsystems **11**
2.1 Introduction 11
2.2 Narrow-angle astrometry challenges 12
2.3 Very Large Telescope Interferometer overview 18
2.4 GRAVITY overview 22
2.5 Observational strategy 33

3 The acquisition camera concept and design **35**
3.1 Introduction 35
3.2 Design and concepts 36
3.3 Acquisition camera modeling: end-to-end simulations 46
3.4 Summary and conclusions 50

4 Data reduction pipeline and software **53**
4.1 Introduction 53
4.2 Top level requirements 53
4.3 Software architecture 54
4.4 Image data reduction concepts and algorithms 55
4.5 Closed loop control software 71
4.6 Software verification and validation 73
4.7 Summary and future improvements 76

5 From optical testing to integration **79**
5.1 Introduction 79
5.2 Instrument assembly and optical alignment at CENTRA/SIM 80
5.3 Acquisition camera integration in GRAVITY at MPE 89
5.4 Summary and conclusions 90

6 Commissioning and on-sky results **93**
6.1 Introduction . . . 93
6.2 Laboratory validation at MPE . . . 94
6.3 On-sky validation at the VLTI . . . 100
6.4 Summary and future improvements . . . 112

7 Conclusions and prospects **117**

Bibliography **123**

List of Figures **143**

List of Tables **145**

A Thesis context **147**
A.1 CENTRA-SIM research group . . . 147
A.2 Research visits and participation in conferences/workshops . . . 147
A.3 PhD funding: acknowledgments . . . 148

B Top level requirements for the acquisition camera **149**
B.1 Field imager . . . 149
B.2 Pupil tracker . . . 149
B.3 Aberration sensor . . . 150
B.4 Pupil imager . . . 150

C First author publications **151**
C.1 Submitted A . . . 152
C.2 Submitted B . . . 165
C.3 UPJE2015 . . . 175
C.4 SPIE2016 . . . 183
C.5 SPIE2014a . . . 193
C.6 SPIE2014b . . . 207

D Co-author publications **219**
D.1 Peer-reviewed . . . 219
D.2 Conference proceedings . . . 219

E Acquisition camera test report, VLT-TRE-GRA-15885-6305 **221**

List of Abbreviations

AO	Adaptive Optics
ADR	Atmospheric Differential Refraction
AMBER	Astronomical Multi-BEam combineR, VLTI
APD	Avalanche Photo-Diode
ARAL	Alignment facility for the VLTI
ASTRA	ASTrometry and phase-Referencing Astronomy on the Keck interferometer
ATs	Auxiliary Telescopes
CaF2	Calcium Fluoride
CCD	Charge Coupled Device
CENTRA	Multidisciplinary Center for Astrophysics, Lisbon and Porto
CIAO	GRAVITY-Coudé Infrared Adaptive Optics, GRAVITY/VLTI
DM	Deformable Mirror
E-ELT	European Extremely Large Telescope
EHT	Event Horizon Telescope
ESO	European Southern Observatory
FINITO	Fringe-tracking Instrument of NIce and TOrino, VLTI
FITS	Flexible Image Transport System
FoV	Field of View
FSM	Field Selector Mirror of star separator, VLTI
FWHM	Full width at half maximum
GRA4MAT	GRAVITY for MATISSE, VLTI
GRAVITY	AO assisted, two-object, multiple-beam-combiner, VLTI
HARMONI	High Angular Resolution Monolithic Optical and Near-infrared Integral field spectrograph, E-ELT
HAWAII	HgCdTe Astronomical Wide Area Infrared Imager
IDL	Interactive Data Language
IMB	Imaging Baseline
IRIS	Infrared Image Sensor of VLTI
LN2	Liquid Nitrogen
M1	Primary mirror of a telescope
M2	Secondary mirror of a telescope

M14	14th mirror in the light path from the telescope side
MACAO	Multi Application Curvature Adaptive Optics, VLTI
MARCEL	Artificial beam generator of the VLTI
mas	milli-arcsecond
MATISSE	Multi AperTure mid-Infrared SpectroScopic Experiment, VLTI
MPE	Max-Planck-Institut für Extraterrestrische Physik, Garching
NAB	Narrow-Angle Baseline
OPD	Optical Path Difference
P2VM	Pixel-to-Visibility Matrix
PAE	Preliminary Acceptance Europe
PMC	Pupil Motion Controller, (GRAVITY)
PRIMA	Phase-Referenced Imaging and Microarcsecond Astrometry, VLTI
PSF	Point Spread Function
PTI	Palomar Testbed Interferometer, Palomar Observatory
rad	radian
RMS	Root Mean Square
S2	One of the Galactic Center stars
SELEX	Selex ES Ltd - A Finmeccanica Company
Sgr A*	Sagittarius A star, super-massive black hole
SIM	Laboratory for Systems, Instrumentation and Modeling in Science and Technology for Space and the Environment
SNR	Signal-to-Noise Ratio
SPHERE	Spectro-Polarimetric High-contrast Exoplanet Research instrument, VLT
T1-T4	Telescope one to four
TTP	Tip-Tilt and Piston mirror
VCM	Variable Curvature Mirror, VLTI
VLBI	Very Long Baseline Interferometry
VLTI	Very Large Telescope Interferometer
WAB	Wide Angle Baseline
YAO	YORICK Adaptive Optics
µas	micro-arcsec
δOPD	Differential Optical Path Difference

Chapter 1

Introduction

Super-massive black holes are among the most fascinating objects in the universe being the seeds of galaxies (Alexander et al., 2005) and playing a role in the formation of cosmological structures. Their existence in the universe is proved by the detection of quasars (Schmidt, 1963) and gravitational waves (Abbott et al., 2016). Our Milky Way Galactic Center also hosts a super-massive black hole – the central compact radio source, Sgr A* (Genzel et al., 2010). Being the nearest member of this species, (the next one is in the Andromeda galaxy, located at about 100 times further out) it offers a unique opportunity to study the physics of high gravitational fields. In this chapter, first I review the important recent observations of the Galactic Center black hole and then I describe the current instrumentation in progress to probe further Sgr A*.

1.1 The Milky Way super-massive black hole

The history of the Milky Way super-massive black hole spans around half-a-century from the initial proposal of its existence (Lynden-Bell, 1969) to the recent experimental evidence of it by stellar orbital dynamics in the Galactic Center (e.g. Gillessen et al., 2009). A proper documentation of the rich history is beyond the scope of this thesis and the interested reader is recommended to the reviews by Genzel et al. (2010) and Reid (2009).

The Galactic Center region was hidden for a long time because of large visible light extinction caused by the interstellar dust in the line of sight from the Earth. As this can only be seen in radio, infrared and X-ray wavelengths, imaging it requires special techniques. By observing the innermost stars at the Galactic Center region (so called S-stars) in the near-infrared wavelengths, scientists have probed the gravitational field of the Galactic Center successfully via stellar orbital dynamics (Ghez et al., 2000; Schödel et al., 2002; Ghez et al., 2005; Gillessen et al., 2009). A concentrated mass of an unseen object is computed through the orbital-fitting of the S-stars (cf. Figures 1.1, 1.2) and is $M = (4.3 \pm 0.3) \times 10^6$ $M_\odot$ (Gillessen et al., 2009). Furthermore, it is found that the fitted focus of the stellar orbits coincides with the location of Sgr A* to within ~ 1 mas[1]

[1] milli-arcsec

(Gillessen et al., 2009). These discoveries led to a compelling evidence that Sgr A* must be a super massive black hole, located 8.33 ± 0.35 kpc[2] away from the Earth. Its Schwarzschild radius

$$r_S = \frac{GM}{c^2},$$

with G the gravitational constant and c the speed of light, spans about 8 million miles, corresponding to 10 micro-arcsec at its distance.

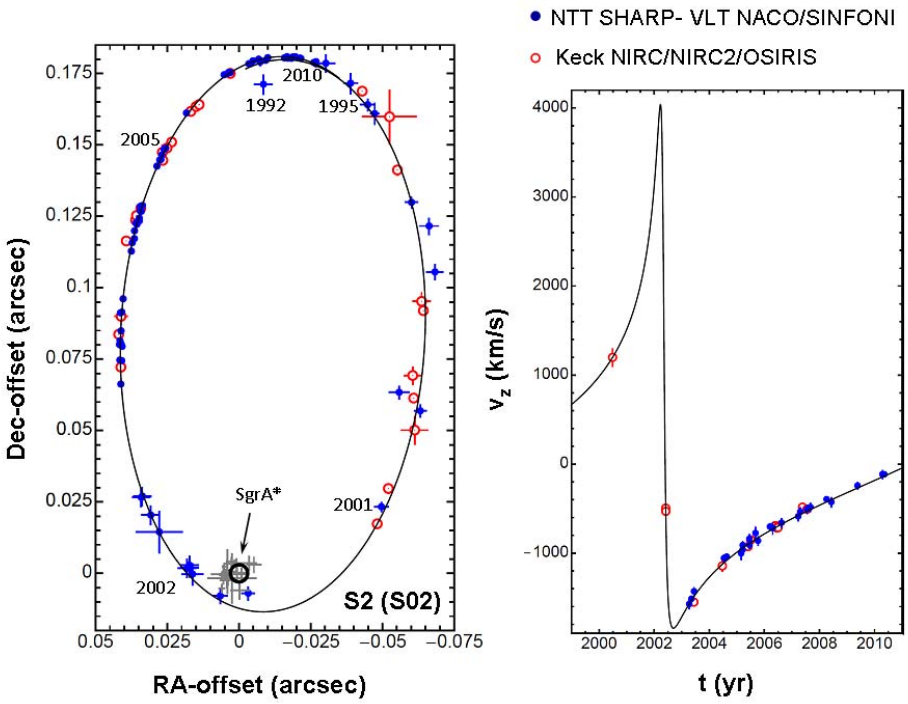

Figure 1.1: Left: The orbit of S2 around Sgr A*. It has a period of 15.2 years and is highly elliptical, with eccentricity of 0.88. Right: The radial velocity of S2. The S2 passed its pericenter, which is located at a distance of $\sim 144\ r_S$ from Sgr A*, in 2002 and hence the abrupt change in its radial velocity. Figure credit Genzel et al. 2010.

One of the current challenges to our understanding of Sgr A* relates to the black hole is its flares. Temporally variable near-infrared emissions are found at the Galactic Center (Genzel et al., 2003; Dodds-Eden et al., 2011, cf. Figure 1.3). These events last for about 1 hour, and their light-curves show significant variations on a typical timescale of 15-20 minutes. The millimeter (Zhao et al., 2001), sub-millimeter (Eckart et al., 2006a; Yusef-Zadeh et al., 2009) and X-ray (Baganoff et al., 2001; Haubois et al., 2012) observations also confirm these flares.

Three popular models were proposed to explain the origin of these flares (cf. Figure 1.4):

1. a hot-spot orbiting the black hole at a few r_S;
2. possibility of jets in the accreting black hole;
3. a model of pure red noise.

[2]kilo-parsec

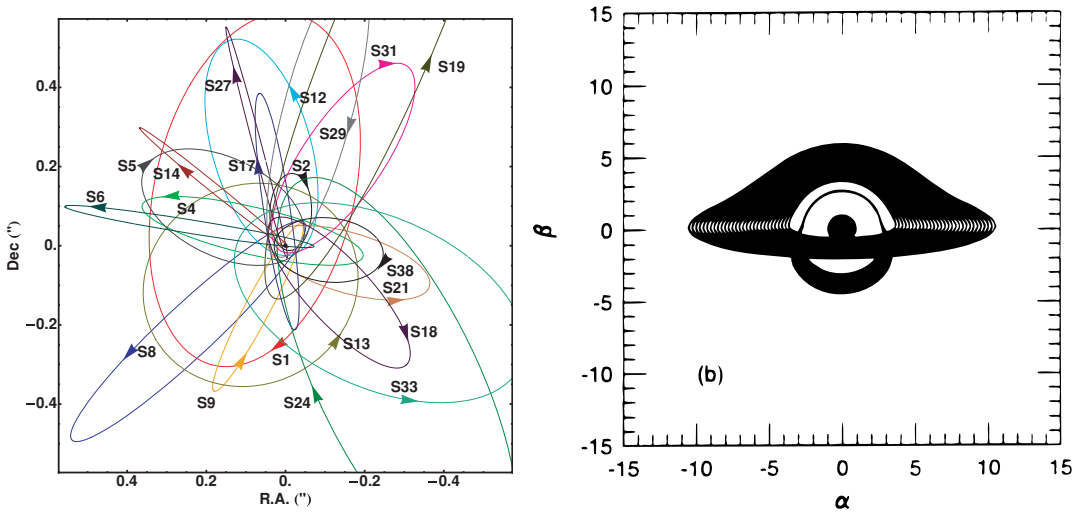

Figure 1.2: Left: Orbits of 26 different S-stars close to Sgr A*, which is centered in the figure. Right: A near-infrared simulation of the black hole shadow: the optical appearance of an accretion disk as the observer looks into the equatorial plane. The axes units are $2r_S$. Figure credit: left panel – Gillessen et al. 2009; right panel – Hollywood and Melia 1997.

The hot-spot model suggests a plasma blob orbiting on the innermost stable circular orbit ($\sim 2r_S$) of the black hole. This model predicts that the light curves of the flares are due to the orbital motion of the hot-spot and associated variation in the polarization (Genzel et al., 2003; Eckart et al., 2006b, 2010). The jet model appears as a natural explanation, because jets are often observed in various accretion disk systems, ranging from active galactic nuclei to binary systems (Falcke et al., 2004; Krolik et al., 2007). In another explanation, the long-term light curves are also interpreted as pure red noise (Mauerhan et al., 2005; Macquart and Bower, 2006; Do et al., 2009).

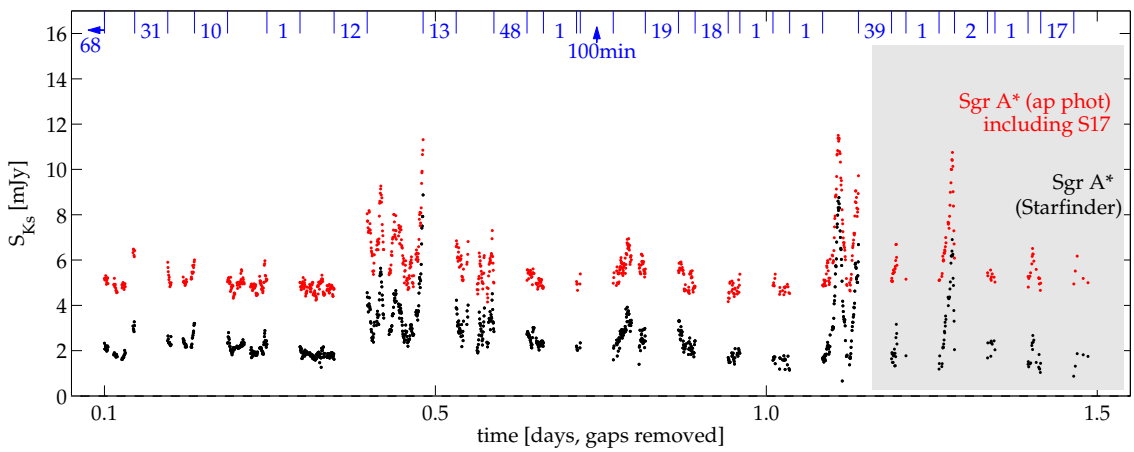

Figure 1.3: Light curves of the near-infrared flares. Figure credit Dodds-Eden et al. 2011.

If the hot-spot model is correct, the flares may be used as dynamical probes of the black hole gravitational field. It is possible that the Einstein's general theory of relativity effects can be observable in the orbit of a flare for two reasons: a) In the inner circular stable orbit, the spot

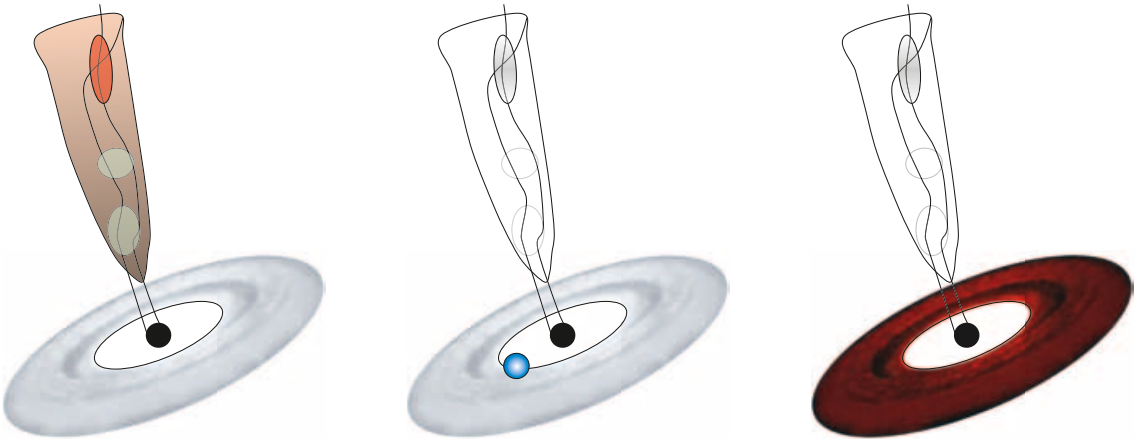

Figure 1.4: Artist depiction (ignoring space-time curvature) of the three most plausible flare modes of Sgr A*: (left) jet model; (middle) hot-spot (blue sphere) orbiting in the inner circular stable orbit; (right) pure red noise model. In the center, the emission of Sgr A* in the near-infrared is negligible in comparison to flares. Figure credit Eisenhauer et al. 2011.

moves with a speed comparable to that of light. At this speed, the spot no longer follows the classical Keplerian orbit but instead relativistic orbit; b) Another is frame dragging effects caused by the spinning of the black hole.

Tracking the trajectory of the blob's center of mass will probably give us the answer whether the flares originate from a jet or from hot spots, or from global fluctuations in the central accretion zone. A recent work (Will, 2008) shows that tracking a source close to the event horizon with a 10 µas precision for one year can allow one to probe the above described physics and also to test the 'no-hair theorem' of the black hole.

1.2 Observational techniques

Our aim is to obtain angular information on Sgr A*, therefore the angular resolution of the observing system is a critical parameter. Under seeing limited conditions the angular resolution is (Roddier, 1999)

$$\theta_s = 0.98\frac{\lambda}{r_0}$$

where λ is the observing wavelength and $r_0 \propto \lambda^{6/5}$ is Fried parameter. For typical observing conditions, in a good site, θ_s is slightly below 1 arcsec in the optical-infrared region, clearly outside the requirements for Sgr A*.

1.2.1 Angular resolution of a telescope

Classical diffraction theory relates the angular resolution of an optical system to its aperture diameter D by the 'Rayleigh Criterion'.

$$\theta_{\mathrm{D}} = 1.22\frac{\lambda}{D} \qquad \text{(rad)} \tag{1.1}$$

where λ is the wavelength of observation. The above criterion comes from an approximate estimation of radius of the first null in the Airy pattern (cf. Figure 1.5). The above limit assumes that the incoming wavefront is aberration free, which is the situation for a space telescope or an Earth telescope with a high performance adaptive optics (Hardy, 1998; Roddier, 1999; Davies and Kasper, 2012).

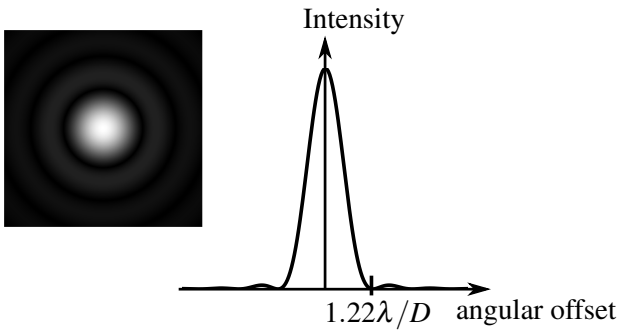

Figure 1.5: Airy pattern: the aberration-free image of a point source in a monochromatic light, imaged with a circular aperture optical system. The first null of intensity happens at $1.22\lambda/D$. Figure adapted from Buscher 2015.

From the above expression (cf. Eq. 1.1), the angular resolution of a typical 8 m class telescope is 56 mas in the K-band (central $\lambda = 2.2\,\mu$m).

The Galactic Center observations presented in Section 1.1 are made with 8-10 meter-class-telescopes and using the adaptive optics. By monitoring stellar motions with these telescopes over a period of several years, scientists have achieved 150-300 micro-arcsec (μas) astrometry. Since the current generation single telescopes do not have the required resolution and the astrometric precision to probe events close to the Schwarzschild radius, various research groups around the world have been putting their efforts to build high sensitive interferometric instruments to achieve the above scientific goals. I will describe them in the following sections.

1.2.2 Interferometry

By combining wavefronts probed by widely separated individual telescopes, the angular resolution can be increased beyond the diffraction-limit of an individual telescope. This technique is called (long baseline) interferometry, where the resolution is no longer dependent on the diameter of the

telescopes but rather on separation (called baseline B) between the telescopes (Monnier, 2003; Glindemann, 2011; Buscher, 2015).

$$\theta_B = \frac{\lambda}{B} \tag{1.2}$$

By combining four 8 m telescopes of the European Very Large Telescope with a baseline of 100 m, a resolution of 12.5 times improvement to a single telescope can be achieved, i.e ~ 4.5 mas in the K-band.

Very Long Baseline Interferometry (VLBI) Recently scientists proposed Event Horizon Telescope (EHT) - a global network of radio telescopes that are placed at various locations on the Earth to deliver a resolution equivalent to that of an Earth size baseline by Very Long Baseline Interferometry (Doeleman et al., 2009). It has the capacity to deliver 21 µas resolution for radiation with wavelength of 1.33 mm.

$$\theta_B = \frac{1.3 \times 10^{-3}\,\mathrm{m}}{12.7 \times 10^{6}\,\mathrm{m}} = 21\,\mu\mathrm{as} \tag{1.3}$$

In this observational technique, a target source is observed simultaneously with all the radio telescopes of the EHT and then the observed data is brought back to a central processing facility where the data is correlated (interfered) and images are reconstructed. The ultimate goal of the EHT is to take images of the effects of strong light-bending (the black hole "shadow') and test the General theory of Relativity (Hollywood and Melia, 1997; Falcke et al., 2000; Johannsen et al., 2016).

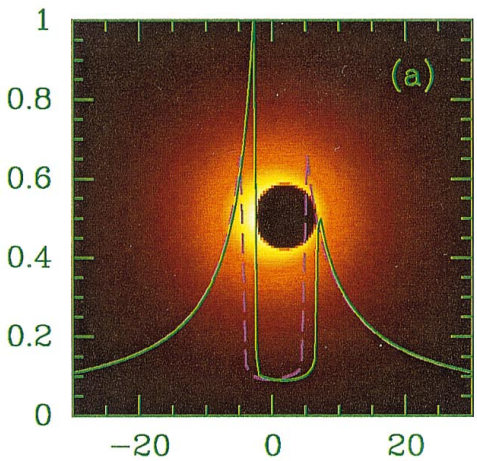

Figure 1.6: A black hole shadow simulated with 1.33 mm wavelength observation. The intensity variations along the X-axis (in arbitrary units) and Y-axis (in distance, r_S) are denoted in solid green and dashed purple curves respectively. Figure credit Falcke et al. 2000.

Few years ago, the EHT successfully observed the event horizon scale structure of the black hole with size ~ 43 µas (Doeleman et al., 2008; Fish et al., 2011; Johnson et al., 2015). They also reported that the correlated flux density of Sgr A* is variable (cf. Figure 1.7).

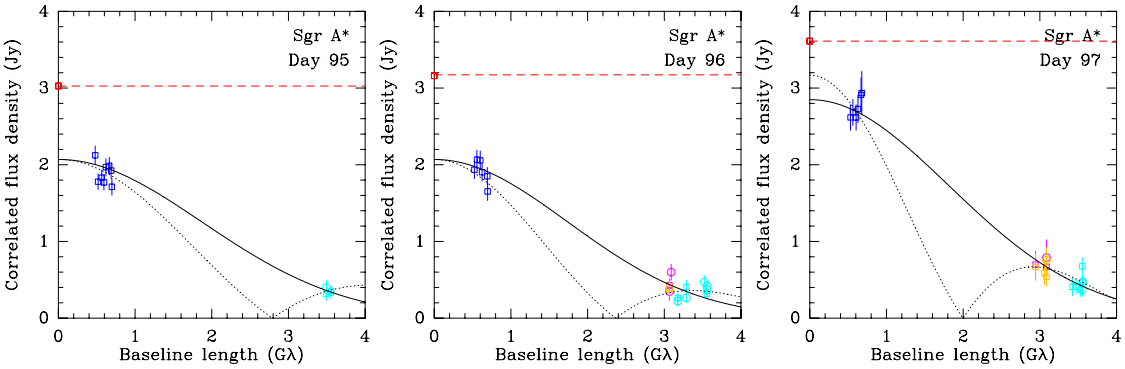

Figure 1.7: Correlated flux density plots of Sgr A* as a function of baseline length. The solid and dashed lines are the best-fit circular Gaussian and ring visibility models respectively for the compact emission in Sgr A*. Fish et al. 2011 reports that the Gaussian model is consistent with the source size of approximately 43 µas on all days. Figure credit Fish et al. 2011.

A recent work proposes a technique to track differential astrometry of the Sgr A* flares at 1.3 mm wavelengths using polarimetry studies (Johnson et al., 2014). The sub-millimeter emission of Sgr A* is due to synchrotron radiation and is thus expected to be highly polarized. Polarimetry observations of the flares allow the possibility of the differential astrometry. Currently, plans are underway to increase the sensitivity of the VLBI array and adding many more baselines to probe physics around the event horizon.

Although the EHT has been producing outstanding results of Sgr A* in complementary to the near-infrared stellar orbital monitoring observations, it has two limitations in studying the physics of the flares. First, the magnitude of the flares is low at 1.3 mm wavelength in comparison to the near-infrared, and significant background emission might be present. Imaging them and measuring the differential astrometry of the flares are very difficult with the claimed EHT resolution and sensitivity. Second, the timing of the project may delay the final observations as the project requires the development and installation of hardware receivers on the numerous antennae to increase sensitivity required for the experiment.

Near-infrared narrow-angle phase-referencing Near-infrared is a critical wavelength regime for the black hole observations for three reasons: a) it allows to study the physics close to the black hole via stellar orbital dynamics which has been proven a highly successful method; b) the density of stars in the near-infrared close to the event horizon is high (100 stars/arcsec^2 with $m_K < 17$ mag within 100 mas field of view Genzel et al. 2010) and that allows us to observe a several targets which have already experienced the effects of the black hole; c) the Sgr A* flares are about one order of magnitude higher at near-infrared than radio wavelengths;

Fortunately, the Very Large Telescope Interferometer (VLTI) of the European Southern Observatory (ESO) could offer 10 µas differential astrometry in the K-band, provided a new instrument is built based on narrow-angle phase-referencing concepts (Shao and Colavita, 1992).

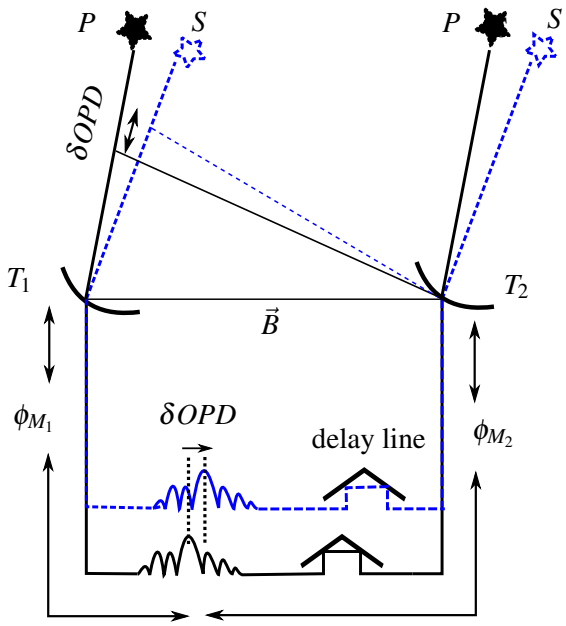

Figure 1.8: The beams of science and reference stars are combined coherently. The internal phase differences between the telescope baseline reference points and the central fringes are measured by a metrology system.

Narrow-angle phase-referencing astrometry works by observing two objects (reference P, science S) simultaneously within the same telescope field of view. Observations of the reference and the science objects made by two telescopes are combined in a reference and a science beam combiners respectively. The differential optical path difference δOPD caused due to the separation of the stars in the sky (cf. Figure 1.8)

$$\vec{\Delta S} = \vec{S} - \vec{P}$$

is proportional to the separation of fringes observed between the two beam combiners as given below

$$\delta OPD = \vec{\Delta S} \cdot \vec{B} + \delta OPD_{\text{atm}} + \delta OPD_{\text{met}} + \delta OPD_{\text{disp}} + \delta OPD_{\text{obj}}, \tag{1.4}$$

where $\vec{B}$ is baseline vector, i.e., separation between the two telescopes, δOPD_{atm} is the atmospheric turbulence contribution to the optical path difference, $\delta OPD_{\text{met}} = \phi_{M_1} - \phi_{M_2}$ is the optical path difference due to internal vibrations and other effects from the telescope to the beam combiner facility, including the delay lines, δOPD_{disp} is the optical path difference error caused due to wavelength dispersion (cf. Section 2.2.3) and δOPD_{obj} is the caused by the intrinsic object shape (for a point source $\delta OPD_{\text{obj}} = 0$).

The differential astrometry equation (Eq. 1.4) becomes

$$\delta OPD = \vec{\Delta S} \cdot \vec{B},$$

provided the atmospheric turbulence is corrected, the baseline vector between telescopes is accurately known, internal light path is accurately measured and corrected by a metrology system and wavelength dispersion is calibrated. The differential astrometry precision of $\Delta S \sim 10\,\mu$as on a baseline $B = 100$ m is achievable provided that the δOPD is measured to an accuracy of 5 nm

$$\Delta S \sim \frac{\delta OPD}{B} \sim \frac{5\text{ nm}}{100\text{ m}}(\text{rad}) = 10\,\mu\text{as}. \tag{1.5}$$

Which is in practice possible with some efforts (cf. Section 2.4.2.8).

1.3 Outline of this thesis

Implementing the narrow-angle phase-referencing is exceedingly difficult in practice at optical/infrared wavelengths. Because the atmospheric turbulence distortions and the instrument/array internal optical path differences are to be corrected up to a fraction of the wavelength, which is of the order of tens of nanometer in the optical/infrared, in comparison to centimeters of radio wavelengths (Colavita, 2009). However, a few interferometers were built by addressing the above difficulties: the first narrow-angle astrometric observations are accomplished with a precision of 160 µas on the Palomar Testbed Interferometer (PTI) (Colavita et al., 1999) and the success of this it led to other narrow-angle astrometry projects such as ASTRA (Woillez et al., 2010) and PRIMA (Delplancke, 2008; Sahlmann et al., 2013). Nevertheless, current facilities do not have the sensitivity and precision required to probe the Galactic Center physics near the event horizon. That is why a new instrument, GRAVITY, has been built. This thesis addresses a particular sub system of GRAVITY, the acquisition camera, that enables accurate beam guiding required to achieve 10 µas astrometry and $\sim$ 4.5 mas interferometric imaging.

In Chapter 2, I introduce the GRAVITY interferometric imaging and narrow-angle astrometry. It starts by describing the important basic aspects of the interferometry, its challenges and then go over into the practical implementation. Chapter 3 describes the design and the hardware concepts of the GRAVITY acquisition camera. The acquisition camera is a beam guiding system. Its data reduction pipeline software plays a crucial role in extracting the aberration parameters of the input telescope beams from its detector images. The image reduction procedures are explained in Chapter 4. Chapter 5 presents the integration of the acquisition camera inside the GRAVITY cryostat and its installation at Paranal Observatory, Chile. Chapter 6 discusses the characterization results of the acquisition camera. An outlook and the conclusions are given in Chapter 7.

1.4 Thesis context: my participation in the GRAVITY instrument project

I joined CENTRA/SIM of Portugal for my PhD in the context of GRAVITY in 2012. CENTRA/SIM is a part of the GRAVITY consortium and responsible for a sub-system, acquisition camera.

My participation in GRAVITY started with optical components testing for the acquisition camera in Lisbon. Where I was involved in the instrument assembly, optical alignments and optical and cryogenics testing of the acquisition camera. In this project, I was primarily responsible for the acquisition camera end-to-end numerical modelling, development of the real-time control software algorithms for the beam guiding and data reduction software, instrument characterization and commissioning of the instrument at the ESO VLTI, Paranal Observatory, Chile. Furthermore, I also led the development of an automatic liquid nitrogen filling controller to test the acquisition camera at cryogenic temperatures.

Chapter 2

The GRAVITY instrument and its subsystems

2.1 Introduction

The high precision narrow-angle astrometry and phase-referenced interferometric imaging required for the Galactic Center black hole experiment is achieved with GRAVITY, using the Very Large Telescope Interferometer. GRAVITY has been built by a consortium, formed by several European institutes, led by the Max Planck Institute for Extraterrestrial Physics (MPE) and including CENTRA/SIM, Portugal. Although the Galactic Center black hole is the primary science target for GRAVITY, it also addresses other science cases (cf. Eisenhauer et al., 2011, for examples).

In practice, implementation of the narrow-angle phase-referencing at optical/infrared wavelengths is rather difficult. The atmospheric turbulence; the knowledge of the accurate baseline vector between any two telescopes and wavelength dispersion are the major sources of the astrometric errors (Shao and Colavita, 1992; Lacour et al., 2014). Previous projects such as PTI (Colavita et al., 1999), the Keck Outrigger astrometry (Hrynevych et al., 2004; Woillez et al., 2010) and the ESO's PRIMA Delplancke 2008; Sahlmann et al. 2013) have shown the importance of building a proper beam stabilization mechanism and laser metrology system to achieve high precision astrometry. Section 2.2 summarizes these narrow-angle astrometry challenges. GRAVITY addresses those difficulties by building several subsystems using current generation technology as described in Section 2.4. This section is preceded by a very brief description of the Very Large Telescope Interferometer. In the end GRAVITY's observational strategy is presented.

2.2 Narrow-angle astrometry challenges

2.2.1 Atmospheric turbulence caused errors

The performance of visible and infrared ground-based telescopes and associated astronomical instruments is significantly limited by the atmospheric turbulence (Hardy, 1998). It degrades the quality of observations and limits the sensitivity towards the fainter astrophysical targets. The design of an instrument for the successful correction of the atmospheric turbulence can be implemented by understanding the following three atmospheric turbulence parameters: the Fried parameter (r_0), the coherence time (τ_0) and the isoplanatic angle (θ_0).

Fried Parameter (r_0) describes the effective telescope pupil over which the root mean square (RMS) wavefront phase error is one square radian and can be expressed in terms of the vertical turbulence distribution, $C_n^2(h)$, and zenith distance, z, as given below (Ishimaru, 1978)

$$r_0 = 0.185 \left(\lambda^{-2} \sec(z) \int_0^{\infty} C_n^2(h) dh\right)^{-3/5} \text{ m}, \tag{2.1}$$

where h is the height above the ground level.

Astronomical seeing is used to indicate how good the observing conditions are. The astronomical seeing can be defined as the diffraction limited image size obtained when a telescope aperture of size r_0 is used

$$\theta_s \sim \frac{\lambda}{r_0}.$$

Coherence time (τ_0) is the timescale difference at which the RMS phase variations over the telescope pupil are one square radian and can be estimated by the expression (Glindemann, 2011)

$$\tau_0 \sim \frac{r_0}{v} \text{ s},$$

where v is the averaged wind-speed. τ_0 sets the temporal correction bandwidth for any atmospheric turbulence correcting system (i.e., adaptive optics: cf. Section 2.4.1 and fringe tracker: cf. Section 2.4.2.6).

Isoplanatic angle (θ_0) is the maximum angular radius at which the RMS error in wavefront phase is one radian and can be estimated from the Fried parameter and the average turbulence height ($\bar{h}$) as given below (Glindemann, 2011)

$$\theta_0 = 0.314 \frac{r_0}{\bar{h}} \text{ rad}. \tag{2.2}$$

The faint astrophysical object's atmospheric turbulence distortions are corrected usually by observing nearby bright star to address the low signal-to-noise ratio (SNR) signals. The above formula, provides the maximum angular radius between the scientific targets and a nearby bright star at which successful correction can be achieved.

With the effects of atmospheric turbulence, the performance of any interferometer will be limited mainly in : a) image blurring and image motion; b) interferometric fringe motion.

2.2.1.1 Image blurring and image motion

With the effects of the atmospheric turbulence, the image of the observed star is split into multiple speckles. The size of each speckle is about the size of the diffraction limit of the telescope (diffraction point spread function). The FWHM of the long integrated speckle image is of the size of the atmospheric seeing at the time of observation (seeing point spread function). It is approximately 1 arcsec in the optical-infrared region at good observing site.

Quasi-diffraction limited imaging can be achieved by correcting the atmospheric turbulence using adaptive optics (Hardy, 1998; Roddier, 1999; Davies and Kasper, 2012). Adaptive optics works by measuring the atmospheric turbulence distortions using a wavefront sensor (by imaging a bright wavefront reference source); modeling an appropriate correction for it; and applying this correction using a deformable mirror (DM). The cycle measure-model-apply must be faster than the coherence time τ_0, which is at the order of a few milliseconds. The wavefront reference source is chosen within the isoplanatic angle distance from the science target so that the correction calculated for the reference is also valid for the science target.

2.2.1.2 Fringe motion

The atmospheric turbulence also induces random piston errors (Glindemann, 2011; Buscher, 2015). The piston error is a phase difference that is constant across the telescope aperture. Although it is, generally, unimportant in a single apperture, for an interferometer the random piston error induces random optical path difference (δOPD_{atm}) variations. As a consequence of that, the fringes of an interferometer are in motion during an observation. If the exposure time of the observation is longer than the atmospheric coherence time τ_0, the random fringe motion will completely blur the fringe contrast and provide low quality visibility and phase measurements.

The atmospheric turbulence caused RMS optical path difference for a given baseline length, B, can be computed as below (Glindemann, 2011).

$$\sigma_{\text{OPD}} = 0.41\lambda \left(\frac{B}{r_0}\right)^{5/6} \tag{2.3}$$

Becasue the wavefront sensors are tied to a single apperture, the adaptive optics system cannot correct the piston variations. However, a fringe tracker system can be used to stabilize the fringes and to restore the fringe contrast. The fringe tracker works by measuring the atmospheric turbulence induced piston error using a fringe sensor and applying the piston correction using delay lines (cf. Section 2.4.2.6). Again the cycle measure-model-apply should be faster than the coherence time. This technology allows the observation of fainter science targets via long temporal integrations by observing the brighter star which is within isoplanatic angular radius.

2.2.1.3 Impact on the astrometry

With the atmospheric turbulence, the astrometric measurements are affected. Shao and Colavita (1992) give an equation to calculate the astrometric error (σ) as a function of the atmospheric turbulence strength, $C_n^2(h)$

$$\sigma^2 \sim 5.25\, B^{-4/3} {\theta_{\rm sep}}^2 t^{-1} \int C_n^2(h) h^2 v^{-1}(h) dh, \tag{2.4}$$

where $\theta_{\rm sep}$ is the separation between two stars in the sky, h is the height above ground level (in meters), t is the observation integration time and $v(h)$ is the wind speed at h. The above expression is applicable for the condition of $\theta_{\rm sep} << B/h$ and $t >> B/v$. For a baseline of $B = 100$ m, the astrometric error is around 10 µas for an integration of $t = 300$ s, at good seeing conditions (Paranal).

2.2.2 Baseline measurement instability

As introduced previously (Eq. 1.4), in the narrow-angle astrometry, the differential separation (differential astrometry) between the reference object and the science object is measured by

$$\delta OPD = \vec{\Delta S} \cdot \vec{B} + \delta OPD_{\rm atm} + \delta OPD_{\rm met} + \delta OPD_{\rm disp} + \delta OPD_{\rm obj}.$$

Where, $\delta OPD_{\rm met}$, $\delta OPD_{\rm disp}$, $\delta OPD_{\rm obj}$ are the differential optical path difference errors in the measurement of the metrology system (see 2.4.2.8), caused by the wavelength dispersion (see 2.2.3) and caused by the intrinsic object shape (for a point source $\delta OPD_{\rm obj} = 0$).

A difficulty in the above equation is the accurate measurement of the baseline vector $\vec{B}$. In order to reach an astrometry of ~ 10 µas, the baseline needs to be measured with an accuracy of a few cm (over the 100 m baseline length). Theoretically the baseline measurement is a well defined quantity, but in practice it is complex because of the occurrence of random motions in the telescope structure and in other optical elements, while tracking the object of interest. Thus a simple definition of the vector connecting one telescope to another no longer valid. In the literature, there are several baselines defined (Colavita et al., 1999; Hrynevych et al., 2004; Sahlmann et al., 2013; Woillez and Lacour, 2013; Lacour et al., 2014) as described below.

Wide angle baseline (WAB) The wide angle baseline is the most commonly used baseline and is related to the absolute angular position of an object in the sky. The wide angle baseline can be defined as the separation between the pivot-points of the telescopes. The pivot-points are the centers of rotation of the telescopes.

Imaging baseline (IMB) A vector connecting the barycentric mean of the effective pupil of each telescope defines the imaging baseline. The effective pupil is described by the weighted average of several pupils in the optical train starting from the telescope pupil to the entrance of the beam combiner pupil (for GRAVITY, beam combiner pupil is the pupil of the single mode fiber,

cf. Section 2.4.2.5). This baseline connects the visibility measured by the beam combiner to the target structure in the sky. There exist two imaging baselines for the dual field interferometer, one for each beam combiner, because each beam combiner has its own effective pupil (different from telescope pupil).

Narrow-angle baseline (NAB) Each telescope has metrology photo-diodes installed in the spider of the secondary mirror. The vector connecting the barycenter of photo-diodes between the two telescopes defines the narrow-angle baseline (in the primary mirror space). This baseline is defined in the telescope coordinates physically. It is used in the astrometric mode and in which both the beam combiners are optically connected by the metrology system.

For more description of the baseline concepts, I refer to the paper written by Lacour et al. (2014). Figure 2.1 presents the all these baselines in the context of GRAVITY.

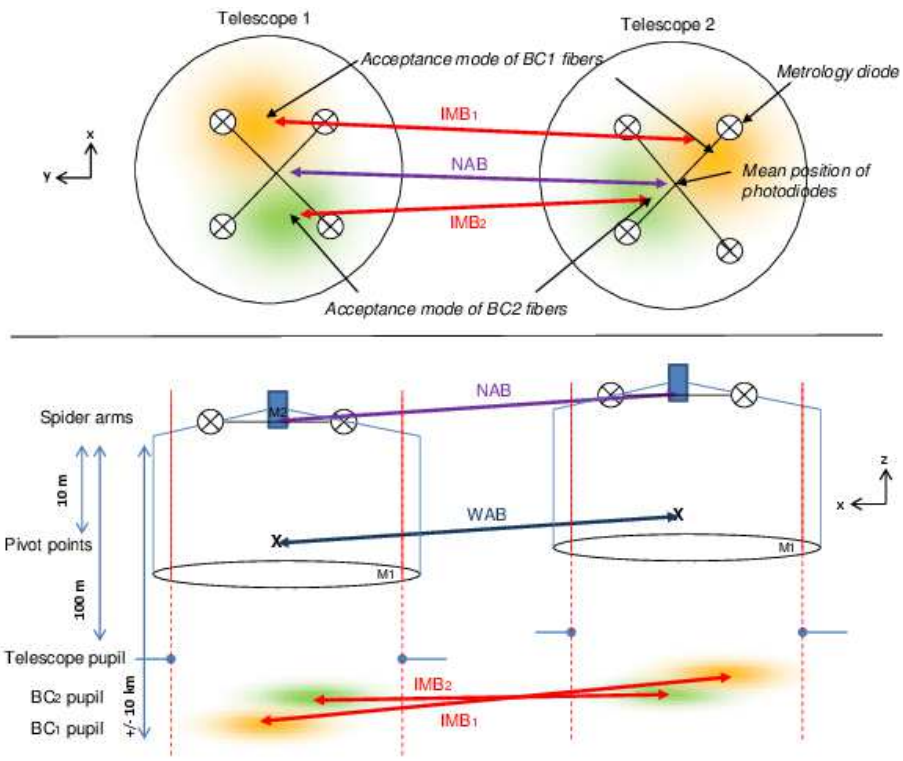

Figure 2.1: For clarity only two-telescope interferometer baseline is presented. The wide angle baseline (WAB) is defined by the two pivot-points. The average of the positions of four metrology diodes (cross-marks) allow us to define the narrow angle baseline (NAB). The imaging baseline is defined by the weighted average of several pupils in the optical train starting from the telescope pupil to the pupil of the fiber. In GRAVITY there are two fibers, one for each beam combiner. Thus it has two imaging baselines IMB1 and IMB2. Figure credit Lacour et al. 2014.

For the accurate astrometric measurements both the narrow angle and the imaging baselines are required to match. The difficulty in measuring the narrow angle baseline is the telescope pointing. Monitoring the effective pupil is the difficult thing for the imaging baseline, because the effective pupil depends on several pupils in the optical train which are under motion (cf. Section 2.3.3

and Figure 2.4) and may suffer pupil vignetting. An astrometric error arises if: a) the metrology beam is not exactly pointing towards the astrophysical source (in the presence of tip-tilt error); b) the limit points of the imaging baseline do not coincide with the narrow angle baseline limit points. The mismatch between the imaging baseline limit-points and the metrology limit-points is the pupil position error.

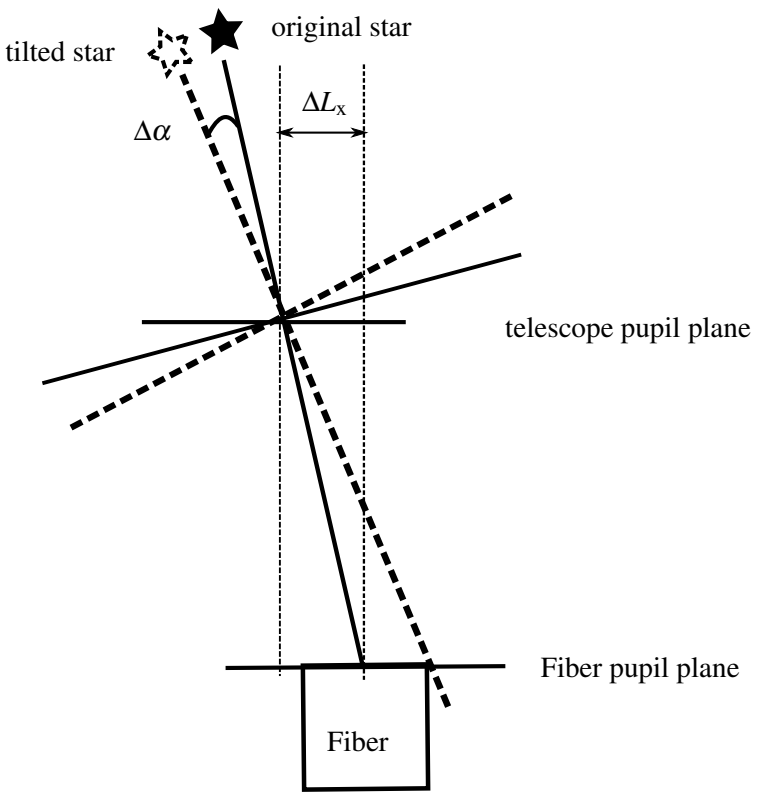

Figure 2.2: A simple description of the field tip-tilts and pupil shifts. The star shown in dashed line is tilted ($\Delta\alpha$) from the original star (solid line). The telescope pupil is shifted laterally (ΔL_x) with respect to the pupil position of the fiber. Due to the field and the pupil shift errors unwanted astrometric errors are experienced. Another effect with the field error is the loss of flux injection of the star's light into the fiber.

The astrometric error associated with the field ($\Delta\alpha$), the lateral pupil (ΔL_x) and longitudinal pupil (pupil defocus, (ΔL_z)) errors can be computed as (cf. Figure 2.2, Lacour et al., 2014)

$$\sigma = \frac{\Delta\alpha\Delta L_x + [1-\cos(\Delta\alpha)]L_z}{B}. \tag{2.5}$$

The typical lateral pupil error is around $\sim 5\%$ of the pupil (~ 0.4 m for an 8 m pupil), which is much larger than the 40 mm required to achieve the 10 μas astrometry. The typical maximum longitudinal pupil error is around 30 km at the UT. Whereas the requirement is 10 km for the 10 μas astrometry (see Table 2.1). Measuring the absolute baseline distance with this accuracy is a non-trivial task with the current technology. Fortunately, it is not necessary to measure the absolute baseline distance between two telescopes but its stabilization would be sufficient as we are interested only in the differential astrometry. The baseline stabilization can be achieved with an

Table 2.1: Astrometric error at the UT due to field and pupil residuals (using Eq. 2.5).

Beam guiding residuals	Residual beam error	δOPD error (One tel.)	astrometry residuals (4 tel.)
Typical errors	$\Delta\alpha \leq 60\,\text{mas}$ $\Delta L_x \leq 0.4\,\text{m}$ $\Delta L_z \leq 30\,\text{km}$	$\leq 153.5\,\text{nm}$	$\leq 633.30\,\mu\text{as}$
Requirements for 10μas astrometry	$\Delta\alpha \leq 10\,\text{mas}$ $\Delta L_x \leq 40\,\text{mm}$ $\Delta L_z \leq 10\,\text{km}$	$\leq 1.95\,\text{nm}$	$\leq 4\,\mu\text{as}$

active pupil stabilization system. By using the GRAVITY acquisition camera (cf. Section 2.4.2.2), the pupil errors are measured and corrected with the pupil actuators so that the mismatch between the imaging baseline and the narrow angle baseline limit points can be minimised.

The field errors are corrected by measuring them with the GRAVITY acquisition camera and the laser based tip-tilt tracking (cf. Section 2.4.2.3).

2.2.3 Wavelength dispersion caused errors

In the narrow-angle astrometry, the instrument internal differential path length error (δOPD_{met} of Eq. 1.4) due to vibrations in the optical train is measured with a metrology system. It works by injecting metrology laser beams into the fibers inside the beam combiner. These beams travel the same optical paths as the science target's light but in the reverse direction. At the telescope, these beams are superimposed and formed fringes. From these fringes the instrument internal differential path length is measured (cf. Section 2.4.2.8).

In GRAVITY, the wavelength of the metrology laser (1.908 µm) used is different from the science wavelength (1.95-2.45 µm, centered at 2.2 µm). With these two different wavelengths, the phase measurements experience wavelength dispersion effect (i.e., change in refractive index with the wavelength) because the beams travel through different media (air, vacuum and fibers). As a consequence of that, the metrology beam and the science target beam experience different optical path lengths. The δOPD_{disp} error caused by dispersion in the air and the fiber can be written as (Lacour et al., 2014)

$$\delta OPD_{\text{disp}}(\lambda_m, \lambda_s) = \Delta_{\text{air}}(n_{\text{air}}^{\lambda_m} - n_{\text{air}}^{\lambda_s}) + \Delta_{\text{fiber}}(n_{\text{fiber}}^{\lambda_m} - n_{\text{fiber}}^{\lambda_s}), \tag{2.6}$$

where Δ_{air} and Δ_{fiber} are the differences of physical lengths in the air and in the fiber respectively. $n_{\text{air}}^{\lambda_m}$ is the refractive index of the air at the metrology wavelength λ_m and $n_{\text{fiber}}^{\lambda_s}$ is the refractive index of the fiber at the science target wavelength λ_s.

Due to the dispersion, the interferometer performance is limited in two ways: a) unwanted astrometric errors are experienced due to different optical path lengths; b) the white light fringe contrast is reduced.

2.2.4 Astrometric error budget

Table 2.2 summarizes the beam guiding and dispersion requirements to keep the astrometry residuals below 10 μas (Lacour et al., 2014).

Table 2.2: The beam guiding requirements for the aimed GRAVITY astrometry (for the UTs for a single baseline).

Error label	beam guiding error	δOPD error	Astrometric error (μas)
Pointing error of the telescope	$\pm 10''$	Baseline error 0.5 mm	5
Structural stability	0.5 mm	Baseline error 0.5 mm	5
Field & lateral pupil error	10 mas & 4 cm	δOPD error 2 nm	4
Field & Longitudinal pupil error	10 mas & 10 km	δOPD error 2 nm	4
Dispersion of air $\Delta_{\rm air}.(n_{\rm air}^{\lambda_{\rm m}} - n_{\rm air}^{\lambda_{\rm s}})$	1 mm . 8×10^{-8}	δOPD error of 80 pm	0.16
Differential length of fiber $\Delta_{\rm fiber}.(n_{\rm fiber}^{\lambda_{\rm m}} - n_{\rm fiber}^{\lambda_{\rm s}})$	10 μm . 2×10^{-4}	δOPD error of 2 nm	4
Non-common path aberrations	$\sim$ 80 nm	δOPD error 3.7 nm	$7.4\sqrt{2}$
Common path aberrations	$0.1\,\lambda_{\rm s}/D$	δOPD error 0.9 nm	$1.8\sqrt{2}$

Having discussed the narrow-angle astrometry challenges, we can now proceed to discuss in detail how the above challenges are addressed. For completeness the VLTI is also very briefly introduced in the next section followed by the GRAVITY instrument in Section 2.4.

2.3 Very Large Telescope Interferometer overview

The Very Large Telescope Interferometer consists of four 8 m Unit Telescopes[1] (UTs) and four 1.8 m Auxiliary Telescopes[2] (ATs). The UTs are located at fixed locations while the ATs can be relocated at any of 30 different positions. A view of the VLTI is shown in Figure 2.3. Below, I describe the VLTI subsystems relevant for GRAVITY.

2.3.1 PRIMA star separator

The main components of the star separator are (Nijenhuis et al., 2008):

[1] https://www.eso.org/sci/facilities/paranal/telescopes/ut.html
[2] https://www.eso.org/public/teles-instr/vlt/auxiliarytelescopes/

Figure 2.3: Aerial view of the ESO's Paranal observatory, in the Chilean Atacama desert. On the platform, four big domes of the four giant 8 m UTs are clearly distinguishable. The four domes in front of the UTs are the four 1.8 m ATs. On the right corner of the platform is the 2.6 m VLT Survey Telescope (VST). A 4.1 m Visible and Infrared Survey Telescope for Astronomy (VISTA), seen in the distance on the next mountain peak from the main platform. Image credit: G. Hüdepohl/ESO.

- **Field splitting** It splits the incoming beam into two beams, each containing the light from one sub-field (object). The field splitting is achieved with a Roof-mirror. This is used for splitting the GRAVITY's wavefront reference source field and science field (cf. Section 2.4).

- **Field selector mirror (STS-FSM)** contains a piezo actuated tip-tilt mirror placed at a pupil plane in the optical path and is used for field adjustments (image shifts in the detector plane). This is used for correcting large tip-tilts which are beyond the correction range of GRAVITY internal tip-tilt actuators.

- **Variable curvature mirror (STS-VCM)** provides a piezo actuated tip-tilt and focus mirror placed at the image plane in the optical path and is used for lateral telescope pupil shift adjustments. This is used for correcting large lateral pupil shifts which are beyond the correction range of GRAVITY internal lateral pupil shift actuators.

2.3.2 Multi-Applications Curvature Adaptive optics (MACAO)

The atmospheric turbulence correction is achieved with MACAO. The MACAO is installed at the Coudé focus and it receives light from the star separators and corrects the wavefront aberrations (caused by the atmospheric turbulence) of the four input UT beams before they are directed to the VLTI delay lines. The MACAO consists of four 60 elements bimorph deformable mirrors and four curvature wavefront sensors for the four UT beams correction and they work in the visible wavelength regime (Arsenault et al., 2003).

2.3.3 Main delay lines

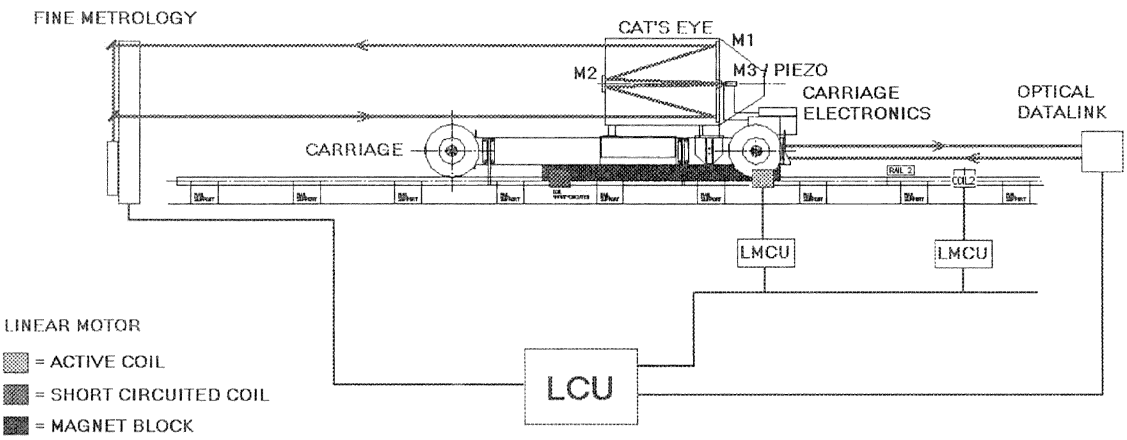

Figure 2.4: Drawing of a main delay line of the VLTI. The delay line carriage rail, cat's eye assembly and the delay line metrology beams (which are used as the reference to apply the exact and accurate amount of delay). The tertiary mirror M3 is the variable curvature mirror. Figure credit Hogenhuis et al. 2003.

The main delay lines are precision carts carrying a cat's eye-type reflector (cf. Figure 2.4) and used to introduce variable optical delay inside the interferometer (Hogenhuis et al., 2003). The delay line system provides two functionalities:

- **OPD compensation** The delay line system corrects three types of optical path differences (OPDs): a) OPDs corresponding to the differences in the optical path lengths caused by the location of different telescopes from the beam combiner; b) OPDs caused due to the location of the astrophysical target in the sky (at Zenith, this OPD becomes zero); c) OPDs induced by the atmospheric turbulence (which are measured by the fringe tracker, cf. Section 2.4.2.6).

- **Preserving wide interferometric field of view** For an interferometer wide field of view observations are possible, if the wavefront sampled by the telescope primary mirror is same as the one entering the beam combiner. While equalizing the optical paths of individual telescopes with the delay lines, the telescope pupil that is entering the entrance of the beam combiner is not in focus. As a consequence of that, the field of view of the interferometer can be small. For the VLTI, a $2''$ field of view is achieved by re-imaging the exit pupil of the telescope at the entrance of the beam combiner, using the delay-line variable curvature mirror (DL-VCM, cf. Figure 2.4) enabled pupil defocus correction (Ferrari et al., 2003). This VCM is used for the longitudinal pupil correction for GRAVITY (cf. Section 2.4.2.2).

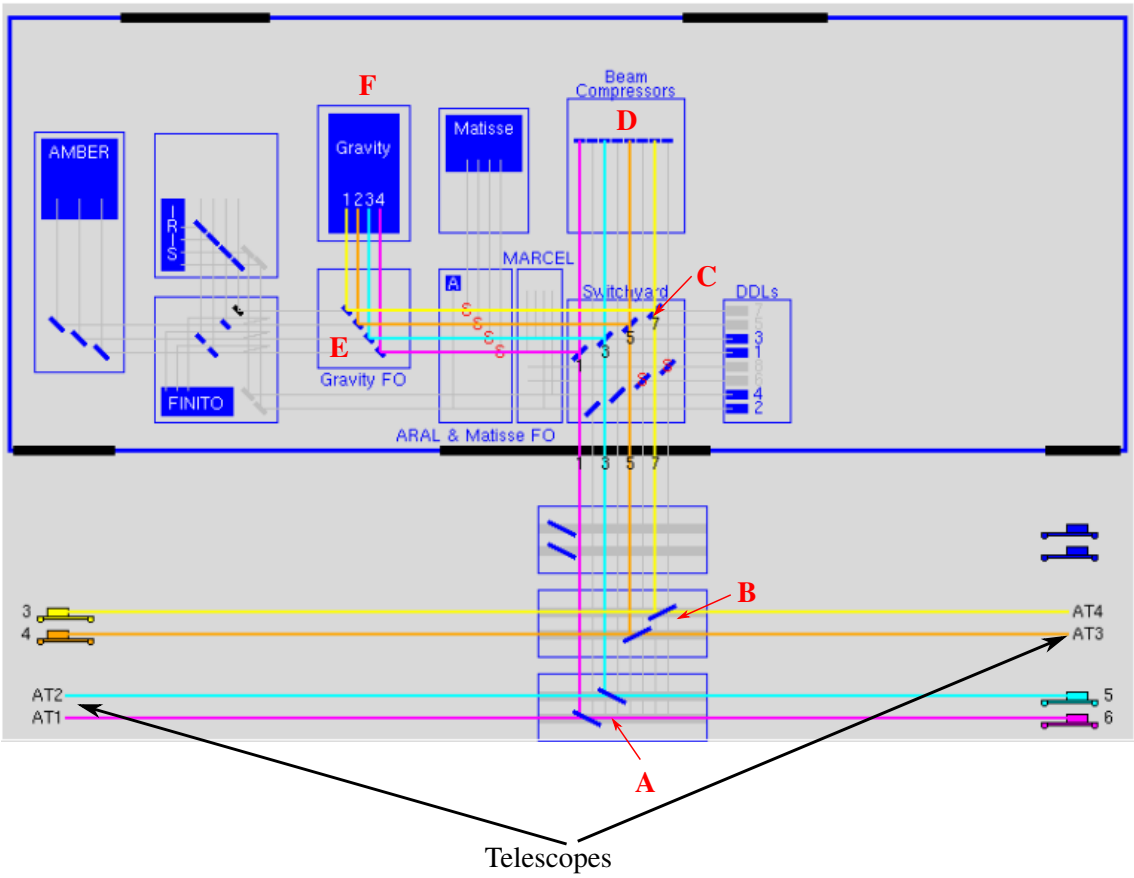

Figure 2.5: Path of the telescope beams into GRAVITY. Here only the ATs are shown. The AT beams are relayed into the VLTI delay lines using the mirrors numbered M12 (labelled **A** and **B** in the figure). The delay lines are in between **A/B** and **C**. For the ATs the switch-yard (**C**) is used to relay the beams directly toward the GRAVITY feeding optics (**E**). For the UTs, the input beams are relayed first to the beam compressors (**D**) and there they undergo beam resizing from 80 mm beam to 18 mm. Once the beams are resized, they enter GRAVITY (**F**) via the GRAVITY feeding optics. Please see the text for the explanation of subsystems.

2.3.4 The path of GRAVITY beams

The schematic overview of the GRAVITY-VLTI system is shown in Figure 2.5. A beautiful animation video of the star's light ray path through GRAVITY is available elsewhere[3]. A short description of the involved subsystems in the optical path is described below.

Beam-compressor The UT beams has 80 mm size and the AT beams has 18 m size. The UT beams are compressed by the beam-compressor to match the AT beam sizes and to provide the same beam diameter for GRAVITY or for any other interferometric instruments while observing whether the UTs or the ATs.

[3] http://www.eso.org/public/videos/eso1622b/

Switch-yard Contains a set of configurable mirrors, which reflect the incoming compressed beams towards GRAVITY.

GRAVITY feeding optics The telescope beams coming from the switch-yard are fed (by means of reflection) to the GRAVITY beam combiner.

The locations of AMBER, FINITO and MATISSE shown in Figure 2.5. They are the other interferometric instruments[4]. IRIS is the infrared image sensor. MARCEL provides four laboratory beams for the instrument calibrations. The location of PIONIER is not depicted. MATISSE is not yet installed.

2.4 GRAVITY overview

In order to understand better the roles of the different GRAVITY subsystems I start by presenting the GRAVITY observational principles for the UTs as shown in Figure 2.6. GRAVITY observes three objects for the astrometric observations: a wavefront reference object, a phase-reference object and a science target. The atmospheric wavefront distortions are corrected using a near-infrared adaptive optics system (cf. Section 2.4.1) observing IRS 7 as the wavefront reference ($m_{\rm K} = 6.5$ mag, separated by $5.57''$ from Sgr A*). IRS 16C ($m_{\rm K} = 9.7$ mag, located $1.23''$ from Sgr A*) is used as the astrometric phase-reference object and for the fringe-tracking (cf. Section 2.4.2.6). The adaptive optics system is not available for the ATs, thus GRAVITY observes the phase-reference object and the science targets only.

In general GRAVITY has two observing modes: a) single field mode; b) dual field mode. In the single field mode, the brightest target's light is shared between the fringe tracker and the science spectrometer. In the dual field mode, two different targets are observed: a bright one for the fringe tracker; a faint one for the science spectrometer.

The wavefront reference object and the VLTI beam (contains the phase-reference and the science targets) are separated by the star separator (cf. Section 2.3.1). The wavefront sensor reference object is sent to the Coudé infrared adaptive optics train and the VLTI beam is sent towards the VLTI delay lines: they ultimately reach the GRAVITY beam combiner (cf. Section 2.4.2).

2.4.1 GRAVITY-Coudé Infrared Adaptive Optics (CIAO)

The Galactic Center is highly obscured in the visible wavelengths and has no bright guide stars for visible wavefront sensing. For this reason, four dedicated near-infrared wavefront sensors have been developed, one for each telescope, working in the H and K-bands (Kendrew et al., 2012; Deen et al., 2014). These have been installed at the Coudé lab. Each wavefront sensor uses a Shack-Hartmann lenslet (9×9 sub-apertures) and images IRS 7. The CIAO units use state of the art technology avalanche photo-diode (APD) detectors from SELEX. The SELEX detectors provide 1 kHz detector frame rate with ultra low noise (readout noise $3e^{-}$/pixel) (Finger et al.,

[4] https://www.eso.org/sci/facilities/paranal/telescopes/vlti/instruments.html

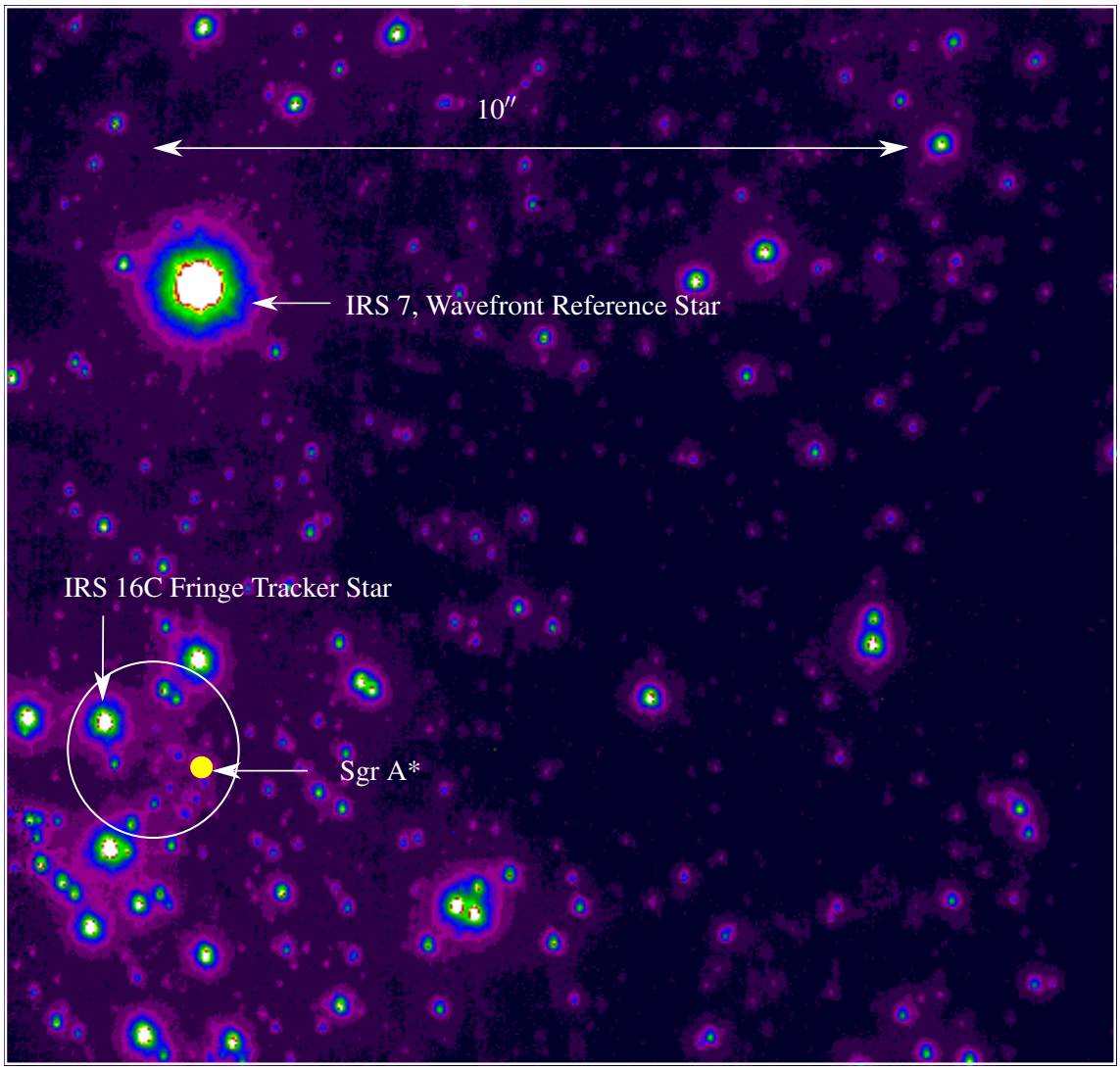

Figure 2.6: Observational strategy for GRAVITY. IRS 7 is used as the wavefront reference source for the Galactic Center observations. IRS 16C is used as the fringe tracker phase-reference star and using it fringes are stabilised. This figure is a NACO observation (Lenzen et al., 2003), taken from the ESO science archive facility.

2014). The CIAO units sense the wavefront distortions of the four input telescope beams and the corrections are applied to the incoming beams using the already existing MACAO deformable mirrors (cf. Section 2.3.2).

2.4.2 GRAVITY beam combiner instrument

The GRAVITY beam combiner instrument implements the coherent beam combination of the four input telescope beams. It consists of several subsystems (cf. Figure 2.7 & Figure 2.8), detailed in the following sub-sections.

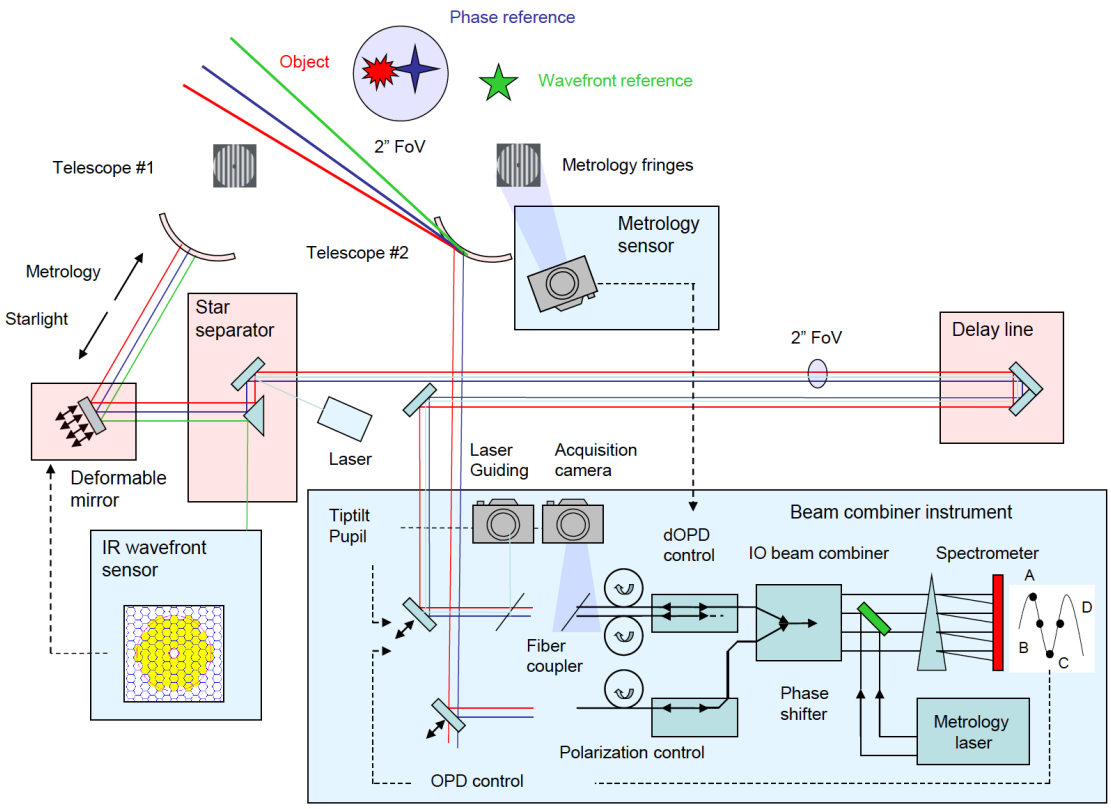

Figure 2.7: The working principle of the GRAVITY beam combiner instrument. The four UTs or the ATs of the VLTI are combined coherently. Infrared wavefront sensor (green color) images the object outside the 2″ field of view, measures the atmospheric turbulence perturbations and corrects with the telescope deformable mirrors. The objects within 2″ field of view are combined in the two interferometric beam combiners – one for fringe-tracking (blue lines) and one for the science object (red lines). The acquisition camera and various laser guiding systems implement the beam stabilization. A dedicated laser metrology traces the optical path length differences for narrow angle astrometry. See the body text for more details. For clarity, only two telescopes, one beam combiner, and one wavefront sensor are shown. Figure credit: Eisenhauer et al. (2011).

2.4.2.1 Fiber coupler and fiber control unit

The fiber coupler unit (cf. Figure 2.9 for the optical layout Pfuhl et al., 2014; Pfuhl, 2012) provides several functionalities:

- **Feeds light into fibers** The beam combination is implemented in GRAVITY using the fiber-fed integrated optics. The purpose of the optical fibers is to provide a single-mode filtering of the incoming wavefront and to transport the light into the integrated optics beam combiner. The fiber coupler provides the optics to inject the light into the fibers: a relay optics and an off-axis parabolic mirror are used to implement it. The fibers are adjusted to the parabolic mirror focus using piezo actuated X, Y and Z-stages.

- **Fibers** The scientific working wavelength of GRAVITY (the K-band, centred at 2.2 µm) requires fluoride fibers.

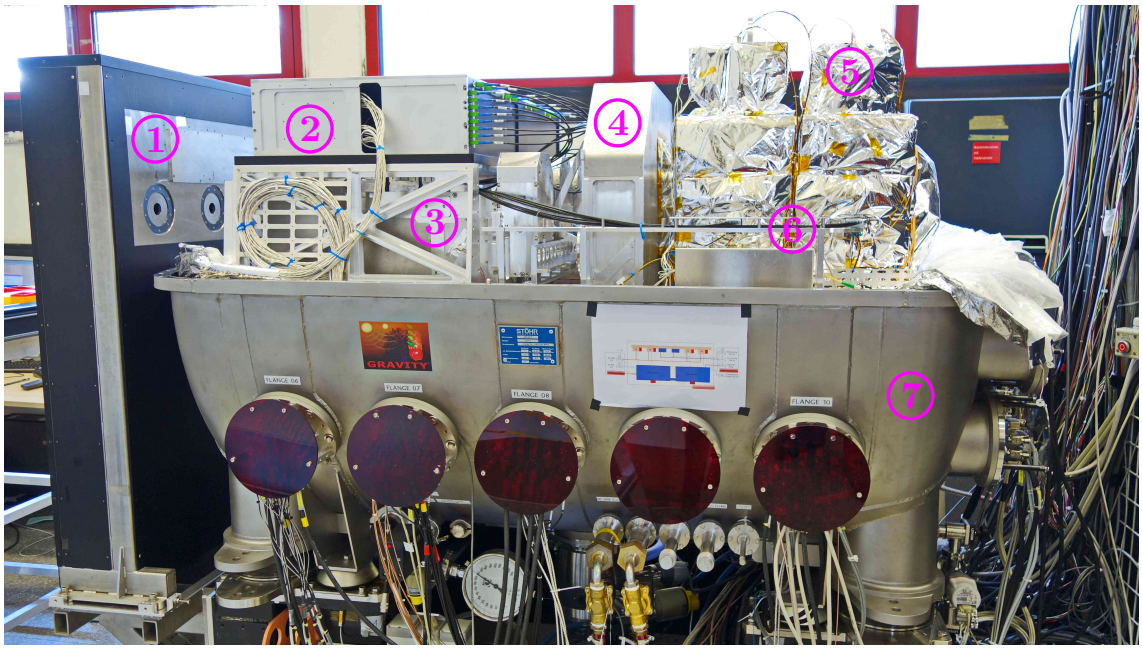

Figure 2.8: Overall view of the GRAVITY beam combiner instrument. 1 – Calibration Unit; 2 – fiber control unit; 3 – fiber coupler; 4 – acquisition camera; 5 – metrology injection; 6 – two spectrometers (fringe tracker and science spectrometer); 7 – cryostat. See the text for the description of each sub system. Image credit GRAVITY consortium.

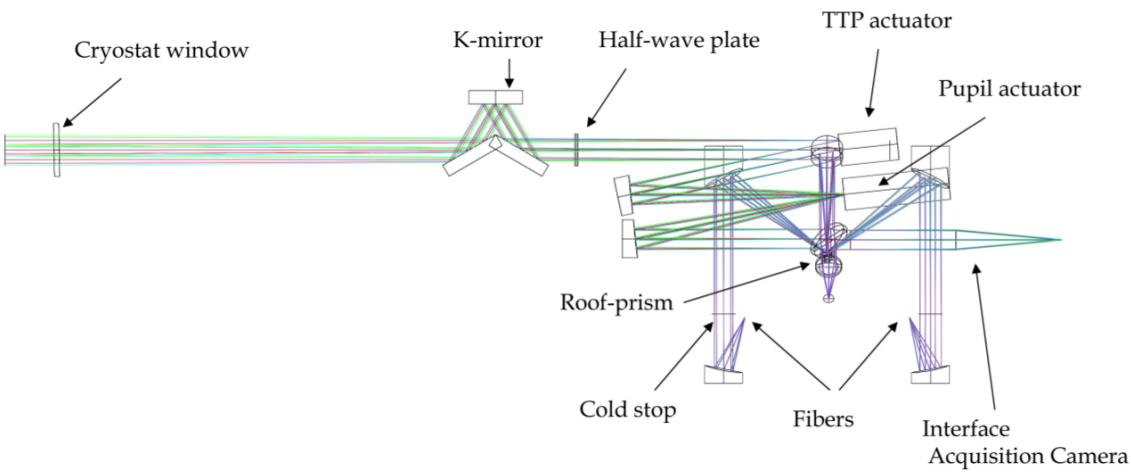

Figure 2.9: Optical layout of the fiber coupler (see text for details). Figure credit Pfuhl 2012.

- **Roof-Prism** A roof-prism is used to split the field. In the dual field mode, the fringe tracker and science objects are separated by the Roof-Prism and injected into respective fibers. In the single field mode, the Roof-Prism acts as a beam-splitter and sends the same object light into both the fibers.
- **Derotation** A motorized K-mirror implements field de-rotation.
- **Half wave-plate** A motorized half-wave plate is used to rotate the linear polarization.

- **Field and pupil correction mirrors** It provides a piezo actuated tip-tilt and piston mirror (TTP) located at a pupil plane in the optical path to correct field motions. Furthermore, it provides a piezo actuated pupil motion control mirror (PMC) located at a field plane in the optical path to correct pupil lateral shifts.

- **Dichroic beam splitter** A dichroic beam splitter reflects the K-band into the fibers (> 1.9 µm) and transmits the H-band light (centered at 1.65 µm, band width $\sim$ 1 µm) into the acquisition camera.

- **Pupil reference laser** For the pupil tracker calibration, it provides an internal calibrator source.

- **Metrology reference** A photo-diode behind the dichroic provides an internal reference signal for the laser metrology.

The fiber control unit provides the functions to adjust the optical path length by stretching the fibers and to adjust random polarization rotation angles of the fibers (non-birefringent fluoride fibers). The random rotation of the polarization by the fibers is compensated with motorized polarization rotators to align the polarization of each telescope. This step improves the fringe contrast. The optical path length of the fibers can be adjusted by stretching the fibers, which are wrapped around a piezo ceramic cylinder.

In GRAVITY random field motions are detected by two sensors: a) acquisition camera; b) laser guide star tip-tilt tracking system. The acquisition camera measures them by imaging astrophysical targets (in H-band). Whereas the laser guide star tip-tilt tracking system (cf. Section 2.4.2.3) is used to measure the field motions caused by the VLTI tunnel atmosphere. These systems are described below.

2.4.2.2 Acquisition camera

In general, the acquisition camera provides four functionalities to characterize the input beams of the four telescopes.

- **Field tracking** The CIAO simulations (Clénet and Gendron, 2011) predict that it corrects atmospheric turbulence of the UT beams with tip-tilt residuals of around 10 mas RMS. The field tracker tracks these residuals for every 0.7 s. For the ATs there is no adaptive optics and so the slow random tip-tilts are tracked by the acquisition camera. By stabilizing these tip-tilts and knowing the star position on the acquisition camera detector, the star's light is injected efficiently into the single mode fiber.

- **Pupil tracking** In between the telescope pupil and the beam combiner, there exists several optical pupils that are under motion due to the optical train vibrations (caused while tracking the object of interest with the delay lines). These pupil motions are measured by imaging four external laser beacons (cf. Figure 2.10) installed on the spiders of secondary mirror

(M2) of the telescopes. A 2×2 lenslet for each telescope is used to measure both the lateral and longitudinal (defocus) pupil shifts.

- **Aberration tracking** The CIAO system sits in the Coudé laboratory, before the VLTI delay line tunnel. CIAO corrects the incoming distorted wavefronts with respect to its reference flat wavefront. However, the VLTI delay lines (laboratory tunnel) are not filled with vacuum. Due to the strong winds at the Paranal Observatory, bad seeing in the tunnel (via chimney effect) is experienced. The aberration sensor of the acquisition camera measures quasi-static wavefront aberrations and non-common path errors between the CIAO systems and the GRAVITY beam combiner, by imaging astrophysical targets using 9×9 lenslet based Shack-Hartmann sensors.

- **Pupil imager** Re-images the telescope exit pupils. It is used for monitoring the telescope pupils during the observations.

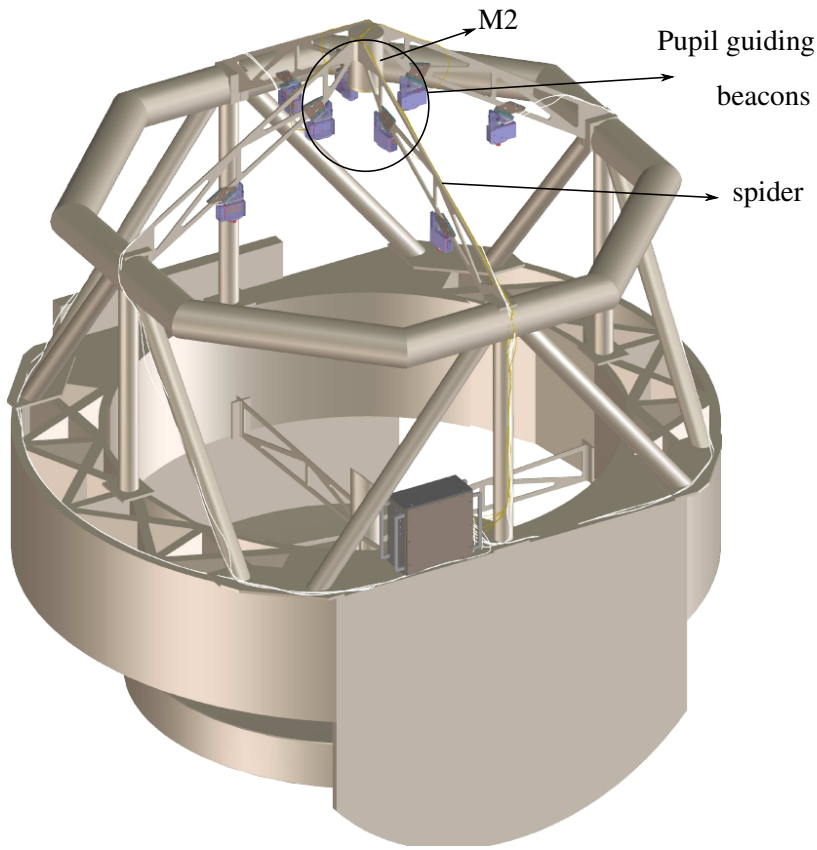

Figure 2.10: Drawing of pupil guiding beacons (green boxes inside the black-circle) and Metrology receiver diodes (green boxes outside the circle) installed on a AT. Figure courtesy: Marcus, H.

The acquisition camera is the work package of my thesis and is described in full detail in Chapters 3 to 6.

2.4.2.3 Laser based tip-tilt tracking

The tunnel seeing is dominated by tip/tilt jitter, which contributes 90% of the wavefront variance (Hippler and Hormuth, 2010). These tip-tilts are under motion with a speed of milliseconds. But the acquisition camera cannot track these fast field motions due to its slow frame rate. An external laser based tip-tilt tracking system has been built to track these tip-tilts with a speed of 1 kHz. It works by injecting a laser beacon beam for each telescope at the star separator and imaging those beams inside GRAVITY using position sensitive diodes (Pfuhl, 2012).

2.4.2.4 Beam stabilization actuators

By using the above sensor measurements the field and the pupil stabilizations of the beams are achieved by two kinds of actuators: a) the VLTI actuators; b) the GRAVITY internal actuators. The PRIMA star separator associated field selector mirror (STS-FSM), variable curvature mirror (STS-VCM) and main delay-line's variable curvature mirror are part of the VLTI actuators. The GRAVITY internal actuators consist of dedicated fast moving tip-tilt and piston mirror and the pupil correction actuated mirrors (cf. Section 2.4.2.1). Small tip-tilts and lateral pupil shifts that are usually found during the closed loop guiding are controlled by the internal actuators. Whereas the large shifts are offloaded to the VLTI actuators. The longitudinal pupil shifts are always corrected by the delay-line variable curvature mirror.

2.4.2.5 Integrated optics

The integrated optics chips implement the actual beam combination of the telescope beams. In each chip, waveguides are realized by doping silica layers with varying refractive indices (Jocou et al., 2010; Perraut and Jocou, 2015). It provides simultaneous pair-wise combination for six baselines existing for the four telescopes. The ABCD sampling for each interferogram is implemented with internal phase-shifters and splitters as shown in Figure 2.11. It provides 24 outputs for the 4 input telescope beams (i.e., 6 baselines $\times$ 4 ABCD outputs). From these outputs the fringe visibility and the phase are estimated.

The integrated optics based beam combination is chosen for GRAVITY over classical beam combination because it provides several advantages such as: a) spatial filtering of the incoming wavefront using the single mode fiber property; b) compactness; c) stability; d) easy maintenance (no alignment required); and its successful usage in previous interferometry projects (especially PIONIER, Bouquin et al. 2011). However, the major disadvantage of it is the moderate throughput ($\sim$ 50%), because of several absorptions in the chip and the fiber.

In GRAVITY two integrated chips are used one for the fringe tracker spectrometer and other for the science spectrometer. The fringe tracker spectrometer is optimized for the highest optical transmission and high speed with a low spectral resolution of $R \sim 5$ and the other spectrometer provides spectrum with three selective modes low, medium and high spectral resolutions respectively (cf. Section 2.4.2.7).

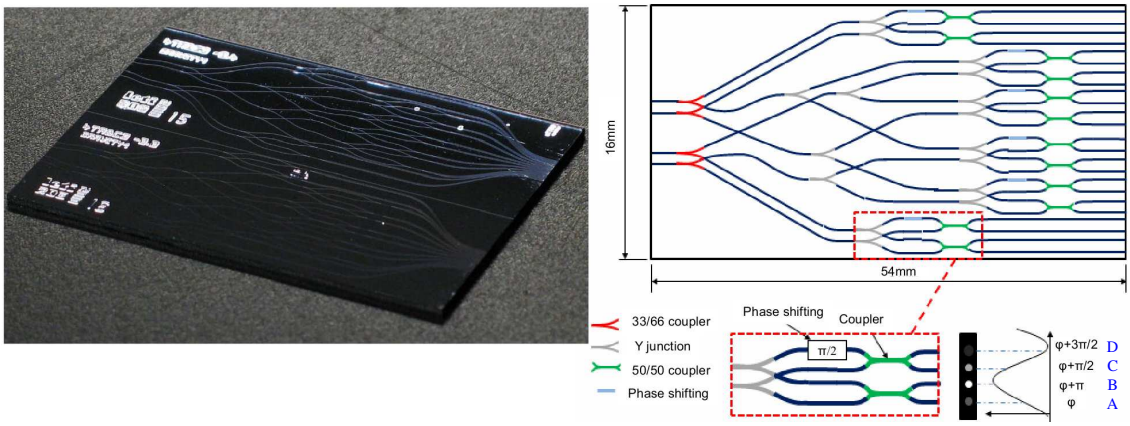

Figure 2.11: Left: Integrated optics beam combiner used in the science and the fringe tracker spectrometers; Right: Description of the beam combiner (top) and of the ABCD cell (bottom). Figure credit Perraut and Jocou 2015.

2.4.2.6 Fringe tracker

As mentioned earlier, the atmospheric piston induced fringe motion is a major limiting factor for the sensitivity of ground-based optical long-baseline interferometers (cf. Section 2.2.1.2). The GRAVITY fringe tracking system tracks the random atmospheric pistons and applies the correction through a fast feedback control loop ($\sim$ 1 kHz). This stabilization of the fringe to a fraction of the wavelength allows a long exposure integration for the science target without smearing its fringe visibility and therefore improves the sensibility of the instrument. Small piston offsets are corrected with the internal TTP mirror actuator and the large piston offsets are offloaded to the main delay lines for the correction.

Apart from its role in the sensitivity improvements, the fringe tracker also plays a crucial role in the astrometric measurements. The term δOPD in Eq. 1.4 is the fringe separation caused by the separation of the phase-reference object and the science target. This term can be rewritten in terms of phase measurements (i.e., phase-reference object phase ϕ_P and the science target phase ϕ_S) as given below

$$\delta OPD = (\phi_S - \phi_P)\frac{\lambda_s}{2\pi}, \tag{2.7}$$

where the phase of the phase-reference object ϕ_P is obtained from the fringe tracker measurements. λ_s is the wavelength of the science beam (K-band, centered at 2.2 µm).

The fringe tracker gets the input signal from the integrated optics and is dispersed by a double prism (Choquet et al., 2010). A Wollaston prism optionally allows the polarimetric separation of the input signal. The fringe tracker is optimized for high speed by recording the fringes on the APD arrays based detector.

The stabilization of fringe motion is implemented in three steps similar to the adaptive optics. In the first part detector images are acquired and from them the phase delay (from fringe phase) and group delay (differential phase associated from different wavelengths) are computed for each

of the six baselines. In the second step correction commands are calculated. In the third they are applied to the piston actuators. The fringe tracker uses the Kalman controller algorithms for optimum correction of the atmospheric and vibration-induced pistons (Menu et al., 2012).

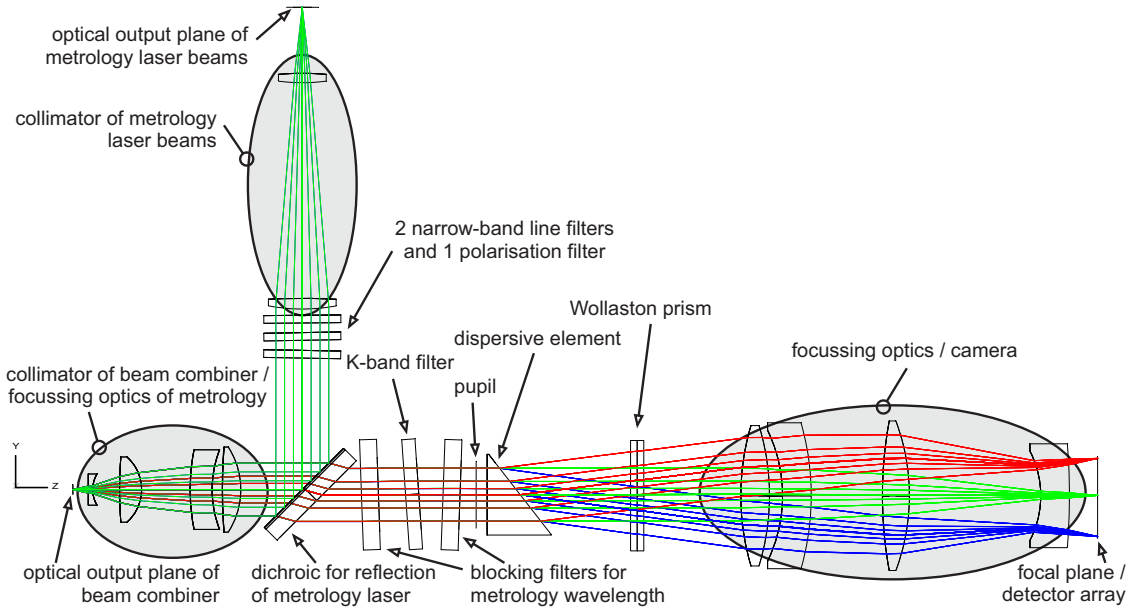

Figure 2.12: The optical layout of the science spectrometer. The output of the integrated optics chip (bottom left of this figure) is dispersed by a grism, split by polarization and imaged on the detector. The K-band filter blocks the metrology beam towards the science detector. The injection optics of metrology feeds metrology laser beam into integrated optics. Figure credit Straubmeier et al. 2014

2.4.2.7 Science spectrometer

The science spectrometer disperses the science target fringes. It is optimized to operate with fainter targets and provides three spectral resolution modes (Straubmeier et al., 2014): a) low (R $\sim$ 22); b) medium (R $\sim$ 500); and c) high (R $\sim$ 4000). The medium and high spectroscopy are achieved with grisms and whereas the very low resolution is implemented with a prism. A Wollaston prism is used to split the polarization. The spectrum signals are imaged on a 2048 $\times$ 2048 pixel based HAWAII 2RG detector. The science spectrometer measures the phase of the science target ϕ_S (cf. Eq. 2.7). Figure 2.8 presents the optical design of the science spectrometer.

2.4.2.8 Laser metrology

As introduced earlier, instrument internal vibrations from the telescope to the beam combiner facility are troublesome for high precise astrometric measurements. This optical path length error ($\delta OPD_{\rm met}$, cf. Eq. 1.4) through the VLTI and the GRAVITY beam combiner has to be known at nanometer level of accuracy. In GRAVITY, these measurements are achieved with a laser metrology system (Gillessen et al., 2012; Gillessen, 2015).

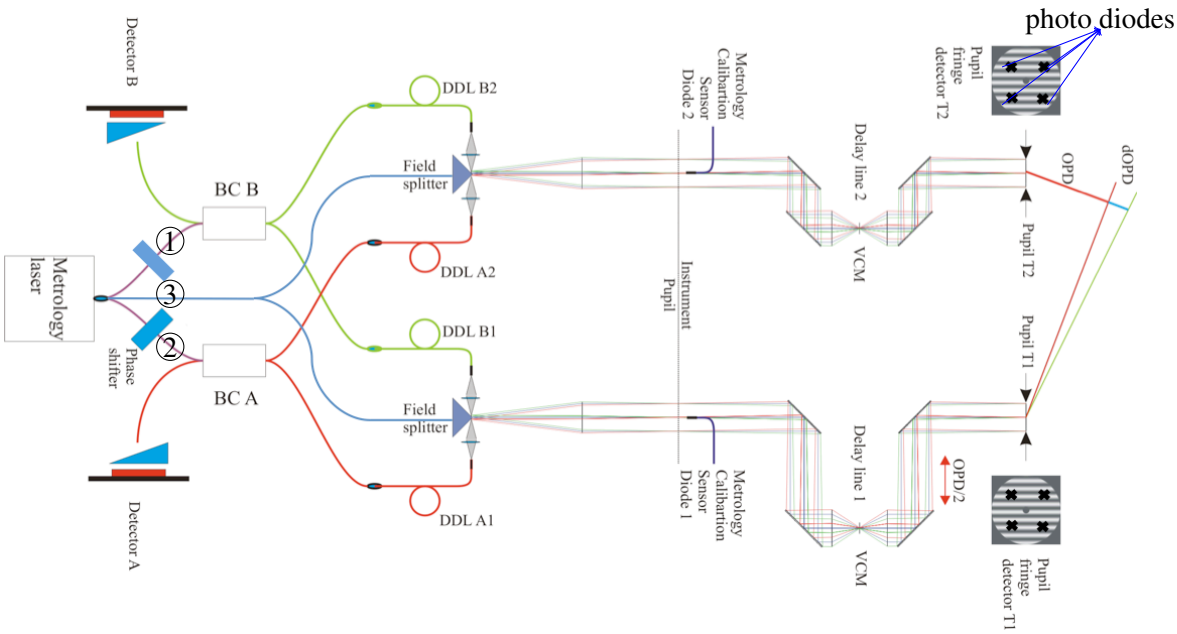

Figure 2.13: The principle of metrology system. Two metrology laser beams (violet in color, noted 1 and 2) are back-propagated from the GRAVITY beam combiners (BC A and BC B) to the telescope secondary mirror (M2) through the same path as the science light (red and green) does forwards. A third bright beam (noted with 3) is injected bypassing the fiber elements (to reduce the beam back-scattering within the fibers) and superimposed with other two. The three-beam fringe pattern is detected at the telescope secondary mirror spiders by sampling the pattern at four locations with photo-diodes. Figure credit Gillessen 2015.

The working principle of the laser metrology is to split a laser beam into two beams with a fixed phase shift and inject them into the integrated optics (Figure 2.13). This is done in the backward direction, through the same path as that of the science light (which moves forwards). A bright third beam with the same wavelength is injected bypassing the fiber elements (to suppress back-scattering in the fluoride glass based fibers) and superimposed with other two beams at the telescope primary space to produce a three beam interference pattern. The three-beam fringe pattern is detected at the M2 spiders by sampling the pattern at four locations with four photo-diodes (cf. Figure 2.10). Using this fringe pattern the instrument internal phase is detected. The system is designed in a novel way such that to measure the $\delta OPD_{\mathrm{met}}$ with a residual RMS error of less than 1 nm (Gillessen et al., 2012).

The metrology laser injection optics is embedded within the spectrometers. The metrology laser beams are collimated, relayed and finally focused onto two of the 24 integrated output channels by using dedicated optics as shown in Figure 2.12.

2.4.2.9 Calibration Unit

In order to test the functionalities of GRAVITY, laboratory telescope beams and stars are generated as part of the Calibration Unit subsystem (Blind et al., 2014). It generates: a) two stars with Strehl

ratios of more than 95% to calibrate and test the subsystems; b) four metrology receiving diodes to test the metrology and; c) four pupil guiding reference laser beacon beams are simulated with a multimode fiber and by using an aluminum mask consisting of four holes. These are used to test and calibrate the acquisition camera pupil tracker. The calibration unit also provides the possibility of inserting linear polarizing filter and rotating phase screens for simulating random atmospheric seeing residuals. This unit is attached in front of the cryostat entrance window of GRAVITY.

2.4.3 Data reduction pipeline

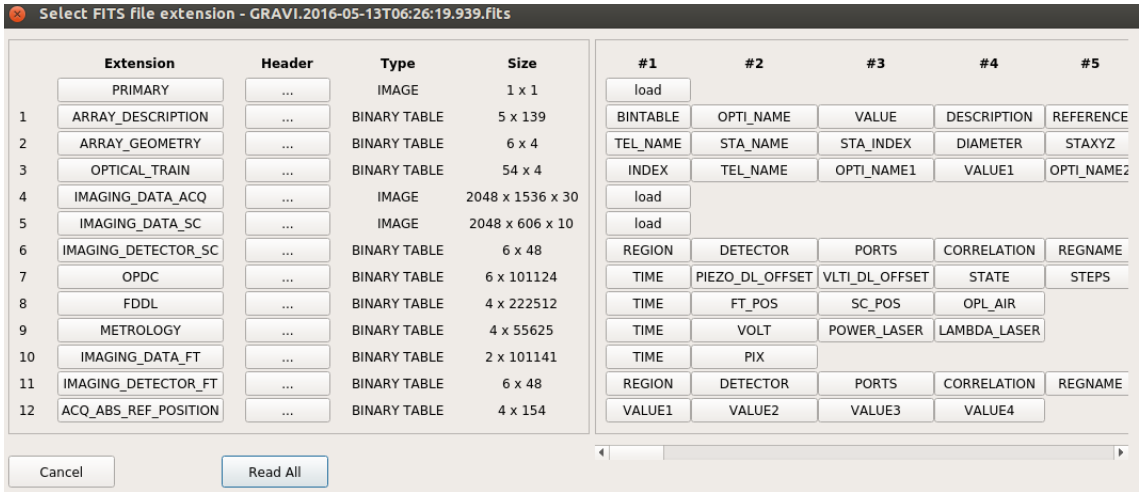

	Extension	Header	Type	Size	#1	#2	#3	#4	#5
	PRIMARY	...	IMAGE	1 x 1	load				
1	ARRAY_DESCRIPTION	...	BINARY TABLE	5 x 139	BINTABLE	OPTI_NAME	VALUE	DESCRIPTION	REFERENCE
2	ARRAY_GEOMETRY	...	BINARY TABLE	6 x 4	TEL_NAME	STA_NAME	STA_INDEX	DIAMETER	STAXYZ
3	OPTICAL_TRAIN	...	BINARY TABLE	54 x 4	INDEX	TEL_NAME	OPTI_NAME1	VALUE1	OPTI_NAME2
4	IMAGING_DATA_ACQ	...	IMAGE	2048 x 1536 x 30	load				
5	IMAGING_DATA_SC	...	IMAGE	2048 x 606 x 10	load				
6	IMAGING_DETECTOR_SC	...	BINARY TABLE	6 x 48	REGION	DETECTOR	PORTS	CORRELATION	REGNAME
7	OPDC	...	BINARY TABLE	6 x 101124	TIME	PIEZO_DL_OFFSET	VLTI_DL_OFFSET	STATE	STEPS
8	FDDL	...	BINARY TABLE	4 x 222512	TIME	FT_POS	SC_POS	OPL_AIR	
9	METROLOGY	...	BINARY TABLE	4 x 55625	TIME	VOLT	POWER_LASER	LAMBDA_LASER	
10	IMAGING_DATA_FT	...	BINARY TABLE	2 x 101141	TIME	PIX			
11	IMAGING_DETECTOR_FT	...	BINARY TABLE	6 x 48	REGION	DETECTOR	PORTS	CORRELATION	REGNAME
12	ACQ_ABS_REF_POSITION	...	BINARY TABLE	4 x 154	VALUE1	VALUE2	VALUE3	VALUE4	

Figure 2.14: A typical GRAVITY observation's fits header (data format). There are several extensions. Extensions IMAGING_DATA_SC, IMAGING_DETECTOR_FT and IMAGING_DATA_ACQ provide images of the science spectrometer, the fringe tracker and the acquisition camera respectively. The extension METROLOGY provides the data of the laser metrology system in the binary table.

GRAVITY produces mainly 4 different sources of data (cf. Figure 2.14):

- Data from the science spectrometer detector: dispersed interferometric fringes and phases.
- Data from the fringe tracker detector: interferometric fringes and phases.
- Data from the metrology: $\delta OPD_{\mathrm{met}}$ measurements.
- Data from the acquisition camera detector: direct imaging of the astrophysical targets in the H-band; images of the pupil tracker and the Shack-Hartmanns.

To calibrate and reduce the above raw data, the data reduction pipeline provides several software recipes (Lapeyrere, 2015). The outputs of the data reduction pipeline are the interferometry standard complex visibilities, phases and reconstructed interferometric images. This software is developed using the ESO ANSI C Common Pipeline Library (CPL) (McKay et al., 2004). The

interferometric image reconstruction is implemented with MiRA: image reconstruction for optical interferometry[5] in YORICK (see Berger et al., 2012, for a review on imaging techniques for optical interferometry).

2.5 Observational strategy

A typical observation with GRAVITY consists of three steps.

- First, the GRAVITY subsystems are calibrated before the start of the night observations using the Calibration Unit (cf. Section 2.4.2.9). These calibrations include several aspects starting from measuring the reference positions for the sensors and to the calibration of the pixel-to-visibility-matrices (P2VM Tatulli et al., 2006) for the both beam combiners (the fringe tracker and the science spectrometer).

- Second, interferometric visibility calibrators are observed. These calibrators are selected close to the science targets considering the atmospheric anisoplanatism. In the dual field mode, the zero point of the metrology is calibrated by swapping the two targets.

  The acquisition of calibrators data is described as follows. Once the telescopes guiding has started, with the help of star separators, the telescope beams are relayed such that the wavefront sensor reference star is sent to the adaptive optics trains and the other beam towards the VLTI delay lines. After the adaptive optics loop is closed, the beam guiding loops (field guiding and pupil guiding) are closed. This beam guiding includes the field, pupil and focus stabilization. Then the brightest object and the science object on the acquisition camera are picked and they are injected into the fringe tracker and the science fibers respectively. In the next step, the fringe tracker optimizes its flux by scanning the tip-tilt mirrors of GRAVITY. Then the fringes are searched by applying OPDs in steps using the internal piston actuator (for large steps main delay lines used). Once the fringes on the fringe tracker are found, the science spectrometer fringes are frozen and integrated for long exposures by feedbacking the fringe tracker phase and group delay measurements to the internal piston actuator. The differential optical path difference caused due to the separation of the phase-reference and the science targets (in µas) in the sky is measured from the phases of the two beam combiners. The instrument internal phase is measured with the laser metrology (cf. Section 2.4.2.8). During observations, several control loops (cf. Figure 2.15) are in operation to make sure the observations successful.

- Third, the above procedure is repeated for the science objects.

The data reduction pipeline reduces the science and calibrated targets data and generates calibrated visibility and phases. Using them, the reconstruction of interferometric images and measurement of astrometry are carried out.

[5] https://cral.univ-lyon1.fr/labo/perso/eric.thiebaut/?Software/MiRA

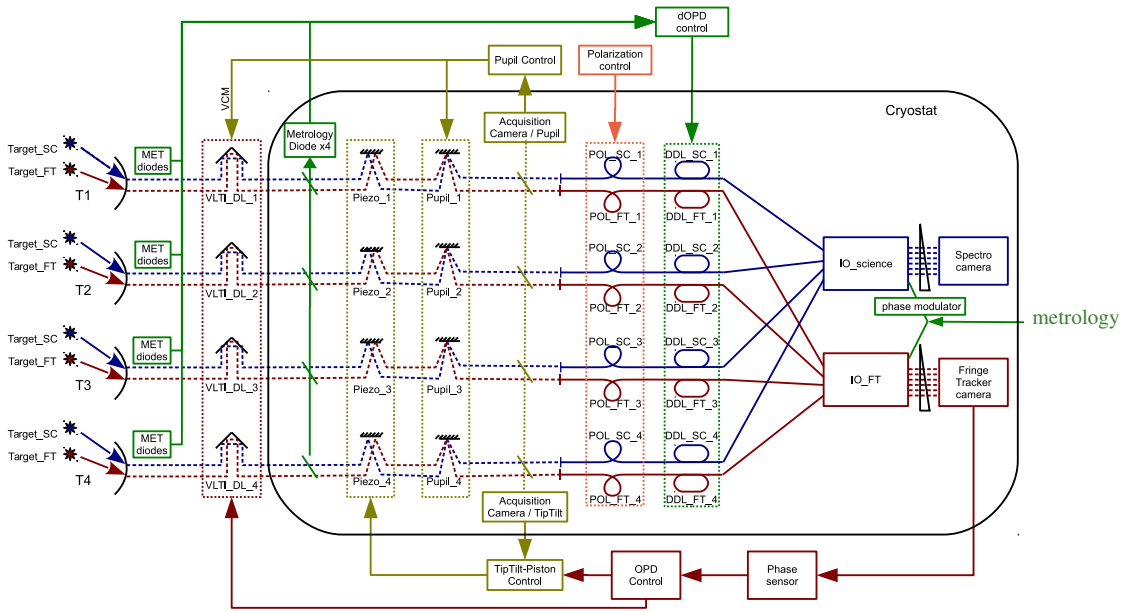

Figure 2.15: Number of active controls that are in operation to achieve the GRAVITY astrometry. The red and blue colors represent optical paths of the fringe tracker (phase-reference) and the science targets respectively. The dotted and solid lines are the light propagation through the air and the single-mode fibers respectively. The green color stands for the metrology system. The tip-tilt and the pupil corrections are enabled by the acquisition camera sensor (in yellow color). The orange color represents the polarization control system. Figure credit Lacour et al. 2014.

Chapter 3

The acquisition camera concept and design

3.1 Introduction

The major error sources for the GRAVITY astrometric measurements are the atmospheric turbulence and the pupil position errors (Section 2.2). The random atmospheric turbulence induced wavefront aberrations in the light path from the sky to the Coudé laboratory are corrected by the GRAVITY-CIAO. Since CIAO does not correct the VLTI tunnel seeing induced fast tip-tilts, they are corrected by the laser based tip-tilt tracking. However, after the above corrections tip-tilt residuals of more than 10 mas remain (Clénet and Gendron, 2011). These tip-tilt errors limit the performance of GRAVITY in two ways: a) efficiency of star light injection into the single mode fibers which are used to transport the light to the integrated optics to make the beam combination; b) unwanted field error causes additional astrometric error (cf. Eq. 2.5). The acquisition camera field tracker has been built to stabilize this star's light injection into the fibers. Furthermore, it measures any differential field drifts occurring between the laser based tip-tilt tracking and the actual field in the sky.

CIAO measures and corrects the incoming distorted wavefronts with respect to its reference wavefront generated from its internal collimated calibration source. However, there are many optics and the VLTI tunnel involved in between CIAO and the GRAVITY beam combiner and they could introduce additional wavefront aberrations to the incoming beam. The quasi-static wavefront aberrations and the non-common path errors that exist between CIAO and the GRAVITY beam combiner also contribute to the astrometric error (Lacour et al., 2014) and these have to be measured by the acquisition camera using 9×9 lenslet based Shack-Hartmann sensors.

The pupil position errors are caused by optical and mechanical misalignments and temperature gradients. In between the telescope pupil and the fiber-fed beam combiner, there exists several optical pupils including the delay lines that are under motion due to the optical train vibrations, while tracking the object of interest. While equalizing the optical paths of the telescopes with the delay lines, the longitudinal pupil position (or pupil defocus) has to be adjusted constantly using

the VCM to preserve the FoV of the VLTI. The VCM corrects the longitudinal pupil positions by adjusting its curvature based on a calibration pointing model. This pointing model is not accurate and introduces a residual longitudinal pupil drift of 3 m at the 80 mm beam (or 30 km at the 8 m telescope beam). The pointing model limitations induce the lateral pupil position errors up to a maximum of around 5% in pupil diameter. Eq. 2.5 allows us to calculate the astrometric error associated with the given pupil position error. For example, we experience an astrometric error of 633.3 µas at the UT, for a 10 mas field error and a 0.4 m (5% of 8 m pupil) lateral pupil position error and a 30 km longitudinal pupil position error, for a single beam combiner ($\sqrt{2}\times$ for the two beam combiners). It is, therefore, necessary to stabilize the pupil motions to reduce the astrometric error and this has been implemented with the acquisition camera pupil tracker.

Having presented the motivation for the acquisition camera functions, we can now proceed to discuss the acquisition camera concepts and its design (Section 3.2). The modeling and the end-to-end simulations of it are presented in Section 3.3.

3.2 Design and concepts

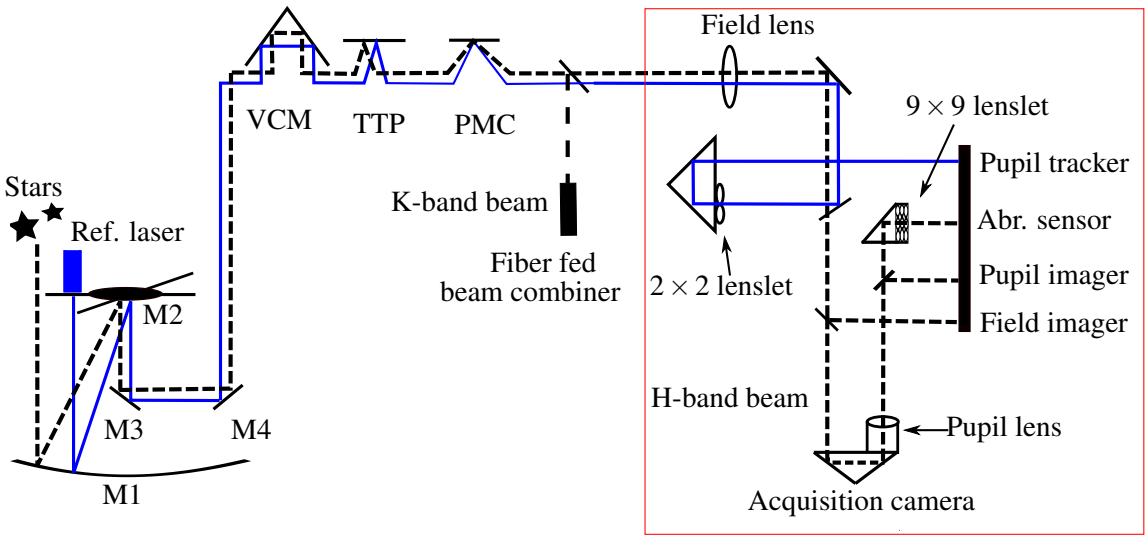

Figure 3.1: One telescope beam case is presented for simplicity. The H-band and the K-band beams are used for the beam guiding and the science measurements, respectively. The H-band beam is distributed among the optical functions of the acquisition camera: the pupil tracker takes the pupil reference laser beams (1.2 µm) and images them with a 2×2 lenslet; the aberration sensor (Abr. sensor) uses a Shack-Hartmann lenslet image; the pupil imager images the telescope pupil using a tele-centric pupil lens; the field imager images the field using its field lens. The box in red color represents acquisition camera optics.

Figure 3.1 presents the optical layout of the acquisition camera. It has four imaging modes: a) pupil tracker; b) aberration sensor; c) pupil imager; d) field imager. It images astrophysical targets (H-band, central wavelength 1.65 µm) and pupil guiding laser beacons (1.2 µm) that are installed on the M2 spiders.

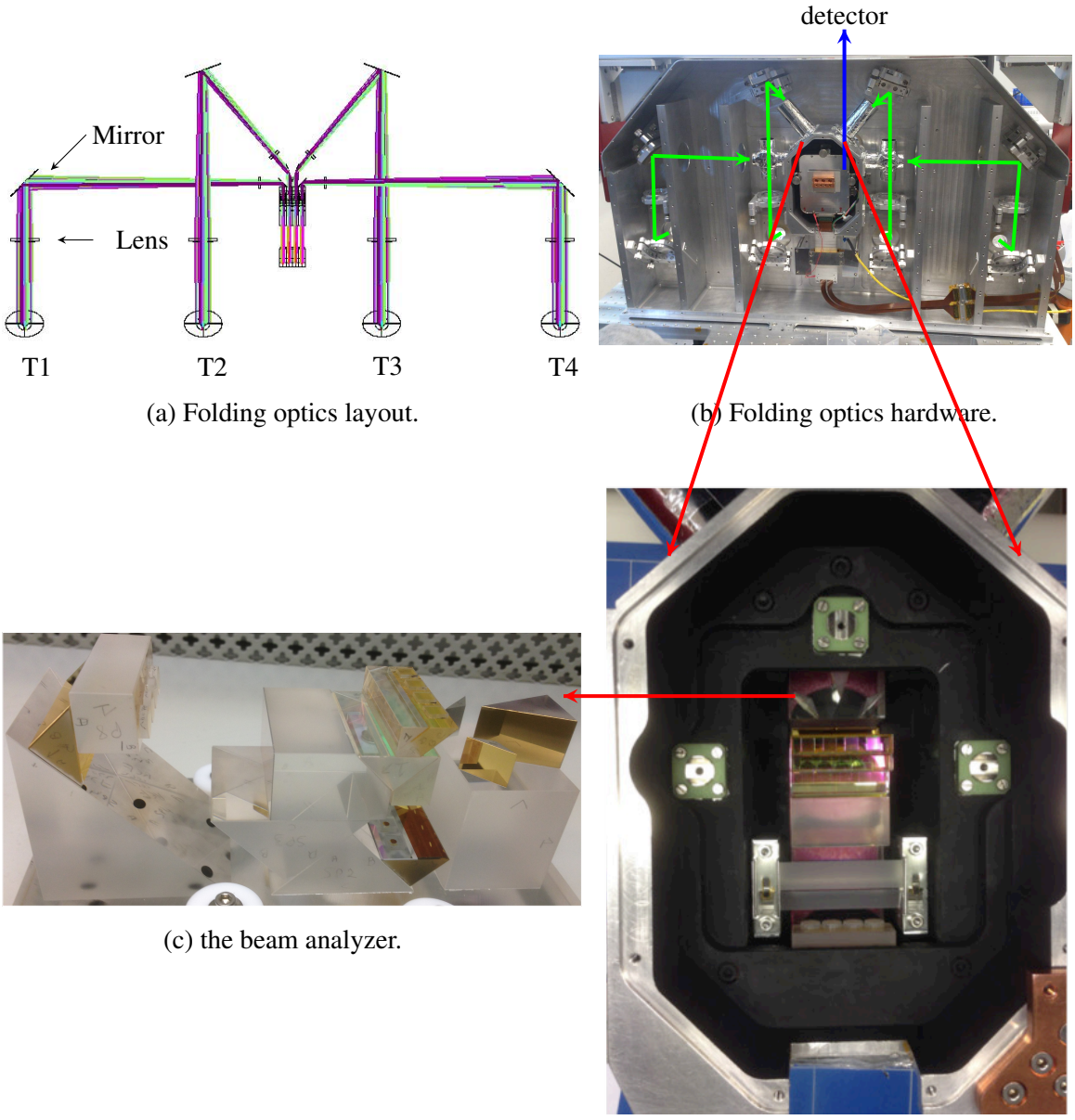

(a) Folding optics layout.

(b) Folding optics hardware.

(c) the beam analyzer.

(d) the beam analyzer mount.

Figure 3.2: The acquisition camera folding optics. a) the folding optics Zemax design. The mirrors are used to relay the input telescope beams into the beam analyzer. The lenses shown are used for the field imaging. b) the hardware of the folding optics. The detector is placed over the beam analyzer (panel d). Figure credits: top left panel – Amorim et al. 2012; bottom panels – the GRAVITY consortium.

It analyzes the images and extracts beam stabilization parameters to enable the field and the pupil guiding by using the TTP mirror, the PMC mirror and the VCM. By doing so it stabilizes the injection of the K-band light of the astrophysical targets into the single mode fibers which transport the beams towards the interferometric beam combiner. The aberration sensor measures the wavefront aberration required for the focus guiding and to correct the non-common path errors.

The pupil imager is used to image the telescope pupil and to track it visually during observations.

The acquisition camera has two subunits: a) folding optics; b) beam analyzer. The folding optics has four optical entrance channels and accepts four 18 mm sized telescope beams and redirects them into the beam analyzer (cf. Figure 3.2). The beam analyzer implements the core optical functions of the acquisition camera, i.e., the pupil tracker, the aberration sensor, the pupil imager and the field imager to analyze the beams.

Each entrance channel (T1 to T4) in the folding optics consists of two plane mirrors and a lens. The input telescope beam is relayed into the beam analyzer using the two mirrors as shown in Figure 3.2. A plane-convex CaF2 lens is embedded in each entrance channel and is used for the field imaging.

The beam analyzer is an assembly of fused silica prisms, slabs, lenses and lens arrays and all of them are bonded together to form a monolithic piece of fused silica glass. Once the beam analyzer is assembled, the individual prisms, lenses and lens arrays cannot be adjusted or realigned. The only possible adjustment can be made is the global positioning of the assembly with respect to the focal plane. Therefore, the optical alignments of the beam analyzer are implemented prior to the bonding. Figure 3.3 illustrates the optical realization of the beam analyzer:

- A dichroic beam splitter (labeled as **a** in Figure 3.3) reflects 1.2 µm wavelengths towards the four 2×2 lenslets (pupil tracker function) and transmits the remaining H-band light.
- The transmitted light is shared among the field imager, the pupil imager and the aberration sensor functions by using two beam splitters.
- A beam-splitter (labeled as **b**) is used to reflect the CaF2 lens imaged field on the detector.
- The pupil imager uses four lenses to image the four telescope pupils.
- The aberration sensor implements four 9×9 lenslets for the Shack-Hartmann wavefront sensing.

All the images are recorded on a HAWAII-2RG detector, which is placed at a distance of ~ 5 mm from the beam analyzer. The beam analyzer is a near-infrared imaging instrument and the HAWAII-2RG detector is required to cool-down to liquid nitrogen temperatures to minimize the thermal background. For this reason, the beam analyzer is manufactured using a single optical material (fused silica) to minimize the possible stress when it is cooled down to the liquid nitrogen temperature (77 K).

The main acquisition camera design requirements result directly from the astrometric error budget of GRAVITY. Appendix B presents the project top-level requirements for the acquisition camera.

3.2.1 Field imager

The basic idea of the field imager is to measure the atmospheric tip-tilts by imaging the astrophysical objects and stabilize these object's light injection into single mode fibers. Keeping in mind

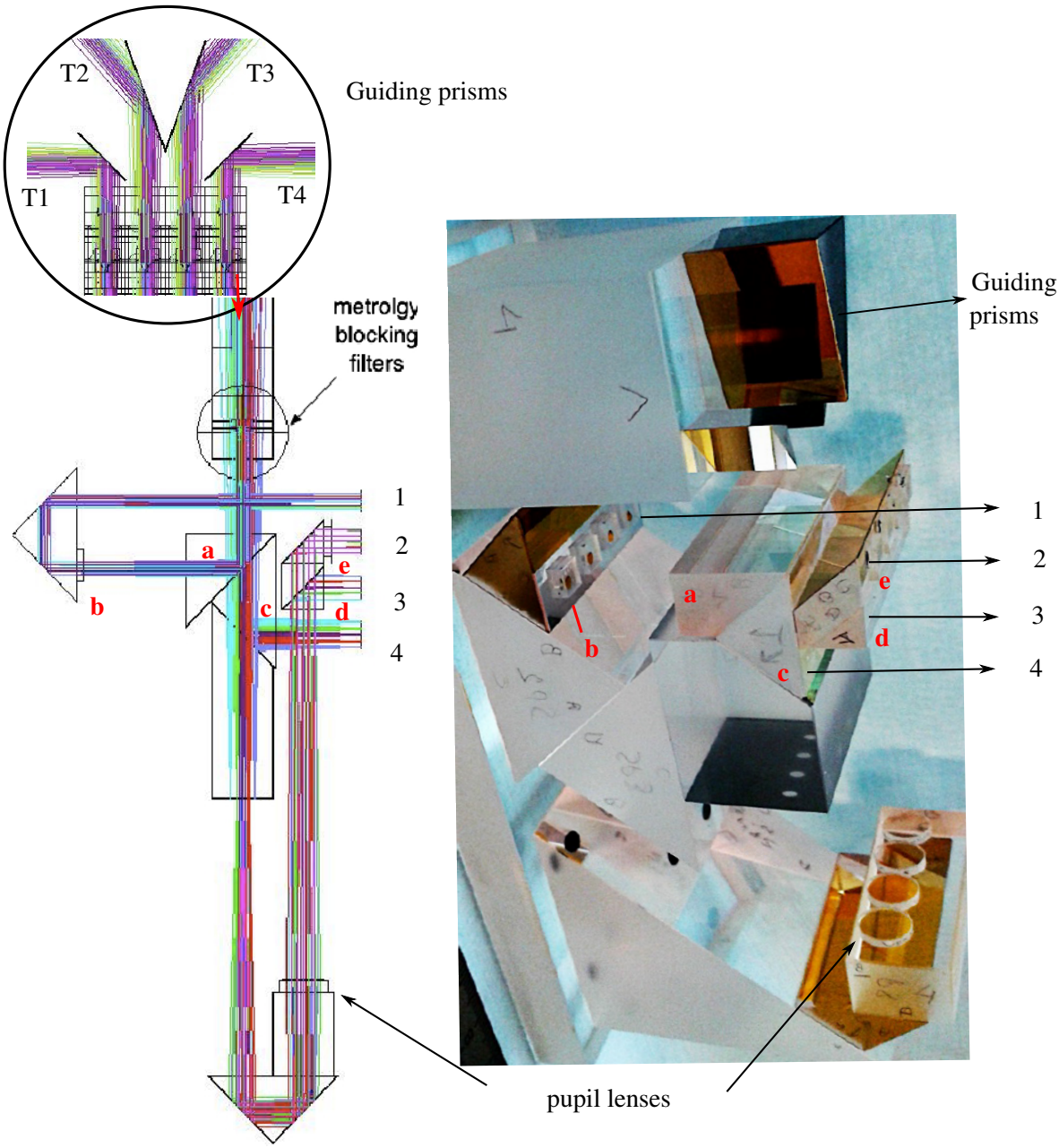

Figure 3.3: Guiding prisms receive beams from the folding optics and guide them towards the dichroic beam splitter (labeled **a** in the Figure). Left bottom panel is the Zemax design of the beam analyzer for one telescope beam. The right panel is the beam analyzer hardware. The light path inside the beam analyzer (from top to bottom in the figure): the dichroic beam splitter (**a**) reflects the 1.2 µm wavelength beams towards the pupil tracker (2×2 lenslets, label (**b**)) and transmits the remaining H-band beam. This H-band beam (>1.2 µm) is shared between the field imager and other imaging modes (i.e., the pupil imager and the aberration sensor) using a beam splitter (**c**). The light sharing between the pupil imager and the aberration sensor is implemented with another beam splitter (**d**). The label (**e**) stands for the Shack-Hartmann. The imaging modes are: 1 – pupil tracker; 2 – aberration sensor; 3 – pupil imager; 4 – field imager. Figure credits: left panel – Amorim et al. 2012; right panel – the GRAVITY consortium.

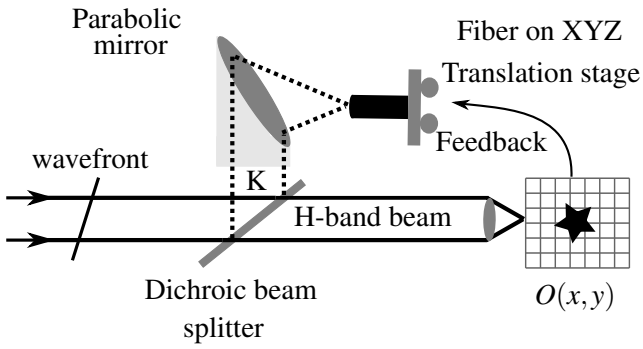

Figure 3.4: Stabilization of the star light injection into a single mode fiber. Accurate position of the star, $O(x,y)$, is detected by the field imager using the H-band beam. By feedbacking the star position to the tip-tilt and piston mirror (situated in front of the fiber feeding optics), the star's light injection is stabilized. The star's K-band light is focused into the single mode fiber using a parabolic mirror.

that the unvigneted FoV of the VLTI is $2''$ and considering a few number of bright objects (around $m_{\mathrm{H}} = 13$ mag) available in the vicinity of the Galactic Center for tip-tilt guiding, a FoV of $4''$ for the field imager is chosen, as a trade-off between vignetting and increase the use of the off-axis functionality.

As mentioned earlier GRAVITY has two imaging modes: a) on-axis mode (single field mode); b) off-axis mode (dual field mode). In on-axis case, the bright star's light injection into the fibers is quite trivial as the star is placed on the on-axis position of the Roof-Prism. At this position the Roof-Prism acts as a beam-splitter and sends light into both the fibers.

In off-axis case the Roof-prism is used as a star separator. The bright and the faint star's light injection into the fibers is more complex and is taken care by satisfying a few number of degrees of freedom as follows: a) separation between the field tracker star and the science star; b) position angle of the two stars in the sky; c) maximum reflectivity positions of the Roof-Prism as the reflectance of the Roof-Prism surface is not uniform. Depending on the separation between the two stars, different maximum reflectance positions are available.

The detector pixel scale is used to connect the angular size of the astrophysical object in arcsec to the image formed on the detector in pixels. The pixel scale (θ_{pix}) parameter is designed from the rule that we want to image the FWHM of the adaptive optics corrected star with the Nyquist-Shannon sampling. The FWHM of the adaptive optics corrected point spread function (PSF) is 42.5 mas in the H-band (centered 1.65 µm). A pixel scale of 17.78 mas per pixel is obtained for 2.4 pixels FWHM. For the ATs, the pixel scale is 78.9 mas with the magnification of 4.44 with respect to the UTs.

The field imager uses the lens embedded in the folding optics to image the field (cf. Figure 3.2). The f-number ($F/\#$) of the field imager is obtained from the Lagrange invariant (McLean, 1997) as given in Eq. 3.1

$$F/\# = \frac{d_{\mathrm{pix}}}{D_{\mathrm{Tel}}\,\theta_{\mathrm{pix}}} \tag{3.1}$$

where d_{pix}, D_{Tel} and θ_{pix} are the pixel size of the detector (18 µm), the diameter of the UTs (8 m)

and the pixel scale (17.78 mas) respectively. By substituting these parameters in the above equation, the $F/\#$ of the system is 26.1. The optical tolerance analysis work assuming the optical accuracy requirement ($\lambda/20$ peak to valley at 633 nm) translates in position tolerances of 100 µm.

3.2.2 Pupil imager

It images telescope pupils using tele-centric pupil lenses, which are fused silica plano-convex lenses with 8 mm in diameter and 15.45 mm in focal length. They re-collimate the incoming beams and image on the detector (cf. Figure 3.3). The pupil image is brought to the detector plane by a reflection on a gold-coated prism surface. The pixel scale of the pupil imager is 53.9 mm and its FoV is 11.2 m at the UT space. The implemented values are given on Table 3.1.

Table 3.1: Pupil imager design specifications.

Specification	Value
Wavelength	H-band
Optics	plano-convex (diameter 8 mm; focal length = 15.45 mm)
Field stop	diameter 1.013 mm
Field of view	11.2 m at the UTs space (208 pixels or 2 arcsec)
Pixel scale	53.9 mm for the UTs

In general, the pupil imager can be used for the lateral pupil tracking. By knowing the shift of the pupil image in X and Y directions on the detector, we can convert them into the pupil lateral shifts on the UT space using the pixel scale. On the detector, the pupil image shifts can be measured by applying a cross-correlation algorithm, which tracks the target pupil image shift with respect to a reference pupil image. However, preliminary design simulations (Amorim and Eisenhauer, 2010) show that the SNR of images using the Galactic Center stars is very low due the due to their low flux (cf. Section 3.2.5). Detector integration of more than one minute is required to achieve decent SNR images and to track the pupil accurately. On the other hand, the pupil drifts in the tunnel change with a time scale of few seconds. Therefore, the pupil shift measurement with the pupil imager on the scale of minutes is not sufficient for a good correction. To address this problem, a laser beacon based pupil tracking system has been developed as described in the next section.

3.2.3 Pupil tracking

The basic working principle of the pupil tracker is to image and track the laser beacons which are installed on the secondary mirror of the telescope. Four reference lasers are mounted on the four symmetric spider arms of the M2 mirror by considering the telescope's primary mirror central obstruction (cf. Figure 3.5). These four laser beacons are imaged by 2×2 lenslets which allow, not only the measurement of the lateral pupil shifts, but also the longitudinal pupil shifts (cf. Figure 3.6).

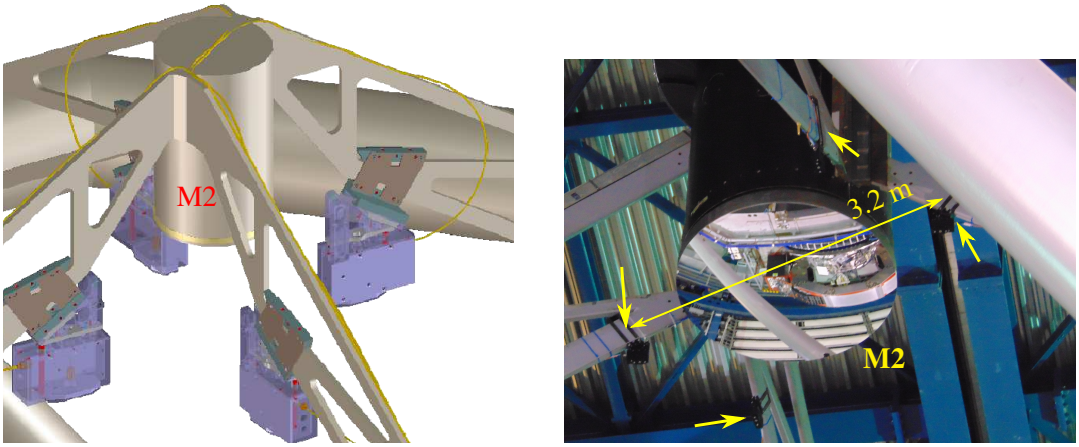

Figure 3.5: Pupil beacons installed on the M2 spiders. Left and right panels are for the ATs and the UTs. All four pupil beacons are fed by a common laser diode via multi-mode fibers.

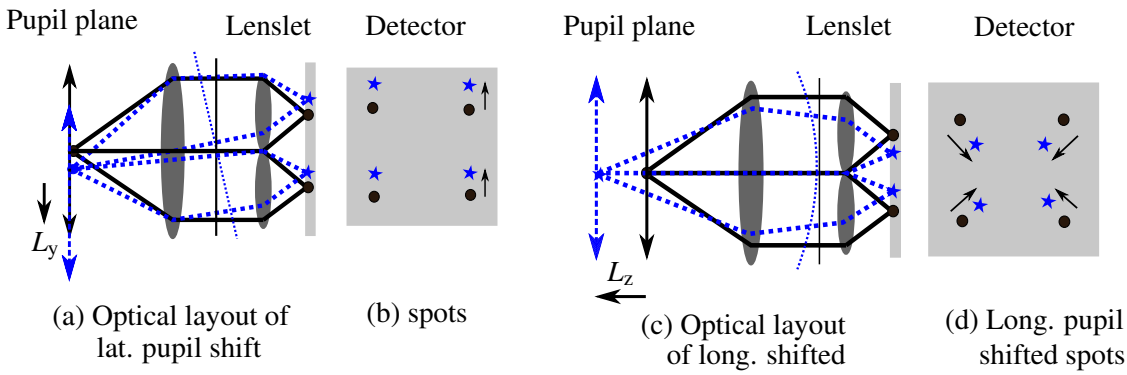

Figure 3.6: A simple layout of the pupil tracker working principle. Reference telescope pupil and corresponding laser spots are represented with the solid lines in black and filled circles respectively. The shifted pupil and corresponding laser spots are represented with the dashed lines in blue and star symbols respectively. A typical lateral shifted pupil is presented in the panels of (a) and (b). A typical longitudinal shifted pupil is presented in the panels of (c) and (d).

Lateral and longitudinal shifts of the pupil are translated as tip-tilt and defocus errors into the incoming beam while falling on the 2×2 lenslet of the pupil tracker optics (cf. Figure 3.6). Via the Fourier transformation property, tilts in a pupil plane are translated into image shifts at its focal plane and vice versa. For a lateral shifted pupil, the 2×2 lenslet formed spots are laterally displaced from the reference telescope pupil formed spots (cf. Figure 3.6 (a) and (b)). For a longitudinal shifted pupil, the detector formed spots either converge (i.e., L_z negative) or diverge (i.e., L_z positive) with respect to reference spots, depending on the direction of the longitudinal displacement (cf. Figure 3.6 (c) and (d).

The wavelength of the laser beacons are chosen as 1.2 µm by considering the following constraints: a) K-band (1.9-2.3 µm) is used by the beam combiner; b) the acquisition camera astrophysical wavelength band is the H-band (1.45-1.85 µm, used for field imaging, pupil imaging and aberration sensor); c) the acquisition camera detector (HAWAII-2RG) working range is 0.85 to

2.5 µm; d) the M9 dichroic mirror available in Coudé laboratory transmits light between 0.45-0.99 µm to the MACAO facility and reflects 1-1.3 µm wavelengths; e) the MACAO visible wavefront sensor is sensitive to wavelengths below 1.1 µm.

The four pupil beacons are basically four output fibers and the light to them is distributed by a single pupil laser diode delivered from the Frankfurt Laser Company. The distribution of power to the pupil beacons is implemented with three fiber splitters. The laser diode, the coupling optics and the fiber splitters are located in an electronic box, which is mounted at the telescope. The attenuated power of the pupil beacons is of the order of nano-watts for the UTs and tens of pico-watts for the ATs (Pfuhl, 2012). The output of the pupil beacons can be tuned by adjusting the laser diode attenuation.

Two laser diodes are placed at a distance of 3.2 m from each other at the UT space (cf. Figure 3.5) and these are mapped to 53.5 pixels on the detector. These laser beams are imaged with a 2×2 lenslet, where each sub-aperture is of size 1.015×1.015 mm and focal length 14 mm. The pixel scale for the AT pupil is 13.5 mm/pixel. The implemented values are given in Table 3.2.

Table 3.2: Pupil tracker design specifications.

Specification	value
Wavelength	1.2 µm
Optics	2×2 lenslet on 2.03×2.03 mm
Field stop	2 arcsec (2 mm size in optics) diameter for the UTs
Field of view of lens	3.38 m for the UT pupils
Pixel scale	1 pixel = 59.8 mm at the UTs

3.2.4 Aberration sensor

The aberration sensor samples the telescope primary mirror with 9×9 sub-aperture lenses. It has 68 effective sub-apertures out of 81 lenslet sub-apertures. The focal length of the sub-apertures resulted from the Lagrange invariant considering the requirement of image scale (250 mas per pixel) and the ratio of the size of telescope entrance pupil to the size of the micro-lens array. The diffraction FWHM on each sub-aperture corresponds to 1.5 pixels. The implemented values are given in Table 3.3.

3.2.5 The light budget

The light budget of the camera can be calculated by using the following equation

$$N_{\mathrm{H}} = N_0 A T d\lambda 10^{-0.4\, m_{\mathrm{H}}}\ (\mathrm{e}^-/\mathrm{s}), \tag{3.2}$$

where m_{H} is the H-band magnitude of star, $N_0 = 9.56 \times 10^9$ photons/(s m^2 µm) is the H-band zero point (Tokunaga, 2000), $\mathrm{d}\lambda = 0.4$ is the width of the H-band, $A = 49.29$ m^2 UTs collecting area. The effective transmissions (T) of the imaging modes are obtained by taking into account the

Table 3.3: Aberration sensor design specifications.

Specification	value
Wavelength	H-band
Optics	9×9 lenslets with diameter 5×5 mm
Sub-aperture	diameter 0.3×0.3 mm, focal length 4.97 mm
Field stop	diameter 1.013 mm
Sub-aperture field of view of lens	4.16 arcsec in the UTs sky
Pixel scale	1 pixel = 250 mas in the UTs sky
No of pixels sub-aperture	16×16

VLTI transmission (23%), the GRAVITY beam combiner optics transmission (80%) which are in the optical path of the acquisition camera, the acquisition camera detector quantum efficiency (80%) and the modes share in the flux. For the aberration sensor (29.4% share in the acquisition camera) it is 4.33% , for the field imager (26.72% share in the acquisition camera) it is 4% and for the pupil imager (15% share in the acquisition camera) it is 2.2%. When the above parameters are substituted in Eq. 3.2, it becomes

$$N_{\mathrm{H}} = 1.89 \times 10^{11} T 10^{-0.4\, m_{\mathrm{H}}}\ (\mathrm{e}^{-}/\mathrm{s}). \tag{3.3}$$

By substituting the transmissions (T) of the imaging modes of the acquisition camera and for $m_{\mathrm{H}} = 13$ mag, we get Table 3.4 counts on the detector. For the case of pupil tracker, the flux of the pupil guiding lasers can be tuned such that the flux on the detector is optimized (peak 6000-7000 e^{-}/pixel).

3.2.6 Detector

The acquisition camera uses second family HgCdTe Astronomical Wide Area Infrared Imager (HAWAII-2RG) to image the telescope beams (cf. Figure 3.7). It is a 2048×2048 pixel array with each pixel occupying 18 µm (Finger et al., 2008). HAWAII-2RG arrays have high quantum efficiency exceeding 80% over their entire sensitive wavelength range from 0.85-2.5 µm. The readout noise of the detector is around 12 $\mathrm{e}^{-}/(\mathrm{pixel\,s})$ operating in the correlated-double-sampling readout mode.

Table 3.4: The light budget of the acquisition camera optical functions, at $m_{\mathrm{H}} = 13$.

Function	% in the beam analyzer	% in sky light	light on detector
Field imager	26.72 %	4%	4.8×10^{4} $\mathrm{e}^{-}/\mathrm{s}$ for a single star
Pupil imager	15%	2.2%	1.8×10^{4} $\mathrm{e}^{-}/\mathrm{s}$ for the pupil
Aberration sensor	29.4 %	4.33%	760 $\mathrm{e}^{-}/\mathrm{s}$ per sub-aperture
Pupil tracker	-	-	Reference laser light, can be tuned

Figure 3.7: (Left) Teledyne HAWAII-2RG readout integrated circuit wafer. (Right) Full detector. Figure credit: left panel Teledyne[1]; right panel, Eisenhauer 2015.

3.2.7 Thermal constraints

Since the acquisition camera is a near-infrared imaging instrument it is required to cool-down near the liquid nitrogen temperatures to minimize the thermal backgrounds. For this reason, the entire camera structure, with exception of the beam-analyzer unit, but including the folding lenses and flat mirrors, is operated at the GRAVITY's bench temperature, 240 K. While the beam-analyzer unit which comprises of the detector unit, the beam analyzer and the beam analyzer mounts is operated between 100 K and 120 K. The detector itself is operated at stable 80 K temperature. The full details of the cryogenics of the acquisition camera is described in Chapter 5.

For the above reason, the camera is opto-mechanically designed to provide a stable and reliable solution to hold the components in place.

3.2.8 Mechanical constraints

Due to lack of space in the VLTI laboratory and the number of subsystems involved in GRAVITY, the physical size of the acquisition camera is constrained to be 530 mm $\times$ 890 mm $\times$ 392 mm. The entrance channels are separated by 240 mm from each other. It has several opto-mechanical parts (cf. Figure 3.8) to make the correct optical alignment (i.e., tip-tilts and focus, cf. Chapter 5 for details).

[1] http://www.teledyne-si.com/ps-infrared-visible-fpas.html

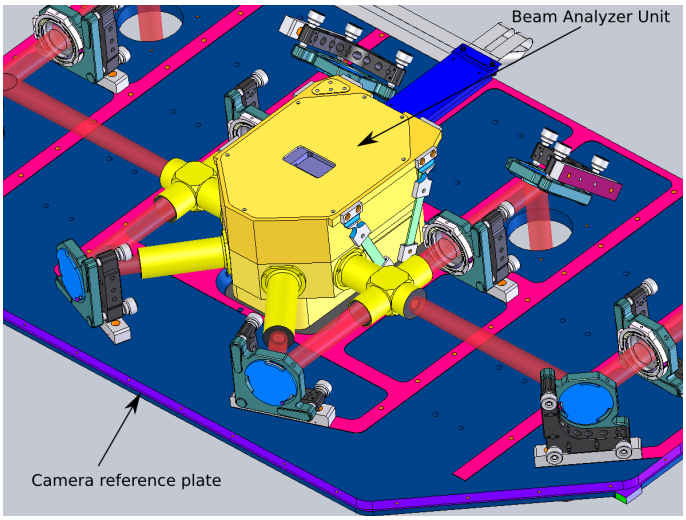

Figure 3.8: Acquisition camera SOLIDWORKS design which presents the tip-tilt and the Z adjusting mounts for lenses and mirrors. Figure credit Amorim et al. 2012.

3.3 Acquisition camera modeling: end-to-end simulations

I was not involved in the opto-mechanical design of the acquisition camera. One of my first tasks was to conduct an end-to-end simulation of the system. The goals were to verify the validity and the accuracy of the acquisition camera concepts and for that I took the following approach.

3.3.1 Approach

The acquisition camera concepts validation is carried out with numerical simulations in three steps. First, software tools are prepared to simulate the system. LIGHTPIPES (Vdovin et al., 1997), an ANSI-C software tool box, models coherent optical devices taking into account the diffraction effects. It consists of a number of functions such as pupil apertures, lenses, beam-splitters and Zernike phases and each function represents an optical element or a step in the light propagation and works with Unix based terminal pipe commands. It is ported to YORICK by the author for the easy interpretation, debugging and plotting. YORICK is an open source interpreted language, similar to IDL or MATLAB and is mostly used for scientific work, data processing, and simulation. The core, CPU intensive routines are coded in C. Next the acquisition camera optical design model (in Zemax) is studied carefully and the relevant parameters are taken to simulate its detector images. Second, acquisition camera detector images are generated by applying the VLTI laboratory experimentally measured field motions, pupil motions (lateral and longitudinal) and higher order wavefront aberrations (Pfuhl, 2012). Throughout these simulations, the fluxes described in Section 3.2.5 are used and random Poisson and readout detector noises (12 e^-/pixel) are applied. Finally, the input beam aberrations are reconstructed back and analyzed to check the acquisition camera performance in terms of accuracy in the presence of adverse imaging conditions and sensitivity towards faint stars.

3.3.2 Field imager

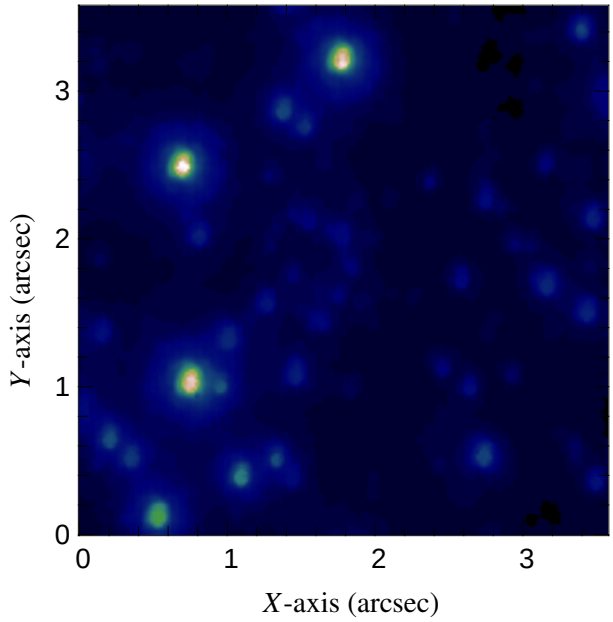

Figure 3.9: A synthetic field image for the Milky Way Galactic Center.

The field imager images $4'' \times 4''$ fields and, in particular, the Galactic Center field. The simulation of the field imager function is realized by obtaining a NACO (Lenzen et al., 2003) Galactic Center image from the ESO archive and scaling it to the field imager pixel scale using spline interpolation. To the resulted image, Poisson and readout detector noises are applied. Figure 3.9 presents a typical field image for the UTs. The end-to-end simulations (by applying the VLTI experimentally measured field motions to the field imager images and measuring back them with the field tracking function) gives 2 mas of the field guiding error.

3.3.3 Pupil tracking

As described in Section 3.2.3, the pupil tracker images four laser beacons that are mounted on the spiders of M2 using a 2×2 lenslet. A typical synthetic image generation of the pupil tracker is implemented in three steps.

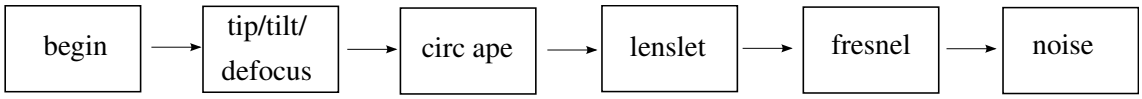

Figure 3.10: Simulation blocks for a pupil guiding laser beacon.

As a first step in the simulation, a 2×2 lenslet image is generated by imaging one single laser beacon. The simulation is carried out with the LIGHTPIPES blocks as shown in Figure 3.10. The laser beacon beams are collimated before entering the acquisition camera and the simulation starts from there. The first block, BEGIN, forms the initial data structures for the collimated beam. Next, the outcome of the BEGIN is aberrated with tip-tilt and defocus aberrations using

Zernike polynomials (these stand for lateral and longitudinal pupil shifts). Later, the wavefront is filtered out through a circular aperture. In the next step, the LENSLET optics is applied. Then, the wavefront is propagated to the focal plane of the lenslet with FRESNL diffraction. Finally, it forms the 2×2 lenslet image for a single laser beacon.

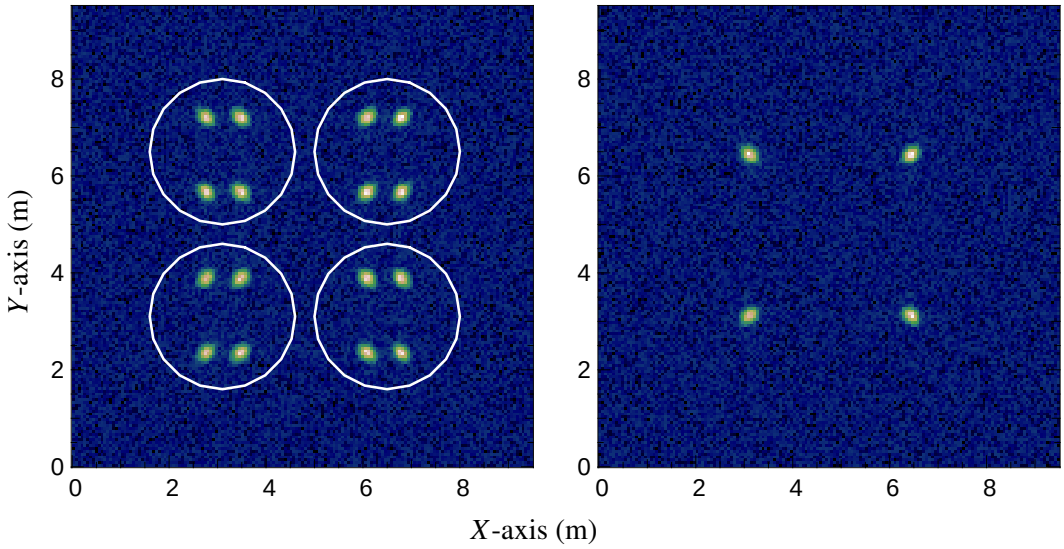

Figure 3.11: Left: a typical pupil tracker image. Each circle represents one sub-aperture lens. Spots in each circle represents four pupil beacons imaged by one sub-aperture lens. The average of these four pupil beacons in each circle is called as barycenter position. Right: a typical pupil tracker reference spots.

The above procedure is repeated for the other three laser beacons. Then all four images are shifted and added according to the positions of the laser beacons on the M2 spiders. Finally, photon statistics and detector readout noise are added. The generated pupil tracker image is presented in Figure 3.11 (left panel). Figure 3.11 (right panel) presents the reference image of the pupil tracker. The reference pupil tracker spots are generated by assuming a laser beacon at the center of M2. The end-to-end simulations (by applying the VLTI experimentally measured lateral and longitudinal pupil motions to the pupil tracker images and measuring back them with the pupil tracking function) gives 4 mm of the lateral pupil and 300 m of the longitudinal guiding error at the UT beam scale.

Table 3.5: The aberration sensor specifications used in YAO parameter file for its modeling.

Number of sub-apertures	9×9
Full pupil size	144 × 144 pixels
Pixel size	250 mas
Operating wavelength	1.65 µm
Telescope size	8 m
Telescope central obstruction	14% of 8 m
Wavelength	1.65 µm
No of pixels per sub-aperture	16 × 16

3.3.4 Aberration sensor

The aberration sensor image (cf. Figure 3.12) is simulated using YAO[2] version 5.3 (Rigaut, 2011; Rigaut and Van Dam, 2013). It is a Monte-Carlo simulation tool for adaptive optics systems. The main parameters adapted in the YAO parameter file are presented in the Table 3.5. The end-to-end simulations (by applying the VLTI experimentally measured wavefront error to the aberration sensor images and measuring back them with the aberration sensor function) gives 70 nm of the wavefront measurement error at the UT beam scale.

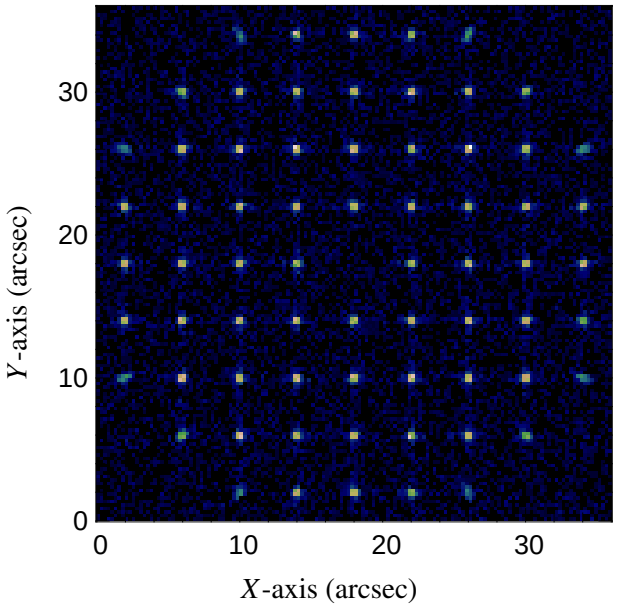

Figure 3.12: A typical aberration sensor image.

3.3.5 Pupil imager

A synthetic image of the pupil is implemented in two steps. First, point spread function of a circular aperture, located in the focal plane of a telescope, is generated assuming the 8 mm pupil lens. Second, the spider arm shadows of the UT are convolved with the above point spread function.

[2] Available at http://frigaut.github.io/yao/

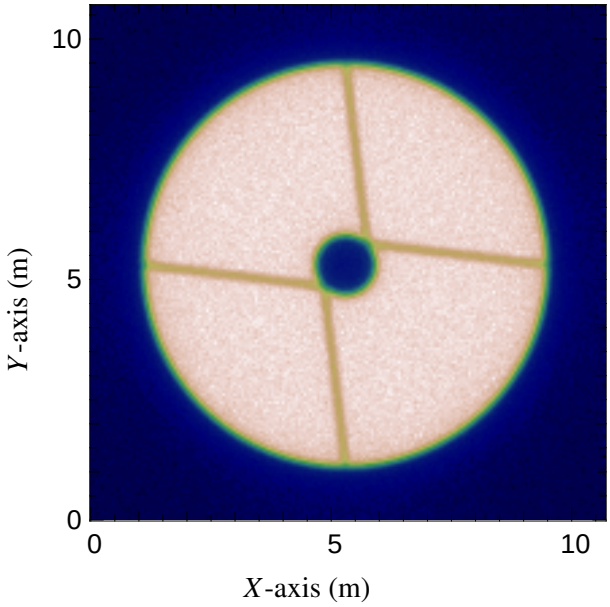

Figure 3.13: A synthetic pupil image for the UTs.

Then photon statistics and detector readout noise effects are added. Figure 3.13 presents a typical pupil image integrated for 10 s. Currently, this function is not used in the beam guiding the system and it does not require any data processing. The pupil imager is used for visual monitoring of the pupil. However, it can be used for lateral pupil tracking as described in Section 4.7.

3.4 Summary and conclusions

The acquisition camera imaging modes are designed to meet the requirements to achieve the 10 µm astrometry as described in Annex B. The design of the field tracker allows efficient injection of star's light into single mode fibers with an accuracy of 2 mas for the 13 mag H-band star. The results of the end-to-end simulations are presented in Sec. 4.6. The novel design of the pupil tracker enables stabilization of lateral and longitudinal pupil. Furthermore, the design allows to do the beam analysis for all four input beams simultaneously and is compact to meet the space requirements. The beam analyzer is built with a single fused silica material (including prisms, lenses and lenslets) to cope up with thermal stress during the cooling down and the warming up. This material is chosen for its low coefficient of thermal expansion ($\sim 10^{-6}\,^{\circ}\mathrm{C}^{-1}$).

The acquisition camera individual imaging modes are simulated in detail. Figure 3.14 presents the full acquisition camera detector image. Once equipped with this simulation one can verify the validity and the accuracy of its concepts. The acquisition data reduction algorithms presented in the next the chapter are tested with these detector images. The test results are presented in Section 4.6.

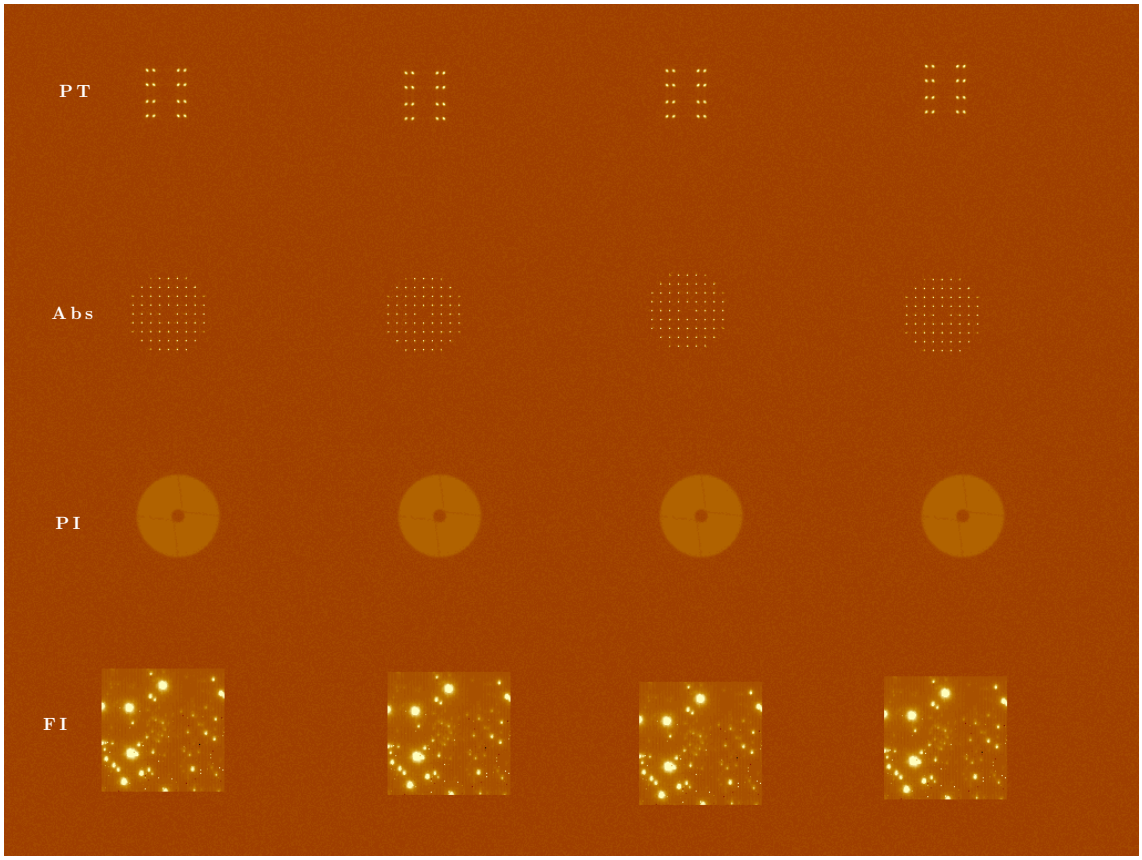

Figure 3.14: Synthetic detector image of the acquisition camera. Each column represents the four imaging modes of it for each telescope. Windows in each column, from top to bottom, are the pupil tracker, the aberration sensor, the pupil imager and the field imager respectively.

Chapter 4

Data reduction pipeline and software

4.1 Introduction

The development of the acquisition camera data reduction pipeline and associated software was the one of the primary responsibilities of the author. The data reduction pipeline software plays a crucial role in extracting the beam aberration parameters of the input telescope beams from its detector images and feedbacking them to the beam correction actuators.

Section 4.2 describes the top level requirements of the beam guiding software. Section 4.3 summarizes the software architecture of the beam guiding. The measurement of the pupil shifts, the tip-tilts and the wavefront aberrations from the detector images are presented in Section 4.4. The validation of the software is carried out using synthetic detector images (Section 4.6). In the last section, improvements to the software are proposed.

4.2 Top level requirements

The acquisition camera data reduction software has several top level requirements briefly described below. The full requirements of the acquisition camera are presented in Annex B.

- **High accuracy and sensitivity** The sensor measurements are required to be measured accurately as they are prerequisite to achieve 10 µas astrometry and accurate interferometric imaging. In addition, high sensitive measurements are expected towards faint targets (low SNR detector images).

- **Robustness** The acquisition camera software is involved in closed loop guiding, the sensor measurements need to be robust as a single wrong measurement could break the guiding loop. In other words, the software should judge the measured values for its correctness before feedbacking them to the actuators. The robustness is important here because the closed loop beam guiding is expected to work in the presence of a wide variety of conditions and also for different types of telescopes (the UTs/ATs).

- **Speed** High computational speed is required to meet the high speed closed loop correction requirement.
- **User friendly** The software should be user reach. This sets a requirement in the development of appropriate panels and buttons in place of terminal commands for an easy usage.
- **Low maintenance cost** GRAVITY has been built by the GRAVITY consortium. After the construction, the instrument is handed-over to ESO. The maintenance and daily operations are taken care by the Paranal observatory staff of the ESO. So in order to reduce the maintenance cost, the software is developed using the ESO standards for software.

4.3 Software architecture

The beam guiding software has two modules: a) sensor software; b) actuator control software. They both work in an instrument workstation (IWS) and are connected to the acquisition camera and the correction hardware via optical fibers network.

The sensor software (Section 4.3.1) reads the acquisition camera detector images every 0.7 s and extracts field motions, pupil motions and wavefront aberrations of the input telescope beams. The extracted parameters are then written to the instrument database. The actuator control software (Section 4.3.2) reads these parameters, converts them into actuator commands and applies correction using the tip-tilt mirror, the pupil motion mirror and M2 for focus correction. The overall architecture of the beam guiding process is shown in Figure 4.1.

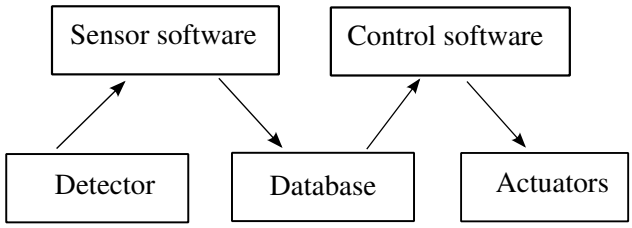

Figure 4.1: An overall view of the beam guiding approach. The sensor software reads the detector images and writes the extracted beam aberration parameters to the instrument database. The control software reads the beam parameters, converts them into actuators commands and sends them to the actuators to apply the beam corrections.

4.3.1 Sensor software

A top level function of the sensor software accesses the detector images via automatic callbacks for each new image produced by the acquisition camera detector. In turn this function calls its low level functions to reduce the images. First the image is preprocessed for sky dark, flat and bad pixels following the standard astronomical image processing practice (Section 4.4.1). Then, a set of dedicated image reduction algorithms implements the data reduction on the detector image and extracts the beam field tip-tilts (Section 4.4.3), pupil motions (cf. Section 4.4.2) and wavefront

aberrations (Section 4.4.4)). These routines work on-line on the instrument in parallel to the observations which are carried out simultaneously for all telescopes beams.

I led the development of this software (original module name `gvacq`) and currently it consists of more than 52,000 lines of documented code. The software is written in C/C++ and developed in the VLT2014 operating system using common pipeline library (CPL). These are the standard ESO framework of softwares.

4.3.2 Actuator control software

The actuator control software controls slow atmospheric field motions, fast tunnel seeing field motions, pupil motions and focus correction for the ATs. The slow field motions, pupil motions and focus correction are measured by the acquisition camera. The fast field motions are measured by the laser guiding system.

The control software reads the beam parameters that are measured by the acquisition camera and the laser guiding system, converts them into the actuator commands (i.e. voltages) and then sends them to various actuators to apply the corrections. The conversion from sensor measurements to actuator commands is done by the coordinate transform software. This software consists of a number of matrices that convert sensor measurements to actuator commands (Section 4.5). For instance, the location of the fiber positioner is given in volts in describing its location, but this corresponds to a certain location on the acquisition camera in pixels. Similarly, the tip-tilt and piston mirror is commanded in volts and moves the position of the field in pixels on the acquisition camera.

The closed loop guiding software is used in: a) alignment of GRAVITY with the VLTI; b) active pupil and field (slow and fast) stabilization; c) active focus correction. This software (`gvttp`) development is led by Ekkehard Wieprecht and I contributed significantly. The software module currently consists of more than 24,000 lines of C++ code.

4.3.3 Data logging

The beam aberration parameters measured by the sensor software and the commands sent to the actuators by the control software are logged in “FITS logs”. Depending on the instrument and testing operations, these log files amount from a few MB up to a few GB per day. This information is used to debug and characterize the instrument and the software performance.

4.4 Image data reduction concepts and algorithms

4.4.1 Pre-processing

In the world of optical astronomy, image data reduction means the reduction of the detector images to its scientific content. Thus a pre-processing of the images is required to remove biases of the instrumental effects from the image. The three main interfering effects for the detector images are approximately constant backgrounds, non-even pixel responses and dead/hot pixels (McLean,

2008). These are corrected appropriately by developing a pre-processing software. The background frames are obtained by acquiring images with the shutters closed. A flat field, to calibrate the non-even response of the pixels is obtained with the Calibration Unit. Dead/hot pixel maps are generated as part of the normal calibration plan of GRAVITY. The dead/hot pixels are ignored while computing the field, pupil and wavefront aberration measurements.

4.4.2 Pupil tracking

The pupil tracker software takes the acquisition camera detector image as an input and delivers the lateral and longitudinal pupil shifts. The operation of pupil tracker is involved, a few difficulties as described below must be addressed. These are taken care in the development of software.

4.4.2.1 Difficulties

- **Rotation** GRAVITY uses a field derotator to compensate for the Earth rotation. Due to this, the pupil tracker spots (2×2 lenslet images of the four pupil reference laser beacons) rotate (Figure 4.2). In this rotation, the simple solution of detecting spot positions by creating windows around the spots would not work.

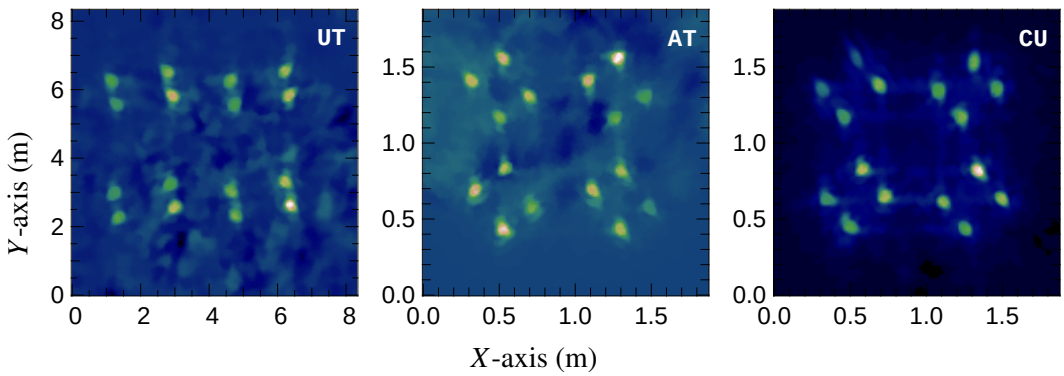

Figure 4.2: From left to right are the pupil tracker images of the UT, the AT and the Calibration Unit. Here the Calibration Unit spots are scaled to the AT. It can be seen in these figures that a rotation of sub-aperture spots is present.

- **Geometry of spots** The geometry of the pupil tracker spots is different (cf. Figure 4.2) for different telescopes (the UTs/ATs) such as different separation between the spots (due to different M2 spider arms geometry) and different spot sizes (due to the diffraction limits of the telescopes).

- **SNR** The pupil tracker experiences noise from high backgrounds from an astrophysical target due to: a) closeness of the operating wavelengths of the pupil tracker (1.2 µm) and the field tracker (H-band); b) because no adequate dichroic filter for the pupil tracker exists in the instrument. Figure 4.3 (left panel) presents a typical case.

- **Pupil vignetting** The pupil tracker experiences optical vignetting problems for some observations. As a consequence, in some occasions the images contain only two or three

sub-apertures out of four sub-apertures of the 2×2 lenslet (Figure 4.3 right panel). The software has to work with this type of dynamic vignetting of the pupil.

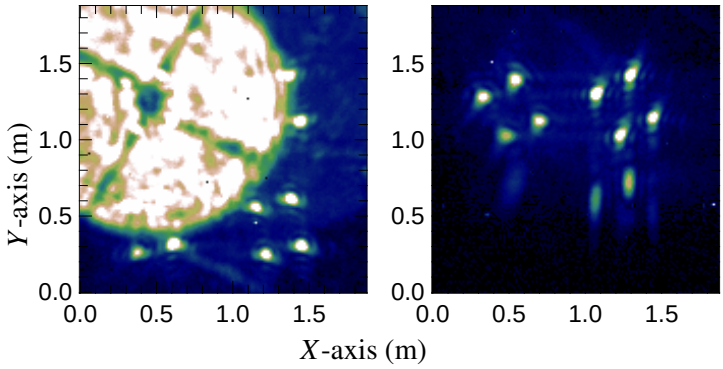

Figure 4.3: Pupil tracker images highlighting the astrophysical background filling (left) and pupil vignetting (right) discussed in the text.

Considering these constraints, two methods for measuring the pupil shifts are studied in this thesis as described in the following sections.

4.4.2.2 Barycenters of the Laser Beacons (BLB)

Measurement of target spot positions This method works in four steps. In the first step, rough locations of the pupil tracker spots are computed using a sigma-filter (predetermined spot FWHM as a threshold). Second, Gaussian fits are applied in the image at these rough locations with a predetermined window size (10×10 pixels) to measure accurate spot positions. Third, using these spot positions, barycenters, average position of the four laser beacons, for each sub-aperture are computed. Finally, the pupil shifts are measured by comparing the barycenter positions with the reference positions which are obtained from an internal calibrator source.

In computing the barycenters, one question that arises is which spot belongs to which sub-aperture. Because the detection of spots using a sigma-filter gives the spot locations that are arranged as per a FWHM but not as per sub-aperture. The re-arrangement of the spots as per sub-aperture is carried out with two kinds of algorithms based on how much vignetting it experienced. If the number of detected spots is less than 10, the software applies "Two-sub-apertures algorithm" otherwise "three/four-sub-apertures algorithm" (Figure 4.4).

Three/four-sub-apertures algorithm First it finds the center (C_{PT}) of the pupil tracker spots pattern in the 200×200 pixel pupil tracker window by taking the average of the spot positions detected by the sigma-filter. This step is important because the pupil tracker spots pattern can be located anywhere within the pupil tracker window due to the random pupil shifts. Using this average position, C_{PT}, the pupil tracker image is divided into four sub-images as shown in Figure 4.4 (left panel). Each sub-image corresponds to a sub-aperture image. By applying again the sigma-filter, the spots corresponding to each sub-aperture are detected.

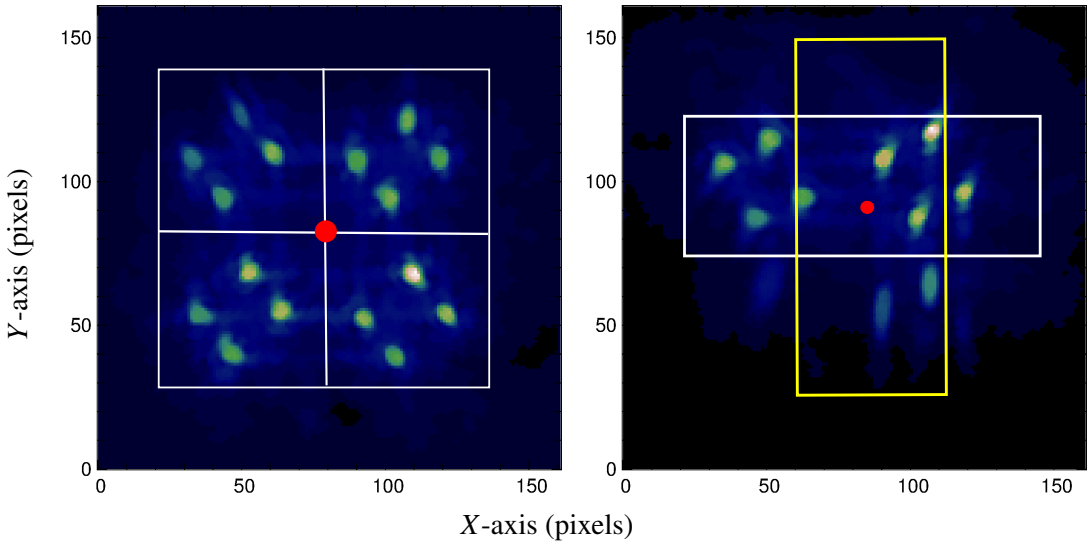

Figure 4.4: Left panel: explains the three/four-sub-apertures algorithm. Right panel: A vignetted pupil tracker image. Rectangular search windows shown above are applied as part of the two-sub-aperture algorithm to determine the spots pattern. The red dot indicates average of detected spots, C_{PT}.

Two-sub-apertures algorithm It works by applying rectangular search windows along the vertical and the horizontal directions to detect whether the sub-apertures are aligned vertically or horizontally as shown in Figure 4.4 (right panel). Once the vertical or horizontal pattern is detected, a question that arises is about their location in the pupil tracker window. The pattern can be either at the left or right in the case of vertical pattern and either top or bottom in the case of horizontal pattern, as shown in the left panel of Figure 4.5. This ambiguity is removed by looking at the pupil tracker reference positions pattern R_j, where j is a sub-aperture number. The barycenters are represented with B_j.

Figure 4.6 presents the flow chart of the measurement of the barycenters. Once the measurement of the barycenters is completed, the pupil shifts are computed as follows.

Pupil shifts measurement for three or four-sub-apertures case For a three sub-apertures case, the missing sub-aperture shifts are predicted as described below by using the geometry of the 2×2 lenslet.

For example, assume that first sub-aperture barycenter $B_1^{(x,y)}$ is missing (Figure 4.5). This barycenter position can be predicted by looking at the other three sub-aperture's barycenter positions. Its X and Y-locations can be obtained from the second and fourth sub-apertures respectively (i.e., $B_1^{\mathrm{x}} = B_2^{\mathrm{x}}$ and $B_1^{\mathrm{y}} = B_4^{\mathrm{y}}$) (for the sub-aperture number notation refer Figure 4.5). Here no rotation in the sub-apertures pattern is assumed for clarity.

- **Case 1, if first sub-aperture missed** Its location is taken from B_2^{x} and B_4^{y}:

$$B_1^{\mathrm{x}} = B_2^{\mathrm{x}}, \qquad B_1^{\mathrm{y}} = B_4^{\mathrm{y}}. \tag{4.1}$$

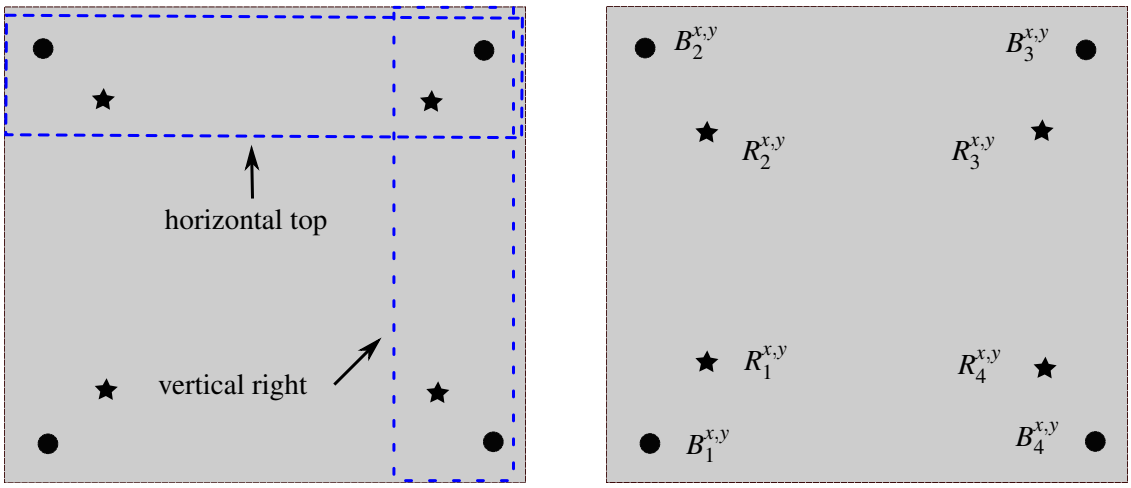

Figure 4.5: Left: Horizontal and vertical pattern in the two-sub-apertures algorithm. Right: Barycenters and reference spot positions of the pupil tracker.

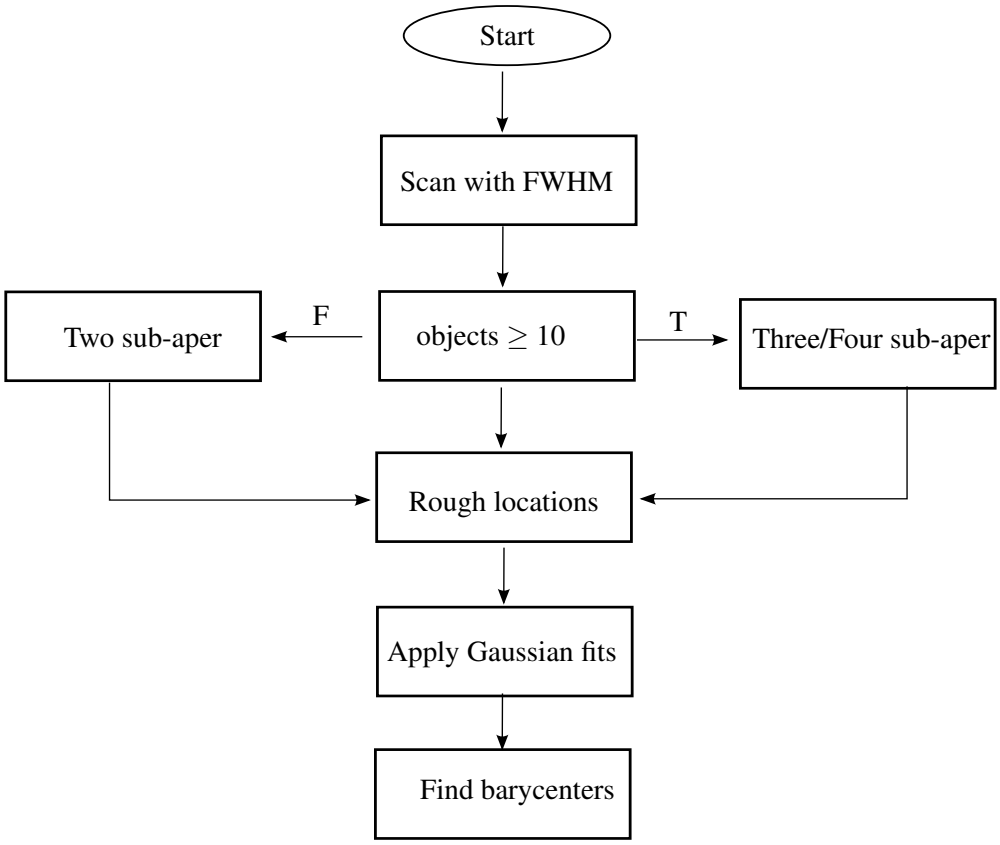

Figure 4.6: An overall view of measuring barycenters of the pupil tracker laser beacons. For description of it please see the text.

- **Case 2, if second sub-aperture missed** Its location is taken from B_1^x and B_2^y.

$$B_2^{\mathrm{x}} = B_1^{\mathrm{x}}, \qquad B_2^{\mathrm{y}} = B_3^{\mathrm{y}}.$$

- **Case 3, if third sub-aperture missed** Its location is taken from B_4^x and B_3^y.

$$B_3^x = B_4^x, \qquad B_3^y = B_2^y.$$

- **Case 4, if fourth sub-aperture missed** Its location is taken from B_3^x and B_4^y.

$$B_4^x = B_3^x, \qquad B_4^y = B_1^y.$$

Using the barycenter (B_j^x, B_j^y) and reference spot positions (R_j^x, R_j^y), spots shifts (S_j^x, S_j^y) are computed as given in Eq. 4.2.

$$S_j^x = B_j^x - R_j^x$$

$$S_j^y = B_j^y - R_j^y \tag{4.2}$$

The spot shifts in X and Y directions allow one to measure the lateral pupil positions (L_x^4 and L_y^4, where 4-stands for four-sub-aperture case) as given below

$$L_x^4(\mathrm{px}) = \frac{\sum_{j=1}^4 S_j^x}{4}, \qquad L_y(\mathrm{px}) = \frac{\sum_{j=1}^4 S_j^y}{4}. \tag{4.3}$$

The amount of divergence or convergence of the spots allows to measure the beam defocus (Salas-Peimbert et al., 2005) and using that one can evaluate the longitudinal pupil position (L_z^4,) as given

$$L_z^4(\mathrm{px}) = \frac{[(S_2^x + S_3^x) - (S_1^x + S_4^x) + (S_1^y + S_2^y) - (S_4^y + S_3^y)]}{8}. \tag{4.4}$$

Pupil shifts for two-sub-apertures case The measurement of pupil shifts (L_x^2, L_y^2 and L_z^2, where 2-stands for the two-sub-aperture case) in the presence of two-sub-apertures is not easy as in the case of four-sub-apertures because the lateral pupil measurement is biased by the longitudinal pupil shift. The pupil shifts in this case are measured as explained below.

- **Vertical and left pattern**

$$L_z^2(\mathrm{px}) = \frac{S_2^y - S_1^y}{2} \qquad L_x^2(\mathrm{px}) = \frac{S_1^x + S_2^x}{2} + L_z^2 \qquad L_y^2(\mathrm{px}) = \frac{S_1^y + S_2^y}{2} \tag{4.5}$$

- **Vertical and right pattern**

$$L_z^2(\mathrm{px}) = \frac{S_3^y - S_4^y}{2} \qquad L_x^2(\mathrm{px}) = \frac{S_3^x + S_4^x}{2} - L_z^2 \qquad L_y^2(\mathrm{px}) = \frac{S_3^y + S_4^y}{2} \tag{4.6}$$

- **Horizontal and top pattern**

$$L_z^2(\mathrm{px}) = \frac{S_3^x - S_2^x}{2} \qquad L_x^2(\mathrm{px}) = \frac{S_2^x + S_3^x}{2} \qquad L_y^2(\mathrm{px}) = \frac{S_2^y + S_3^y}{2} - L_z^2 \tag{4.7}$$

- **Horizontal and bottom pattern**

$$L_z^2(\mathrm{px}) = \frac{S_4^x - S_1^x}{2} \qquad L_x^2(\mathrm{px}) = \frac{S_1^x + S_4^x}{2} \qquad L_y^2(\mathrm{px}) = \frac{S_1^y + S_4^y}{2} + L_z^2 \tag{4.8}$$

Robustness of measurements In a closed loop system, the sensor measurements need to be very precise as a wrong measurement could break the loop. The sensor measured parameters are carefully checked for outliers with several criteria and if one of the criteria is verified they are rejected before sending them to the actuators.

4.4.2.3 Auto and cross-correlation method

As the above method becomes complex in the presence of optical vignetting, a correlation method was studied in order to reduce the code complexity. This method measures the pupil shifts as described below.

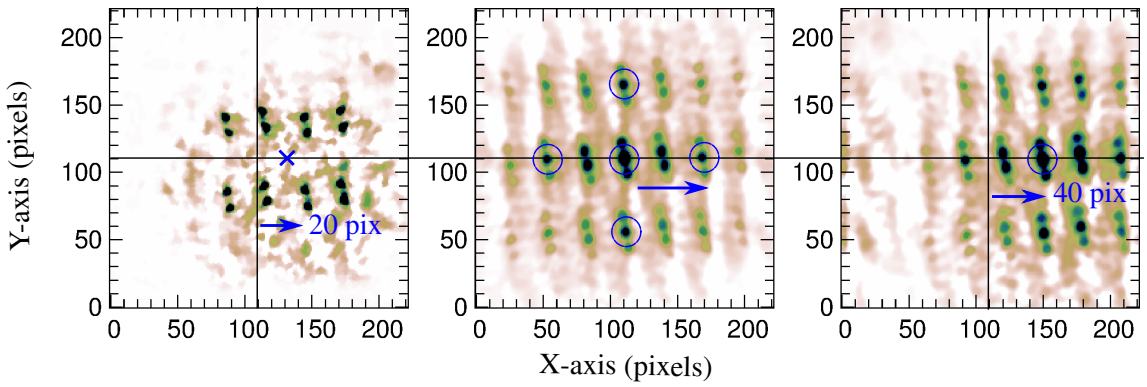

Figure 4.7: Correlation method of measuring pupil shifts. Left: A typical pupil tracker image taken with the UT3. It is shifted laterally along X-axis by 20 pixels. Middle: Auto-correlation of the image itself. The separation between the central peak and anyone of the outer peaks in the circles gives the pupil defocus. Right: Cross-correlation (Poyneer, 2003; Press et al., 2002) of the pupil tracker image and its 180 degree rotated image. The lateral shift can be measured as half of the correlation peak shift from its reference grid (here the double shift comes from the 180 degree rotation image). In the figure example, the correlation shift is 40 pixel, which corresponds to the 20 pixel lateral shift.

Longitudinal pupil Figure 4.7 also presents the longitudinal pupil shift measurement by computing the auto-correlation (Press et al., 2002) of the pupil tracker image. The outer peaks shown in circles are the correlation peaks formed when one sub-aperture spots matched with another

sub-aperture spots. The central peak is formed when the pupil tracker image correlated itself. Depending on the pupil defocus, the outer peaks shown in circles are either converged or diverged with respect to the central peak. The longitudinal defocus can be measured as given by

$$L_z = \sqrt{\left(P_{\text{outer}}(x) - P_{\text{central}}(x)\right)^2 + \left(P_{\text{outer}}(y) - P_{\text{central}}(y)\right)^2}, \tag{4.9}$$

where P_{center} and P_{outer} are the locations of the center peak and the location of any one of the outer peaks represented in circles respectively in the auto-correlation image of Figure 4.7.

Lateral pupil Figure 4.7 presents the lateral pupil shift measurement by computing cross-correlation between the pupil tracker image and its 180 degree rotated image. The cross-correlation peak represents the center of the pupil. The global movement of the cross-correlation peak allows us to measure the lateral pupil shift. The peak location is computed by taking a Gaussian fit by applying a small window over it. The lateral pupil shift can be calculated as given by

$$L_{(\text{x/y})} = \frac{P^{\text{Target}}_{\text{central}}(x/y) - P^{\text{Ref}}_{\text{central}}(x/y)}{2}, \tag{4.10}$$

where $P^{\text{Target}}_{\text{central}}$ and $P^{\text{Ref}}_{\text{central}}$ are the locations of the central cross-correlation peaks for the target and for the reference source respectively.

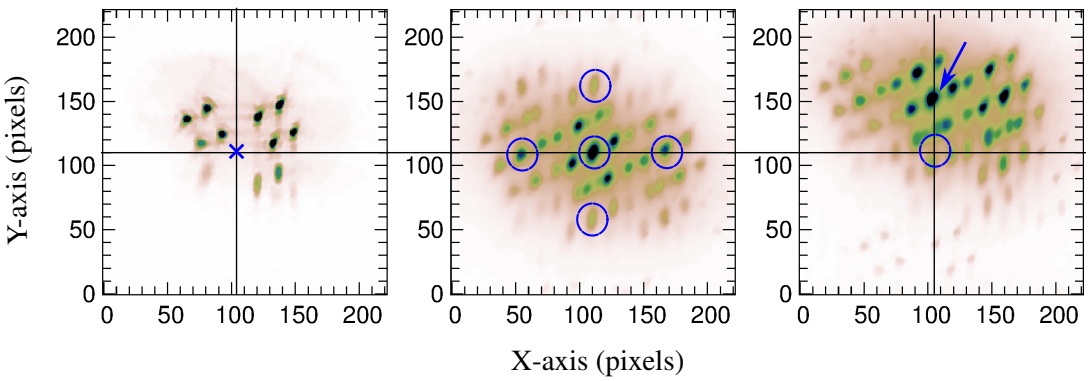

Figure 4.8: Left: a vignetted pupil tracker image. Middle: auto-correlation image; Right: cross-correlation image. Measurement of the pupil shifts in the presence of vignetting. This pupil tracker image has zero pupil shift. But the cross-correlation peak does not represent the center of the pupil, because it is biased in the absence of the other two sub-apertures.

Selection of final method Using the correlation method, the measurement of the longitudinal pupil shift is quite trivial but the lateral pupil shift measurement is very complex in the presence of pupil vignetting and astrophysical backgrounds. It is because the cross-correlation central peak no longer represents the center of the pupil in the presence of these effect. A typical pupil which is vignetted is presented in Figure 4.8. The right panel shows the cross-correlation peak (arrow) which is not at the expected location (ring), because the cross-correlation peak location is biased due to the absence of other spots.

However, this method can in principle be used to measure accurate pupil position by detecting missing spots pattern and using if and else conditions. But currently, the first method has been installed and is under usage, because it is tested and debugged for a long time and has been working successfully.

4.4.3 Field tracking

The field tracking software measures image motions of the astrophysical targets; The software is implemented in two blocks: a) measures brightest object position; b) corrects atmospheric differential refraction offsets in the object position measured in the first part.

4.4.3.1 Top level requirements

The top level requirements for the field tracking are presented in Annex B. They are briefly mentioned here for clarity.

- **Accurate star position detection** The field motion measurements are required to be accurate (the RMS error should be less than 2 mas for a $m_{\mathrm{H}} = 13$ mag star, for the UTs) as this is a prerequisite to achieve the 10 µas astrometry and for the stabilization of high flux injection into the fiber-fed GRAVITY beam combiner.

- **Should work in crowded field** The Galactic Center region of the sky is very crowded with many stars, the software should be robust to it.

4.4.3.2 Object tracking

Field tracker software tracks the brightest star in the field. The star position measurement is implemented in two steps. In the first step, stars in the field are scanned using a predetermined star FWHM as a threshold (sigma-filtering). Second, the detected stars are sorted on the basis of their flux. A Gaussian fit is applied to the brightest star to obtain its accurate position $O(x,y)$. Using this star position, the fiber is aligned to the acquisition camera to inject the K-band beam into it.

4.4.3.3 Atmospheric differential refraction

Atmospheric differential refraction (ADR) effects are of relevance since the H-band photo-center reference, $O(x,y)$ is used to guide the K-band beam into the fibers. Figure 4.9 depicts the atmospheric differential refraction (ADR) effects (Roe, 2002) that exist between the H and the K-bands.

To improve the coupling efficiency of the light injection into the fiber and to minimize the additional tip-tilt errors, the ADR offsets need to be corrected. These offsets can be calculated (Schubert and Walterscheid, 2000) using the operating wavelength of the acquisition camera (λ_{AC}) and of the beam combiner (λ_{BC}) as given

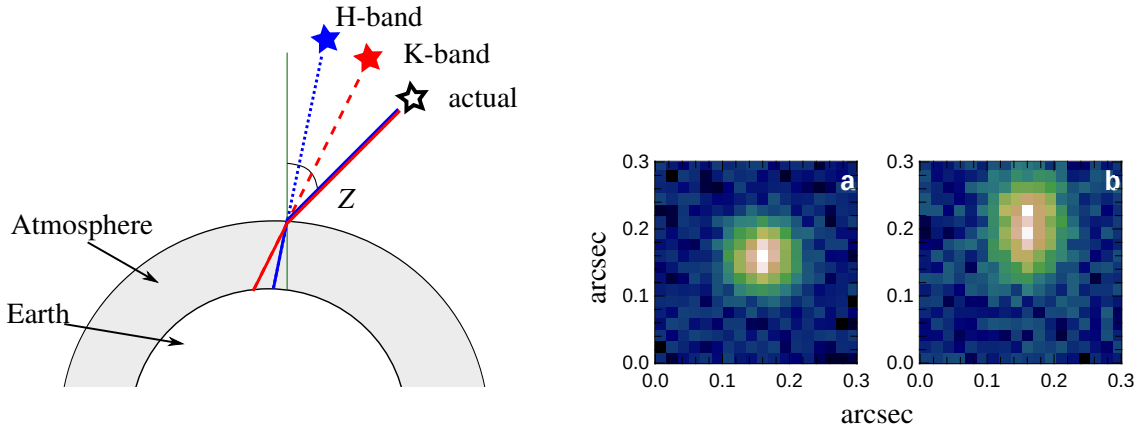

Figure 4.9: Left: As a consequence of refraction, the blue light (H-band) bends more than the red light (K-band). That means blue center is more angularly shifted towards the zenith in comparison to the red light. Right: (a) a typical field image for the UTs; (b) the ADR affected field image for the UTs at a zenith distance of 50°. In the ADR affected image, the star image is spectrally elongated which is similar to that of a prism dispersion.

$$\Delta R \sim 206265 \left(\frac{n^2_{\lambda_{\rm BC}} - 1}{2n^2_{\lambda_{\rm BC}}} - \frac{n^2_{\lambda_{\rm AC}} - 1}{2n^2_{\lambda_{\rm AC}}} \right) \tan z \qquad \text{(arcsec)} \tag{4.11}$$

where $n_{\lambda_{\rm AC}}$ and $n_{\lambda_{\rm BC}}$ are the refractive indices of the wavelengths $\lambda_{\rm AC}$ and $\lambda_{\rm BC}$ respectively and are calculated by using Eq. 4.12. 206265 is the scale factor converting radians into arcsec. z is the zenith distance. Refractive index for a given λ can be calculated as (Schubert and Walterscheid, 2000)

$$\begin{aligned} n(\lambda, p, t, p_w) &= 1 + (64.328 + \frac{29498.1}{146 - \lambda^{-2}} + \frac{255.4}{41 - \lambda^{-2}}) \times (\frac{pT_s}{p_s t} 10^{-6}) \\ &- 43.49(1 - \frac{7.956 \times 10^{-3}}{\lambda^2}) \frac{p_w}{p_s} 10^{-6} \end{aligned} \tag{4.12}$$

where t, p, p_w are the observatory conditions such as temperature, pressure, partial pressure of water respectively; and $p_s = 1013.25$ mbar and T_s =288.15 K.

Stars with different spectral types will have different amounts of atmospheric dispersion and this effect is called differential color refraction (Stone, 2002), a blue star has its effective wavelength towards the lower extreme of the H-band and a red star has its effective wavelength towards the upper extreme of the H-band.

Figure 4.10 (left panel) presents the estimated ADR shifts, for $\lambda_{\rm BC} = 2.2\,\mu$m and $\lambda_{\rm AC}$ is substituted as 1.4 to 2.2 µm (using Eq. 4.11).

Effective wavelength computation Since the effective wavelength of the acquisition camera image changes with the color of the target star, its value is modeled as a function of the H-K

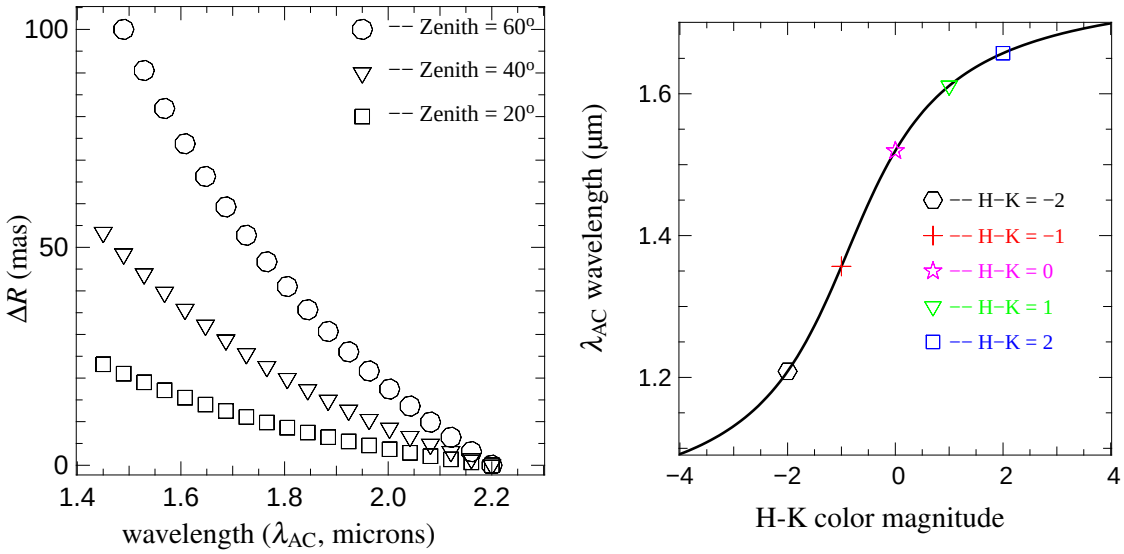

Figure 4.10: Left: ADR shifts obtained at different zenith distances, $z = 20°$, $40°$ and $60°$, and for various wavelengths. In this calculation a typical Paranal observatory conditions are used. Right: Effective wavelengths of stars when imaged on the acquisition camera as a function of their H-K color.

color of that target, by considering the target spectrum, atmospheric transmission and telescope and instrument transmissions (filters, reflection of mirrors and efficiency of the detector).

The modeling of the effective wavelength of the acquisition camera, $\lambda_{\rm AC}$, is done in five parts. First, a field image is generated by using a NACO's Galactic Center archive image. Second, ADR shifts are computed for all the acquisition camera imaging wavelengths 1.0-1.85 μm with respect to its central 1.65 μm wavelength (using Eq. 4.11). Third, for each wavelength step (2 nm), the field image is shifted by the amount of ADR shifts measured in the second part. Fourth, for each wavelength the effective transmission (star's source spectrum, atmospheric transmission and telescope and instrument transmission) is computed. Next a data cube, consisting of shifted and transmission scaled field images as a function of wavelength, is generated. Finally, using this data cube, the ADR affected final field image is created by integrating an observational exposure for the acquisition camera imaging wavelengths.

$$I_{\rm ADR} = \int_{\lambda_{\rm min}}^{\lambda_{\rm max}} I(\lambda)\, T_{\rm eff}(\lambda)\, {\rm d}\lambda, \tag{4.13}$$

where $I_{\rm ADR}$ is the final field image affected by the ADR. $I(\lambda)$ is the field image, for a given wavelength, which is affected by the ADR shift (between λ and H-band central wavelength, 1.65 μm). $T_{\rm eff}(\lambda)$ is the combined transmission (atmospheric transmission, instrument transmission and source spectrum). From this image, the effective wavelength of the acquisition camera is modeled as

$$\lambda_{\rm AC} = 1.38 + \frac{0.78}{\pi} \times \arctan(0.73\, C_{H-K} - 0.93 + \frac{\pi}{2}), \tag{4.14}$$

where C_{H-K} is the color of the star, and the arctan function was chosen because it mimics the observed behaviour in the simulation.

Having the $\lambda_{\rm AC}$ and $\lambda_{\rm BC}$, the ADR shift is measured using Eq. 4.11 in arcsec. The conversion from arcsec into the acquisition camera detector coordinates is done as following.

Conversion of ADR shift into detector coordinate system The ΔR shift (arcseconds) can be related to the detector (X, Y) coordinates with respect to the sky using parallactic ($\theta_{\rm Par}$) and position ($\theta_{\rm Pos}$) angles (cf. Figure 4.11) as given (in Eq. 4.15, Roe, 2002).

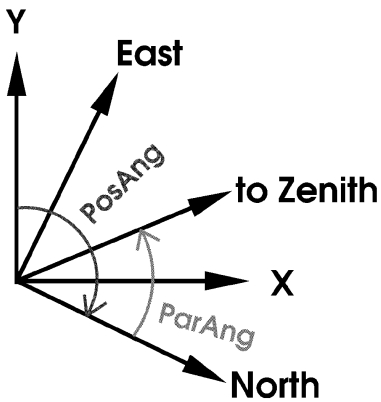

Figure 4.11: The definition of position and parallatic angles on the detector coordinates (X, Y). The position angle ($\theta_{\rm Pos}$) is defined as the clockwise angle measured from the positive Y-direction on the detector coordinate to the vector pointing north on the sky. The parallactic angle ($\theta_{\rm Par}$) is defined as the counterclockwise angle measured from the vector pointing north on the sky to the vector pointing to the zenith. Figure credit: Roe (2002).

$$X_{\rm ADR} = \frac{\Delta R}{\theta_{\rm pix}} \sin(\theta_{\rm Pos} - \theta_{\rm Par})$$

$$Y_{\rm ADR} = \frac{\Delta R}{\theta_{\rm pix}} \cos(\theta_{\rm Pos} - \theta_{\rm Par}) \tag{4.15}$$

where $\theta_{\rm pix}$ is the acquisition camera field imager pixel scale. The Zenith angle, the parallactic angle and the north axis vector angle are already measured using the VLTI geometry. For our computation, I read them from the VLTI database and used to compute the $(X_{\rm ADR}, Y_{\rm ADR})$ offsets on the detector coordinates.

ADR correction The ADR model works by taking the H-K color of the star as the input and computing the effective wavelength for the acquisition camera. The effective wavelength of the beam combiner is taken as 2.2 µm for all calculations. The effective wavelengths of the acquisition camera and the beam combiner are substituted in Eq. 4.11 and the ADR shift in arcsec is computed. Figure 4.12 (left panel) presents the ADR shifts in arcsec as a function Zenith distance, z. Next the ADR shift is converted into the detector coordinates using Eq. 4.15. Figure 4.12 (right panel)

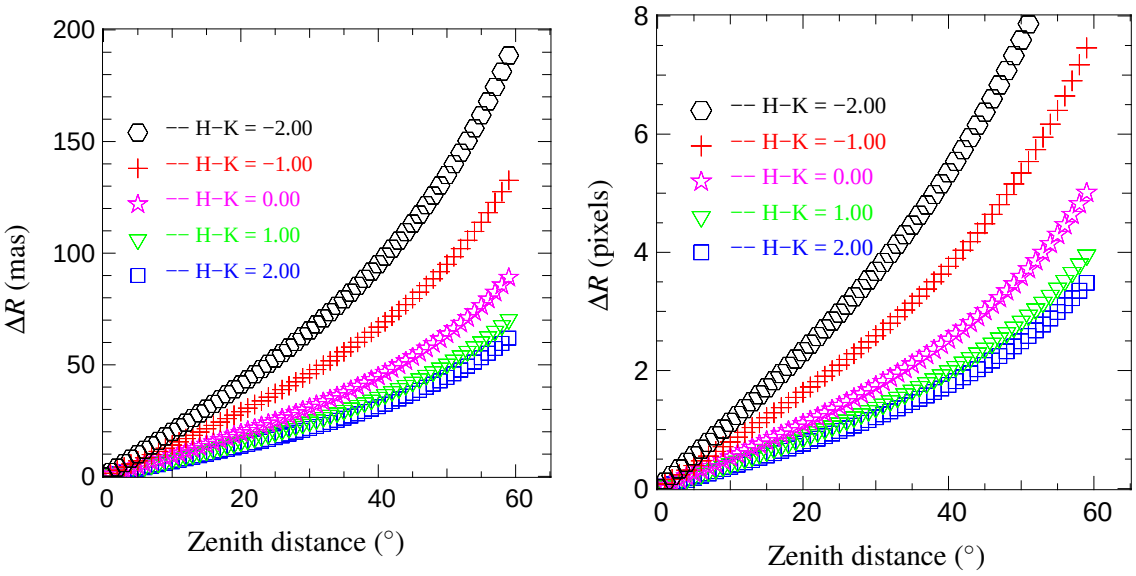

Figure 4.12: ADR shifts as a function of zenith angle at various H-K colors. The left panel in arcsec and right panel in pixels (for the UTs).

presents the ADR shifts in the detector coordinates as a function of Zenith distance, z. Finally the ADR corrected star position is computed by the following transforms

$$O^{'}(x) = O(x) - X_{\mathrm{ADR}} \tag{4.16}$$

$$O^{'}(y) = O(y) - Y_{\mathrm{ADR}} \tag{4.17}$$

Software working flow The software works by reading factory values from the instrument database such as image window coordinates on the detector, Gaussian fit window sizes, sigma-filter star FWHM and H-K color of the star. These parameters can be fine-tuned depending on the demand of a particular observation. For instance, the ADR model uses default H-K color = 0. The H-K color of the star can be changed using a database writing and it can also rewritten using Broker for Observation Blocks (OB). In the end, the measured beam parameters are written to the "corrections" part of the instrument database.

4.4.4 Aberration sensing

The aberration sensor images 9×9 Shack-Hartmann lenslet spots. Figure 4.13 presents the principle of the Shack-Hartmann wavefront sensor. For a plane wavefront incidence on the Shack-Hartmann lenslet, the Shack-Hartmann spots are focused on the optical axis of the each sub-aperture lens. These spots positions are considered as reference positions. For an aberrated wavefront, the detector spots are shifted from these reference positions. The measurement of these spot shifts allows one to estimate the incident aberrated wavefront shape.

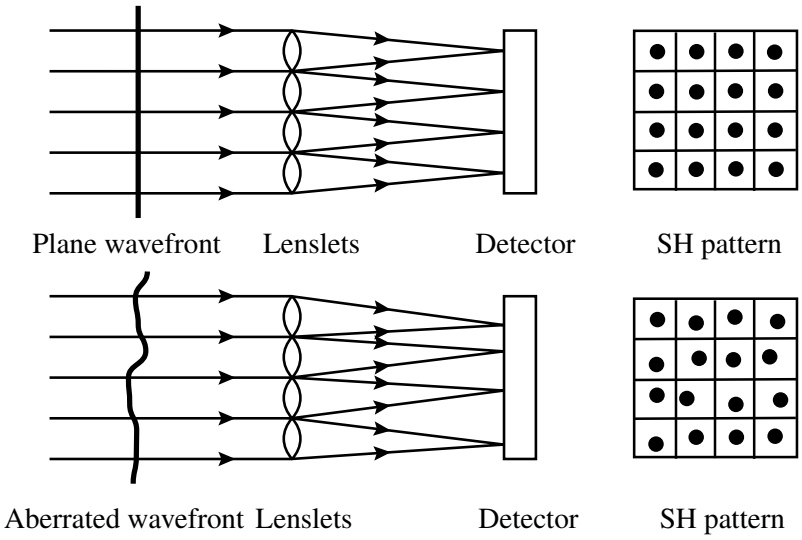

Figure 4.13: Concepts of the Shack-Hartmann wavefront sensing. Top panels: For a plane wavefront incidence on the Shack-Hartmann lenslet, the formed spots on the detector are focused on the optical axis of the each sub-aperture lens. Bottom panels: For an aberrated wavefront, the Shack-Hartman imaged spots are displaced from the reference centers. Figure credit Buscher 2015.

To measure the incoming wavefront aberrations, the aberration sensor software has been developed as part of the acquisition camera software. The aberration sensor software takes the Shack-Hartmann detector images of all four telescopes as input and the wavefront profile is reconstructed for each beam (in 28 Zernike coefficients) as output. This full algorithm is implemented in three steps. As a first step in the software, aberrated Shack-Hartmann spot centroid positions are computed using standard centroid algorithms: a) Multiple Gaussian fits are used for a point source spots; b) the cross-correlation algorithm is used for extended scene images (Section 4.4.5). Second, by comparing the spot positions with the reference grid, wavefront slopes are computed. Third, using these slopes, the aberrated wavefront which corresponds to the Zernike polynomials is modeled (Dai and Mahajan, 2007; Noll, 1976).

Conversion from slopes to Zernike coefficients Wavefront aberrations $W(x,y)$ can be approximated as a superposition of Zernike polynomials Z_i

$$W(x,y) = \sum_{i=1}^{q} C_i \, Z_i(x,y), \tag{4.18}$$

where C_i is the Zernike coefficient of the Z_i Zernike mode expansion and q is the number of Zernike coefficients used in the approximation.

The derivative of the above equation with respect to X and Y gives the wavefront slopes in both directions

$$\frac{\partial W(x,y)}{\partial x} = \sum_{i=1}^{q} C_i \frac{\partial Z_i(x,y)}{\partial x} \qquad \frac{\partial W(x,y)}{\partial y} = \sum_{i=1}^{q} C_i \frac{\partial Z_i(x,y)}{\partial y} \tag{4.19}$$

The wavefront and its slopes are related as below, for a sub-aperture lens diameter d

$$W(x,y) = \sum_{i=1}^{p} \frac{\partial W(x,y)}{\partial x} d + \frac{\partial W(x,y)}{\partial y} d. \tag{4.20}$$

From the Eq. 4.19, we can relate the slopes of a wavefront with derivatives of Zernike polynomials in matrix form

$$C = Z^{-1} W, \tag{4.21}$$

where C, Z and W are the matrices containing Zernike coefficients, partial derivatives of the Zernike polynomials and local slope measurements corresponding to the incoming aberrated wavefront respectively

$$\begin{bmatrix} C_1 \\ \\ C_2 \\ \vdots \\ C_{q-1} \\ \\ C_q \end{bmatrix} = \begin{bmatrix} \frac{\partial Z_1(x_1,y_1)}{\partial x} & \frac{\partial Z_2(x_1,y_1)}{\partial x} & \cdots & \frac{\partial Z_q(x_1,y_1)}{\partial x} \\ \vdots & & & \\ \frac{\partial Z_1(x_p,y_p)}{\partial x} & \frac{\partial Z_2(x_p,y_p)}{\partial x} & \cdots & \frac{\partial Z_q(x_p,y_p)}{\partial x} \\ \frac{\partial Z_1(x_1,y_1)}{\partial y} & \frac{\partial Z_2(x_1,y_1)}{\partial y} & \cdots & \frac{\partial Z_q(x_1,y_1)}{\partial y} \\ \vdots & & & \\ \frac{\partial Z_1(x_p,y_p)}{\partial y} & \frac{\partial Z_2(x_p,y_p)}{\partial y} & \cdots & \frac{\partial Z_q(x_p,y_p)}{\partial y} \\ & & & \end{bmatrix}^{-1} \begin{bmatrix} \frac{\partial W(x_1,y_1)}{\partial x} \\ \vdots \\ \frac{\partial W(x_p,y_p)}{\partial x} \\ \frac{\partial W(x_1,y_1)}{\partial y} \\ \vdots \\ \frac{\partial W(x_p,y_p)}{\partial y}. \end{bmatrix} \tag{4.22}$$

The partial derivatives of the Zernike polynomials matrix Z are constant and not altered with the atmospheric turbulence, noise and system errors. The Zernike coefficients, C, result from multiplying the inverse of the derivative of the Zernike polynomials, Z^{-1} with slope vector, W.

Measurement of the partial derivatives for 28 Zernike polynomials using analytical equations is quite complex. In the adaptive optics community, it is usual to calibrate this matrix using a deformable mirror. Since there is no deformable mirror for GRAVITY, the slopes-to-Zernike matrix Z^{-1} is generated by simulations. This is carried out in two steps. First, Zernike phases are generated corresponding to the Zernike coefficients starting from the piston to 28th coefficient. Second, these phases are propagated through the Shack-Hartmann sensor and corresponding local slopes are determined. These local slopes are the derivatives of the corresponding Zernike polynomial as given in Eq. 4.19. These simulations are implemented using YAO. The inverse of Z is calculated using singular value decomposition.

Software working flow The software works by reading factory values from the instrument database such as Shack-Hartmann image window coordinates on the detector and Gaussian fit window sizes. Reference positions of the Shack-Hartmann are computed by using the GRAV-

ITY Calibration Unit's internal source in the beginning of the observational night. Using these reference positions, target Shack-Hartmann spot positions are computed with Gaussian fits. Comparison of the target positions with the reference positions gives the wavefront slopes.

4.4.5 Wavefront sensing with extended objects

The aberration sensor not only observes point sources but also extended sources such as binary stars and crowded stellar fields, such as the Galactic Center field. Measurement of the centroid positions for the extended scene lenslet images is carried out with the correlation algorithms because the traditional point source centroid algorithms fail (Poyneer, 2003; Löfdahl, 2010).

In the correlation algorithms, evaluation of centroid involves two sub-computations: a) correlation estimation between the target and the reference. The peak of the correlation gives the image shift or slope in integer pixel precision. b) the sub-pixel precision image shifts are computed by applying a peak-finding algorithm to the correlation peak.

The estimated image shifts are usually affected by the systematic errors due to pixel-locking or peak-locking effects (Nobach and Honkanen, 2005). The nature of the systematic error is that the measured image shifts are concentrated at the closest integral pixel value. These are caused by the low pixel sampling of the images. The magnitude of the systematic errors depends on the type of extended scene and the combination of correlation algorithm and peak-finding algorithm used. To reduce the systematic errors, several correlation and peak-finding algorithms were investigated in the field of feature tracking and strain measurement. However, the real-time Shack-Hartmann wavefront sensing is significantly different from their work. The Shack-Hartmann wavefront sensing involves: a) different type of images; b) images of small fields of view (for example, 16 x 16 pixels); c) real-time measurements.

In this study we approached the problem in three ways. First, the performance of three different correlation algorithms (cross-correlation Poyneer 2003; sum of squared differences; sum of absolute differences Löfdahl 2010) from the state of the art is investigated for three classes of sub-aperture images (point source, elongated laser guide star, extended scenes). It was found that the cross-correlation is most robust to the point source and the elongated laser guide star. The sum of squared differences algorithm performs better (less failure rates) for the extended scenes although it involves large systematic errors.

Second, the performance study was extended to different peak-finding algorithms (parabola fit Poyneer 2003; quadratic polynomial fit Löfdahl 2010; Gaussian fit Nobach and Honkanen 2005; threshold center of gravity; pyramid fit Bailey 2003) using the three classes of sub-aperture images. The study revealed that the pyramid fit is preferable for the extended scenes, while the quadratic polynomial fit performs better for the elongated laser guide star. The threshold center of gravity performs better in a low SNR scenario cases, although the systematic errors in the measurements are large. It is found that no peak finding model is good enough in reducing both the systematic and the RMS centroid errors.

Third, a technique which is used in the fluid mechanics is applied here to overcome the above limitations (Sjödahl, 1994). In this technique, the image sampling prior to the actual correlation

matching is increased. The technique is realized in the image domain and is implemented in two steps to improve its computational efficiency: a) in the first step, the image shift is estimated by executing the cross-correlation algorithm at the original image sampling; b) next the cross-correlation is performed at a sub-pixel level spatial sampling by confining the correlation search to a small field of view (4×4 pixels) centered at the position obtained in the first step.

Studies reveal that the image sampling improvement technique outperforms the other two approaches. It improves the image-shift measurement accuracy (wavefront sensing) by a factor of 3 in terms of both the systematic and the RMS errors, at the expense of twice the computational cost. The full results will be submitted elsewhere (cf. annex C.3).

4.4.6 Pupil imager

Currently this function is used for monitoring the pupil visually, so it does not require any image processing.

4.5 Closed loop control software

Figure 4.14 presents the block diagram for the closed loop field and pupil guiding enabled by the acquisition camera. By comparing the acquisition camera measurements (called process variable, PV) to the desired beam stabilization targets (called the set point, SP) the difference error is calculated. Classical proportional and integral (PI) controller mathematics (Astrom and Murray, 2010) is applied on the error values to calculate the PI output values for the fast and converged correction. This PI output values (in pixels) are then converted into actuator commands (voltages). By using them the actuators (TTP and PMC) corrections are applied on the input beam. The acquisition camera measures the influence of the actuators and feedbacks data for the commands every 0.7 s, then the whole loop is repeated. In case of positive feedback, the process variable is added to the set point and if it is negative feedback then it is subtracted from the set point.

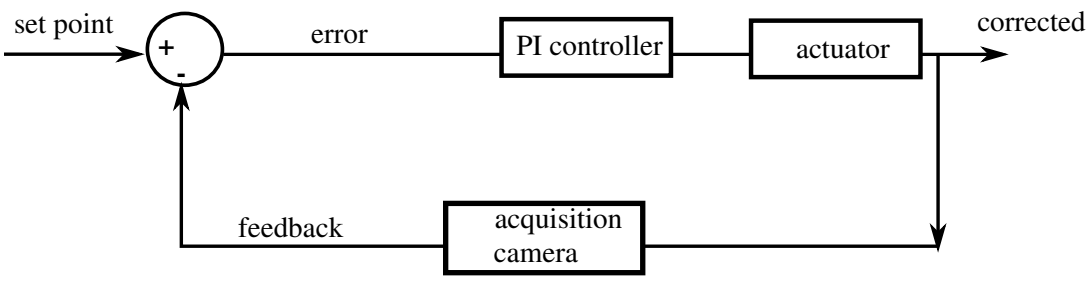

Figure 4.14: The block diagram for closed loop field and pupil guiding.

The PI control output value consists of proportional error value added with integral error value as given below

$$u(t) = K_\mathrm{p}\, e(t) + \frac{K_\mathrm{i}}{T_\mathrm{i}} \int_0^t e(t)\, dt,$$

where, $e(t)$ = set point-process variable, K_p, K_i are the proportional and the integral gains. T_i is the reset time. The K_p, K_i and T_i are tunable parameters for the optimized performance.

An interaction matrix (I) connects the acquisition camera sensor (tip-tilts or pupil shifts) measurements (M) to the voltages to be applied to the actuators (V) as given in Eq. 4.23.

$$M = I\,V \tag{4.23}$$

The interaction matrix is constructed by applying amplitude 1 V voltages to the actuators in X and Y-axes and measuring its response on the acquisition camera. For example, in the case of field guiding, when 1 V is applied on the TTP in both X and Y directions, the object moves in the field imager by, say, O^1_x and O^1_y pixels. Then the interaction matrix becomes as given below

$$I_\mathrm{TTP} = \begin{bmatrix} O^1_\mathrm{x} & 0 \\ 0 & O^1_\mathrm{y} \end{bmatrix}$$

Having the interaction matrix in hand, for a given acquisition camera object position measurement, $M_\mathrm{FI} = [O_\mathrm{x},\ O_\mathrm{y}]^T$, the correction commands to the TTP actuators (in V), $V = [TV_\mathrm{x},\ TV_\mathrm{y}]^T$ can be obtained as given below

$$\begin{bmatrix} TV_\mathrm{x} \\ TV_\mathrm{y} \end{bmatrix} = \begin{bmatrix} O^1_\mathrm{x} & 0 \\ 0 & O^1_\mathrm{y} \end{bmatrix}^{-1} \begin{bmatrix} O_\mathrm{x} \\ O_\mathrm{y} \end{bmatrix},$$

In the same way, for a given acquisition camera pupil offset measurements, $M_\mathrm{PT} = [L_\mathrm{x},\ L_\mathrm{y}]^T$, T–transpose, the correction commands applied to the PMC actuators, $V = [PV_\mathrm{x},\ PV_\mathrm{y}]^T$ can be obtained as given below

$$\begin{bmatrix} PV_x \\ PV_y \end{bmatrix} = \begin{bmatrix} L^1_\mathrm{x} & 0 \\ 0 & L^1_\mathrm{y} \end{bmatrix}^{-1} \begin{bmatrix} L_\mathrm{x} \\ L_\mathrm{y} \end{bmatrix},$$

where the interaction matrix for the PMC is measured by applying 1 amplitude voltages in X and Y-axes and measuring the response on the pupil tracker in units, say, L^1_x and L^1_y pixel shifts along X and Y-axis and is detonated as

$$I_\mathrm{PMC} = \begin{bmatrix} L^1_\mathrm{x} & 0 \\ 0 & L^1_\mathrm{y} \end{bmatrix}$$

The variable curvature mirror, VCM, accepts the longitudinal pupil offset commands in meters and those are directly measured in the same units by the pupil tracker.

4.6 Software verification and validation

The validity and the accuracy of the software methods or algorithms are verified by using the simulated synthetic detector images presented in Chapter 3.3. One thousand detector images of the acquisition camera are generated by applying the VLTI laboratory experimentally measured field motions (up to a maximum of 50 mas without AO for ATs), pupil motions (lateral: 5% of pupil diameter; and longitudinal: up to 3 m for the 80 mm beam size) and higher order wavefront aberrations.

Next the input VLTI beam properties are reconstructed back. The software performance in terms of accuracy is analyzed in the presence of adverse imaging conditions and sensitivity towards the faint stars. The details are presented in the next sections.

4.6.1 Field imager

Field tracking accuracy studies are carried out as a function of known input field errors and star magnitudes. Field images are generated for various known input tip-tilts ranging from 0 to 2.0 arcsec (with a step size of 0.2 arcsec) and also for various star magnitudes ranging from $m_{\mathrm{H}} = 10$ mag to $m_{\mathrm{H}} = 16$ mag. The field motions in arcsec are converted into the image plane (pixel coordinates) using its pixel scale. The field motions are applied to the images by shifting them using the Fourier transform shift theorem. For each step of tip-tilt or star magnitude, 1000 statistical realizations of the field images are generated including read-out and Poisson noises. The input tip-tilts are reconstructed back by fitting the star position with a Gaussian fit using the window size of 10×10 pixels.

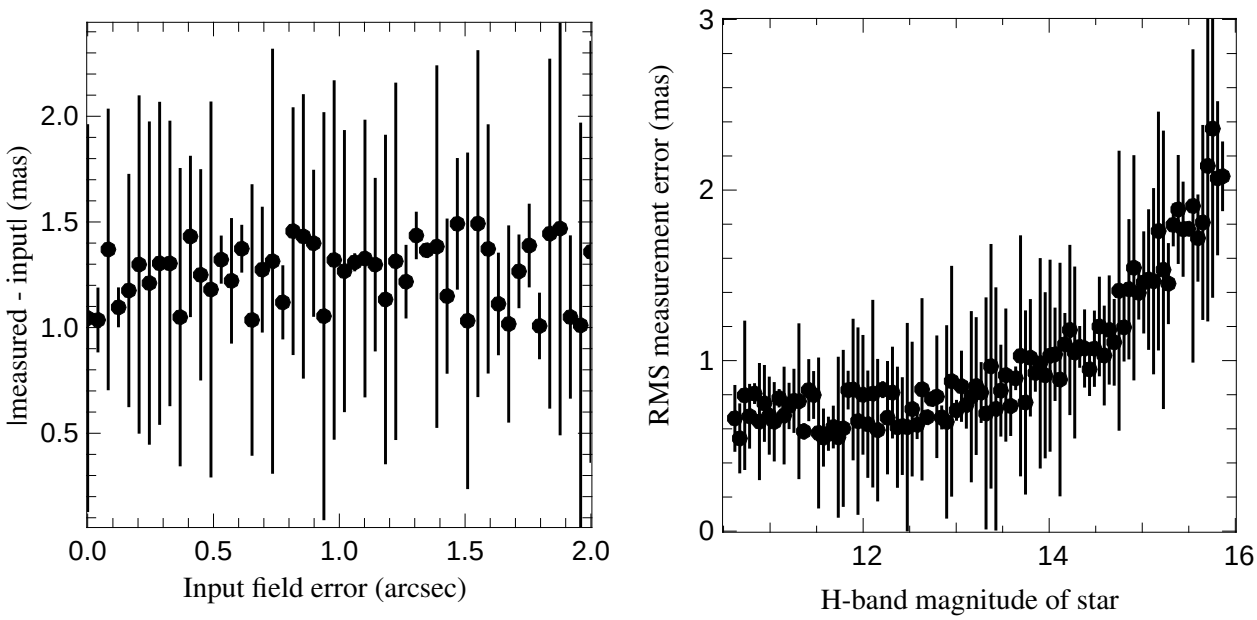

Figure 4.15: Accuracy measurements of the field imager. Left: Absolute error measurement as a function of input field error. Right: RMS error measurement as a function of star magnitude.

Figure 4.15 presents the results. The RMS statistical errors corresponding to an integration time of 0.7 s are 1 mas, for a $m_{\mathrm{H}} = 13$ mag star. The absolute and the RMS errors as a function of input field error are within the GRAVITY specifications (2 mas RMS error requirement for 13 mag star). The increment of the RMS error with increasing magnitude is due to the low SNR of the object. The results show that the tip-tilt correction specifications can be achieved even for very short exposures of 0.7s suggesting that the method can work even with much fainter stars.

4.6.2 Pupil tracking

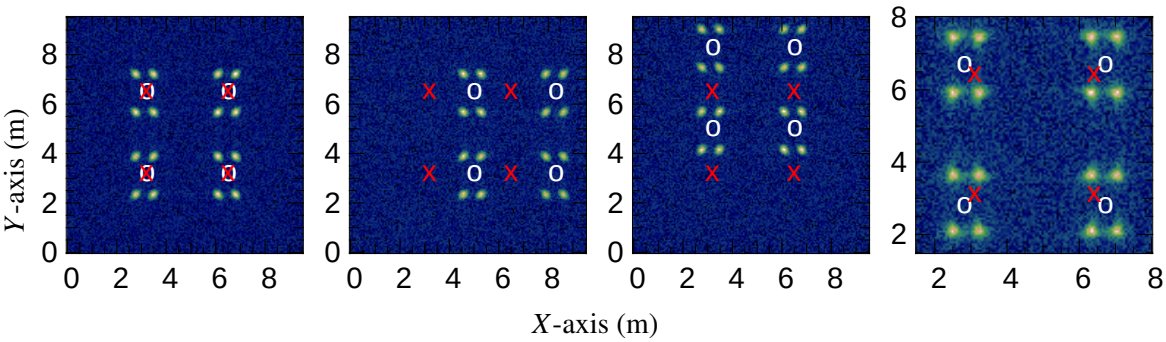

Figure 4.16: Left: a typical pupil tracker image with zero pupil shifts. Middle left: pupil tracker image with lateral shift along X-axis. Middle right: pupil tracker image with lateral shift along Y-axis. Right: pupil tracker image with longitudinally shift. The red-crosses and white-rings are the reference R_j and the barycenter B_j positions respectively.

Pupil tracking accuracy studies are carried out as a function of known input lateral and longitudinal pupil shifts. For this, a series of known input pupil shifts (lateral and longitudinal) are applied to the pupil tracker and associated images are generated. The pupil lateral and the longitudinal shifts are applied to the input beams as tip-tilt and defocus error before the incoming beams fall on the 2×2 lenslet. The reconstruction of the input pupil shifts from the pupil tracker images is carried out with the methods described in Section 4.4.2.

Figure 4.16 presents a variety of pupil tracker images obtained at different imaging conditions. The mismatch between the barycenter positions (average of four pupil beacons imaged by each sub-aperture, denoted with white circles) and the reference spot positions (red crosses) graphically demonstrates the lateral pupil shifts and the longitudinal pupil shifts.

Figure 4.17 presents the results. The absolute (6 mm at the UT, 50 mm at 80 mm of lateral and longitudinal) and the RMS (4 mm at the UT, 30 mm at the 80 mm of lateral and longitudinal) measurement errors are within the GRAVITY specifications (requirement: 40 mm of the lateral pupil RMS measurement error; 1 m of the longitudinal pupil RMS measurement error for the 80 m beam). The increment of the absolute and the RMS errors with increasing the longitudinal pupil shift (pupil defocus) is due to the defocus of the pupil tracker spots. The Gaussian fits applied on these defocused spots are giving large fitting errors.

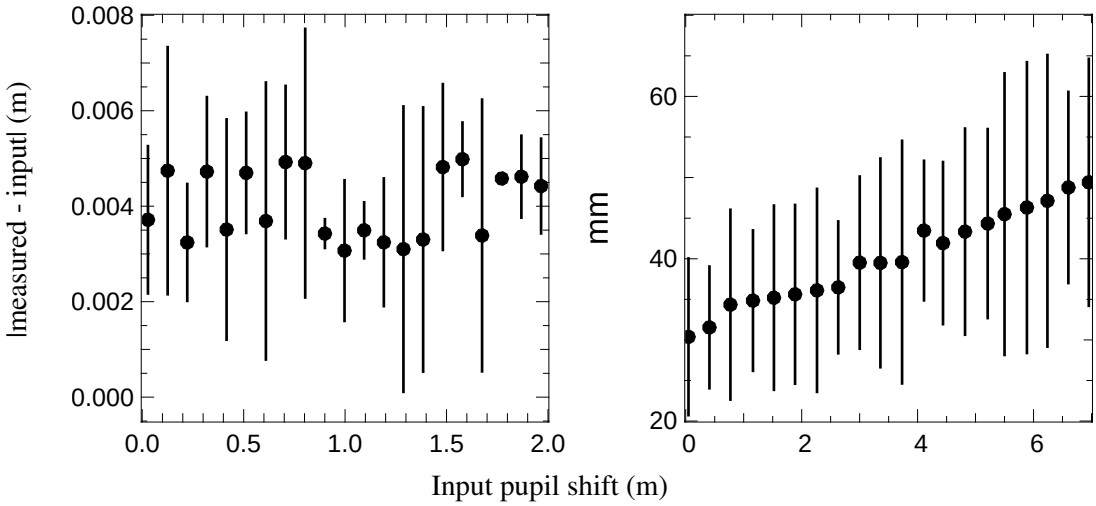

Figure 4.17: Left: Lateral pupil shift measurement error scaled to the UT beam. Right: Longitudinal pupil shift measurement error scaled to 80 mm beam.

4.6.3 Aberration sensor

The VLTI measured wavefront aberrations are applied to the Shack-Hartmann lenslets in two steps: a) generated a final Zernike phase screen by taking the linear combination of various Zernike coefficients associated phases (Zernike coefficient amplitudes taken from Pfuhl (2012)); b) the final Zernike phase is applied to the Shack-Hartmann images in the Fourier plane using YAO.

Figure 4.18 presents the reconstructed wavefront error as a function of magnitude of star in H-band for a 0.7 s integration. These input aberrations are measured back with 80 nm accuracy for a 13 mag star in the H-band, with 5 s integration.

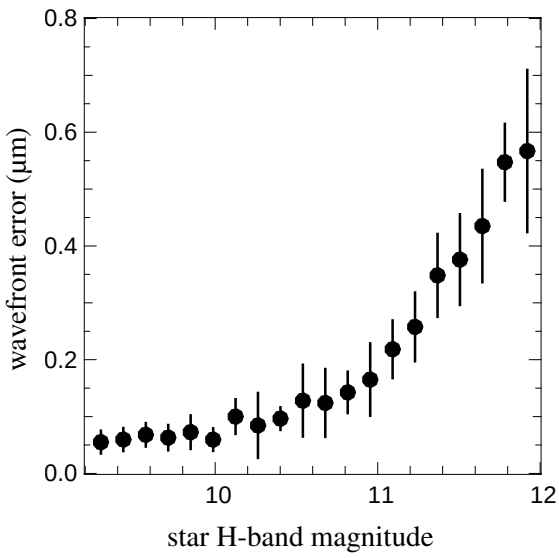

Figure 4.18: Wavefront measurement accuracy as a function of the star magnitude, for a 0.7 s integration.

Table 4.1 presents the summary of the end-to-end modelling results.

Table 4.1: Beam guiding errors computed from the end-to-end modelling of the acquisition camera.

Parameter	Beam guiding requirements (RMS)	End-to-end simulation results (RMS)
Lateral pupil guiding	40 mm	4 mm
Longitudinal pupil guiding	30 km	300 m
Field guiding	10 mas	2 mas
Wavefront measurement	80 nm	70 nm

4.6.4 Computational time

In normal operation the software gives preference to field guiding. It means that the acquisition camera software first tracks the field and then writes to the database. The database writing triggers the actuator controller software to apply the corrections. Then the pupil shifts are measured and written to the database. Finally it measures Zernike coefficients corresponding to the incoming wavefront.

This preferential approach is important to correct the beam as soon as the field is tracked. Next, preference is given to the pupil guiding. Finally, the Zernike coefficients are measured and then the software waits for the next detector image.

Currently the field, the pupil and the aberration tracking have been implemented with the speeds of 0.1 s, 0.2 s and 0.2 s respectively.

4.7 Summary and future improvements

This chapter presents the acquisition camera software methods and the data reduction algorithms starting from acquiring detector images, extracting beam aberration parameters from the detector images and applying corrections to the beams using various actuators. To study the performance of the acquisition camera, end-to-end simulations are carried out. The results reveal that the measurement accuracies are within the GRAVITY specifications.

The developed software has been tested in detail by simulating a wide variety of imaging conditions including the VLTI laboratory experimentally measured beam aberrations. The reconstruction of the input aberration parameters are carried out with the software methods developed in this chapter and they involve following RMS errors: a) 1.5 mas error for the field tracking; b) 3 mm for lateral pupil tracking; c) 35 mm for longitudinal pupil tracking; d) 100 nm RMS error for the reconstruction of the input wavefront error. The results shows that the field and pupil beam stabilization requirements can be achieved within the GRAVITY specifications. The validation of the software with a laboratory generated beams and on-sky at the Paranal observatory, Chile is presented in Chapter 6.

While writing this thesis, the software continues to give the desired performance, however, there is scope for future improvements in: a) pupil tracking in the presence of a bright astrophysical target; b) field tracking; c) code cleaning.

Pupil tracking in the presence of a bright astrophysical target Currently the pupil tracker works for stars fainter than 1 mag, for the ATs. For stars brighter than 1 mag, currently, the pupil tracking does not work due to the astrophysical target background (Section 6.2.1). In this context, the pupil imager could be used, instead of the pupil tracker, for lateral pupil tracking as it gets enough flux. A cross-correlation algorithm can be used to track the pupil image with respect to a reference pupil image and this allows one to measure lateral pupil shifts. The reference image for this algorithm can be a long exposure pupil image that is centered at the zero pupil position with respect to internal calibrator source.

Field tracking The field tracking is implemented by tracking the brightest star (fringe tracker object) in the field. It works fine except in a situation where two stars in the field have the same flux. Currently, this problem is solved manually by reducing the window size to only one star, so that the second star is not seen by the software.

The user effort can be minimized by developing an automatic software so that a mouse click on the interested target would solve the problem by selecting a reasonable window around that target.

Code documentation Some parts of the code (15-20%) are missing proper documentation as they were developed during the commissioning, where the time was short and the main goal was to make the software work. There are some plans to finish this work after writing this thesis.

Chapter 5

From optical testing to integration

5.1 Introduction

With the design parameters as described in Chapter 3, the optical and mechanical parts are procured by the CENTRA/SIM team. Assembly, integration and optical testing of the folding optics, the beam analyzer mounts and the detector mounts are carried out at the CENTRA/SIM laboratory. Due to its complexity, the positioning, alignment and gluing of the beam analyzer are contracted to WINLIGHT OPTICS company, France. Since there had been a delay in the delivery of the beam analyzer, a simplified beam analyzer (containing only field imager mode) was developed at Lisbon, as it is an important mode and required for testing the other subsystems of GRAVITY (the fringe tracker and the science spectrometers work based on the field imager enabled star's light injection into single mode fibers).

After the initial tests of the acquisition camera at CENTRA/SIM, it was shipped to MPE and was integrated within the GRAVITY cryostat by the end of 2013. There its optical concepts and software were characterized with the laboratory telescope beams and the artificial stars. These were generated using the GRAVITY Calibration Unit. Once the Preliminary Acceptance Europe tests had been finished, GRAVITY was shipped to the Paranal Observatory, Chile and was integrated in the VLTI laboratory in 2015.

Section 5.2 describes the optical testing, the assembly and the optical alignments of the acquisition camera that are carried out at Lisbon. The optical alignment optimization and preliminary characterization of the acquisition camera detector image that are carried out at MPE is described in Section 5.3. Ths chapter ends with the summary and conclusions of the assembly and the optical alignment are presented.

I was responsible for optical testing and the development of appropriate liquid nitrogen filling control system. I participated in the assembly and the optical alignment of the folding optics which were led by Paulo Gordo.

5.2 Instrument assembly and optical alignment at CENTRA/SIM

The instrument assembly and the optical alignment are carried out in four steps: a) optical testing of the acquisition camera's procured optical components; b) assembly of the acquisition camera using its optical components; c) optical alignment of the assembled system at room temperatures; and d) verification of the optical alignment at the cryogenic temperatures by developing a cryogenic system.

5.2.1 Optical testing

The optical components which are procured consists of several lenses, mirrors, prisms and lenslets. The optical testing of the above components is implemented in two different approaches. First, the optical surface accuracy tests of the mirrors, the lenses and prisms are carried out. Second, lenslets are tested for their image quality and focus lengths characterization.

5.2.1.1 Optical surface accuracy measurement

The surface accuracy of the optical elements (mirrors, lenses and prisms) are tested using Fizeau type interferometer Intellium Z100. Figure 5.1 presents the basic layout of the Fizeau interferometer.

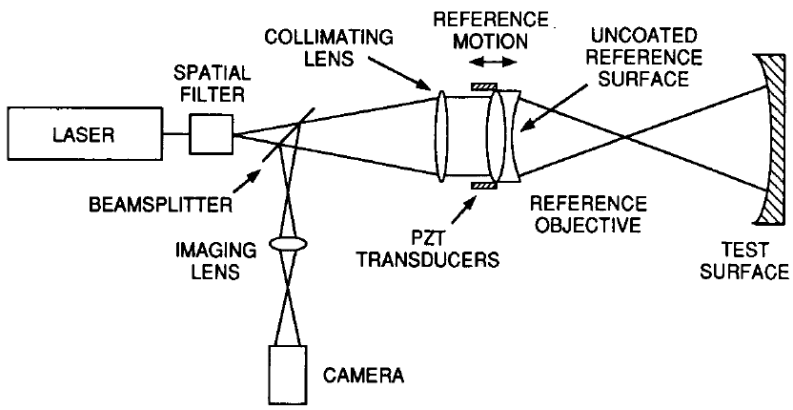

Figure 5.1: Schematic arrangement of the Fizeau interferometer. A collimated beam generated from a monochromatic light is used to test the target surface. It combines a reference beam (reflected from reference flat) and the target beam (reflected from the test surface, which contains optical aberration) and makes an interferogram on a recording medium (usually a charge coupled device, CCD). Surface quality of the target surface is measured by observing the fringe pattern and the number fringes involved. Figure taken from Z100 user manual.

The Fizeau type interferometer Intellium Z100 uses an He-Ne laser (632.8 nm) and the fringes are recorded on a CCD camera. The surface quality of the test surface is measured by observing the fringe pattern and the number fringes involved (Malacara, 2007). I conducted the measurement and confirmed that the surfaces of the mirror and the lenses are with $\lambda/20$ peak to valley accuracy (for $\lambda = 632.8$ nm). Prism surfaces accuracy tests found that one of the prisms didn't fill the

specifications and so it was sent back to the company to re-polish. The polished prism surface accuracies are around $\lambda/10$.

5.2.1.2 Characterizing the lenslets

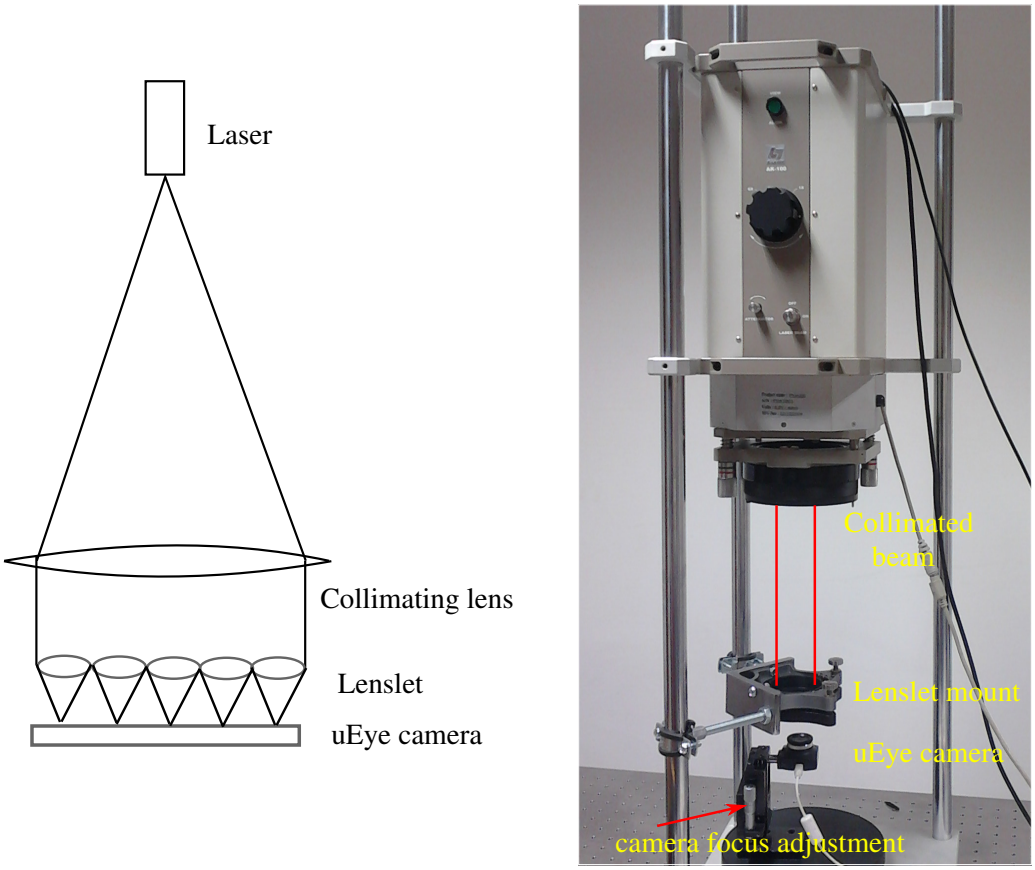

Figure 5.2: Left: Optical layout to characterize the lenslets. Right: Fizeau interferometer Intellium Z100 setup's collimated beam is used to test the lenslets. The lenslets are mounted in the optics holder situated above the uEye camera. The uEye camera is focused to the lenslet focal lengths using a vertical translation stage.

Four 2×2 lenslets and 9×9 lenslets are in usage for the beam analyzer. For this purpose we procured two sets of lenslets with sizes 5×5 and 12×12 (only the central parts were used). These lenslets are characterized by inputting collimated beams and imaging their spots on the IDS Imaging uEye camera (cf. Figure 5.2). For this characterization, custom made lenslet holders are prepared and for the image analysis a dedicated software is developed using uEye camera application programming interface (API) and DPUSER image processing library[1]. The measured results are within design specifications and the best performing pieces are selected for gluing.

[1] Available at: http://www.mpe.mpg.de/~ott/dpuser/

5.2.2 Assembly

The assembly of the acquisition camera can be divided into two parts: a) assembly of the camera enclosure, folding optics, beam analyzer mount and the detector; b) assembly of the beam analyzer.

5.2.2.1 Assembly of the camera enclosure and folding optics

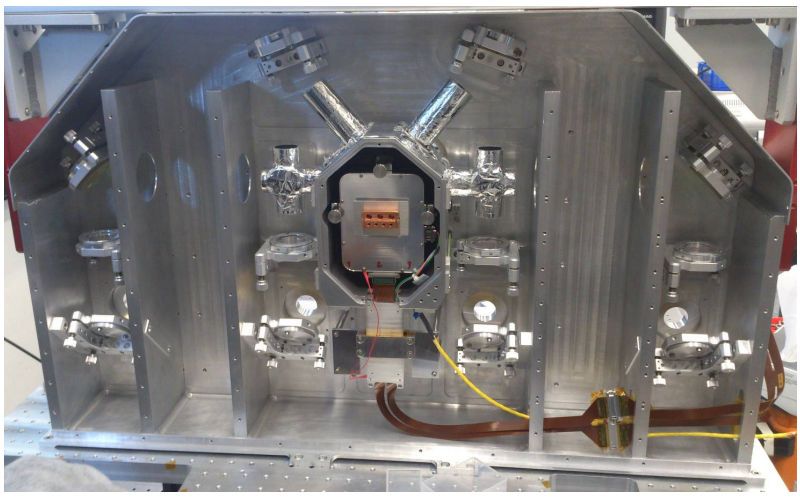

Figure 5.3: The acquisition camera enclosure, folding optics and the beam analyzer mounts as assembled.

Figure 5.3 presents the assembly of the acquisition camera as implemented. Figure 5.4 presents the opto-mechanical components which are mounted to accommodate large thermal expansions or thermal expansion differentials of the optics and the mechanics, as the acquisition camera operation involves cooling down and warming up.

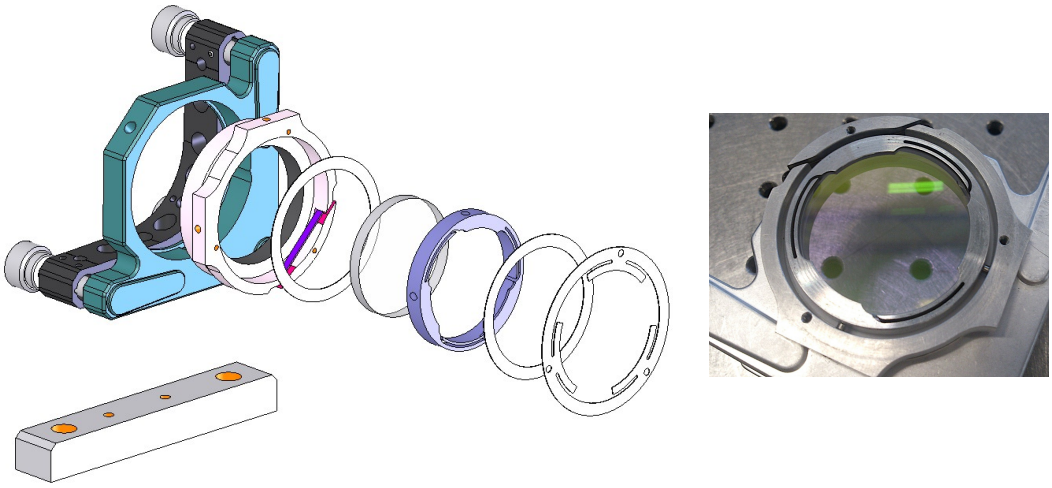

Figure 5.4: Left: Lens mounting using standard vacuum tip-tilt and Z stage and custom mechanics to hold the mount. The lens and mirror mountings, manufactured spring features. Right: stress release lens mounting as manufactured. Figure credit Gordo and Amorim 2015.

5.2.2.2 Assembly of the beam analyzer

The beam analyzer assembly consists of two steps: a) optical alignment; b) gluing. The tolerances in the optical alignment of the beam analyzer components should be less than 100 µm. Therefore, high accuracy alignment tools and procedures are required to ensure the positioning with the minimized errors. Although the team has the expertise in making the accurate alignment of the beam analyzer, due to the lack of precise positioning technology in the laboratory, the beam analyzer assembling process was contracted to WINLIGHT OPTICS, France. The team submitted the procured optics and the design specifications to the company which then delivered the aligned and the glued beam analyzer.

Figure 5.5 presents the alignment setup proposed for the pupil imager. The pupil imager imaging mode consists of two prisms and four plano-convex lenses. The setup consists of precise mechanical reference mounting tools. After cementing the two prisms, the lenses can be aligned on top of the second rectangular prism. Next the lenses can be cemented with optical grade UV cured glue.

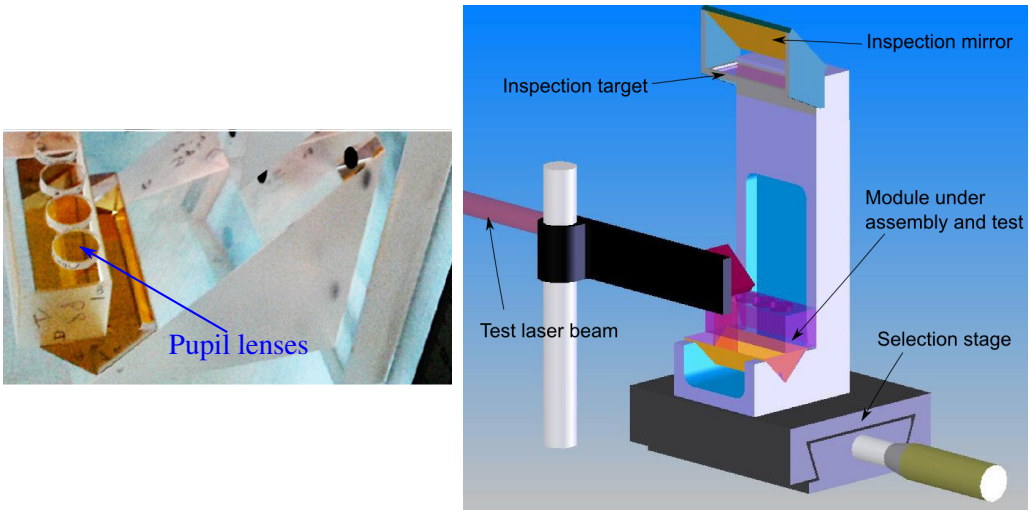

Figure 5.5: Left: pupil lenses. Right: pupil lenses alignment and assembly setup. The lenses can be aligned with the help of laser test beam and a mirror above the pupil lenses allows comfortable operator viewing angle while aligning. The precision linear stage where the tool mounted is used to select any of the four lenses. Figure right panel credit Lima and Amorim 2012.

As aforementioned, the beam analyzer alignment and gluing was contracted, but there was a delay in the delivery. For this reason, a simple beam analyzer is assembled (with the field imager function only) at CENTRA/SIM as shown in Figure 5.6.

5.2.3 Cryogenics

The acquisition camera images near-infrared beams using the HAWAII-2RG detector. The detector and the beam analyzer optics are required to cool down near to liquid nitrogen (LN2) temperatures to get a decent SNR signal on the detector by reducing the thermal background.

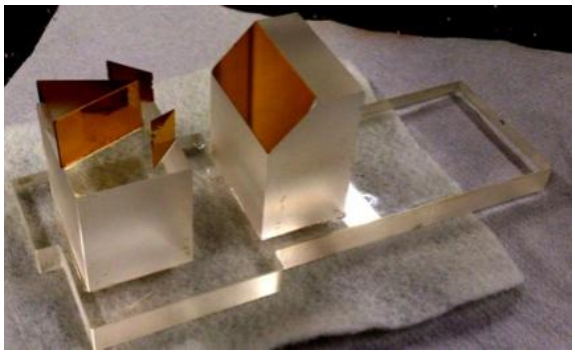

Figure 5.6: Simplified beam analyzer as built. It contains only the field imager mode.

The acquisition camera hardware was developed at CENTRA/SIM before it was integrated within GRAVITY. A cryogenic system was built at Lisbon laboratories to validate and test the optical alignment and the performance. Considering the thermal and the optical interfaces the design of the cryostat was implemented (cf. Figure 5.7).

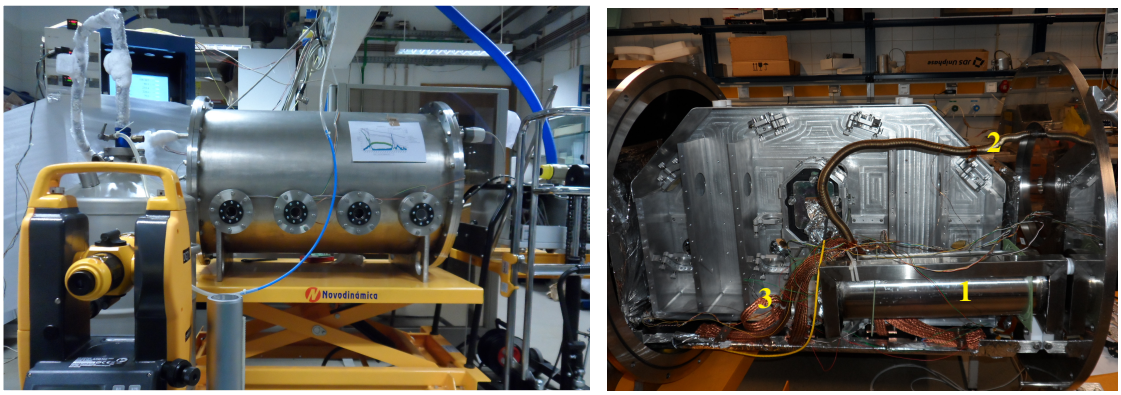

Figure 5.7: Left: cryostat used to cool down the acquisition camera. The theodolite is used to verify the optical alignment at cold temperatures. Right: the acquisition camera installed within the cryostat. Labels in the figure indicate: 1 – LN2 storage tank; 2 – LN2 pipe which transports liquid from the outside dewar to the LN2 tank; 3 – copper straps.

As previously mentioned, the different parts of the acquisition camera are maintained at different temperatures (i.e., the detector 77 K, the beam analyzer 100-120 K and the enclosure 240 K). The thermal power is distributed for them appropriately by connecting copper straps (so called cold finger) that are linked to the LN2 tank, which is available within the cryostat. To balance the required cooling, the acquisition camera is equipped with thermal heaters to warm them if necessary. The LN2 tank in the cryostat is filled time to time with a large LN2 dewar situated outside the cryostat. Since the acquisition camera optical test or analysis experiments are carried out for a few days to weeks, the liquid nitrogen filling from the dewar to the LN2 tank is required to be automated.

I implemented an automated LN2 filling using "open-close" based control using a solenoid valve by monitoring temperature of the detector and how much the LN2 tank is empty. The open-close control works by opening and closing the solenoid valve for a different periods of

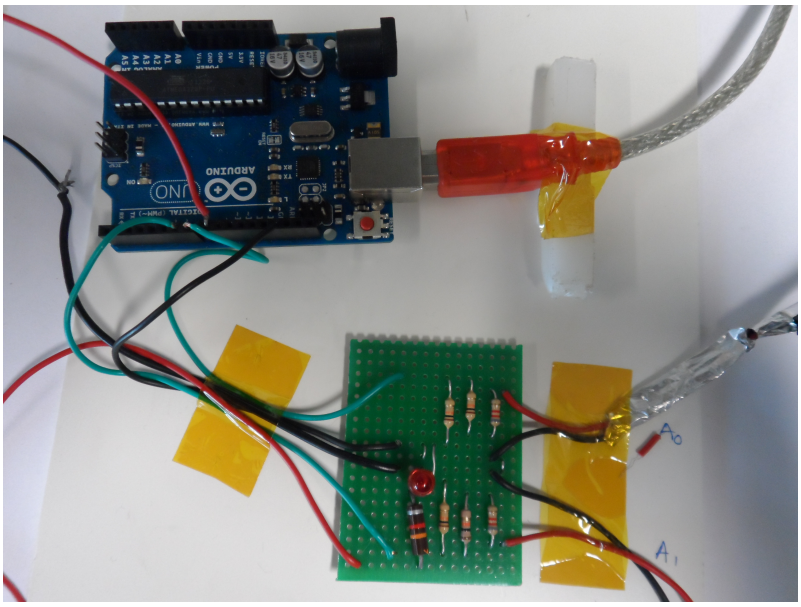

Figure 5.8: The Arduino micro processor and electronic circuits to receive signals from the temperature sensors and feedback mechanism for the solenoid valve.

times. In the system, the detector temperature is monitored using the ESO delivered Lakeshore cryogenic temperature monitor (model 224). This temperature monitoring is important to maintain the temperature cooling rate of the detector less than 2 K/min for the purpose of not to damage the detector mechanically. The LN2 tank empty status is monitored because if the valve is opened for a long period of time the LN2 tank can overflow, which is not desired. The LN2 tank empty status is monitored by installing two PT100 temperature sensors: one at the bottom of the LN2 tank (bottom sensor); second at the mouth of the LN2 tank (top sensor). The temperatures from the PT100 sensors are read using the Omega controllers (cf. left panel of Figure 5.9). The bottom sensor feedbacks the control whether the LN2 tank is empty or not. When the tank is empty, the solenoid valve is turned open and the LN2 is pumped from the dewar to the tank. The top sensor gives information about whether the tank is full or partially full and based on that the solenoid valve reacts. The time periods of keeping the solenoid valve open and close are tuned such that the detector cooling rate is always well below the 2 K/min limit.

An Arduino micro-controller chip[2] based processing unit is used to analyze the signals received from the PT100 temperature sensors and the detector (cf. Figure 5.8). A logical Arduino software is written to analyze these signals and issue a final command to the solenoid valve to open or close it. This allows to pump the liquid steadily and maintain the detector cooling rate within limits. For more details please refer Anugu et al. (2015) in Annex C.3. Also the temperature of camera enclosure is monitored and maintained at its desired temperature (240 K). When the temperature of the camera enclosure goes below 240 K, the temperature is maintained at this level by heating up in different locations using installed resistors.

[2] https://www.arduino.cc/

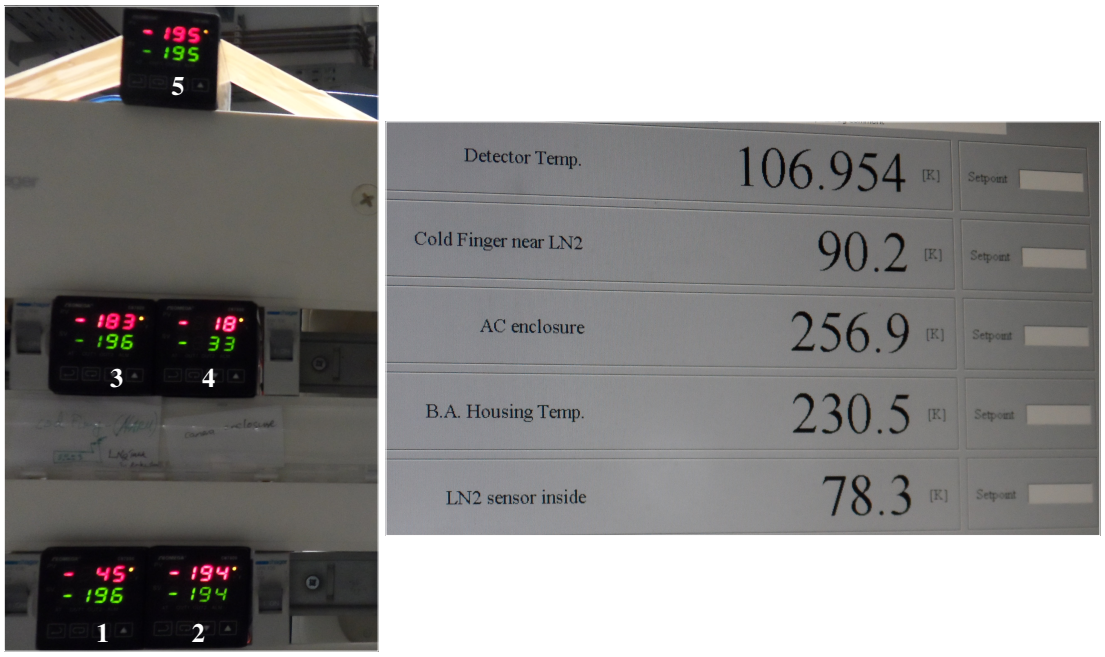

Figure 5.9: Left: Omega controllers display the temperatures of the various sensors that are installed inside the acquisition camera cryostat. In the left panel, the red color represents the temperatures measured in degree Celsius: 1– Beam analyzer; 2– temperature sensor at the mouth of the LN2 tank; 3–the copper strap temperature (cold finer); 4–camera enclosure; 5–temperature sensor at the bottom of the LN2 tank. Right: temperatures (in K) of various sensors are logged and displayed.

In order to understand the system behavior and to verify the optical performance at different temperatures, the temperatures of the detector, the beam analyzer, the camera enclosure and the valve open-close states are logged for every 1 s. The logged temperatures are displayed in the lab (cf. right panel of Figure 5.9). The logging and the displaying software are implemented using a combination of tcl-tk and C programming languages.

5.2.4 Optical alignment

The acquisition camera optical alignment can be divided into three separate steps: a) aligning the beam analyzer optics – involves positioning of the prisms, the lenses and the lenslets accurately and gluing them (carried out by WINLIGHT OPTICS); b) aligning the folding optics with respect to the beam analyzer – involves alignment of tip-tilts for the mirrors, the focus adjustment for the lenses and global shift of the beam analyzer; c) aligning the detector with respect to the beam analyzer – involves X and Y axis positioning and focus positioning.

The optical alignment of the folding optics with respect to the beam analyzer is executed in two steps. First, coarse alignment is carried out at room temperatures by using a theodolite. Second, the alignments made using the theodolite are verified by inputting laboratory telescope beams to the acquisition camera, imaging those beams on the detector and measuring focus misalignments from

the detector images. These misalignments are corrected later when the instrument was warmed up.

5.2.4.1 Folding optics alignments with respect to the beam analyzer using theodolite at room temperature

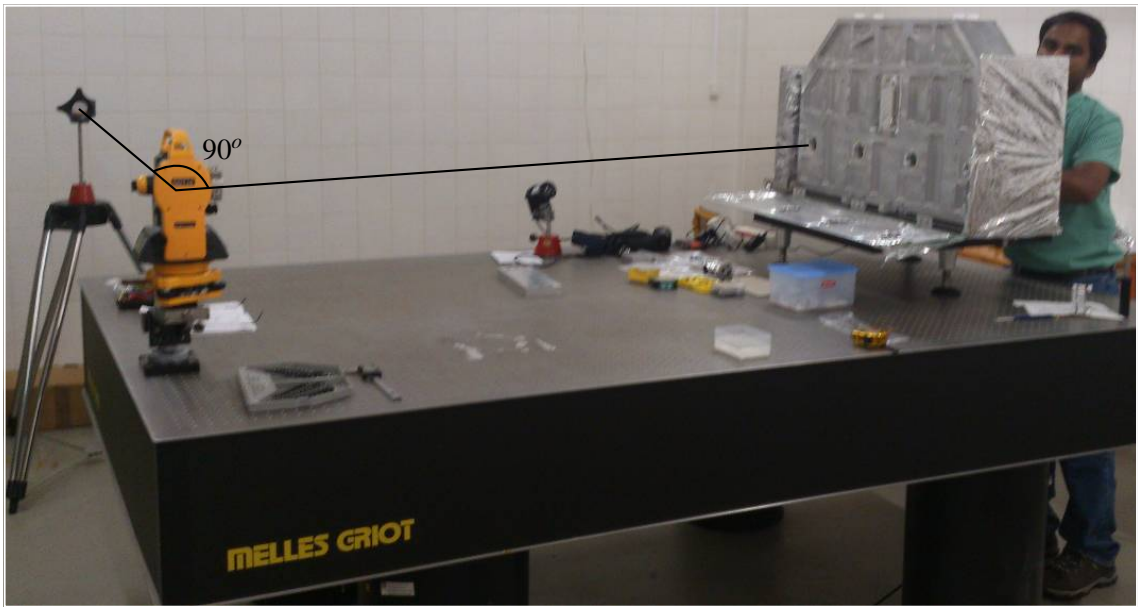

Figure 5.10: A schematic view of the optical alignment of the acquisition camera using a theodolite. The theodolite is installed in front of the first entrance channel of the acquisition camera. The mirrors and lenses are aligned by mounting cross-hairs on them and aligning those cross-hairs with the beam analyzer cross-marks. Photo credit: Paulo Gordo.

The optical alignment is implemented by putting a set of cross-hairs at the mirrors, the lenses and the detector targets (cf. Figure 5.11) and aligning them using a theodolite. The theodolite is a small, movable telescope mounted within two perpendicular axes of rotation, one vertical and one horizontal. It has a reading accuracy of 1 arcsec and a focusing range from few centimeters to infinity. The focusing range is useful for viewing of the cross-hairs that are mounted on various locations. The theodolite auto-collimation measurements are used to make relative alignments between the optical axis of a target object with respect a reference. Auto-collimation occurs when collimated light originated from the theodolite is returned along the same path after its reflection from the reflective surface.

The tip-tilt alignment of the mirrors and the lenses is achieved by making a set of cross-hairs on them, which are then aligned with respect to the beam analyzer dummy cross targets. In other words, the optical axis of the mirrors and the lenses are matched with the beam analyzer dummy cross-hair targets. This alignment is an iterative process and is accomplished by tilting the mirrors until the image of the cross-hairs of the dummy camera are brought on the centers of the optical axis of the mirrors and the lenses.

The alignment is implemented in the following steps.:

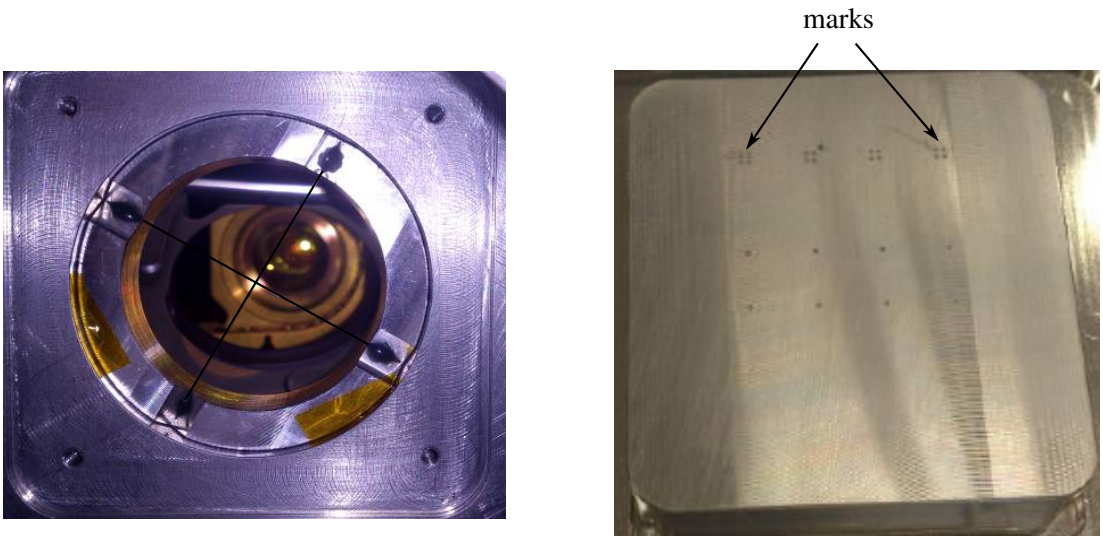

Figure 5.11: Left: A typical cross hair glued on the lens. Right: dummy detector with marks.

1. The theodolite is installed perpendicular to one of the entrance channels of the acquisition camera and aligned an external mirror perpendicular to the acquisition camera (cf. Figure 5.10). The mirror coordinates are used as the reference.

2. The two mirrors are aligned. During this step, the lens is not mounted. First mirror alignment is implemented by matching the mirror cross-hair with the dummy beam analyzer cross-mark. This is achieved by iterative adjustments of the mirror's tip and tilt. Having the first mirror aligned with respect to the beam analyzer reference, the next step is to go for the second mirror alignment. The second mirror is aligned by matching the cross-hairs of the two mirrors with the beam analyzer cross-mark.

3. The lenses are aligned. The lens is mounted with a cross-hair. The lens is aligned by matching two of its cross-hairs originated from two surface reflections. This alignment is achieved by iterative lens translation and tip-tilt adjustments. The focus adjust of the lens is described in Section 5.3.

4. The alignment of the position of the imaging modes (pupil tracker, field imager and pupil imager) on the detector is achieved using a detector dummy with marks on it. The alignment of the pupil is achieved by laterally shifting (global shift) the entrance mirror pupil.

5. The previous procedures are repeated for all four channels.

5.2.4.2 Positioning the beam analyzer with respect to the detector

The beam analyzer mount is built and positioned such that focus is correctly positioned with respect to the detector. The other possible misalignments that occur are X and Y positioning errors. There was a small mis-positioning of the beam analyzer with respect to the detector along

the Y axis (the beam analyzer moved up by 1 mm). However, the detector (2048×2048, where 1 pixel size, 18 µm) is large enough to accommodate that error. The unused detector pixels are clipped by the software.

5.2.4.3 Folding optics alignments with respect to the beam analyzer using theodolite at cold temperatures

The optical alignment made at room temperatures is verified using the theodolite at various temperatures while making the cooling down cycle. The optical alignment verification experiments at low temperatures are carried out several times to monitor the life of the optics or mechanics. The characterization results summary is that the optical alignment accuracies are accomplished at the room temperature and remained within specifications at the cold temperatures. No optical or mechanical damages are found.

5.3 Acquisition camera integration in GRAVITY at MPE

Once the acquisition camera initial optical testing was finished, it was commissioned within the GRAVITY cryostat at MPE at the end of 2013. The acquisition camera took its first light with laboratory generated stars using the GRAVITY Calibration Unit. Initially the simplified beam analyzer was used until the final beam analyzer was delivered.

As the acquisition camera lies inside the vacuum cryostat, the pupil-masking technique is used to verify the focus alignment. The basic idea of this technique is that when the system is defocused, the target star position shifts from the original position, when the pupil is masked (cf. Figure 5.12). This technique is analogous to the Foucault knife-edge test, but the masking is done in the pupil plane. By measuring the target shift on the detector plane (pixels), the defocus value in the physical units (mm) is estimated from the physical propagation model using the Zemax design simulations.

In front of the acquisition camera, moving neutral density filters[3] are installed to attenuate the H-band astrophysical target's light. The purpose of them is to not saturate the acquisition camera detector when operating with the bright and blue targets. By using these neutral density filters, the pupil is masked and misalignments in the focal length are measured. With these measurements, the focus offsets are corrected.

Image quality of the acquisition camera is, generally, characterized in terms of the Strehl ratio. The Strehl ratio is defined as the ratio between the peak intensity of the aberrated image of a point source to the peak intensity of the diffraction limited image (aberration free). The Strehl ratios of the detector images are computed using the ESO eclipse software Strehl command (Devillard, 2001). Table 5.1 summarizes these results. The T1-T4 are the entrance channels of the acquisition camera from left to right. The T4 Strehl ratio is moderate (63%) because of the misalignment of the focus. The FWHMs of stars are computed using the Gaussian fits. The error

[3]Neutral density filters attenuate the intensity equally along all the wavelengths.

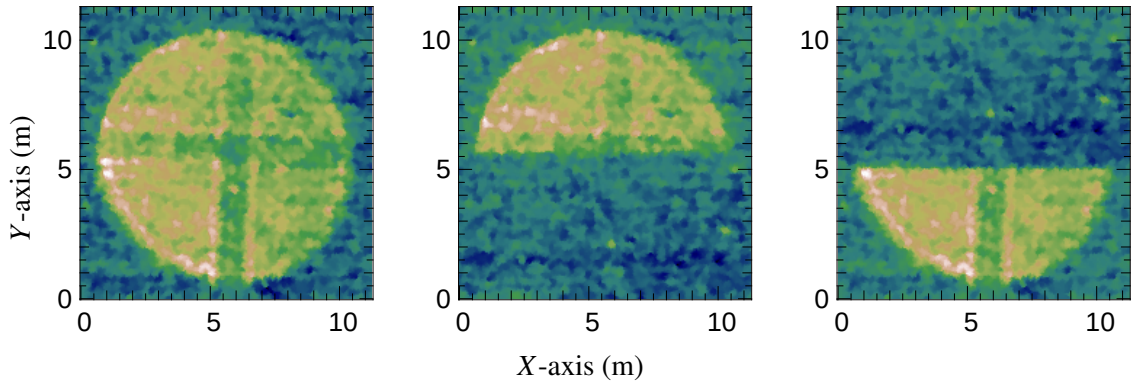

(a) Pupil masking to characterize focus. Left: No pupil masking; Middle: bottom pupil masking; Right: Top pupil masking.

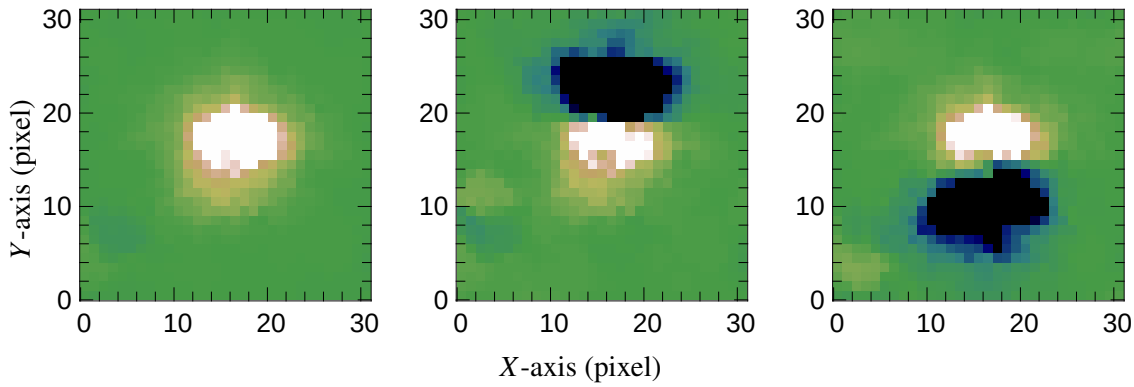

(b) Left: Target position without-pupil-masking. Middle: Difference of images of the target without-pupil-masking (white spot) and with-bottom-pupil-masking (black spot). Right: Difference of images of the target without-pupil-masking (white spot) and with-top-pupil-masking (black spot).

Figure 5.12: Characterizing the focus of the camera with pupil masking technique. The spot shift with and without pupil masking experiment gives the focus error.

in the measurements is less than 5%. Full characterization results of the acquisition camera optical and software concepts are described in Chapter 6.

Table 5.1: Image quality of the acquisition camera. The error in the measurements is less than 5%.

Telescope arm	Strehl ratio	FWHM (pixel)	Pixel scale (mas)
T1	0.9	2.7	18.23
T2	0.9	3.1	18.51
T3	0.7	3.2	18.20
T4	0.6	3.5	18.76

5.4 Summary and conclusions

In the course of my thesis, the acquisition camera optical components are tested, the camera assembled and optically aligned with the simple beam analyzer. Optical alignment is implemented

in two steps: a) coarse level optical alignments are implemented using theodolite. These room temperature optical alignments are verified at cryogenic temperatures by developing a cryostat and automated liquid pumping mechanism; b) The coarse level optical alignments are optimized by analyzing the detector images and applying the corrections to the measured misalignments.

The results of the optical tests of the components are within design specifications. The optical alignment accuracies are within specifications for two telescopes (T1 and T2) and decent for other two telescopes (T3 and T4). This alignment was found reasonable given the risk of damaging the current alignment when trying to improve it.

Figure 5.13: Installation of GRAVITY at Paranal Observatory, the Atacama desert, Chile, in October 2015. Photo credit: the GRAVITY consortium.

Chapter 6

Commissioning and on-sky results

6.1 Introduction

Once the integration part was finished, the acquisition camera has been characterized in several aspects using a laboratory generated telescope beams and targets. I did the characterization of the acquisition camera in several fronts as listed below.

- Limiting target brightnesses (faint and bright end) for acquisition camera operation.
- On-line tests of the data reduction software with real detector images.
- Verification of the beam tracking accuracy in comparison with the simulations.
- The robustness of the closed loop beam guiding.

Based on the verification tests carried out at MPE, the instrument passed Preliminary Acceptance Europe (PAE) in May 2015. After, GRAVITY was shipped to Paranal Observatory, Chile, in August 2015 and tested if there were any malfunctions due to the shipment from Europe to Paranal. Once these technical checks were completed, GRAVITY has been installed in the VLTI laboratory on the top of the mountain, in the first week of October, 2015.

I was also responsible for the acquisition camera commissioning and its characterization at MPE and at Paranal observatory. Since the beginning of the integration of the acquisition camera hardware at MPE, the camera was continuously adjusted to perform better in terms of beam tracking accuracy, sensitivity towards the fainter and brighter targets, and faster closed loop guiding. In this period, the instrument was tested under various conditions that allowed us to understand it in detail in terms of its capabilities and limits of operation.

Section 6.2 describes the validation of the acquisition camera performance with a laboratory generated telescope beams and targets at MPE. Section 6.3 summarizes the on-sky characterization results obtained at Paranal Observatory. This discussion includes the problems that we faced during the initial days of the instrument commissioning runs and the solutions implemented to address them. At the end, possible future improvements are discussed.

6.2 Laboratory validation at MPE

Figure 6.1 presents the real time display of the acquisition camera when the beams are fed into it.

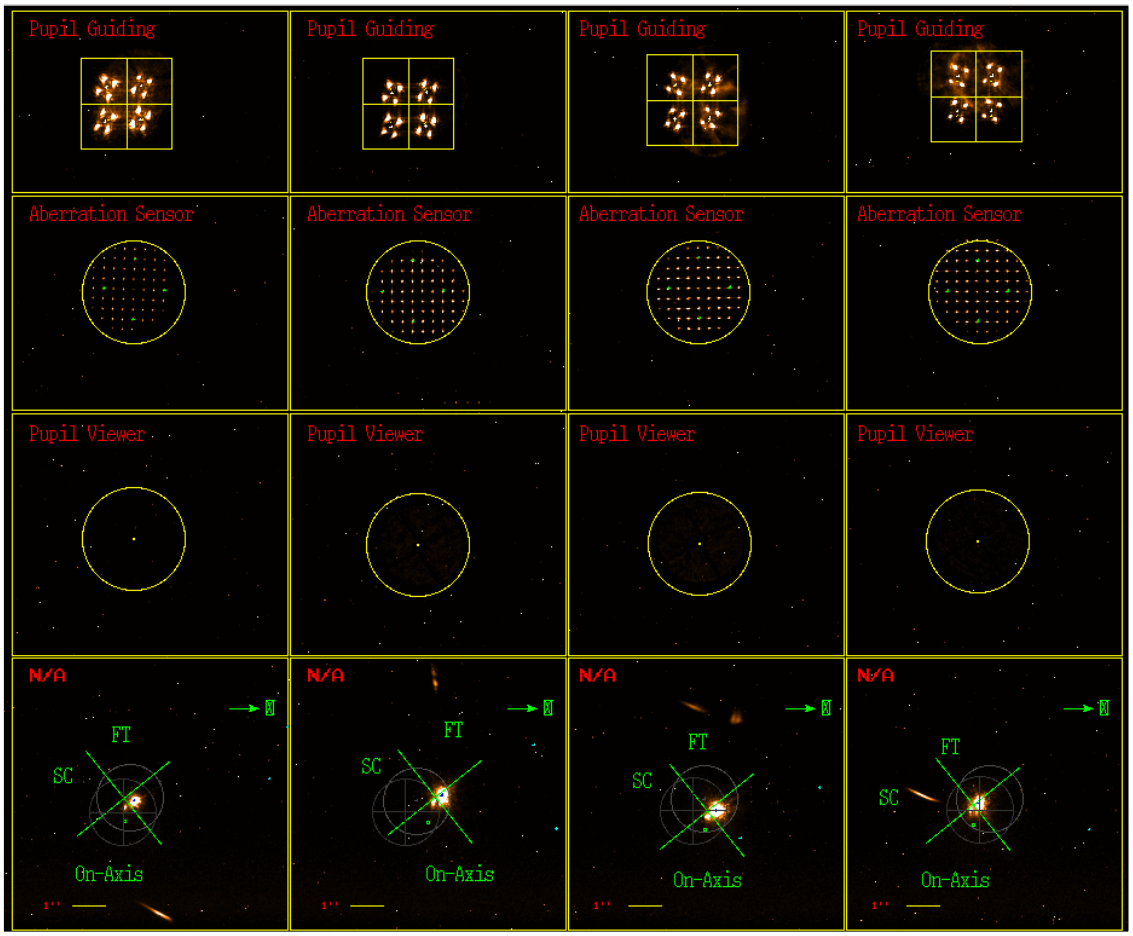

Figure 6.1: Real time display panel of the acquisition camera. Each column represents the four imaging modes of it for each telescope. Windows in each column, from top to bottom, are the pupil tracker, the aberration sensor, the pupil imager and the field imager respectively. The top and the bottom circles (size of 2 arcsec) in the field imager window are the FoVs of the pupil tracker and the pupil imager/aberration sensor respectively.

6.2.1 Basic camera characterization

When any camera is built, for the first light, one worries about basic things such as design specifications, mainly, image quality, pixel scales and throughput of the instrument are valid or not. I will discuss them one by one in the following paragraphs.

Image quality Image quality of all imaging modes are characterized in terms of the Strehl ratio and the FWHM as summarized in Table. 6.1.

Dynamic range The field imager holds a 3 mag dynamic range between the bright and the faint object for the ATs. It means that if the magnitude difference between the bright and the faint more than 3 mag, the faint object cannot be seen. This dynamic range is relevant because the selection of the fringe tracker object and the science target has to respect this limit.

Field tracker pixel scale Pixel scale of the field imager is estimated by imaging a binary star. The value is determined by computing the separation of stars on the detector (in pixels) and relating this quantity to the real separation of the binary star in arcsec. The measured value is within 5% error of the design value of 17.78 mas. Most of the error sources in the measurement are due to optical distortions available in the camera.

Pixel scale of pupil tracker The pupil tracker pixel scale is measured by equating the separation of external laser beacons observed on the detector (in pixels) to the separation of those beacons installed on the telescope of the Calibration Unit. The measured value is within 5 percentage error of the design value of 59.98 mm.

Table 6.1: The Strehl ratio, FWHM and pixel scales as built

Tel. arm	Strehl ratio	FWHM (pixel)	Pixel scale (mas/pixel)
T1	0.90	2.65	18.73
T2	0.85	3.12	18.72
T3	0.70	3.18	18.74
T4	0.63	3.51	18.76

Focus characterization and improvement Another important aspect of the acquisition camera is focus characterization to improve the image quality. This characterization is implemented by measuring the Strehl ratio of the images and the FWHM of the stars. The improvements to the image quality is achieved by improving the focus of the system as mentioned in Section 5.3.

Field of views of the imaging modes Sizes of the fields and the field centers of all imaging modes are measured as they are used in the real time display of the detector, in the calibration purposes and in the data reduction software.

The field sizes are estimated by scanning (applying tilts) a target over the field of view windows. During the scanning, the flux in each window and position of the target are recorded. By noticing the flux maximum and minimum, the diameter of the field of view of each mode is measured as shown in Figure 6.2. The size of a step function gives the size of FoV. The FoVs for the pupil tracker, the aberration sensor and the pupil imager are measured as 2 arcsec with a 2 percentage error. The centers of FoVs are also estimated by computing the center of the step function as shown in Figure 6.2. Although not shown, the FoV of the field imager is checked via scanning a target in the field imager window by moving the field selector of the star separator.

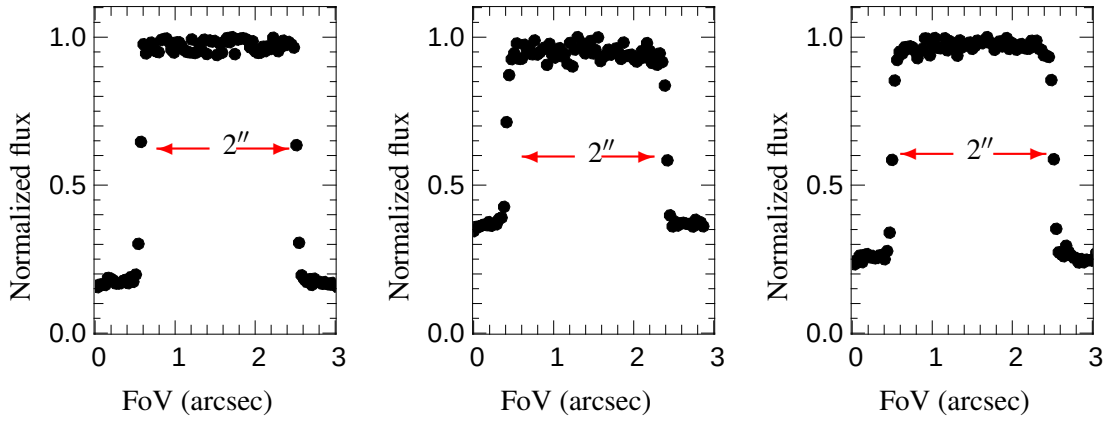

Figure 6.2: The ordinates left to right represent the measured flux over the windows of the pupil tracker, the pupil imager and the aberration sensor respectively. The flux measured in each window is normalized to its maximum. Abscissas present the position of the target used in the scanning that corresponds to FoV.

It is found that the field stops of the pupil tracker and pupil imager/aberration sensor are slightly mismatched and because of that the pupil tracker exhibits vignetting about 25% in the worst case. To address this problem for the pupil tracker, the software is modified so that it can measure lateral and longitudinal pupil positions with the non-vignetted sub-apertures (two or three) of the 2×2 lenslet as explained in Section 4.4.2. For the aberration sensor, target beam wavefronts are estimated by automatically detecting the non-vignetted sub-aperture spots.

Figure 6.3 (left panel) presents the FoVs of the pupil tracker and pupil imager/aberration sensor. Due to the non-overlapping of the pupil tracker field stop with the pupil imager/aberration sensor field stop, the camera experiences pupil vignetting (cf. middle panel). Figure 6.3 (right panel) presents a typical astrophysical target background filled pupil.

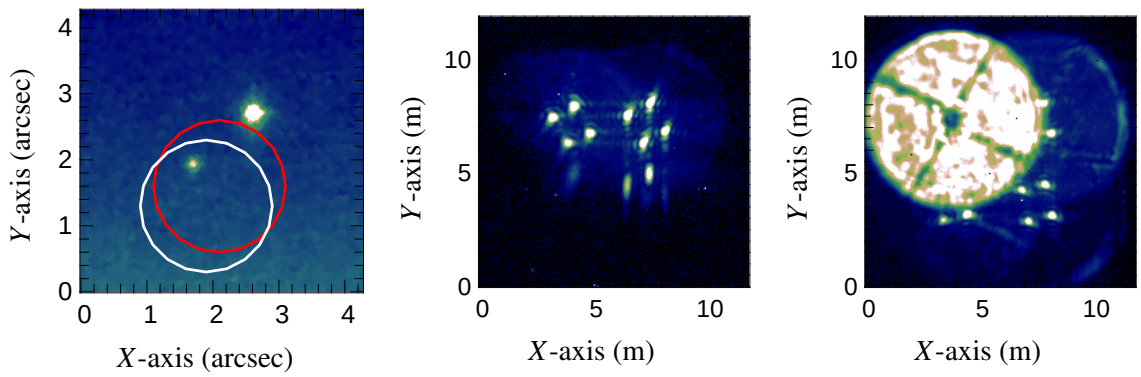

Figure 6.3: Left: The 4 arcsec window is the FoV of the field imager. The red and white rings are the FoVs of the pupil tracker and the pupil imager/aberration sensor respectively. Middle: a typical vignetted pupil tracker window. Right: a typical pupil tracker window filled with an astrophysical target backgrounds.

6.2.2 Beam tracking performance characterization

Once the basic characterization was finished, the important beam tracking accuracy characterization has been accomplished. This characterization involves the tests of accuracy of the pupil tracking, the field tracking and the aberration sensing at several imaging conditions as discussed below.

Pupil tracking The lateral pupil tracking accuracy tests are implemented in two steps by manipulating the pupil correcting actuators (cf. Section 2.4.2.1). First, a known lateral pupil shifts (L_{x_0}) are applied to the incoming beams by applying pupil shifts with the pupil correcting actuator. Second, the input pupil shifts are then measured (say, L_x) using the pupil tracker function. The measured lateral pupil tracking accuracy as a function of the input pupil shifts is presented in Figure 6.4. The lateral pupil tracking accuracy is better than 4 mm at the UT beam scale (0.05% of the UT diameter) and the RMS measurement error is 2 mm.

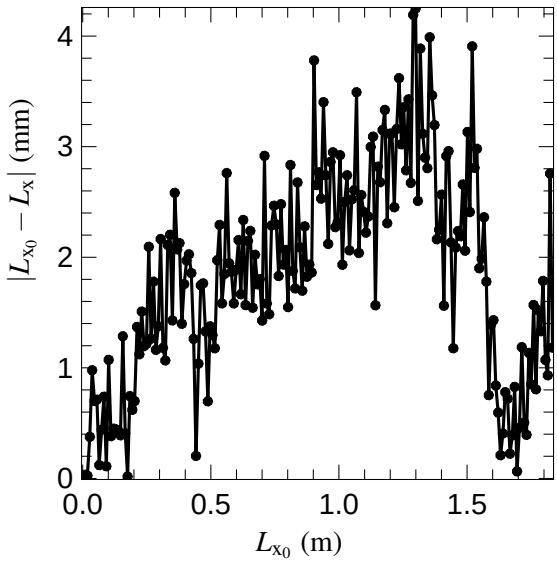

Figure 6.4: The lateral pupil position measurement accuracy in absolute error $|L_x - L_{x_0}|$ as a function of the input lateral pupil shift L_{x_0}. The measurements are scaled to the UT scale.

As described in Section 4.4.2.1, GRAVITY uses a field derotator to compensate the earth rotation for each input beam. Due to this, the pupil tracker spots rotate. The pupil tracking accuracy is tested in the presence of pupil rotation by manipulating the field derotators. The RMS error of the lateral and longitudinal pupil shifts measurement accuracy is well below 4 mm and 400 km at the UT beam respectively under the pupil rotation. Whereas the required lateral and longitudinal pupil RMS specifications for the 10 µas astrometry are 40 mm and 10 km respectively.

The longitudinal pupil tracking absolute accuracy characterization is carried out during the commissioning runs due to non-availability of the VCM infrastructure at MPE.

Field tracking The field tracking accuracy characterization is accomplished in three fronts: a) RMS error and absolute error; b) RMS error as a function of a target magnitude; c) target flux injection into the fibers.

To measure the absolute accuracy of the field tracker, several known tip-tilts (θ_i) are applied to the incoming beams by moving the tip-tilt and piston mirror (cf. Section 2.4.2.1) and measured back the input field error (θ_o) using the field tracker function. The absolute and RMS tracking errors are presented in Figure 6.5 (left panel). That are around ~ 2 mas and the RMS error is ~ 1 mas. These measurements are carried out with a star of 15 mag H-band.

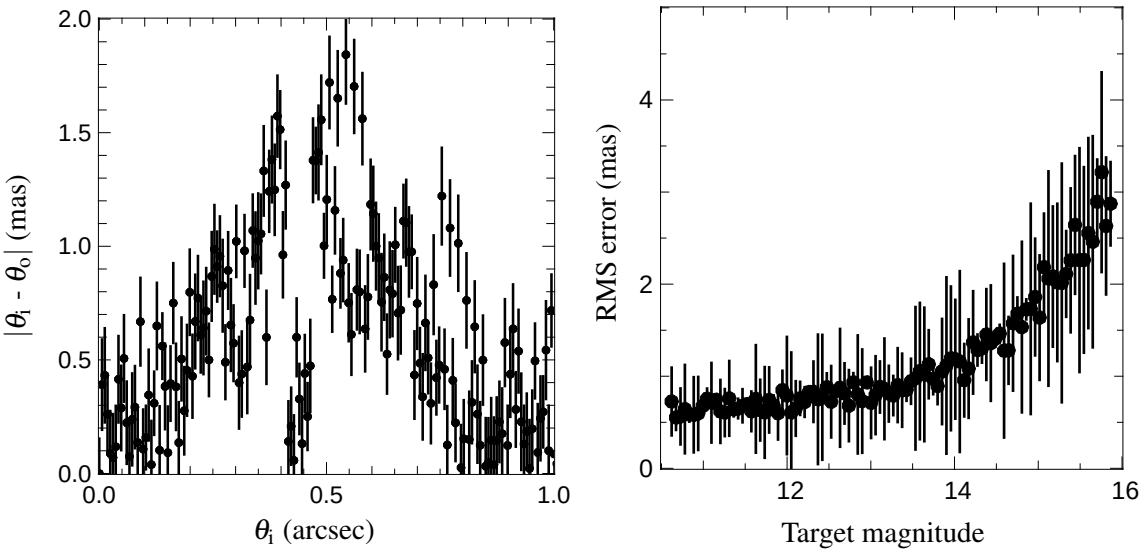

Figure 6.5: The field tracker performance. Left: The field tracking error in absolute difference $|\theta_i - \theta_o|$ as a function of true object position θ_i. Right: field tracking error in the RMS error of the as a function of target magnitude.

Figure 6.5 (right panel) presents the RMS error of the field tracker as a function of target magnitude. These targets are realized by the Calibration Unit and by varying the voltage of the lamp (cf. Section 2.4.2.9). Figure 6.6 presents how the flux injection in the fiber is reduced. By enabling the field stabilization, the coupling efficiency of the fiber is maintained around 80%.

Beam aberration tracking The wavefront estimation accuracy characterization is realized in two steps. First, the focal lengths of the Shack-Hartmann lenslet are calibrated. For this, a set of known tilts are applied to the incoming flat wavefront by manipulating the TTP mirror. For N input tilt angles (θ_i, $i = 1$ to N), N focal lengths are obtained for each sub-aperture from the relation, $f_i = \Delta x_i / \theta_i$, where x_i is the amount of pixel shift of a sub-aperture spot on the detector for the input tilt, θ_i. The average of the N focal lengths for each sub-aperture is taken as the calibrated focal length.

Second, a known tip-tilt and defocus wavefront aberrations are applied to the incoming beams and measured them back using the aberration sensor function. Figure 6.7 presents the RMS wave-

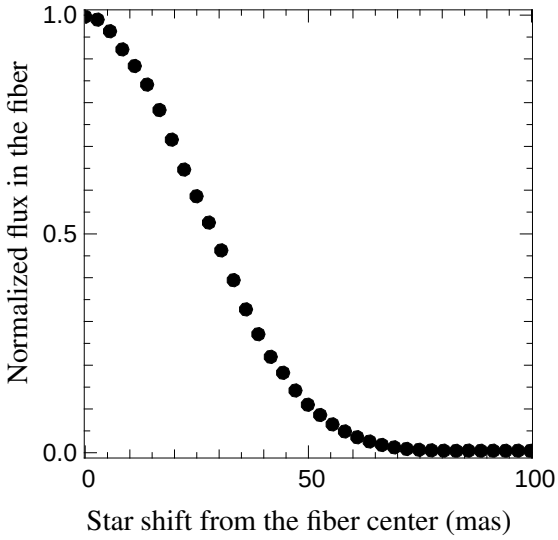

Figure 6.6: How the target star's flux injection into fiber is dropped-down with unwanted tip-tilts. This plot is generated by observing flux in the fringe tracker beam combiner while manipulating the tip-tilt and piston mirror.

front error observed as a function of the input wavefront error. The RMS wavefront error introduced by the aberration sensor while measuring an input wavefront error is around $\lambda/25$.

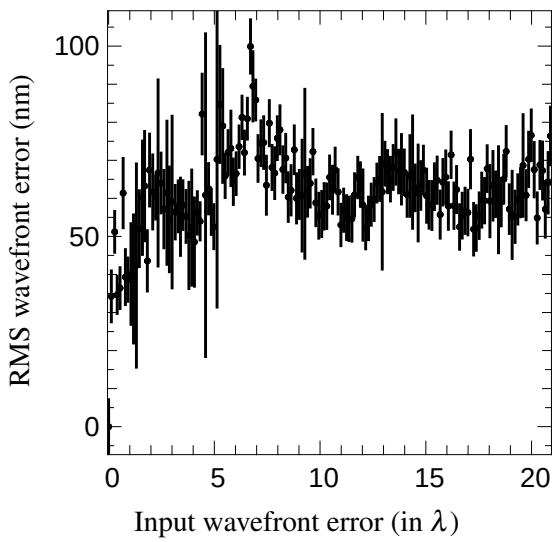

Figure 6.7: The RMS wavefront error introduced by the aberration sensor while measuring an input wavefront error.

6.3 On-sky validation at the VLTI

First light for GRAVITY took place with the ATs in October 2015 and with the UTs in March 2016. Figure 6.8 shows the imaging modes of the acquisition camera observed with the UT.

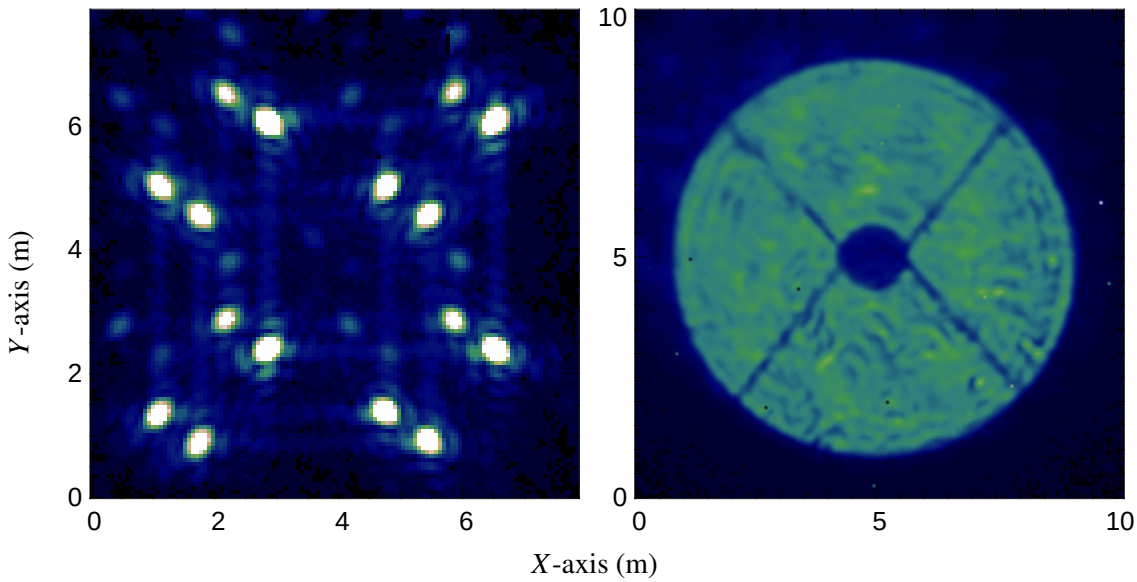

(a) Left: pupil tracker. Right: pupil imager.

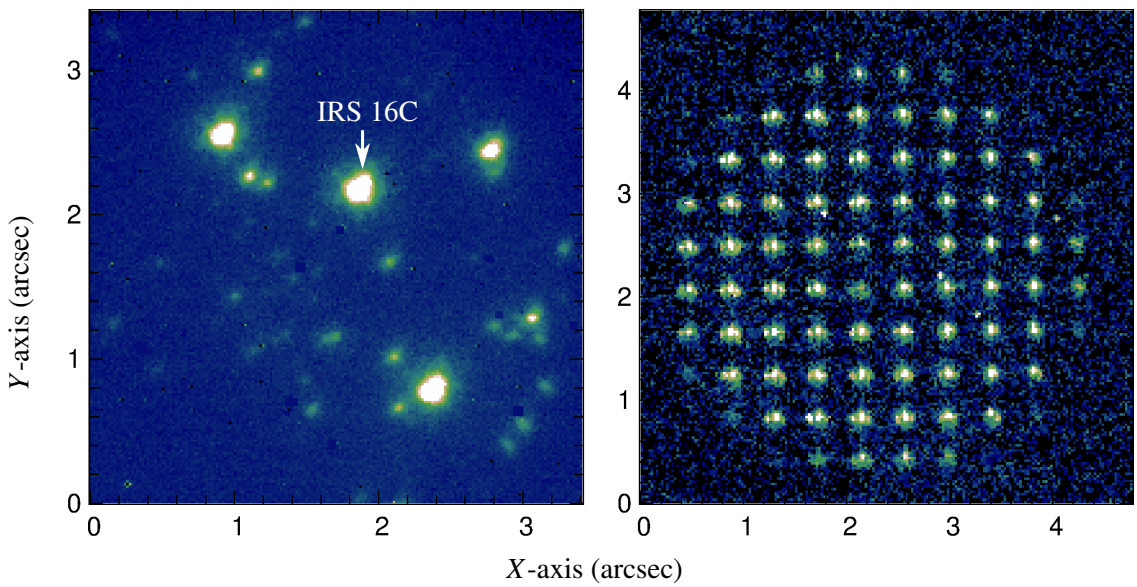

(b) Left: field imager. The image is flipped and presents some rotation with respect to Fig. 2.6. The circle is 2 arcsec in diameter. Right: aberration sensor. Note that these are raw images and not preprocessed.

Figure 6.8: Imaging modes of the acquisition camera. Observations of the astrophysical target Galactic Center with the UTs.

6.3.1 The approach to beam guiding

Beam stabilization of GRAVITY is achieved in three steps. First, at the telescope level. It involves telescope pointing, field derotation, image stabilization (adaptive optics for the UTs using CIAO-MACAO; tip-tilts correction and focus correction for the ATs with the M2).

Second, the VLTI field and pupil are aligned coarsely to the zero points of the GRAVITY internal actuators prior to the interferometric observations. This alignment is realized with the actuators of the field selector mirror, the pupil mirror (M14, laterally and longitudinally movable) of the star separator and the delay line VCM of the VLTI.

Finally, fast and accurate beam guiding is realized by the GRAVITY internal actuators during the interferometric observations. The second level alignment of the VLTI field and pupil to the center of the GRAVITY internal actuators is advantageous because the closed loop stabilization can be achieved with the GRAVITY internal actuators without going out of stroke while using them for correction. Table 6.2 and 6.3 summarize the control loops that are used to implement the beam stabilization for GRAVITY for the ATs and the UTs respectively.

Table 6.2: Beam stabilization control loops for the ATs case

Stabilization function	Actuator	Sensor
Telescope guiding	Torque motors	CCD
AT focus correction	M2	aberration sensor
Coarse field guiding	star separator FSM	field tracker
Coarse pupil guiding	star separator-VCM	pupil tracker
Fine field guiding	GRAVITY-TTP	field tracker
Fine pupil guiding	GRAVITY-PMC	pupil tracker

Table 6.3: Beam stabilization control loops for the UTs case

Stabilization function	Actuator	Sensor
Slow wavefront correction	M1 active optics	visible Shack-Hartmann sensor
Wavefront correction	MACAO DMs	CIAO
Non common path error	MACAO DMs	aberration sensor
Coarse field guiding	star separator FSM	field tracker
Coarse pupil guiding	star separator VCM	pupil tracker
Fine field guiding	GRAVITY TTP	field tracker
Fine pupil guiding	GRAVITY PMC	pupil tracker

The second and the third level beam offset corrections are accomplished using the acquisition camera sensed field and pupil offsets. The aberration sensor measurements are used to correct the non-common path aberrations that exist between GRAVITY and CIAO-MACAO of the UTs and to correct the focus error of the ATs with M2.

During a typical interferometric observation, GRAVITY experiences a maximum field motion of around 0.71 arcsec (for the UTs) and a lateral pupil shift of around 5% of the pupil in the worst

scenario. These small field and pupil offset corrections are implemented in the closed loop using the GRAVITY internal actuators with a correction speed of 0.7 s. The GRAVITY internal field and pupil actuators have the capacity to correct 3.2 arcsec field (for the UT) and 20% of the lateral pupil shifts within their range of strokes.

6.3.2 On-sky characterization approach

To characterize instrument performance, during active observations, I wrote a dedicated script to read the instrument database parameters and in addition to this, the detector images are also stored. The detector images are analyzed offline and prepared a large database which contains both the online and the offline database parameters. The data presented in the following sections is gathered in between November 2015 and May 2016 commissioning runs.

6.3.3 Pupil guiding

Longitudinal pupil tracking characterization The longitudinal pupil tracking was not characterized at MPE because of the lack of infrastructure. I characterized this mode during the initial days of the commissioning. In this experiment, several known longitudinal pupil shifts are applied to the beam by moving the VLTI variable curvature mirror (VCM) pressure and those input pupil shifts are measured back by the pupil tracker function. The methods followed to measure the pupil shifts are presented in Section 4.4.2.

The longitudinal pupil characterization results are presented in Figure 6.9. The absolute tracking accuracy is better than 40 mm for the 80 mm tunnel beam. This is equivalent to 400 m[1] at the UT.

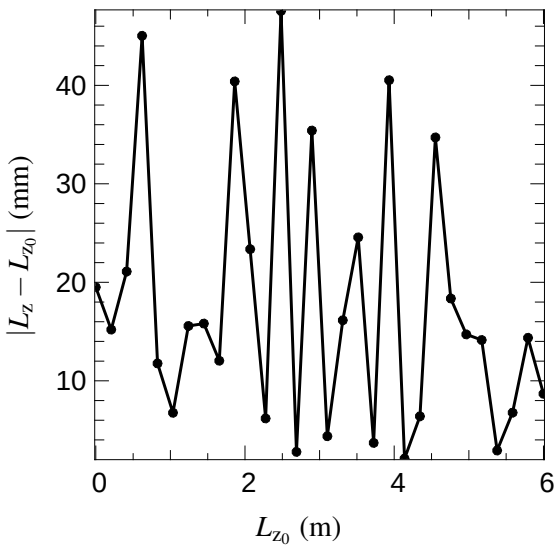

Figure 6.9: The longitudinal pupil position measurement error in the absolute difference ($|L_z - L_{z_0}|$) at 80 mm tunnel beam as a function of the input longitudinal pupil position L_{z_0} in meters.

[1] Magnification of longitudinal pupil shift from the 80 mm tunnel beam to the UT size is 10^4.

Figure 6.10 shows the telescope pupil image before and after closing the loop. It can be seen that the pupil is sharp when the loop closed.

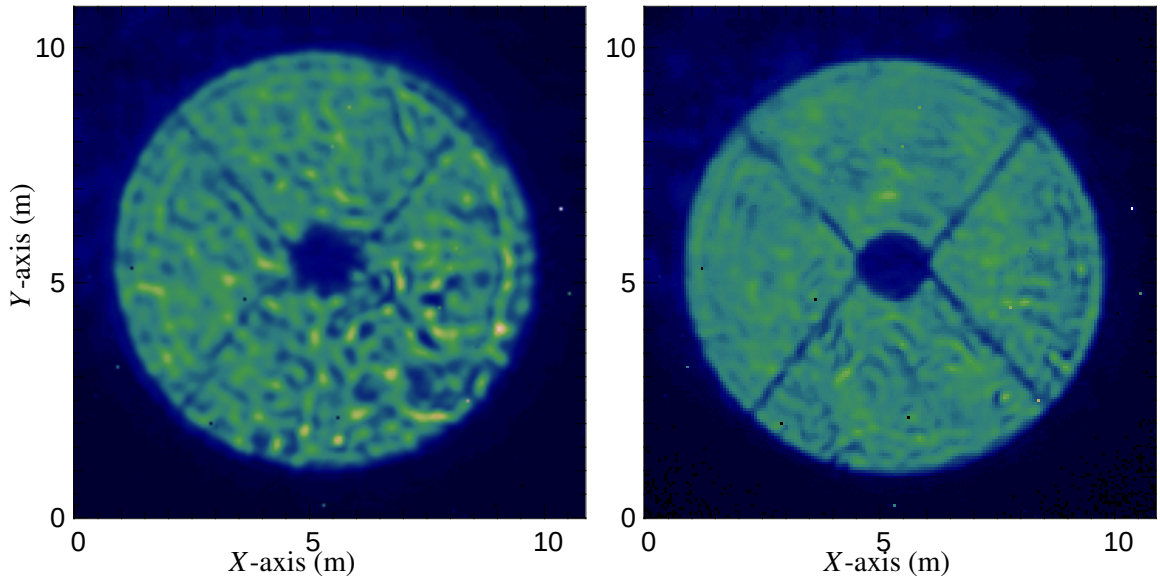

Figure 6.10: Pupil images obtained before and after closing the loop of the pupil guiding.

For large pupil defocus case, the pupil tracker spots are defocused. Using these spots, the pupil tracking measurements cannot work. To solve this problem, the VLTI pupils are aligned by looking at the acquisition camera pupil imager or Infrared Image Sensor (IRIS) (Gitton et al., 2004). In this case, the IRIS acts like a pupil imager but it has lot of flux (full broad band) in comparison to the acquisition camera.

Operation in the presence of bright star The pupil tracker experiences high backgrounds from an astrophysical target due to the closeness of the operating wavelengths of the pupil tracker (1.2 µm) and the field tracker (H-band, 1.65 µm) and because of no adequate filter for the pupil tracker. The operation of the pupil guiding for an interferometric observation depends on two factors: a) flux of the pupil guiding laser beacons; b) magnitude of the astrophysical target. To remove the astrophysical target background, a new software mode, BLINK, is implemented. The basic idea of this mode is to remove the background by switching OFF and ON the pupil beacons. During the turn OFF period, the background caused by the astrophysical target is stored and is subtracted from the subsequent frame. The performance of the pupil guiding is improved using this BLINK mode additionally by 2 mag.

Characterization of the pupil tracker as a function of target magnitude is an important activity that allows us to understand the pupil tracker operational limits. The performance of the pupil guiding is measured in two metrics: a) number of failures per 100 frames for each magnitude; b) the RMS error in the measurement. Table 6.4 and Figure 6.11 presents the results. The pupil tracker works best at 1 mag or above.

Table 6.4: Number of failures of the pupil tracker when operated it with bright astrophysical targets

object K-magnitude	object name	No. of failures	RMS error at UT scale (L_x)
0	HD 12274	25	3 cm
0.9	WDS J10468-4925A	5	1 cm
1.06	R For	0	1 cm
1.74	HD 41047	0	6 mm
2.36	HD 89998	0	6 mm
2.75	HD 14376	0	6 mm

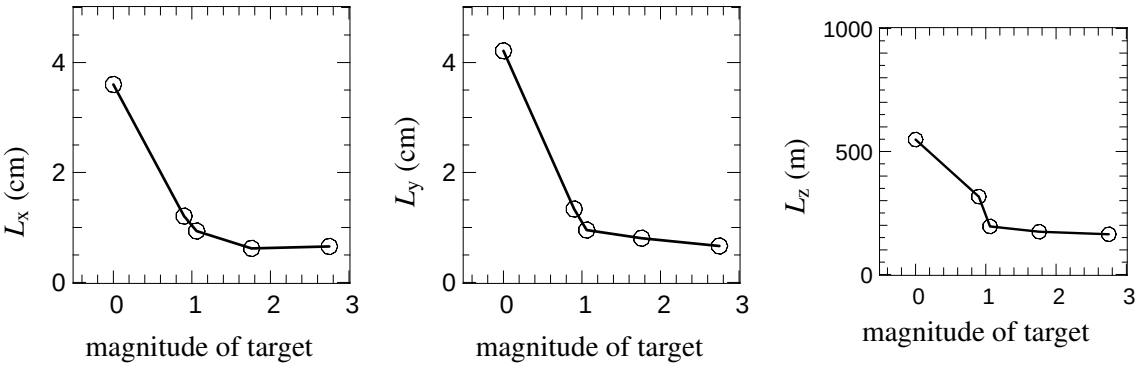

Figure 6.11: Pupil tracker performance (scaled to the UTs) as a function of the magnitude of several target stars. Left to right windows are the lateral pupil residuals along X and Y directions and the longitudinal pupil residuals.

Figure 6.12 shows a typical lateral pupil guiding residuals observed on the night of 19 March 2016. The RMS error of the pupil tracker residuals remains smaller than ± 10 mm (scaled to the UTs). The observation is made with a target with an 1 mag in H-band, using the BLINK mode.

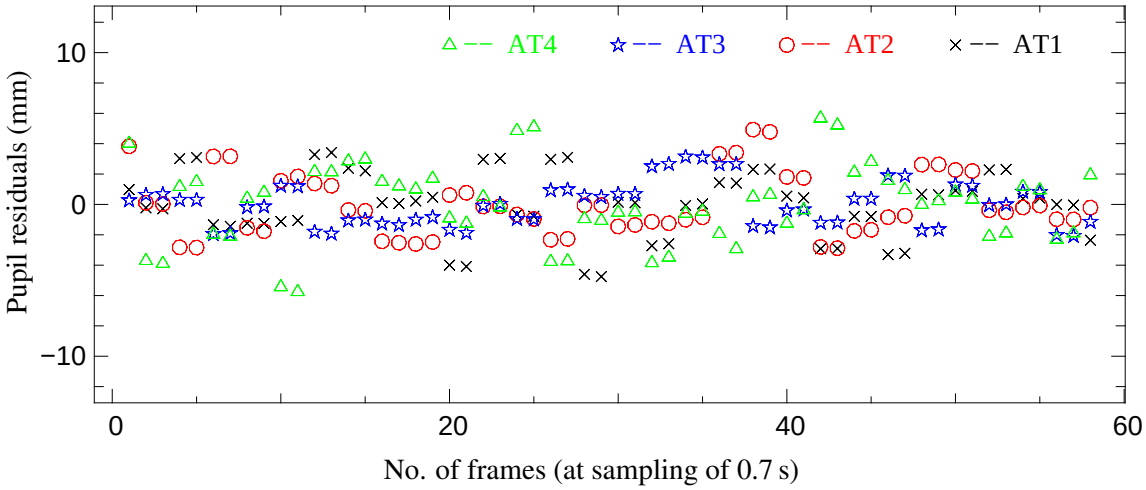

(a) Lateral pupil along X-axis.

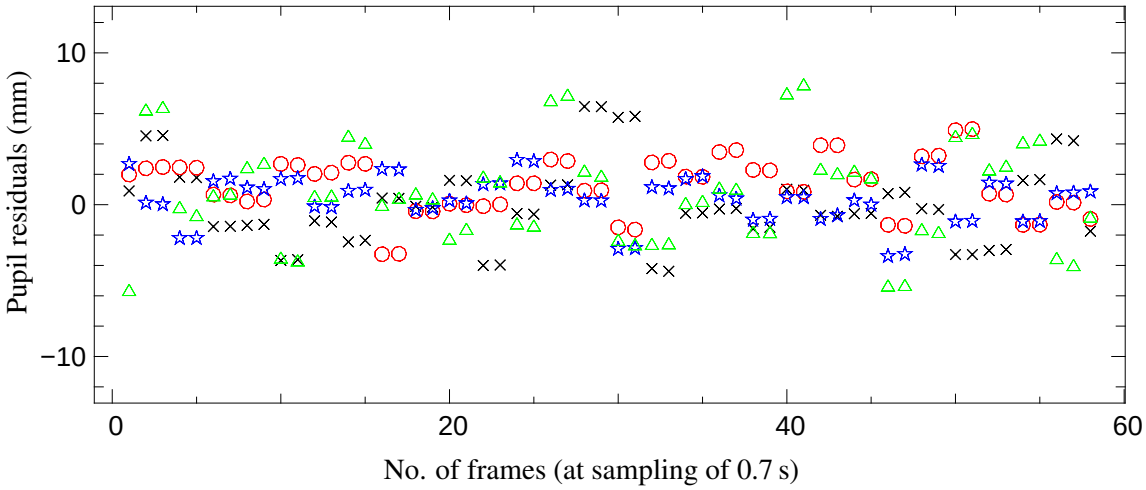

(b) Lateral pupil along Y-axis.

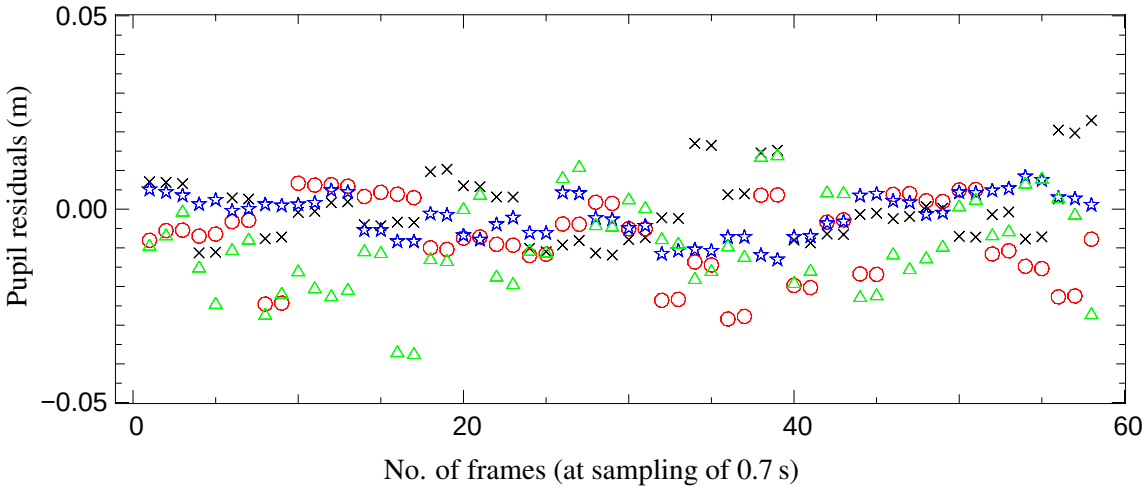

(c) Longitudinal pupil.

Figure 6.12: Pupil guiding residuals observed for 60 frames on the night of 19th March 2016. The star is 1 mag for the ATs. The measured lateral pupil shifts are at the UT scale. The longitudinal pupil shift is at 80 mm beam scale.

6.3.4 Field guiding

The characterization of the field guiding is realized by observing several dual-field targets across the sky and injecting their flux into fibers, checking the stability of injection using the field tracker. Figure 6.13 and 6.14 present the field guiding residuals observed at the ATs and the UTs. The RMS error of the field tracker residuals is smaller than ± 10 mas for the UTs. The seeing for this observation was 1.56 arcsec. Please note that the field tracker function is designed to work in the presence of adaptive optics. The 2 mas specification cannot be reached for the ATs, because currently no adaptive optics is present.

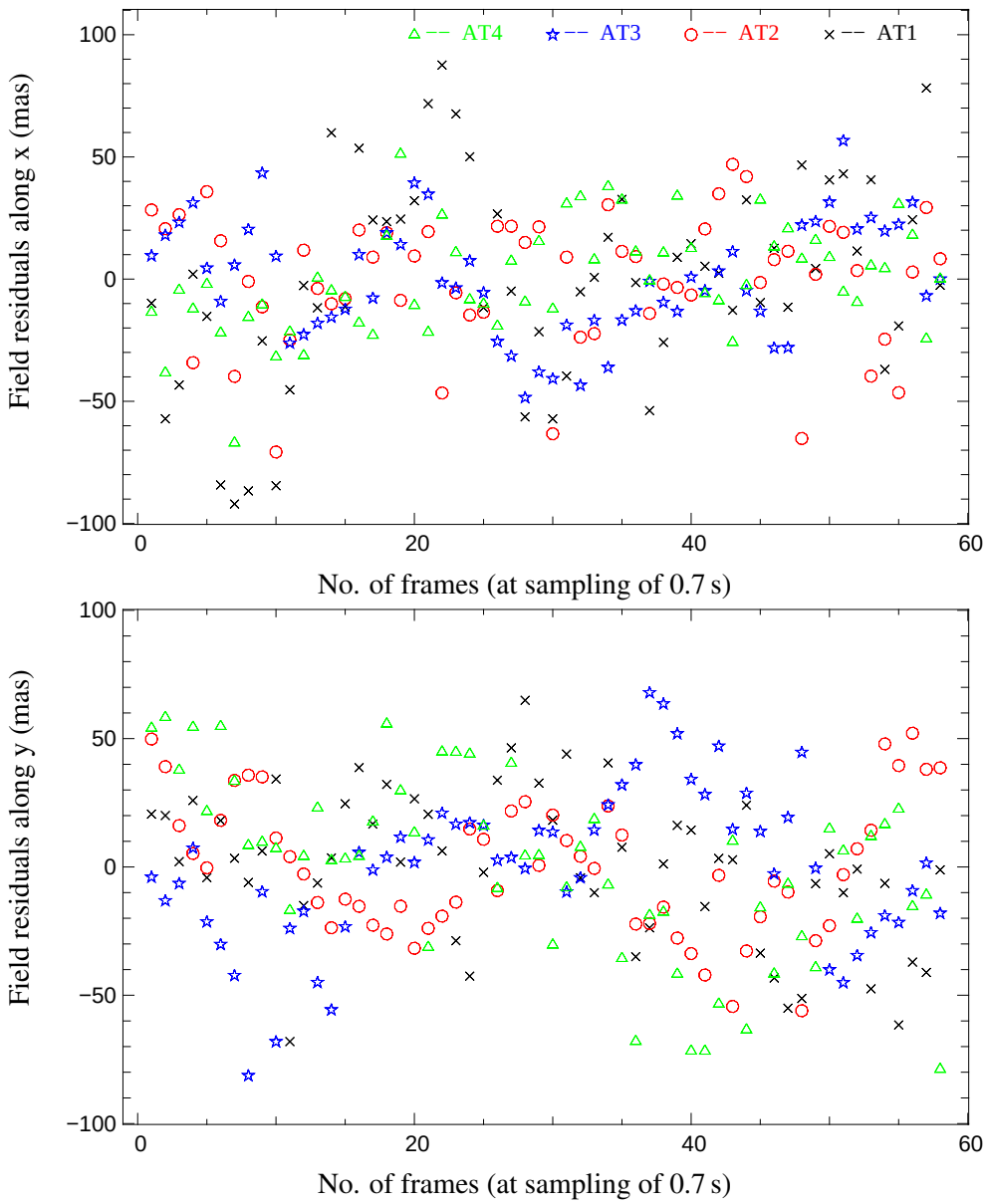

Figure 6.13: Field guiding residuals for object (HD 41047, 6.94 mag in H-band) when observed with the ATs.

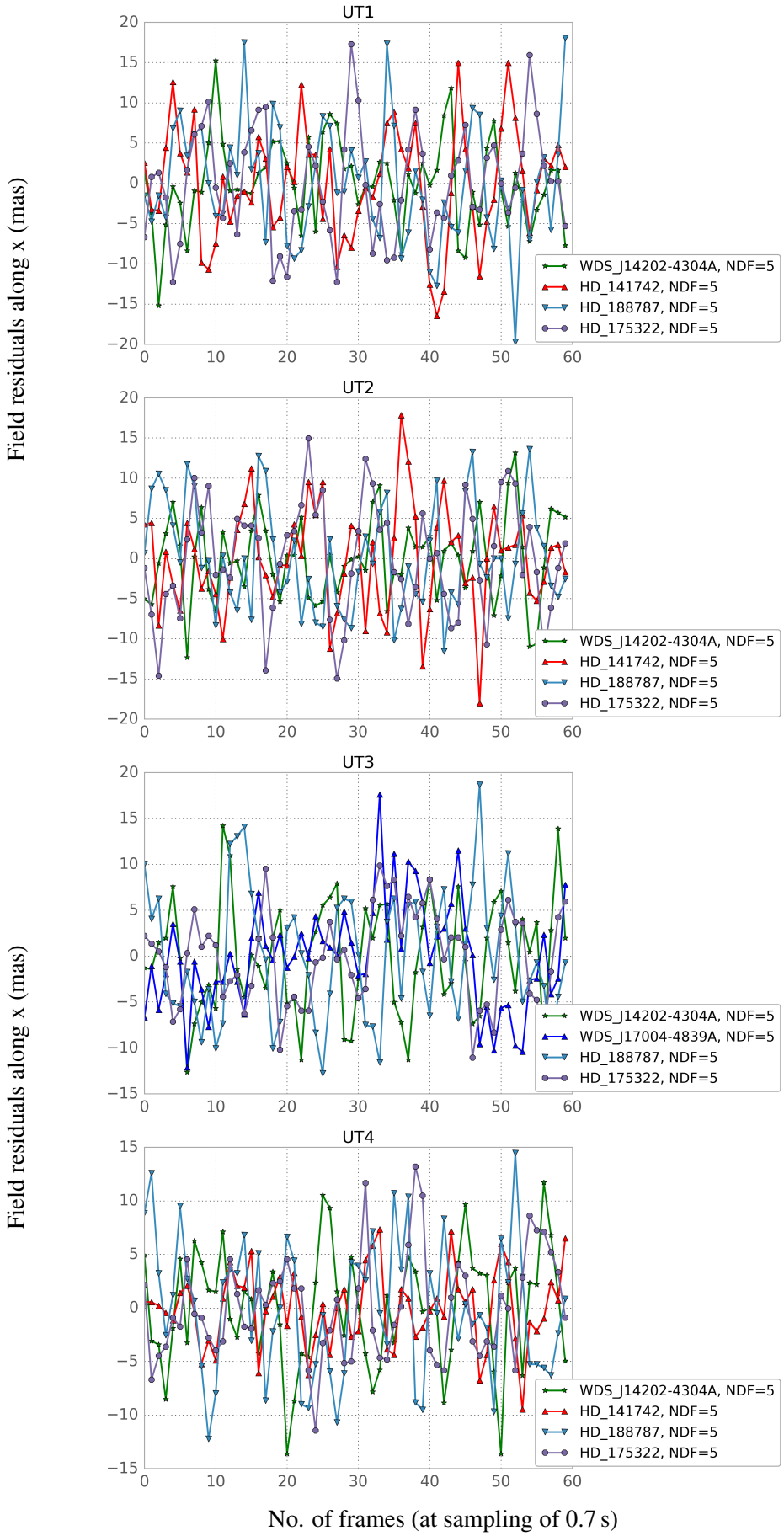

Figure 6.14: The field guiding residuals for different stars observed with the UTs.

Atmospheric differential refraction correction Tests for the atmospheric differential refraction correction software was done in 2016 May via simulating different altitudes and Zenith angles by manipulating the AT pointing coordinates. Preliminary tests of the ADR were done very quickly for the UTs. Although all the software testing tools ready, its full characterization was not yet done due to lack of dedicated time for it and also all the UTs are not equipped with the CIAO units. But it will be characterized in the future commissionings.

6.3.5 Aberration sensing

Focus measurement Observations with the ATs require focus adjustments at the start of the observations. The focus adjustments are carried out automatically for GRAVITY using the M2 mirror. The main motivation for the automatic adjustment is due to occurrence of dynamical focus drifts during an observation.

The focus measurements are realized with the aberration sensor. It measures local slopes and decomposes the input aberrated wavefront into 28 Zernike coefficients. To cope up with the pupil vignetting problems, the software automatically resizes the lenslet array size to cover only non-vignetting pupil as explained in Section 4.4.4.

However, in the low SNR situation, the focus measurement using all sub-apertures slopes is not accurate due to the outliers in the slopes. Because the conversion from the slopes to the Zernikes has been done using a predetermined slopes-to-Zernikes matrix, which has equal weights to all the slopes. To improve the focus measurement two other methods were implemented as described in Section 4.4.4. First, using the auto-correlation method. Second, using the field imager star FWHM. The latter method has the advantage of working with the faint stars observations, because the field imager flux is more concentrated than that of the aberration sensor. The conversion from the FWHM to the focus value is done with the help of a pre-calculated look-up table. This method is limited with regards the sign of the defocus and it requires a scanning with the M2 for a local FWHM minimum (cf. Figure 6.15). The validation of these focus measurements is carried out by introducing a known focus error with the M2 mirror.

The Zernike based focus measurement has been installed and is under usage (Figure 6.16), because it measures 28 Zernikes coefficients and can be used for both the ATs focus adjustment and the UTs non-common path aberration correction without any confusion. The focus measurement with the FWHM of the star was rejected because of scanning with the M2 has high risk of reducing its life expectancy.

Non-common path errors correction between CIAO and GRAVITY As described in Section 2.4.1, CIAO senses the incoming beam wavefront aberrations with respect to MACAO internal calibrator source. However, there are many optics and tunnel seeing in between CIAO and the GRAVITY beam combiner and these may introduce additional wavefront aberrations to the incoming beam.

The GRAVITY aberration sensor can measure the above additional aberrations and also the residuals of MACAO, with a speed of $\sim$1 Hz. While writing this thesis, our team and I kept efforts

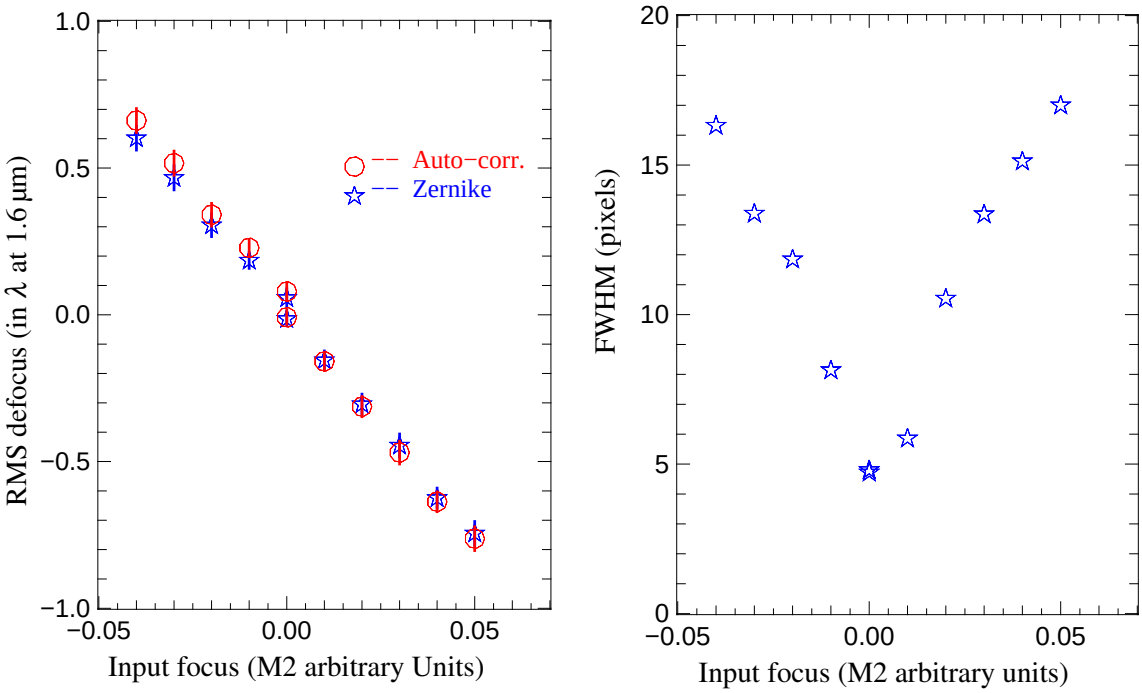

Figure 6.15: Defocus measurement.

on a feedback mechanism between the aberration sensor and CIAO. The aberration sensor and CIAO are calibrated for the highest flux achievable within the fibers. The calibration is achieved by inputting several known wavefronts generated by the deformable mirror that are known in Zernike modes. For each selected mode, several amplitudes which vary from -5 µm to 5 µm are inputted. For each amplitude, flux in the fiber is measured. Using this data, the local maximum of flux as a function of amplitude is searched. This gives the best amplitude for a given Zernike mode, which is required to cancel out the non-common path aberrations existed between CIAO and the aberration sensor. This amplitude scanning is repeated for all Zernike modes that are available with the deformable mirror (except piston). In the above scanning for each step, the aberration sensor Shack-Hartmann spots are recorded. The frame where the highest flux obtained is taken as the reference for aberration sensor. For this image, a long exposure is allowed to remove the random noise.

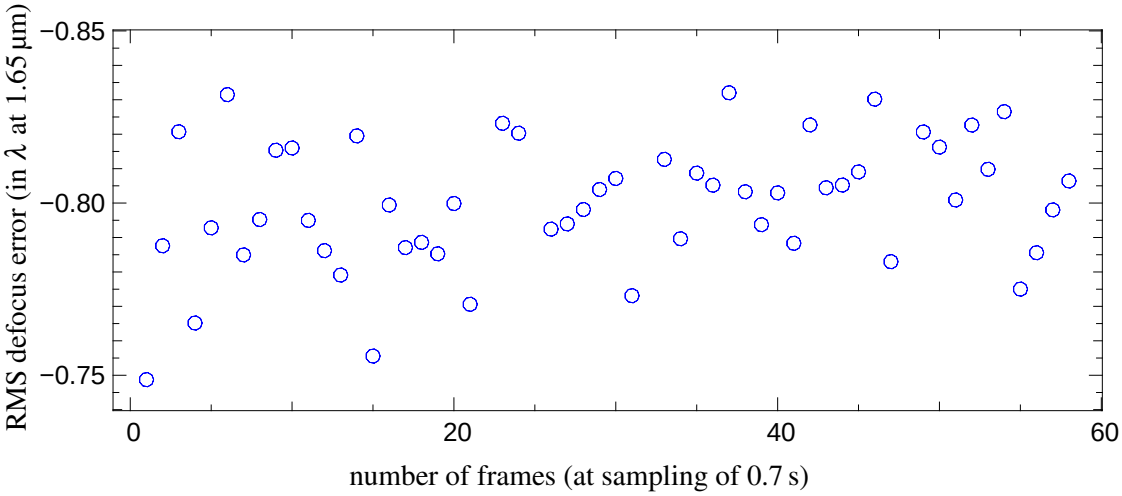

(a) Input focus M2 at 0.5 position.

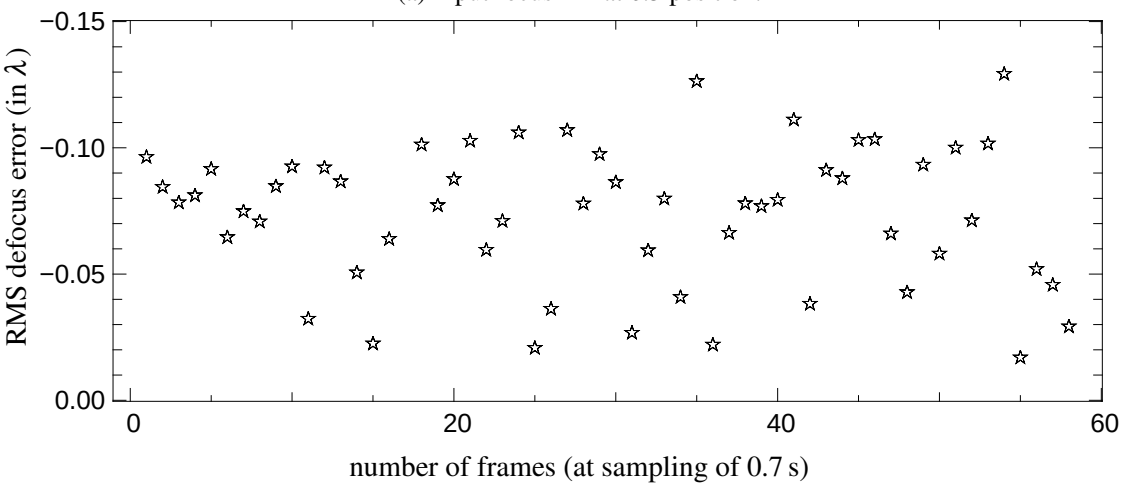

(b) Input focus M2 at 0.0 position.

Figure 6.16: Aberration sensor focus measurement performance: a) when M2 at position 0; b) M2 at position 0.5; The seeing was 1.5 at arcsec.

6.3.6 Closed loop optimization

Speed The closed loop beam guiding speed is set by the acquisition camera detector frame speed. It uses HAWAII-2RG detector with the size of 2048×2048 pixels and the frames are readout with a speed of 1 Hz. The imaging modes do not use the entire portion of the detector, thus, the detector is clipped to 2048×1536 pixels to increase the frame rate of the detector.

To optimize the beam guiding, gains of the PI controllers were characterized. In these tests, known relative shifts are applied to the field and the pupil by manipulating the TTP and the PMC devices. For different gains, the difference between the desired correction (SP) and the actual correction (PV) is computed and plotted as shown in Figure 6.17. In this tests, the proportional gain K_p is kept as 1 and integral gain K_i is changed.

It can be seen that the integral gain $K_i = 1$ is the best gain for the field guiding, because of its fast correction and no overshooting. Whereas for the pupil tracker, gain $K_i = 2$ is good. These

tests for the pupil guiding are carried out using the BLINK mode in the presence of a bright astrophysical target. It can be seen from the figure that the sensor measures pupil shifts for every two frames, because one frame is used for the background correction in this mode.

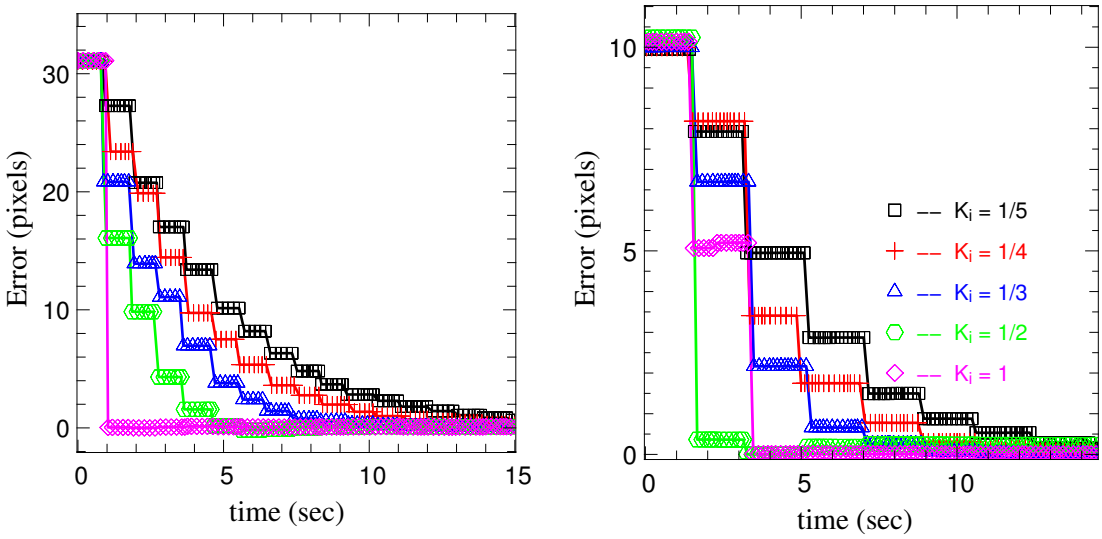

Figure 6.17: The integral controller gain optimization for the field and the pupil guiding.

Judging measurements In a closed loop system, the sensor measurements need to be very precise as a wrong measurement could break the loop. The sensor measured parameters are carefully checked for outliers and if there is any they are rejected before sending them to the actuators (cf. Section 4.4.2).

6.3.7 Maintenance and calibrations required before interferometric observations

The acquisition camera real time software works by reading a set of reference window configurations and reference positions. These reference positions may vary in weeks or months scale. Some examples of parameters are: a) fiber positions variation with the interferometric mode of operation, single or dual object; b) reference positions for the pupil tracker set by the internal source; c) the reference Shack-Hartmann positions set by the internal calibration source. Before using the acquisition camera for interferometric observations the reference positions are measured. These calibrations are realized by executing observation block (OB) templates, which in turn executes a sequence of observing templates defined by the parameter settings in the OB.

6.3.8 Astrometry error with field and pupil errors

The total astrometric error produced by field and pupil errors from the four telescopes can be calculated as given below

$$\sigma_T = \sqrt{\sigma_{T1}^2 + \sigma_{T2}^2 + \sigma_{T3}^2 + \sigma_{T4}^2} \tag{6.1}$$

Table 6.5: Astrometric residual error comparison: performance using the calibration unit generated laboratory beams and on-sky beams.

Beam guiding	Residual beam error	δOPD error(1 tel.)	astrometry residuals (4 tel.)
Typical errors	$\Delta\alpha \leq 60\,\text{mas}$ $\Delta L_x \leq 0.4\,\text{m}$ $\Delta L_z \leq 30\,\text{km}$	$\leq 153.5\,\text{nm}$	$\leq 633.3\,\mu\text{as}$
Requirements for 10μas astrometry	$\Delta\alpha \leq 10\,\text{mas}$ $\Delta L_x \leq 40\,\text{mm}$ $\Delta L_z \leq 10\,\text{km}$	$\leq 1.93\,\text{nm}$	$\leq 4\,\mu\text{as}$
Numerical modelling	$\Delta\alpha \leq 2\,\text{mas}$ $\Delta L_x \leq 4\,\text{mm}$ $\Delta L_z \leq 200\,\text{m}$	$\leq 0.038\,\text{nm}$	$\leq 0.16\,\mu\text{as}$
With laboratory beams performance	$\Delta\alpha \leq 2\,\text{mas}$ $\Delta L_x \leq 4\,\text{mm}$ $\Delta L_z \leq 400\,\text{m}$	$\leq 0.039\,\text{nm}$	$\leq 0.16\,\mu\text{as}$
On-sky performance	$\Delta\alpha \leq 10\,\text{mas}$ $\Delta L_x \leq 12\,\text{mm}$ $\Delta L_z \leq 400\,\text{m}$	$\leq 0.58\,\text{nm}$	$\leq 2.40\,\mu\text{as}$

During a typical interferometric observation, GRAVITY experiences, typically, a field motion of around 60 mas, a lateral pupil shift of around 40 mm (5% of the UT pupil) and a longitudinal pupil motion of 30 km as mentioned in Table 2.1. The total astrometric error which is caused by these field and pupil errors is around 633.3 µas at the baseline of 100 m. By using the acquisition camera field and pupil guiding (with guiding errors of 10 mas in field, 4 mm in lateral pupil and 400 m in longitudinal pupil), the total astrometric error is reduced to 2.4 µas for four telescopes. These astrometric errors are computed using the Eq. 2.5 and Eq. 6.1. Note that this error does not consider other sources of errors contributing to the total GRAVITY error budget. Table 6.5 summarizes the field and pupil guiding errors obtained via numerical modelling, with calibration unit generated beams and with on-sky beams.

6.4 Summary and future improvements

The acquisition camera is characterized in many fronts using laboratory telescope beams and with the beams of the ATs and the UTs. Its concepts are tested successfully during the commissioning runs since October 2015 (in total of 6). The results have shown that the acquisition camera measured parameters are within the GRAVITY specifications.

While the acquisition camera continues to give outstanding performance to enable the smooth and efficient beam combination for imaging and astrometry, there is scope for future improvements in: a) sensitivity; b) calibration of aberration sensor with the deformable mirror; c) Lateral pupil shifts measurement in the presence of bright astrophysical target; d) geometric distortion calibration of the acquisition camera to enable accurate astrometry. I will detail them below.

Sensitivity improvements The operation of faint stars limit the performance of the field tracking and the aberration tracking. On the other hand, operation of bright stars is troublesome for the pupil tracker due to the unwanted background coming from the target star flux.

GRAVITY has 5 and 10 mag attenuation neutral density filters. The acquisition camera uses these filters to attenuate the excessive flux of bright targets in H-band in comparison to the K-band, in order not to saturate the detector. Also to certain extent the simultaneous operation of the field imager, aberration sensor and pupil tracker is prolonged by choosing a suitable neutral density filter.

However, the simultaneous operation of all modes is troublesome for some stars (either faint for the aberration sensor or bright for the pupil tracker) because of large magnitude difference (5 mag) in between the existing filters. One way to solve this problem is by purchasing a 2.5 mag neutral density filter. Another approach is decreasing the detector frame rate to increase the flux in the aberration sensor, but this is at the cost of slow guiding of the field and the pupil.

Aberration sensor calibration Currently, the aberration sensor software is using simulated slopes-to-Zernikes matrix, to convert local slopes of a target wavefront to Zernike coefficients. It is desired to calibrate the Shack-Hartmann slopes-to-Zernikes matrix using a deformable mirror by applying several known Zernike coefficients (Dai et al., 2007).

Lateral pupil tracking Currently the pupil imager function is used for monitoring the pupil with visual inspection, so it does not require any image processing. However, the pupil imager can be used for lateral pupil tracking in the presence of a bright astrophysical source. The cross-correlation algorithm can be used to track the pupil image and measure pupil shifts with respect a reference pupil image. The reference image for this algorithm can be a long exposure pupil image.

Camera calibration to improve astrometry GRAVITY measures astrometry by measuring the differential phase between the science and the fringe tracker stars. Since these are phase measurements, if the two stars separated more than λ/B, they suffer phase 2π wrapping ambiguity. Currently, this problem is solved using the NACO observations. In this regard, acquisition camera field images can substitute the NACO observations provided if the camera is calibrated in two fronts: a) geometric distortion calibration (Yelda et al., 2010); b) shift of target positions on the detector as a function of spectral response or color (transverse chromatic aberration, cf. Figure 6.18). This calibration could be achieved by comparing the acquisition camera detector images with the

HST globular cluster images. This work is highly interesting because, it allows us to track the S2 star with the acquisition camera itself.

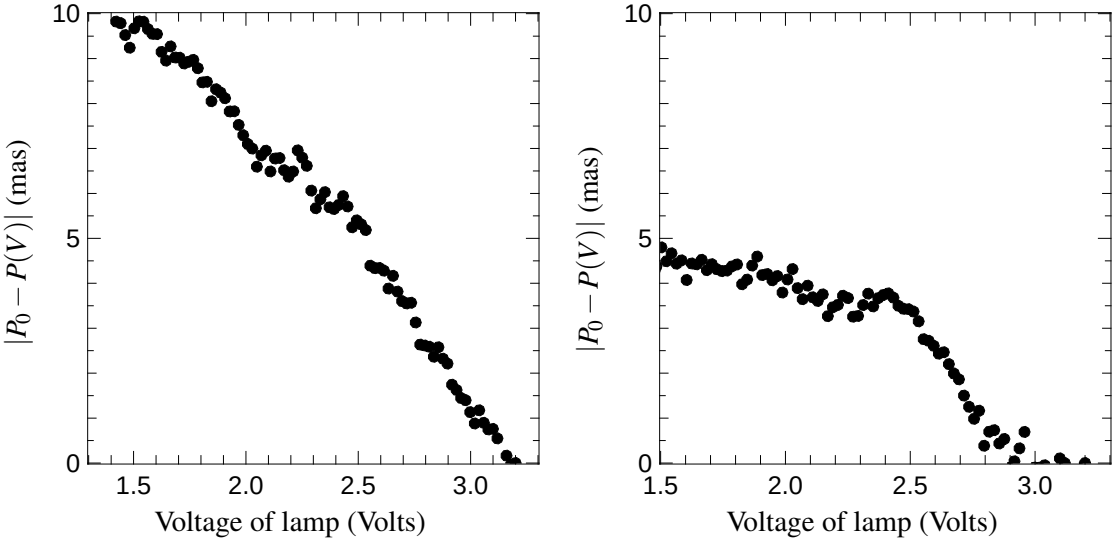

Figure 6.18: Shift of target position as a function of color (color changed with the voltage of lamp). The target is realized using the Calibration Unit. P_0 and $P(V)$ are the positions of the target at 1.4 V and V respectively.

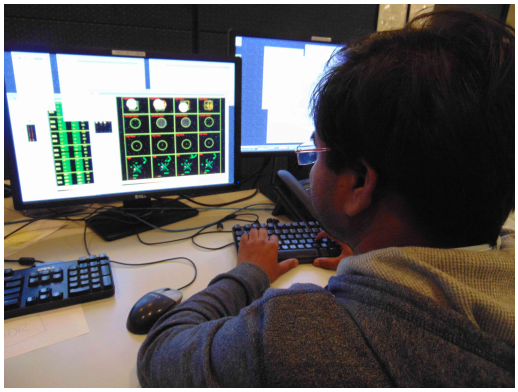

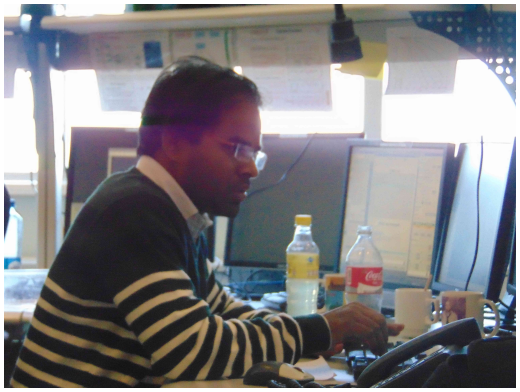

Figure 6.19: Pictures of the author taken during the work at the VLTI console, Paranal Observatory. Photo credit: António Amorim.

Chapter 7

Conclusions and prospects

GRAVITY has been built to provide high precision narrow-angle astrometry (10 µas) and phase-referenced interferometric imaging ($\sim$ 4.5 mas) in the astronomical K-band, with the scientific goal of probing the Milky Way super-massive black hole at the Galactic Center (cf. chapter 1). There are several practical difficulties in implementing the narrow-angle astrometry. The atmospheric turbulence and the error in measuring accurate baseline length between any two telescopes are among the major challenges. Due to these, the performance of the GRAVITY interferometer can be severely limited in several ways: a) instrument sensitivity – the efficient light injection of stars into the single mode fibers is affected in the presence of the random atmospheric tip-tilts; b) astrometric errors – unwanted tip-tilts and baseline errors cause astrometric errors. To meet these challenges, the acquisition camera (among other subsystems) has been built. It images and analyzes the incoming telescope beams and enables the required beam stabilization.

CENTRA-SIM (with staff from University of Lisbon and University of Porto) of Portugal took the responsibility of constructing the GRAVITY acquisition camera. It implements four optical functions to track the multiple beams of the Very Large Telescope Interferometer (VLTI).

- **Pupil tracker** is designed to reduce the mismatch error between the imaging and the metrology baselines which are used for the GRAVITY astrometry. It images and tracks four pupil reference lasers that are mounted on the spiders of each telescope's secondary mirror using a 2×2 lenslet.

- **Field tracker** images astrophysical objects and tracks image (tip-tilt) drifts. It is designed to inject star's light into the single mode fibers which are used to transport the light to the integrated optics where beam combination takes place.

- **Aberration tracker** is designed to implement focus guiding for the ATs and the non-common path error correction between CIAO and GRAVITY. It measures quasi static aberrations of the incoming distorted beams using four 9×9 Shack-Hartmanns.

- **Pupil imager** is designed to reimage and monitor the telescope pupils.

The hardware is built with almost aberration free optics. Furthermore, in the construction, thermal stress-free optics is used as it is a cryogenic instrument which requires cooling down to liquid nitrogen temperatures to reduce the thermal background. The estimation of beam stabilization parameters from the acquisition camera detector image is carried out with a dedicated data reduction software for every 0.7 s.

As a CENTRA team member, I participated in the construction of the acquisition camera and this thesis is a result of that work. I was responsible for the end-to-end simulations, real-time data reduction pipeline and control software, acquisition camera characterization and commissioning of the instrument at the ESO Very Large Telescope Interferometer, Paranal Observatory. I have contributed to the hardware assembly, optical components testing, optical and cryogenics testing and integration of the camera into GRAVITY. The camera is described in detail in chapters 3-6, starting from the camera design to its installation and validation of concepts in the sky.

The acquisition camera was characterized for its stability and has been successfully used for the astrophysical target observations over six months. The measured parameters are used in: a) alignment of GRAVITY with the VLTI; b) active pupil and field stabilization; c) defocus correction; d) engineering purposes as described below:

- **Field guiding** The accuracy of the field tracking is 2 mas RMS error. With this accurate field stabilization, the star's light injection into single mode fibers is improved (around 80% coupling efficiency). The field guiding residuals are around $\pm$ 10 mas (observations are made without CIAO and the laser based tip-tilt tracking).

- **Pupil guiding** The standard deviation of the lateral residuals are smaller than $\pm$ 0.2 pixels RMS error on the detector (i.e., 12 mm at the UTs). The longitudinal pupil tracking residuals are within 40 mm RMS at 80 mm beam scale (400 m at the UT scale). The pupil tracker experiences high backgrounds from bright astrophysical targets due to: closeness of operating wavelengths of the pupil tracker (operating at 1.2 µm) and the field tracker (operates at H-band – 1.65 µm) and; b) no adequate dichroic filter for the pupil tracker. Currently, the pupil tracker works for stars fainter than 1 mag when operating with the ATs.

- **Focus guiding and non-common path error correction** Quasi-static higher order wavefront aberration measurements are measured with 80 nm RMS measurement error for bright astrophysical objects (6 mag for the ATs). These aberration measurements are used for focus guiding for the ATs and the non-common path errors corrections between CIAO and GRAVITY.

The end-to-end simulations, the laboratory beam characterization and on-sky characterization with the ATs and UTs confirm that the acquisition camera measurements are within the GRAVITY specifications (see Table 6.5). By stabilizing the telescope beams, the astrometric error induced by the field and the pupil errors is minimized from 633μas to below 2.4 μas.

However to improve the system's performance further, a few improvements can be implemented as detailed in the following paragraphs.

- **Field guiding** One improvement is the characterization of the atmospheric differential refraction. Currently the full software is ready and the preliminary characterizations are done. But, the full characterization is in pending. It can be carried out in two steps. First, the acquisition camera is to be pointed out at different stars of various altitudes and the injection of star light into the fiber can be optimized. For each such experiment, the offset between the position predicted by the model and the actual position is to be measured. From this measurement the residual atmospheric differential refraction can be estimated. Second, the same experiment should be repeated to study the dependency of the H-K magnitudes.

- **Pupil guiding** Currently, the pupil tracker performance is degraded due to the presence of bright astrophysical targets. This performance can be improved by tracking the pupil imager as it gets enough flux in it in the presence of bright targets ($m_{\mathrm{H}} < 1$ mag). The tracking of the pupil image can be implemented with a cross-correlation algorithm, which allows to measure the lateral pupil shifts by correlating the pupil image with respect to a reference pupil image.

- **Aberration sensor** The aberration sensor performance can be improved by calibrating slopes-to-Zernike matrix. Its sensitivity can also be increased by purchasing a 2.5 mag neutral density filter and using it appropriately, instead of the current 5 mag filter.

- **Acquisition camera geometric distortion calibration** Geometric distortion calibrations can be useful for astrometry and is important in the present context because the NACO observations are used to remove 2π wrapping ambiguity that arises for the GRAVITY interferometric astrometry observations. If the acquisition camera is calibrated, it can act as a substitution for the NACO observations.

Relevance to outside GRAVITY

The concepts developed in this thesis can be interesting for other research areas as described below.

- **GRA4MAT** MATISSE (Lopez et al., 2014) is the VLTI interferometric instrument that works in the L, M and N-bands. It does not have an internal fringe tracker and is planned to use the fringe tracker of GRAVITY (Egner et al., 2016). The acquisition camera work is crucial to inject star's K-band light into the single mode fibers, which transport light to the fringe tracker.

- **Interferometric astrometry** The GRAVITY acquisition camera is an important advancement for the narrow-angle astrometry as the previous projects (the Keck Outrigger astrometry Hrynevych et al. 2004; Woillez et al. 2010 and the ESO's PRIMA Sahlmann et al. 2013) have shown that difficulties can arise in the astrometric measurements if an efficient pupil tracking and stabilization mechanism are not implemented. The present solution will be of use in future projects requiring phase referenced astrometry.

- **Pupil tracking** The pupil tracking concepts are interesting for wide field of view (off-axis) interferometry. For an interferometer, a wide field of view is possible if the wavefront sampled by the telescope primary mirror is same as that entering into the beam combiner. But due to the dynamical change of the distance between the telescope primary mirror and the beam combiner within the delay lines, the telescope pupil is not in focus at the entrance of the beam combiner. As a consequence of that the wide field of view cannot be preserved. In practice, this can be achieved with the pupil tracker which can measure the pupil defocus so that the telescope exit pupil can be re-imaged correctly at the entrance of the beam combiner using a VCM.

  The pupil tracking concepts are also interesting for high contrast systems. In these systems, lateral pupil stabilization is required to minimize the effect of quasi-static aberrations (e.g. SPHERE, Montagnier et al., 2007).

  It is interesting for E-ELT instruments such as HARMONI (Hernández et al., 2014). In these instruments the signal-to-noise ratio of spectrograph can be improved by reducing the background that arises from the telescope pupil. The background reduction is currently planned by using a rotating pupil mask, which rotates with the telescope pupil synchronously during observations. Unfortunately, unwanted pupil shifts are generated due to possible misalignments in the rotation axis and hardware misalignments from the telescope to the Nasmyth platform. The pupil tracking work in this thesis may be useful to ensure the rotation of the pupil mask in synchronous with the telescope pupil.

  Furthermore, it is also in relevance to correct the misregistration of telescope pupils in between the deformable mirror and the wavefront sensor, where they have moving optics in between them. For example, a case, where the deformable mirror placed at the telescope, the wavefront sensor placed inside the beam combiner laboratory and having delay lines moving optics.

  The lateral pupil shifts can be measured in three different ways from the acquisition camera. They are: a) from the pupil tracker images by applying the pupil tracking algorithms (Sec. 4.4.2); b) from the pupil imager images by applying a cross-correlation algorithm; c) from the Shack-Hartmann images by monitoring the intensity of the edge sub-apertures (Montagnier et al., 2007). It will be a interesting project in comparing these three methods as a function of magnitude of a star and accuracy.

- **Field tracking** In this thesis, high coupling efficiency of injection of near-infrared beams into single mode fibers is demonstrated. These concepts can be applicable to fiber-fed astronomy such as spectroscopy, interferometry, high-precision radial velocity determination and astrophotonics (e.g. Bland-Hawthorn and Kern, 2009).

- **Aberration sensor** Extended scene wavefront measurement algorithms developed in the course of this thesis work can be interesting for solar adaptive optics (e.g. Löfdahl, 2010)

and extreme large telescope laser guide star adaptive optics systems (e.g. Schreiber et al., 2009).

GRAVITY Outlook

At the time of writing, GRAVITY has finished several commissioning runs (carried roughly once in a month starting from November 2015). Now, the commissioning of the GRAVITY beam combiner is almost finished. With regards to near-infrared wavefront sensors (CIAO) for the UTs, now two units have been commissioned and two more are planned to install by the end of this year. Currently, the teams are concentrating in understanding the astrometric error sources and associated data reduction pipeline development.

Recently, GRAVITY made its first observations[1] of the Galactic Center's S2 with UTs. These observations confirm that the fringe tracker object (IRS 16C) and the science object (S2) do not have binary companions. This is a great result for the team, because if the object was binary it would have complicate the astrometric observations and the analysis. The ultimate goal of the consortium is to get ready GRAVITY in full force for the next periapse passage of S2 around the black hole, that will occur in 2018.

[1] https://www.eso.org/public/news/eso1622/

Bibliography

B. Abbott, R. Abbott, T. Abbott *et al.*, "Observation of Gravitational Waves from a Binary Black Hole Merger," *Physical Review Letters*, vol. 116, no. 6, p. 061102, feb 2016. [Online]. Available: http://adsabs.harvard.edu/abs/2016PhRvL.116f1102A

D. M. Alexander, I. Smail, F. E. Bauer *et al.*, "Rapid growth of black holes in massive star-forming galaxies,," *Nature*, vol. 434, no. 7034, pp. 738–40, apr 2005. [Online]. Available: http://adsabs.harvard.edu/abs/2005Natur.434..738A

A. Amorim and F. Eisenhauer, "Beam Stabilization & Control, VLT-TRE-GRA-15885-7101, 1.0," the European Southern Observatory, Garching, Tech. Rep., 2010.

A. Amorim, J. Lima, N. Anugu *et al.*, "The final design of the GRAVITY acquisition camera and associated VLTI beam monitoring strategy," in *Optical and Infrared Interferometry III. Proceedings of the SPIE, Volume 8445, article id. 844534, 14 pp. (2012).*, F. Delplancke, J. K. Rajagopal, and F. Malbet, Eds., vol. 8445, sep 2012, p. 844534. [Online]. Available: http://proceedings.spiedigitallibrary.org/proceeding.aspx?doi=10.1117/12.925993

N. Anugu, A. Amorim, P. Garcia *et al.*, "A low cost auto-filling and refrigeration rate regulated liquid nitrogen controller for near infrared instruments," *U.Porto Journal of Engineering, p. 45-51*, pp. 45–51, 2015. [Online]. Available: http://www.open-jim.org/index.php/upjeng/article/viewFile/123/141

R. Arsenault, J. Alonso, H. Bonnet *et al.*, "MACAO-VLTI: an adaptive optics system for the ESO interferometer," in *Adaptive Optical System Technologies II*, P. L. Wizinowich and D. Bonaccini, Eds., vol. 4839, feb 2003, pp. 174–185. [Online]. Available: http://proceedings.spiedigitallibrary.org/proceeding.aspx?articleid=873464

K. J. Astrom and R. M. Murray, *Feedback systems: an introduction for scientists and engineers*. Princeton university press, 2010. [Online]. Available: http://press.princeton.edu/titles/8701.html

F. K. Baganoff, M. W. Bautz, W. N. Brandt *et al.*, "Rapid X-ray flaring from the direction of the supermassive black hole at the Galactic Centre,," *Nature*, vol. 413, no. 6851, pp. 45–8, sep 2001. [Online]. Available: http://adsabs.harvard.edu/abs/2001Natur.413...45B

D. G. Bailey, "Sub-pixel estimation of local extrema," in *Image and Vision Computing*, vol. 414, no. 414-419. Image and Vision Computing, 2003, pp. 414–419. [Online]. Available: http://www-ist.massey.ac.nz/dbailey/sprg/pdfs/2003_IVCNZ_414.pdf

J. P. Berger, F. Malbet, F. Baron *et al.*, "Imaging the heart of astrophysical objects with optical long-baseline interferometry," *Astronomy and Astrophysics Review*, vol. 20, apr 2012. [Online]. Available: http://arxiv.org/abs/1204.4363http://dx.doi.org/10.1007/s00159-012-0053-0

J. Bland-Hawthorn and P. Kern, "Astrophotonics: a new era for astronomical instruments," *Optics Express, Vol. 17, Issue 3, p.1880-1884*, vol. 17, pp. 1880–1884, feb 2009. [Online]. Available: http://arxiv.org/abs/0902.0415http://dx.doi.org/10.1364/OE.17.001880

N. Blind, F. Eisenhauer, M. Haug *et al.*, "GRAVITY: the Calibration Unit," *Optical and Infrared Interferometry IV*, vol. 9146, p. 12, jul 2014. [Online]. Available: http://adsabs.harvard.edu/abs/2014arXiv1407.6660B

J.-B. L. Bouquin, J. P. Berger, B. Lazareff *et al.*, "PIONIER: a 4-telescope visitor instrument at VLTI," *Astronomy & Astrophysics, Volume 535, id.A67, 14 pp.*, vol. 535, sep 2011. [Online]. Available: http://arxiv.org/abs/1109.1918http://dx.doi.org/10.1051/0004-6361/201117586

D. F. Buscher, *Practical Optical Interferometry*. Cambridge, UK, Cambridge University Press, 2015. [Online]. Available: http://adsabs.harvard.edu/abs/2015poi..book.....B

E. Choquet, F. Cassaing, G. Perrin *et al.*, "GRAVITY: design and performance of the fringe tracker," in *Optical and Infrared Interferometry II. Edited by Danchi*, vol. 7734, 2010, pp. 77 341Z–77 341Z–13. [Online]. Available: http://adsabs.harvard.edu/abs/2010SPIE.7734E.59C

Y. Clénet and E. Gendron, "GRAVITY Wavefront Sensor Adaptive Optics Performance, VLT-TRE-GRA-15882-5201, 4.0," the European Southern Observatory, Garching, Tech. Rep., 2011.

M. M. Colavita, J. K. Wallace, B. E. Hines *et al.*, "The Palomar Testbed Interferometer," *The Astrophysical Journal*, vol. 510, no. 1, pp. 505–521, jan 1999. [Online]. Available: http://adsabs.harvard.edu/abs/1999ApJ...510..505C

M. M. Colavita, "Adverse effects in dual-feed interferometry," *New Astronomy Reviews*, vol. 53, no. 11-12, pp. 344–352, nov 2009. [Online]. Available: http://adsabs.harvard.edu/abs/2009NewAR..53..344C

G.-M. Dai and V. N. Mahajan, "Zernike annular polynomials and atmospheric turbulence,," *Journal of the Optical Society of America. A, Optics, image science, and vision*, vol. 24, pp. 139–155, 2007. [Online]. Available: http://adsabs.harvard.edu/abs/2007JOSAA..24..139D

Y. Dai, F. Li, X. Cheng *et al.*, "Analysis on Shack–Hartmann wave-front sensor with Fourier optics," *Optics & Laser Technology*, vol. 39, no. 7, pp. 1374–1379, oct 2007. [Online]. Available: http://adsabs.harvard.edu/abs/2007OptLT..39.1374D

R. Davies and M. Kasper, "Adaptive Optics for Astronomy," *Annual Review of Astronomy and Astrophysics*, vol. 50, no. 1, pp. 305–351, sep 2012. [Online]. Available: http://adsabs.harvard.edu/abs/2012ARA{%}26A..50..305D

C. Deen, P. Yang, A. Huber *et al.*, "Integration and bench testing for the GRAVITY Coudé IR adaptive optics (CIAO) wavefront sensor," in *Adaptive Optics Systems IV*, E. Marchetti, L. M. Close, and J.-P. Véran, Eds., vol. 9148, aug 2014, p. 91482T. [Online]. Available: http://proceedings.spiedigitallibrary.org/proceeding.aspx?doi=10.1117/12.2055127

F. Delplancke, "The PRIMA facility phase-referenced imaging and micro-arcsecond astrometry," *New Astronomy Reviews*, vol. 52, no. 2-5, pp. 199–207, jun 2008. [Online]. Available: http://adsabs.harvard.edu/abs/2008NewAR..52..199D

N. Devillard, "ESO C Library for an Image Processing Software Environment (eclipse)," *Astronomical Data Analysis Software and Systems X*, vol. 238, 2001. [Online]. Available: http://adsabs.harvard.edu/abs/2001ASPC..238..525D

T. Do, A. M. Ghez, M. R. Morris *et al.*, "A near-IR variability study of the Galactic black hole: a red noise source with no detected periodicity," *The Astrophysical Journal*, vol. 691, no. 2, pp. 1021–1034, feb 2009. [Online]. Available: http://adsabs.harvard.edu/abs/2009ApJ...691.1021D

K. Dodds-Eden, S. Gillessen, T. K. Fritz *et al.*, "The Two States of Sgr A* in the Near-infrared: Bright Episodic Flares on Top of Low-level Continuous Variability," *The Astrophysical Journal*, vol. 728, no. 1, p. 37, feb 2011. [Online]. Available: http://adsabs.harvard.edu/abs/2011ApJ...728...37D

S. Doeleman, E. Agol, D. Backer *et al.*, "Imaging an Event Horizon: submm-VLBI of a Super Massive Black Hole," *Astro2010: The Astronomy and Astrophysics Decadal Survey*, 2009. [Online]. Available: http://adsabs.harvard.edu/abs/2009astro2010S..68D

S. S. Doeleman, J. Weintroub, A. E. E. Rogers *et al.*, "Event-horizon-scale structure in the supermassive black hole candidate at the Galactic Centre,," *Nature*, vol. 455, no. 7209, pp. 78–80, oct 2008. [Online]. Available: http://adsabs.harvard.edu/abs/2008Natur.455...78D

A. Eckart, F. K. Baganoff, R. Schödel *et al.*, "The flare activity of Sagittarius A," *Astronomy and Astrophysics*, vol. 450, no. 2, pp. 535–555, may 2006. [Online]. Available: http://adsabs.harvard.edu/abs/2006A{%}26A...450..535E

A. Eckart, R. Schödel, L. Meyer *et al.*, "Polarimetry of near-infrared flares from Sagittarius A Star," *Astronomy and Astrophysics*, vol. 455, no. 1, pp. 1–10, aug 2006. [Online]. Available: http://adsabs.harvard.edu/abs/2006A{%}26A...455....1E

A. Eckart, M. Zamaninasab, C. Straubmeier *et al.*, "Signatures of strong gravity with GRAVITY," in *Optical and Infrared Interferometry II. Edited by Danchi*, vol. 7734, 2010, pp. 77 340X–77 340X–11. [Online]. Available: http://adsabs.harvard.edu/abs/2010SPIE.7734E..27E

S. Egner, J. Woillez, R. Abuter *et al.*, "GRA4MAT: combining GRAVITY and MATISSE at the VLTI," in *Proc. SPIE*, vol. SPIE2016, 2016. [Online]. Available: https://spie.org/AS/conferencedetails/astronomical-interferometry

F. Eisenhauer, "Beam Combiner Instrument System Design, VLT-TRE-GRA-15880-3101, 4.0," the European Southern Observatory, Garching, Tech. Rep., 2015.

F. Eisenhauer, W. Brandner, C. Straubmeier *et al.*, "GRAVITY: Observing the Universe in Motion," *The Messenger*, vol. 143, no. March, pp. 16–24, 2011. [Online]. Available: http://adsabs.harvard.edu/abs/2011Msngr.143...16E

H. Falcke, E. Kording, and S. Markoff, "A scheme to unify low-power accreting black holes," *Astronomy and Astrophysics*, vol. 414, no. 3, pp. 895–903, feb 2004. [Online]. Available: http://adsabs.harvard.edu/abs/2004A{%}26A...414..895F

H. Falcke, F. Melia, and E. Agol, "Viewing the Shadow of the Black Hole at the Galactic Center," *The Astrophysical Journal*, vol. 528, no. 1, pp. L13–L16, jan 2000. [Online]. Available: http://adsabs.harvard.edu/abs/2000ApJ...528L..13F

M. Ferrari, G. R. Lemaitre, S. P. Mazzanti *et al.*, "Variable curvature mirrors: implementation in the VLTI delay-lines for field compensation," in *Interferometry for Optical Astronomy II*, vol. 4838, 2003, pp. 1155–1162. [Online]. Available: http://adsabs.harvard.edu/abs/2003SPIE.4838.1155F

G. Finger, R. J. Dorn, S. Eschbaumer *et al.*, "Performance evaluation, readout modes, and calibration techniques of HgCdTe Hawaii-2RG mosaic arrays," in *High Energy, Optical, and Infrared Detectors for Astronomy III. Edited by Dorn, David A.; Holland, Andrew D. Proceedings of the SPIE, Volume 7021, article id. 70210P, 13 pp. (2008).*, D. A. Dorn and A. D. Holland, Eds., vol. 7021, aug 2008, p. 70210P. [Online]. Available: http://proceedings.spiedigitallibrary.org/proceeding.aspx?doi=10.1117/12.787971

G. Finger, I. Baker, D. Alvarez *et al.*, "SAPHIRA detector for infrared wavefront sensing," in *Adaptive Optics Systems IV*, E. Marchetti, L. M. Close, and J.-P. Véran, Eds., vol. 9148, aug 2014, p. 914817. [Online]. Available: http://proceedings.spiedigitallibrary.org/proceeding.aspx?doi=10.1117/12.2057078

V. L. Fish, S. S. Doeleman, C. Beaudoin *et al.*, "1.3 mm Wavelength VLBI of Sagittarius A*: Detection of Time-Variable Emission on Event Horizon Scales," *The Astrophysical Journal*, vol. 727, no. 2, p. L36, feb 2011. [Online]. Available: http://adsabs.harvard.edu/abs/2011ApJ...727L..36F

R. Genzel, R. Schödel, T. Ott *et al.*, "Near-infrared flares from accreting gas around the supermassive black hole at the Galactic Centre,," *Nature*, vol. 425, no. 6961, pp. 934–7, oct 2003. [Online]. Available: http://adsabs.harvard.edu/abs/2003Natur.425..934G

R. Genzel, F. Eisenhauer, and S. Gillessen, "The Galactic Center massive black hole and nuclear star cluster," *Reviews of Modern Physics*, vol. 82, no. 4, pp. 3121–3195, dec 2010. [Online]. Available: http://adsabs.harvard.edu/abs/2010RvMP...82.3121G

A. M. Ghez, M. Morris, E. E. Becklin *et al.*, "The accelerations of stars orbiting the Milky Way's central black hole," *Nature*, vol. 407, no. 6802, pp. 349–351, 2000. [Online]. Available: http://adsabs.harvard.edu/abs/2000Natur.407..349G

A. M. Ghez, S. Salim, S. D. Hornstein *et al.*, "Stellar Orbits around the Galactic Center Black Hole," *The Astrophysical Journal*, vol. 620, no. 2, pp. 744–757, feb 2005. [Online]. Available: http://adsabs.harvard.edu/abs/2005ApJ...620..744G

S. Gillessen, "GRAVITY Metrology, VLT-TRE-GRA-15880-8001, 4.0," the European Southern Observatory, Garching, Tech. Rep., 2015.

S. Gillessen, F. Eisenhauer, S. Trippe *et al.*, "Monitoring stellar orbits around the massive Black Hole in the Galactic Center," *The Astrophysical Journal*, vol. 692, no. 2, pp. 1075–1109, feb 2009. [Online]. Available: http://adsabs.harvard.edu/abs/2009ApJ...692.1075G

S. Gillessen, M. Lippa, F. Eisenhauer *et al.*, "GRAVITY: metrology," in *SPIE Astronomical Telescopes + Instrumentation*, F. Delplancke, J. K. Rajagopal, and F. Malbet, Eds. International Society for Optics and Photonics, sep 2012, p. 84451O. [Online]. Available: http://proceedings.spiedigitallibrary.org/proceeding.aspx?articleid=1357092

P. B. Gitton, S. A. Leveque, G. Avila, and T. Phan Duc, "IRIS: an infrared tilt sensor for the VLTI," in *New Frontiers in Stellar Interferometry*, vol. 5491, 2004, p. 944. [Online]. Available: http://adsabs.harvard.edu/abs/2004SPIE.5491..944G

A. Glindemann, *Principles of Stellar Interferometry*, ser. Astronomy and Astrophysics Library. Springer Berlin Heidelberg, 2011. [Online]. Available: http://adsabs.harvard.edu/abs/2011psi.book.....G

P. Gordo and A. Amorim, "GRAVITY acquisition camera, VLT-TRE-GRA-15885-6301, 4.0," the European Southern Observatory, Garching, Tech. Rep., 2015.

J. W. Hardy, *Adaptive optics for astronomical telescopes*. Oxford University Press, 1998. [Online]. Available: http://adsabs.harvard.edu/abs/1998aoat.book.....H

X. Haubois, K. Dodds-Eden, A. Weiss *et al.*, "Flares and variability from Sagittarius A*: five nights of simultaneous multi-wavelength observations," *Astronomy & Astrophysics*, vol. 540, p. A41, mar 2012. [Online]. Available: http://adsabs.harvard.edu/abs/2012A{&}A...540A..41H

E. Hernández, L. F. Rodríguez, J. V. Gigante *et al.*, "Conceptual design of a cryogenic pupil mechanism with continuous complex movements for HARMONI," in *Advances in Optical and Mechanical Technologies for Telescopes and Instrumentation*, R. Navarro, C. R.

Cunningham, and A. A. Barto, Eds., vol. 9151, jul 2014, p. 91513F. [Online]. Available: http://proceedings.spiedigitallibrary.org/proceeding.aspx?doi=10.1117/12.2055933

S. Hippler and F. Hormuth, "VLTI tunnel seeing measurements, VLT-TRE-GRA-15880-4365, 3.0," the European Southern Observatory, Garching, Tech. Rep., 2010.

H. Hogenhuis, M. Visser, and F. Derie, "Commissioning of the VLTi delay lines on mount Paranal," pp. 1148–1154, 2003. [Online]. Available: http://adsabs.harvard.edu/abs/2003SPIE.4838.1148H

J. M. Hollywood and F. Melia, "General Relativistic Effects on the Infrared Spectrum of Thin Accretion Disks in Active Galactic Nuclei: Application to Sagittarius A*," *The Astrophysical Journal Supplement Series*, vol. 112, no. 2, pp. 423–455, oct 1997. [Online]. Available: http://adsabs.harvard.edu/abs/1997ApJS..112..423H

M. A. Hrynevych, I. Ligon, Edgar R., and M. M. Colavita, "Baseline monitoring for astrometric interferometry," in *New Frontiers in Stellar Interferometry*, vol. 5491, 2004, p. 1649. [Online]. Available: http://adsabs.harvard.edu/abs/2004SPIE.5491.1649H

A. Ishimaru, *Wave propagation and scattering in random media.* Vol. 1, New York (NY, USA): Academic Press, 1978. [Online]. Available: http://www.sciencedirect.com/science/book/9780123747013

L. Jocou, K. Perraut, A. Nolot *et al.*, "The GRAVITY integrated optics beam combination," in *Optical and Infrared Interferometry II. Edited by Danchi*, vol. 7734, 2010, pp. 773 430–773 430–12. [Online]. Available: http://adsabs.harvard.edu/abs/2010SPIE.7734E..96J

T. Johannsen, A. E. Broderick, P. M. Plewa *et al.*, "Testing General Relativity with the Shadow Size of Sgr A*," *Physical review letters*, vol. 116, no. 3, p. 031101, jan 2016. [Online]. Available: http://adsabs.harvard.edu/abs/2016PhRvL.116c1101J

M. D. Johnson, V. L. Fish, S. S. Doeleman *et al.*, "RELATIVE ASTROMETRY OF COMPACT FLARING STRUCTURES IN Sgr A* WITH POLARIMETRIC VERY LONG BASELINE INTERFEROMETRY," *The Astrophysical Journal*, vol. 794, no. 2, p. 150, oct 2014. [Online]. Available: http://adsabs.harvard.edu/abs/2014ApJ...794..150J

——, "Resolved magnetic-field structure and variability near the event horizon of Sagittarius A*,," *Science (New York, N.Y.)*, vol. 350, no. 6265, pp. 1242–5, dec 2015. [Online]. Available: http://adsabs.harvard.edu/abs/2015Sci...350.1242J

S. Kendrew, S. Hippler, W. Brandner *et al.*, "The GRAVITY Coude Infrared Adaptive Optics (CIAO) system for the VLT Interferometer," *eprint arXiv:1207.2945*, 2012. [Online]. Available: http://adsabs.harvard.edu/abs/2012arXiv1207.2945K

J. Krolik, J. Hawley, and S. Hirose, "The Relationship between Accretion Disks and Jets," *Triggering Relativistic Jets (Eds. William H. Lee & Enrico Ramírez-Ruiz) Revista Mexicana de Astronomía y Astrofísica (Serie de Conferencias) Vol. 27*, vol. 27, pp. 1–7, 2007. [Online]. Available: http://adsabs.harvard.edu/abs/2007RMxAC..27....1K

S. Lacour, F. Eisenhauer, S. Gillessen *et al.*, "Reaching micro-arcsecond astrometry with long baseline optical interferometry; application to the GRAVITY instrument," *Astronomy & Astrophysics*, apr 2014. [Online]. Available: http://arxiv.org/abs/1404.1014

V. Lapeyrere, "Data Reduction Library Design, VLT-TRE-GRA-15882-9502, 4.0," the European Southern Observatory, Garching, Tech. Rep., 2015.

R. Lenzen, M. Hartung, W. Brandner *et al.*, "NAOS-CONICA first on sky results in a variety of observing modes," in *Instrument Design and Performance for Optical/Infrared Ground-based Telescopes. Edited by Iye*, M. Iye and A. F. M. Moorwood, Eds., vol. 4841, mar 2003, pp. 944–952. [Online]. Available: http://adsabs.harvard.edu/abs/2003SPIE.4841..944L

J. Lima and A. Amorim, "Beam Analyzer Procurement Specifications, 1.0," Faculty of sciences, University of Lisbon, Tech. Rep., 2012.

M. G. Löfdahl, "Evaluation of image-shift measurement algorithms for solar Shack-Hartmann wavefront sensors," *Astronomy & Astrophysics*, vol. 524, p. A90, nov 2010. [Online]. Available: http://adsabs.harvard.edu/abs/2010A{%}26A...524A..90Lhttp://adsabs.harvard.edu/abs/2010A{&}A...524A..90L

B. Lopez, S. Lagarde, W. Jaffe *et al.*, "An Overview of the MATISSE Instrument — Science, Concept and Current Status," *The Messenger, vol. 157, p. 5-12*, vol. 157, pp. 5–12, 2014. [Online]. Available: https://www.eso.org/sci/publications/messenger/archive/no.157-sep14/messenger-no157-5-12.pdf

D. Lynden-Bell, "Galactic Nuclei as Collapsed Old Quasars," *Nature*, vol. 223, no. 5207, pp. 690–694, aug 1969. [Online]. Available: http://adsabs.harvard.edu/abs/1969Natur.223..690L

J. Macquart and G. C. Bower, "Understanding the Radio Variability of Sagittarius A*," *The Astrophysical Journal*, vol. 641, no. 1, pp. 302–318, apr 2006. [Online]. Available: http://adsabs.harvard.edu/abs/2006ApJ...641..302M

D. Malacara, "Optical shop testing," *Optical shop testing edited by Daniel Malacara. 3rd ed. Published by John Wiley*, 2007. [Online]. Available: http://adsabs.harvard.edu/abs/2007ost..book.....M

J. C. Mauerhan, M. Morris, F. Walter, and F. K. Baganoff, "Intraday Variability of Sagittarius A* at 3 Millimeters," *The Astrophysical Journal*, vol. 623, no. 1, pp. L25–L28, apr 2005. [Online]. Available: http://adsabs.harvard.edu/abs/2005ApJ...623L..25M

D. J. McKay, P. Ballester, K. Banse *et al.*, "The common pipeline library: standardizing pipeline processing," in *Optimizing Scientific Return for Astronomy through Information Technologies. Edited by Quinn, Peter J.; Bridger, Alan. Proceedings of the SPIE, Volume 5493, pp. 444-452 (2004).*, P. J. Quinn and A. Bridger, Eds., vol. 5493, sep 2004, pp. 444–452. [Online]. Available: http://proceedings.spiedigitallibrary.org/proceeding.aspx?articleid=848002

I. S. McLean, "Near infrared instrumentation for large telescopes." *VIIth Canary Islands Winter School of Astrophysics: Instrumentation for large telescopes, p. 203 - 240*, pp. 203–240, 1997. [Online]. Available: http://adsabs.harvard.edu/abs/1997ilt..book..203M

——, *Electronic Imaging in Astronomy: Detectors and Instrumentation*. Second Edition, Praxis Publishing, 2008. [Online]. Available: http://adsabs.harvard.edu/abs/2008eiad.book.....M

J. Menu, G. Perrin, E. Choquet, and S. Lacour, "Kalman-filter control schemes for fringe tracking," *Astronomy & Astrophysics*, vol. 541, p. A81, may 2012. [Online]. Available: http://adsabs.harvard.edu/abs/2012A{&}A...541A..81M

J. D. Monnier, "Optical interferometry in astronomy," *Reports on Progress in Physics*, vol. 66, no. 5, pp. 789–857, may 2003. [Online]. Available: http://adsabs.harvard.edu/abs/2003RPPh...66..789M

G. Montagnier, T. Fusco, J. L. Beuzit *et al.*, "Pupil stabilization for SPHERE's extreme AO and high performance coronagraph system," *Optics Express*, vol. 15, nov 2007. [Online]. Available: http://arxiv.org/abs/0711.1332http://dx.doi.org/10.1364/OE.15.015293

J. Nijenhuis, H. Visser, H. de Man *et al.*, "Simultaneous observation of two stars using the PRIMA Star Separator," in *Optical and Infrared Interferometry*, vol. 7013, jul 2008, p. 70133F. [Online]. Available: http://proceedings.spiedigitallibrary.org/proceeding.aspx?doi=10.1117/12.789943

H. Nobach and M. Honkanen, "Two-dimensional Gaussian regression for sub-pixel displacement estimation in particle image velocimetry or particle position estimation in particle tracking velocimetry," *Experiments in Fluids*, vol. 38, no. 4, pp. 511–515, mar 2005. [Online]. Available: http://adsabs.harvard.edu/abs/2005ExFl...38..511N

R. J. Noll, "Zernike polynomials and atmospheric turbulence," *Optical Society of America*, vol. 66, pp. 207–211, 1976. [Online]. Available: http://adsabs.harvard.edu/abs/1976JOSA...66..207N

K. Perraut and L. Jocou, "GRAVITY Beam Combiner Instrument Integrated Optics, VLT-TRE-GRA-15884-6501, 4.0," the European Southern Observatory, Garching, Tech. Rep., 2015.

O. Pfuhl, M. Haug, F. Eisenhauer *et al.*, "The fiber coupler and beam stabilization system of the GRAVITY interferometer," in *SPIE Astronomical Telescopes + Instrumentation*, J. K. Rajagopal, M. J. Creech-Eakman, and F. Malbet, Eds. International Society for Optics and Photonics, jul 2014, p. 914623. [Online]. Available: http://proceedings.spiedigitallibrary.org/proceeding.aspx?articleid=1891951

O. Pfuhl, "The GRAVITY interferometer and the Milky Way's nuclear star cluster," jul 2012. [Online]. Available: http://edoc.ub.uni-muenchen.de/14877/1/Pfuhl{_}Oliver.pdf

L. A. Poyneer, "Scene-Based Shack-Hartmann Wave-Front Sensing: Analysis and Simulation," *Applied Optics*, vol. 42, no. 29, p. 5807, oct 2003. [Online]. Available: http://www.osapublishing.org/viewmedia.cfm?uri=ao-42-29-5807{&}seq=0{&}html=true

W. Press, S. Teukolsky, W. Vetterling, and B. Flannery, *Numerical Recipes in C++: The Art of Scientific Computing*. Cambridge University Press, 2002. [Online]. Available: http://www.citeulike.org/user/middell/article/1321549

M. J. Reid, "Is there a Supermassive Black Hole at the Center of the Milky Way?" *International Journal of Modern Physics D*, vol. 18, no. 06, pp. 889–910, jun 2009. [Online]. Available: http://adsabs.harvard.edu/abs/2009IJMPD..18..889R

F. Rigaut, "https://github.com/frigaut/yao," 2011. [Online]. Available: https://github.com/frigaut/yao

F. Rigaut and M. Van Dam, "Simulating Astronomical Adaptive Optics Systems Using Yao," *Proceedings of the Third AO4ELT Conference. Firenze*, 2013. [Online]. Available: http://adsabs.harvard.edu/abs/2013aoel.confE..18R

F. Roddier, "Adaptive optics in astronomy," *Cambridge University Press*, 1999. [Online]. Available: http://adsabs.harvard.edu/abs/1999aoa..book.....R

H. G. Roe, "Implications of Atmospheric Differential Refraction for Adaptive Optics Observations," *Publications of the Astronomical Society of the Pacific*, vol. 114, no. 794, pp. 450–461, apr 2002. [Online]. Available: http://adsabs.harvard.edu/abs/2002PASP..114..450R

J. Sahlmann, T. Henning, D. Queloz *et al.*, "The ESPRI project: astrometric exoplanet search with PRIMA," *Astronomy & Astrophysics*, vol. 551, p. A52, feb 2013. [Online]. Available: http://adsabs.harvard.edu/abs/2013A{%}26A...551A..52S

D. P. Salas-Peimbert, D. Malacara-Doblado, V. M. Durán-Ramírez *et al.*, "Wave-front retrieval from Hartmann test data," *Applied Optics*, vol. Vol. 44, no. 20, pp. 4228–4238, 2005. [Online]. Available: http://dx.doi.org/10.1364/AO.44.004228

M. Schmidt, "3C 273 : A Star-Like Object with Large Red-Shift," *Nature*, vol. 197, no. 4872, pp. 1040–1040, mar 1963. [Online]. Available: http://adsabs.harvard.edu/abs/1963Natur.197.1040S

R. Schödel, T. Ott, R. Genzel *et al.*, "A star in a 15.2-year orbit around the supermassive black hole at the centre of the Milky Way,," *Nature*, vol. 419, no. 6908, pp. 694–6, oct 2002. [Online]. Available: http://adsabs.harvard.edu/abs/2002Natur.419..694S

L. Schreiber, I. Foppiani, C. Robert *et al.*, "Laser guide stars for extremely large telescopes: efficient Shack-Hartmann wavefront sensor design using the weighted centre-of-gravity algorithm," *Monthly Notices of the Royal Astronomical Society*, vol. 396, no. 3, pp. 1513–1521, jul 2009. [Online]. Available: http://adsabs.harvard.edu/abs/2009MNRAS.396.1513S

G. Schubert and R. L. Walterscheid, "Earth," *Allen's astrophysical quantities*, 2000. [Online]. Available: http://adsabs.harvard.edu/abs/2000asqu.book..239S

M. Shao and M. M. Colavita, "Potential of long-baseline infrared interferometry for narrow-angle astrometry," *Astronomy and Astrophysics*, vol. 262, pp. 353–358, aug 1992. [Online]. Available: http://adsabs.harvard.edu/abs/1992A%26A...262..353S

M. Sjödahl, "Electronic speckle photography: increased accuracy by nonintegral pixel shifting,," *Applied optics*, vol. 33, no. 28, pp. 6667–73, oct 1994. [Online]. Available: http://www.osapublishing.org/viewmedia.cfm?uri=ao-33-28-6667{&}seq=0{&}html=true

R. Stone, "A New Method for Computing Differential Color Refraction," *Publications of the Astronomical Society of the Pacific*, vol. 114, no. 800, pp. 1070–1086, oct 2002. [Online]. Available: http://www.jstor.org/stable/10.1086/342676http://adsabs.harvard.edu/abs/2002PASP..114.1070S

C. Straubmeier, S. Yazici, M. Wiest *et al.*, "The GRAVITY spectrometers: optical design and first light," in *SPIE Astronomical Telescopes + Instrumentation*, J. K. Rajagopal, M. J. Creech-Eakman, and F. Malbet, Eds. International Society for Optics and Photonics, jul 2014, p. 914629. [Online]. Available: http://proceedings.spiedigitallibrary.org/proceeding.aspx?articleid=1891957

E. Tatulli, t. A. Consortium, A. Chelli *et al.*, "Interferometric data reduction with AMBER/VLTI.Principle,estimators and illustration," *Astronomy and Astrophysics, Volume 464, Issue 1, March II 2007, pp.29-42*, vol. 464, pp. 29–42, mar 2006. [Online]. Available: http://arxiv.org/abs/astro-ph/0603046http://dx.doi.org/10.1051/0004-6361:20064799

A. T. Tokunaga, "Infrared Astronomy," *Allen's astrophysical quantities, 4th ed. Edited by Arthur N. Cox. ISBN: 0-387-98746-0. Publisher: New York: AIP Press; Springe r, 2000, p.143*, p. 143, 2000. [Online]. Available: http://www.springer.com/us/book/9780387951898

G. Vdovin, H. van Brug, and F. van Goor, "LightPipes: software for education in coherent optics," in *Fifth International Topical Meeting on Education and Training in Optics*. Delft, Netherlands: SPIE, Volume 3190, 1997. [Online]. Available: http://adsabs.harvard.edu/abs/1997SPIE.3190...82V

C. M. Will, "Testing the General Relativistic "No-Hair" Theorems Using the Galactic Center Black Hole Sagittarius A*," *The Astrophysical Journal*, vol. 674, no. 1, pp. L25–L28, feb 2008. [Online]. Available: http://stacks.iop.org/1538-4357/674/i=1/a=L25

J. Woillez and S. Lacour, "Wide-angle, Narrow-angle, and Imaging Baselines of Optical Long-baseline Interferometers,," *The Astrophysical Journal*, vol. 764, no. 1, p. 109, feb 2013. [Online]. Available: http://iopscience.iop.org/0004-637X/764/1/109/article/

J. Woillez, R. Akeson, M. Colavita *et al.*, "ASTRA: astrometry and phase-referencing astronomy on the Keck interferometer," in *Proceedings of the SPIE*, vol. 7734, jul 2010, p. 773412. [Online]. Available: http://adsabs.harvard.edu/abs/2010SPIE.7734E..12W

S. Yelda, J. R. Lu, A. M. Ghez *et al.*, "Improving Galactic Center Astrometry By Reducing the Effects of Geometric Distortion," *The Astrophysical Journal*, vol. 725, no. 1, pp. 331–352, dec 2010. [Online]. Available: http://adsabs.harvard.edu/abs/2010ApJ...725..331Y

F. Yusef-Zadeh, H. Bushouse, M. Wardle *et al.*, "Simultaneous multi-wavelength observations of Sgr A* during 2007 April 1-11," *The Astrophysical Journal*, vol. 706, no. 1, pp. 348–375, nov 2009. [Online]. Available: http://adsabs.harvard.edu/abs/2009ApJ...706..348Y

J.-H. Zhao, G. C. Bower, and W. M. Goss, "Radio Variability of Sagittarius A—a 106 Day Cycle," *The Astrophysical Journal*, vol. 547, no. 1, pp. L29–L32, jan 2001. [Online]. Available: http://adsabs.harvard.edu/abs/2001ApJ...547L..29Z

List of Figures

1.1 Left: The orbit of S2 around Sgr A*. It has a period of 15.2 years and is highly elliptical, with eccentricity of 0.88. Right: The radial velocity of S2. The S2 passed its pericenter, which is located at a distance of $\sim 144\ r_S$ from Sgr A*, in 2002 and hence the abrupt change in its radial velocity. Figure credit Genzel et al. 2010. 2

1.2 Left: Orbits of 26 different S-stars close to Sgr A*, which is centered in the figure. Right: A near-infrared simulation of the black hole shadow: the optical appearance of an accretion disk as the observer looks into the equatorial plane. The axes units are $2r_S$. Figure credit: left panel – Gillessen et al. 2009; right panel – Hollywood and Melia 1997. 3

1.3 Light curves of the near-infrared flares. Figure credit Dodds-Eden et al. 2011. . . 3

1.4 Artist depiction (ignoring space-time curvature) of the three most plausible flare modes of Sgr A*: (left) jet model; (middle) hot-spot (blue sphere) orbiting in the inner circular stable orbit; (right) pure red noise model. In the center, the emission of Sgr A* in the near-infrared is negligible in comparison to flares. Figure credit Eisenhauer et al. 2011. 4

1.5 Airy pattern: the aberration-free image of a point source in a monochromatic light, imaged with a circular aperture optical system. The first null of intensity happens at $1.22\lambda/D$. Figure adapted from Buscher 2015. 5

1.6 A black hole shadow simulated with 1.33 mm wavelength observation. The intensity variations along the X-axis (in arbitrary units) and Y-axis (in distance, r_S) are denoted in solid green and dashed purple curves respectively. Figure credit Falcke et al. 2000. 6

1.7 Correlated flux density plots of Sgr A* as a function of baseline length. The solid and dashed lines are the best-fit circular Gaussian and ring visibility models respectively for the compact emission in Sgr A*. Fish et al. 2011 reports that the Gaussian model is consistent with the source size of approximately 43 μas on all days. Figure credit Fish et al. 2011. 7

1.8 The beams of science and reference stars are combined coherently. The internal phase differences between the telescope baseline reference points and the central fringes are measured by a metrology system. 8

2.1 For clarity only two-telescope interferometer baseline is presented. The wide angle baseline (WAB) is defined by the two pivot-points. The average of the positions of four metrology diodes (cross-marks) allow us to define the narrow angle baseline (NAB). The imaging baseline is defined by the weighted average of several pupils in the optical train starting from the telescope pupil to the pupil of the fiber. In GRAVITY there are two fibers, one for each beam combiner. Thus it has two imaging baselines IMB1 and IMB2. Figure credit Lacour et al. 2014. 15

2.2 A simple description of the field tip-tilts and pupil shifts. The star shown in dashed line is tilted ($\Delta\alpha$) from the original star (solid line). The telescope pupil is shifted laterally (ΔL_x) with respect to the pupil position of the fiber. Due to the field and the pupil shift errors unwanted astrometric errors are experienced. Another effect with the field error is the loss of flux injection of the star's light into the fiber. . . 16

2.3 Aerial view of the ESO's Paranal observatory, in the Chilean Atacama desert. On the platform, four big domes of the four giant 8 m UTs are clearly distinguishable. The four domes in front of the UTs are the four 1.8 m ATs. On the right corner of the platform is the 2.6 m VLT Survey Telescope (VST). A 4.1 m Visible and Infrared Survey Telescope for Astronomy (VISTA), seen in the distance on the next mountain peak from the main platform. Image credit: G. Hüdepohl/ESO. . . 19

2.4 Drawing of a main delay line of the VLTI. The delay line carriage rail, cat's eye assembly and the delay line metrology beams (which are used as the reference to apply the exact and accurate amount of delay). The tertiary mirror M3 is the variable curvature mirror. Figure credit Hogenhuis et al. 2003. 20

2.5 Path of the telescope beams into GRAVITY. Here only the ATs are shown. The AT beams are relayed into the VLTI delay lines using the mirrors numbered M12 (labelled **A** and **B** in the figure). The delay lines are in between **A/B** and **C**. For the ATs the switch-yard (**C**) is used to relay the beams directly toward the GRAVITY feeding optics (**E**). For the UTs, the input beams are relayed first to the beam compressors (**D**) and there they undergo beam resizing from 80 mm beam to 18 mm. Once the beams are resized, they enter GRAVITY (**F**) via the GRAVITY feeding optics. Please see the text for the explanation of subsystems. 21

2.6 Observational strategy for GRAVITY. IRS 7 is used as the wavefront reference source for the Galactic Center observations. IRS 16C is used as the fringe tracker phase-reference star and using it fringes are stabilised. This figure is a NACO observation (Lenzen et al., 2003), taken from the ESO science archive facility. . 23

2.7 The working principle of the GRAVITY beam combiner instrument. The four UTs or the ATs of the VLTI are combined coherently. Infrared wavefront sensor (green color) images the object outside the 2″ field of view, measures the atmospheric turbulence perturbations and corrects with the telescope deformable mirrors. The objects within 2″ field of view are combined in the two interferometric beam combiners – one for fringe-tracking (blue lines) and one for the science object (red lines). The acquisition camera and various laser guiding systems implement the beam stabilization. A dedicated laser metrology traces the optical path length differences for narrow angle astrometry. See the body text for more details. For clarity, only two telescopes, one beam combiner, and one wavefront sensor are shown. Figure credit: Eisenhauer et al. (2011). 24

2.8 Overall view of the GRAVITY beam combiner instrument. 1 – Calibration Unit; 2 – fiber control unit; 3 – fiber coupler; 4 – acquisition camera; 5 – metrology injection; 6 – two spectrometers (fringe tracker and science spectrometer); 7 – cryostat. See the text for the description of each sub system. Image credit GRAVITY consortium. 25

2.9 Optical layout of the fiber coupler (see text for details). Figure credit Pfuhl 2012. 25

2.10 Drawing of pupil guiding beacons (green boxes inside the black-circle) and Metrology receiver diodes (green boxes outside the circle) installed on a AT. Figure courtesy: Marcus, H. 27

2.11 Left: Integrated optics beam combiner used in the science and the fringe tracker spectrometers; Right: Description of the beam combiner (top) and of the ABCD cell (bottom). Figure credit Perraut and Jocou 2015. 29

2.12 The optical layout of the science spectrometer. The output of the integrated optics chip (bottom left of this figure) is dispersed by a grism, split by polarization and imaged on the detector. The K-band filter blocks the metrology beam towards the science detector. The injection optics of metrology feeds metrology laser beam into integrated optics. Figure credit Straubmeier et al. 2014 30

2.13 The principle of metrology system. Two metrology laser beams (violet in color, noted 1 and 2) are back-propagated from the GRAVITY beam combiners (BC A and BC B) to the telescope secondary mirror (M2) through the same path as the science light (red and green) does forwards. A third bright beam (noted with 3) is injected bypassing the fiber elements (to reduce the beam back-scattering within the fibers) and superimposed with other two. The three-beam fringe pattern is detected at the telescope secondary mirror spiders by sampling the pattern at four locations with photo-diodes. Figure credit Gillessen 2015. 31

2.14 A typical GRAVITY observation's fits header (data format). There are several extensions. Extensions IMAGING_DATA_SC, IMAGING_DETECTOR_FT and IMAGING_DATA_ACQ provide images of the science spectrometer, the fringe tracker and the acquisition camera respectively. The extension METROLOGY provides the data of the laser metrology system in the binary table. 32

2.15 Number of active controls that are in operation to achieve the GRAVITY astrometry. The red and blue colors represent optical paths of the fringe tracker (phase-reference) and the science targets respectively. The dotted and solid lines are the light propagation through the air and the single-mode fibers respectively. The green color stands for the metrology system. The tip-tilt and the pupil corrections are enabled by the acquisition camera sensor (in yellow color). The orange color represents the polarization control system. Figure credit Lacour et al. 2014. . . . 34

3.1 One telescope beam case is presented for simplicity. The H-band and the K-band beams are used for the beam guiding and the science measurements, respectively. The H-band beam is distributed among the optical functions of the acquisition camera: the pupil tracker takes the pupil reference laser beams (1.2 µm) and images them with a 2×2 lenslet; the aberration sensor (Abr. sensor) uses a Shack-Hartmann lenslet image; the pupil imager images the telescope pupil using a telecentric pupil lens; the field imager images the field using its field lens. The box in red color represents acquisition camera optics. 36

3.2 The acquisition camera folding optics. a) the folding optics Zemax design. The mirrors are used to relay the input telescope beams into the beam analyzer. The lenses shown are used for the field imaging. b) the hardware of the folding optics. The detector is placed over the beam analyzer (panel d). Figure credits: top left panel – Amorim et al. 2012; bottom panels – the GRAVITY consortium. 37

3.3 Guiding prisms receive beams from the folding optics and guide them towards the dichroic beam splitter (labeled **a** in the Figure). Left bottom panel is the Zemax design of the beam analyzer for one telescope beam. The right panel is the beam analyzer hardware. The light path inside the beam analyzer (from top to bottom in the figure): the dichroic beam splitter (**a**) reflects the 1.2 µm wavelength beams towards the pupil tracker (2×2 lenslets, label (**b**)) and transmits the remaining H-band beam. This H-band beam (>1.2 µm) is shared between the field imager and other imaging modes (i.e., the pupil imager and the aberration sensor) using a beam splitter (**c**). The light sharing between the pupil imager and the aberration sensor is implemented with another beam splitter (**d**). The label (**e**) stands for the Shack-Hartmann. The imaging modes are: 1 – pupil tracker; 2 – aberration sensor; 3 – pupil imager; 4 – field imager. Figure credits: left panel – Amorim et al. 2012; right panel – the GRAVITY consortium. 39

3.4 Stabilization of the star light injection into a single mode fiber. Accurate position of the star, $O(x,y)$, is detected by the field imager using the H-band beam. By feedbacking the star position to the tip-tilt and piston mirror (situated in front of the fiber feeding optics), the star's light injection is stabilized. The star's K-band light is focused into the single mode fiber using a parabolic mirror. 40

3.5 Pupil beacons installed on the M2 spiders. Left and right panels are for the ATs and the UTs. All four pupil beacons are fed by a common laser diode via multi-mode fibers. 42

3.6 A simple layout of the pupil tracker working principle. Reference telescope pupil and corresponding laser spots are represented with the solid lines in black and filled circles respectively. The shifted pupil and corresponding laser spots are represented with the dashed lines in blue and star symbols respectively. A typical lateral shifted pupil is presented in the panels of (a) and (b). A typical longitudinal shifted pupil is presented in the panels of (c) and (d). 42

3.7 (Left) Teledyne HAWAII-2RG readout integrated circuit wafer. (Right) Full detector. Figure credit: left panel Teledyne[2]; right panel, Eisenhauer 2015. 45

3.8 Acquisition camera SOLIDWORKS design which presents the tip-tilt and the Z adjusting mounts for lenses and mirrors. Figure credit Amorim et al. 2012. 46

3.9 A synthetic field image for the Milky Way Galactic Center. 47

3.10 Simulation blocks for a pupil guiding laser beacon. 47

3.11 Left: a typical pupil tracker image. Each circle represents one sub-aperture lens. Spots in each circle represents four pupil beacons imaged by one sub-aperture lens. The average of these four pupil beacons in each circle is called as barycenter position. Right: a typical pupil tracker reference spots. 48

3.12 A typical aberration sensor image. 49

3.13 A synthetic pupil image for the UTs. 50

3.14 Synthetic detector image of the acquisition camera. Each column represents the four imaging modes of it for each telescope. Windows in each column, from top to bottom, are the pupil tracker, the aberration sensor, the pupil imager and the field imager respectively. 51

4.1 An overall view of the beam guiding approach. The sensor software reads the detector images and writes the extracted beam aberration parameters to the instrument database. The control software reads the beam parameters, converts them into actuators commands and sends them to the actuators to apply the beam corrections. 54

4.2 From left to right are the pupil tracker images of the UT, the AT and the Calibration Unit. Here the Calibration Unit spots are scaled to the AT. It can be seen in these figures that a rotation of sub-aperture spots is present. 56

4.3 Pupil tracker images highlighting the astrophysical background filling (left) and pupil vignetting (right) discussed in the text. 57
4.4 Left panel: explains the three/four-sub-apertures algorithm. Right panel: A vignetted pupil tracker image. Rectangular search windows shown above are applied as part of the two-sub-aperture algorithm to determine the spots pattern. The red dot indicates average of detected spots, C_{PT}. 58
4.5 Left: Horizontal and vertical pattern in the two-sub-apertures algorithm. Right: Barycenters and reference spot positions of the pupil tracker. 59
4.6 An overall view of measuring barycenters of the pupil tracker laser beacons. For description of it please see the text. 59
4.7 Correlation method of measuring pupil shifts. Left: A typical pupil tracker image taken with the UT3. It is shifted laterally along X-axis by 20 pixels. Middle: Auto-correlation of the image itself. The separation between the central peak and anyone of the outer peaks in the circles gives the pupil defocus. Right: Cross-correlation (Poyneer, 2003; Press et al., 2002) of the pupil tracker image and its 180 degree rotated image. The lateral shift can be measured as half of the correlation peak shift from its reference grid (here the double shift comes from the 180 degree rotation image). In the figure example, the correlation shift is 40 pixel, which corresponds to the 20 pixel lateral shift. 61
4.8 Left: a vignetted pupil tracker image. Middle: auto-correlation image; Right: cross-correlation image. Measurement of the pupil shifts in the presence of vignetting. This pupil tracker image has zero pupil shift. But the cross-correlation peak does not represent the center of the pupil, because it is biased in the absence of the other two sub-apertures. 62
4.9 Left: As a consequence of refraction, the blue light (H-band) bends more than the red light (K-band). That means blue center is more angularly shifted towards the zenith in comparison to the red light. Right: (a) a typical field image for the UTs; (b) the ADR affected field image for the UTs at a zenith distance of 50°. In the ADR affected image, the star image is spectrally elongated which is similar to that of a prism dispersion. 64
4.10 Left: ADR shifts obtained at different zenith distances, $z = 20°$, 40° and 60°, and for various wavelengths. In this calculation a typical Paranal observatory conditions are used. Right: Effective wavelengths of stars when imaged on the acquisition camera as a function of their H-K color. 65
4.11 The definition of position and parallatic angles on the detector coordinates (X, Y). The position angle (θ_{Pos}) is defined as the clockwise angle measured from the positive Y-direction on the detector coordinate to the vector pointing north on the sky. The parallactic angle (θ_{Par}) is defined as the counterclockwise angle measured from the vector pointing north on the sky to the vector pointing to the zenith. Figure credit: Roe (2002). 66

4.12 ADR shifts as a function of zenith angle at various H-K colors. The left panel in arcsec and right panel in pixels (for the UTs). 67

4.13 Concepts of the Shack-Hartmann wavefront sensing. Top panels: For a plane wavefront incidence on the Shack-Hartmann lenslet, the formed spots on the detector are focused on the optical axis of the each sub-aperture lens. Bottom panels: For an aberrated wavefront, the Shack-Hartman imaged spots are displaced from the reference centers. Figure credit Buscher 2015. 68

4.14 The block diagram for closed loop field and pupil guiding. 71

4.15 Accuracy measurements of the field imager. Left: Absolute error measurement as a function of input field error. Right: RMS error measurement as a function of star magnitude. 73

4.16 Left: a typical pupil tracker image with zero pupil shifts. Middle left: pupil tracker image with lateral shift along X-axis. Middle right: pupil tracker image with lateral shift along Y-axis. Right: pupil tracker image with longitudinally shift. The red-crosses and white-rings are the reference R_j and the barycenter B_j positions respectively. 74

4.17 Left: Lateral pupil shift measurement error scaled to the UT beam. Right: Longitudinal pupil shift measurement error scaled to 80 mm beam. 75

4.18 Wavefront measurement accuracy as a function of the star magnitude, for a 0.7 s integration. 75

5.1 Schematic arrangement of the Fizeau interferometer. A collimated beam generated from a monochromatic light is used to test the target surface. It combines a reference beam (reflected from reference flat) and the target beam (reflected from the test surface, which contains optical aberration) and makes an interferogram on a recording medium (usually a charge coupled device, CCD). Surface quality of the target surface is measured by observing the fringe pattern and the number fringes involved. Figure taken from Z100 user manual. 80

5.2 Left: Optical layout to characterize the lenslets. Right: Fizeau interferometer Intellium Z100 setup's collimated beam is used to test the lenslets. The lenslets are mounted in the optics holder situated above the uEye camera. The uEye camera is focused to the lenslet focal lengths using a vertical translation stage. 81

5.3 The acquisition camera enclosure, folding optics and the beam analyzer mounts as assembled. 82

5.4 Left: Lens mounting using standard vacuum tip-tilt and Z stage and custom mechanics to hold the mount. The lens and mirror mountings, manufactured spring features. Right: stress release lens mounting as manufactured. Figure credit Gordo and Amorim 2015. 82

5.5 Left: pupil lenses. Right: pupil lenses alignment and assembly setup. The lenses can be aligned with the help of laser test beam and a mirror above the pupil lenses allows comfortable operator viewing angle while aligning. The precision linear stage where the tool mounted is used to select any of the four lenses. Figure right panel credit Lima and Amorim 2012. 83
5.6 Simplified beam analyzer as built. It contains only the field imager mode. 84
5.7 Left: cryostat used to cool down the acquisition camera. The theodolite is used to verify the optical alignment at cold temperatures. Right: the acquisition camera installed within the cryostat. Labels in the figure indicate: 1 – LN2 storage tank; 2 – LN2 pipe which transports liquid from the outside dewar to the LN2 tank; 3 – copper straps. 84
5.8 The Arduino micro processor and electronic circuits to receive signals from the temperature sensors and feedback mechanism for the solenoid valve. 85
5.9 Left: Omega controllers display the temperatures of the various sensors that are installed inside the acquisition camera cryostat. In the left panel, the red color represents the temperatures measured in degree Celsius: 1– Beam analyzer; 2–temperature sensor at the mouth of the LN2 tank; 3–the copper strap temperature (cold finer); 4–camera enclosure; 5–temperature sensor at the bottom of the LN2 tank. Right: temperatures (in K) of various sensors are logged and displayed. . . 86
5.10 A schematic view of the optical alignment of the acquisition camera using a theodolite. The theodolite is installed in front of the first entrance channel of the acquisition camera. The mirrors and lenses are aligned by mounting cross-hairs on them and aligning those cross-hairs with the beam analyzer cross-marks. Photo credit: Paulo Gordo. 87
5.11 Left: A typical cross hair glued on the lens. Right: dummy detector with marks. . 88
5.12 Characterizing the focus of the camera with pupil masking technique. The spot shift with and without pupil masking experiment gives the focus error. 90
5.13 Installation of GRAVITY at Paranal Observatory, the Atacama desert, Chile, in October 2015. Photo credit: the GRAVITY consortium. 91

6.1 Real time display panel of the acquisition camera. Each column represents the four imaging modes of it for each telescope. Windows in each column, from top to bottom, are the pupil tracker, the aberration sensor, the pupil imager and the field imager respectively. The top and the bottom circles (size of 2 arcsec) in the field imager window are the FoVs of the pupil tracker and the pupil imager/aberration sensor respectively. 94
6.2 The ordinates left to right represent the measured flux over the windows of the pupil tracker, the pupil imager and the aberration sensor respectively. The flux measured in each window is normalized to its maximum. Abscissas present the position of the target used in the scanning that corresponds to FoV. 96

6.3 Left: The 4 arcsec window is the FoV of the field imager. The red and white rings are the FoVs of the pupil tracker and the pupil imager/aberration sensor respectively. Middle: a typical vignetted pupil tracker window. Right: a typical pupil tracker window filled with an astrophysical target backgrounds. 96
6.4 The lateral pupil position measurement accuracy in absolute error $|L_{\mathrm{x}} - L_{\mathrm{x}_0}|$ as a function of the input lateral pupil shift L_{x_0}. The measurements are scaled to the UT scale. 97
6.5 The field tracker performance. Left: The field tracking error in absolute difference $|\theta_{\mathrm{i}} - \theta_{\mathrm{o}}|$ as a function of true object position θ_{i}. Right: field tracking error in the RMS error of the as a function of target magnitude. 98
6.6 How the target star's flux injection into fiber is dropped-down with unwanted tip-tilts. This plot is generated by observing flux in the fringe tracker beam combiner while manipulating the tip-tilt and piston mirror. 99
6.7 The RMS wavefront error introduced by the aberration sensor while measuring an input wavefront error. 99
6.8 Imaging modes of the acquisition camera. Observations of the astrophysical target Galactic Center with the UTs. 100
6.9 The longitudinal pupil position measurement error in the absolute difference ($|L_{\mathrm{z}} - L_{\mathrm{z}_0}|$) at 80 mm tunnel beam as a function of the input longitudinal pupil position L_{z_0} in meters. 102
6.10 Pupil images obtained before and after closing the loop of the pupil guiding. . . . 103
6.11 Pupil tracker performance (scaled to the UTs) as a function of the magnitude of several target stars. Left to right windows are the lateral pupil residuals along X and Y directions and the longitudinal pupil residuals. 104
6.12 Pupil guiding residuals observed for 60 frames on the night of 19th March 2016. The star is 1 mag for the ATs. The measured lateral pupil shifts are at the UT scale. The longitudinal pupil shift is at 80 mm beam scale. 105
6.13 Field guiding residuals for object (HD 41047, 6.94 mag in H-band) when observed with the ATs. 106
6.14 The field guiding residuals for different stars observed with the UTs. 107
6.15 Defocus measurement. 109
6.16 Aberration sensor focus measurement performance: a) when M2 at position 0; b) M2 at position 0.5; The seeing was 1.5 at arcsec. 110
6.17 The integral controller gain optimization for the field and the pupil guiding. . . . 111
6.18 Shift of target position as a function of color (color changed with the voltage of lamp). The target is realized using the Calibration Unit. P_0 and $P(V)$ are the positions of the target at 1.4 V and V respectively. 114
6.19 Pictures of the author taken during the work at the VLTI console, Paranal Observatory. Photo credit: António Amorim. 115

List of Tables

2.1 Astrometric error at the UT due to field and pupil residuals (using Eq. 2.5). . . . 17
2.2 The beam guiding requirements for the aimed GRAVITY astrometry (for the UTs for a single baseline). 18

3.1 Pupil imager design specifications. 41
3.2 Pupil tracker design specifications. 43
3.3 Aberration sensor design specifications. 44
3.4 The light budget of the acquisition camera optical functions, at $m_{\mathrm{H}} = 13$. 44
3.5 The aberration sensor specifications used in YAO parameter file for its modeling. 49

4.1 Beam guiding errors computed from the end-to-end modelling of the acquisition camera. 76

5.1 Image quality of the acquisition camera. The error in the measurements is less than 5%. 90

6.1 The Strehl ratio, FWHM and pixel scales as built 95
6.2 Beam stabilization control loops for the ATs case 101
6.3 Beam stabilization control loops for the UTs case 101
6.4 Number of failures of the pupil tracker when operated it with bright astrophysical targets 104
6.5 Astrometric residual error comparison: performance using the calibration unit generated laboratory beams and on-sky beams. 112

Appendix A

Thesis context

A.1 CENTRA-SIM research group

CENTRA is a multidisciplinary center for astrophysics and it consists of three research groups: a) Scientific and Space Instrumentation, Modeling (SIM); b) Gravitation in Técnico (GRIT); c) Cosmos and Stars (COSTAR). SIM has offices in Faculty of Sciences, University of Lisbon and Faculty of Engineering, University of Porto. Currently, the SIM research group consists of 3 permanent faculty members, 4 post-docs and 4 PhD students.

My PhD is registered in the Faculty of Engineering, University of Porto. During my PhD, first two years I spent most of my time in Lisbon working on the hardware and later I worked on the software from Porto.

A.2 Research visits and participation in conferences/workshops

During this project, I spent almost 3 months at the Max Planck Institute for Extraterrestrial Physics. The purpose of my visits was the installation, characterization of instrument and software tests. I also traveled to Chile 5 times in 2015 and 2016 as part of the GRAVITY commissioning.

I participated in three high angular resolution schools:

- ESO school, "International PhD School F. Lucchin: Science and Technology with E-ELT", Sicily, Italy, 8-20, October, 2015.
- "8th VLTI summer school: High angular resolution in astrophysics: optical interferometry from theory to observations", Köln, Germany, 6-13, September 2015.
- Santander International Summer School "Reaching the Limits of the Sky", Astronomical Instrumentation in the 21st Century, Santiago, Chile, 17-28, November,2014.

And below are the list of conferences that I attended:

- CHARA, year twelve review, Nice, France, 13-14 March, 2016

- Coimbra Solar Physics meeting "Ground based Solar Observations in the Space Instrumentation Era", Coimbra, Portugal, 5-9 October, 2015.
- Doctoral Symposium on Engineering Physics, Faculty of Engineering, University of Porto, Porto, Portugal, 11-12 June, 2015.
- XXVI Encontro Nacional de Astronomia e Astrofísica (ENAA), Porto, Portugal, 8-9 September, 2014.
- SPIE Astronomical Telescopes + Instrumentation, Montréal, Canada, 22-27 June, 2014.

A.3 PhD funding: acknowledgments

During the first year I was funded by grant from the project "Second Generation Instrumentation for the VLTI" with reference PTDT-CTE-AST/098034/2008 . In January 2013, I was awarded PhD scholarship for a period of 4 years from the International Doctorate Network in Particle Physics, Astrophysics and Cosmology (IDPASC). Both were funded by Fundação para a Ciência e a Tecnologia.

I received 7 times travel grants from Fizeau for the purposes of research work at Lisbon, Garching and Paranal Observatory, Chile and also to attend interferometric schools at Barcelonnette and Köln. They in turn received funding from the European Community's Seventh Framework Programme under Grant Agreement 312430 (OPTICON).

Appendix B

Top level requirements for the acquisition camera

The acquisition camera implements four functionalities: a) field imaging and tracking; b) pupil tracking; c) aberration sensing; d) pupil imager. The top level requirements to achieve the 10 µas are as follows.

B.1 Field imager

- Field of view: 4 arcsec diameter for the UTs.
- Pixel scale: 17.78 mas for the UTs and 78.94 mas for the ATs.
- Image quality: Strehl ratio $> 80\%$ averaged over H-band ($1.45 \cdots 1.85$ µm).
- Object position measurement accuracy: 10 mas RMS error for the 13 mag star H-band for the 1 s exposure at the UTs.

B.2 Pupil tracker

- Wavelength of pupil beacon: 1.2 µm.
- Optics: 2×2 lenslets to image pupil guiding laser beacons.
- Field stop size: 2 arcsec diameter for the UTs.
- Field of view of lenslet: 3.2 m diameter for the UTs.
- Pixel scale: 59.8 mm/pixel for the UTs.
- Image quality of spots: Strehl ratio > 80% .

- Accuracy: a) lateral pupil tracking accuracy better than 4 cm RMS error at the UT pupil (9 mm for the ATs, scale factor between the UTs and the ATs is $8/1.8 = 4.44$); b) longitudinal pupil tracking accuracy better than 1 m RMS error at 80 mm beam. The magnification factor between the UTs and 80 mm beam is $(8/80 \times 10^{-3})^2 = 10^4$.

B.3 Aberration sensor

- Field stop size: 2 arcsec diameter for the UTs.
- Accuracy: Measures quasi-static aberrations better than 80 nm rms for 9th magnitude star per sec at the UT.
- Should provide 28 Zernike polynomial coefficients in the coordinate system of the VLTI lab.

B.4 Pupil imager

- Field of view: 11.2 m for the UTs.
- Field of view of sub-aperture: 4 arcsec diameter for the UTs.
- Pixel scale: 53.9 mm/pixel for the UTs.
- Image quality: Strehl $> 80\%$ averaged over H-band ($1.45 \cdots 1.85\,\mu$m).

Appendix C

First author publications

C.1 Submitted A

MONTHLY NOTICES of the Royal Astronomical Society

Methods for multiple telescope beam imaging and guiding in the near infrared

Journal:	*Monthly Notices of the Royal Astronomical Society*
Manuscript ID	MN-17-4052-MJ
Manuscript type:	Main Journal
Date Submitted by the Author:	19-Nov-2017
Complete List of Authors:	Anugu, Narsireddy; Universidade do Porto Faculdade de Engenharia, Engenharia Física; University of Exeter School of Physics and Astronomy, School of Physics, Astrophysics Group
Keywords:	instrumentation: interferometers < Astronomical instrumentation, methods, and techniques, instrumentation: adaptive optics < Astronomical instrumentation, methods, and techniques, instrumentation: high angular resolution < Astronomical instrumentation, methods, and techniques

SCHOLARONE™ Manuscripts

MNRAS 000, 1–12 (2017) Preprint 19 November 2017 Compiled using MNRAS LATEX style file v3.0

Methods for multiple telescope beam imaging and guiding in the near infrared

N. Anugu,[1,2]★ A. Amorim,[3] P. Gordo,[3] F. Eisenhauer,[4] O. Pfuhl,[4] M. Haug,[4] E. Wieprecht,[4] E. Wiezorrek,[4] J. Lima,[3] G. Perrin,[5] W. Brandner,[6] C. Straubmeier,[7] J.-B. Le Bouquin,[8] and P.J.V Garcia[1]

[1] *Faculdade de Engenharia, Universidade do Porto, rua Dr. Roberto Frias, 4200-465 Porto, Portugal; Centro Multidisciplinar de Astrofísica (CENTRA), Universidade de Lisboa, Portugal*
[2] *School of Physics, Astrophysics Group, University of Exeter, Stocker Road, Exeter EX4 4QL, UK*
[3] *Universidade de Lisboa - Faculdade de Ciências, Campo Grande, 1749-016 Lisboa, Portugal; Centro Multidisciplinar de Astrofísica (CENTRA), Universidade de Lisboa, Portugal*
[4] *Max Planck Institute for extraterrestrial Physics, Giessenbachstr., 85748 Garching, Germany*
[5] *Observatoire de Paris Meudon, 92195 Meudon Cedex, Paris, France*
[6] *Max-Planck-Institut für Astronomie, Königstuhl 17, 69117, Heidelberg, Germany*
[7] *1. Physikalisches Institut, Universität zu Köln, Zülpicher Str. 77, 50937 Köln, Germany*
[8] *Institut de Planétologie et d´Astrophysique de Grenoble (IPAG), Grenoble, France*

Accepted XXX. Received YYY; in original form ZZZ

ABSTRACT

Atmospheric turbulence and precise measurement of the astrometric baseline vector between any two telescopes are two major challenges in implementing phase referenced interferometric astrometry and imaging. They limit the performance of a fibre-fed interferometer by degrading the instrument sensitivity and astrometric measurements precision and by introducing image reconstruction errors due to inaccurate phases. A multiple beam acquisition and guiding camera was built to meet these challenges for a recently commissioned four beam combiner instrument, GRAVITY, at the ESO Very Large Telescope Interferometer. For each telescope beam it measures: a) field tip-tilts by imaging stars in the sky; b) telescope pupil shifts by imaging pupil reference laser beacons installed on each telescope using a 2×2 lenslet; c) higher order aberrations using a 9×9 Shack-Hartmann. The telescope pupils are imaged for a visual monitoring while observing. These measurements enable active field and pupil guiding by actuating a train of tip-tilt mirrors placed in the pupil and field planes, respectively. The Shack-Hartmann measured quasi-static aberrations are used to focus the Auxiliary Telescopes and allow the possibility of correcting the non-common path errors between the Unit Telescopes adaptive optics systems and GRAVITY. The guiding stabilizes light injection into single-mode fibres, increasing sensitivity and reducing the astrometric and image reconstruction errors. The beam guiding enables to achieve astrometric error less than $50\,\mu$as. Here, we report on the data reduction methods and laboratory tests of the multiple beam acquisition and guiding camera and its performance on-sky.

Key words: instrumentation: interferometers, instrumentation: adaptive optics, instrumentation: high angular resolution, atmospheric effects

1 INTRODUCTION

GRAVITY (GRAVITY collaboration et al. 2017A) is a dual feed phase referencing interferometric imaging and a narrow-angle astrometric instrument. It has been built for the ESO Very Large Telescope Interferometer (VLTI) and was born with the aim to monitor stellar sources in the vicinity of the Galactic Centre supermassive black hole (Genzel et al. 2010; Eisenhauer et al. 2011). It combines four beams coherently in the K-band of either Unit Telescopes (UTs, 8 m) or Auxiliary Telescopes (ATs, 1.8 m). It is designed to deliver a differential astrometry of

★ E-mail: narsireddy.anugu@fe.up.pt

© 2017 The Authors

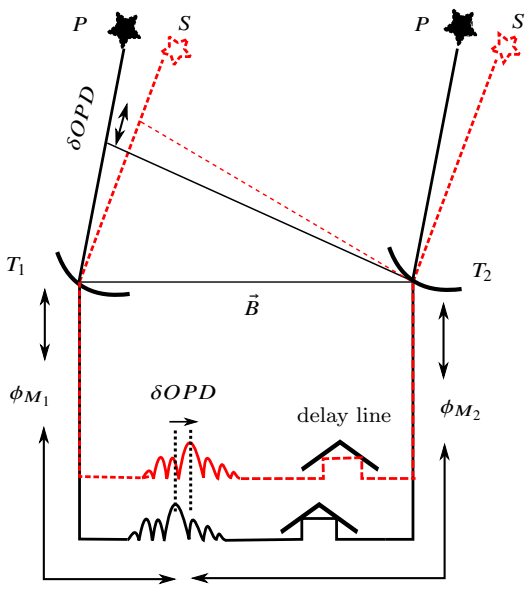

Figure 1. GRAVITY working principle. The beams of science S and reference P stars are combined simultaneously. The GRAVITY metrology system measures the differential optical path between the two stars introduced by the VLTI beam relay and the GRAVITY beam combiner instrument. The ϕ_{M_1} and ϕ_{M_2} are the phases between the beam combiner and the telescopes (T_1 and T_2). $\vec{B}$ is the baseline vector.

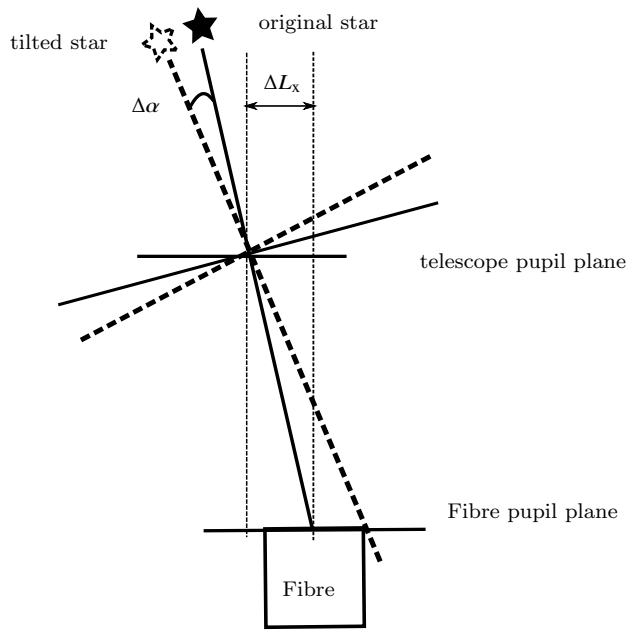

Figure 2. Influence of field drift and pupil lateral shift in the beam while injecting light into a single-mode fibre. The star shown in dashed line is tilted ($\Delta\alpha$) with respect to the original star (solid line). The telescope pupil is shifted laterally (ΔL_x) with respect to the fibre pupil.

around 10 microarcseconds (μas) and an angular resolution of around 4 milliarcseconds (mas). It works by observing a reference star at position $\vec{P}$ and a science star at position $\vec{S}$: fringes for each star are obtained in separate beam combiners (cf. Figure 1). The differential separation of stars in the sky is proportional to the differential optical path difference (δOPD) observed in the beam combiner instrument. To first-order approximation, the differential optical path difference is related to the differential separation of stars and the baseline vector ($\vec{B}$) by

$$\delta OPD = (\vec{S} - \vec{P}) \cdot \vec{B}.$$

The coherent beam combination of star light is implemented using a single-mode fibre-fed integrated optics chip (Benisty et al. 2009; Jocou et al. 2014). The δOPD between the science and reference beam combiners is measured with a dedicated laser metrology system (Lippa et al. 2016; GRAVITY collaboration et al. 2017A).

Adaptive optics correction residuals such as slow field drifts (tip/tilts) and non-common path aberrations and telescope/optical pupil motions[1] (lateral and longitudinal or pupil defocus shifts) are a concern to be corrected. They degrade the performance in terms of: a) instrument sensitivity, because of star's light injection problems into the single-mode fibres in the presence of field drifts; b) astrometric errors due to field drifts and pupil shifts caused baseline paradox (Lacour et al. 2014; Woillez & Lacour 2013; Colavita 2009); c) image reconstruction errors due to inaccurate phases[2].

The astrometric error caused by the presence of field tip-tilts ($\Delta\alpha$), lateral (ΔL_x) and longitudinal (ΔL_z) pupil shifts is (cf. Figure 2, Lacour et al. 2014)

$$\sigma_T \sim \frac{\Delta L_x \sin(\Delta\alpha) + \Delta L_z \left[1 - \cos(\Delta\alpha)\right]}{B} \quad \text{rad.} \tag{1}$$

In order to achieve the GRAVITY goal of 10 μas astrometric precision, the telescope beams must be corrected with residuals in the field to less than 10 mas root-mean-square (RMS) deviation error[3], the lateral pupil to less than 40 mm RMS and the longitudinal pupil to less than 10 km RMS, at the UTs (Lacour et al. 2014). To enable these corrections a four beam imaging and guiding instrument, the multiple beam acquisition and guiding camera, was built.

The paper is presented as follows. In Section 2, the optical layout and functions of the multiple beam acquisition and guiding camera are briefly described. The methods of extraction of the beam guiding parameters from the image are presented in Section 3. Section 4 and 5 present the instrument concepts validation and characterization results at the laboratory and on-sky. The paper ends with a summary and conclusions.

[1] Optical train vibrations cause pupil motions while tracking the object of interest with the delay lines.

[2] Of relevance for, e.g., imaging stellar high signal-to-noise surfaces.

[3] This is given by $\sim 0.2\lambda_K/D$, with $\lambda_K = 2.2\,\mu$m, $D = 8$ m (Lacour et al. 2014).

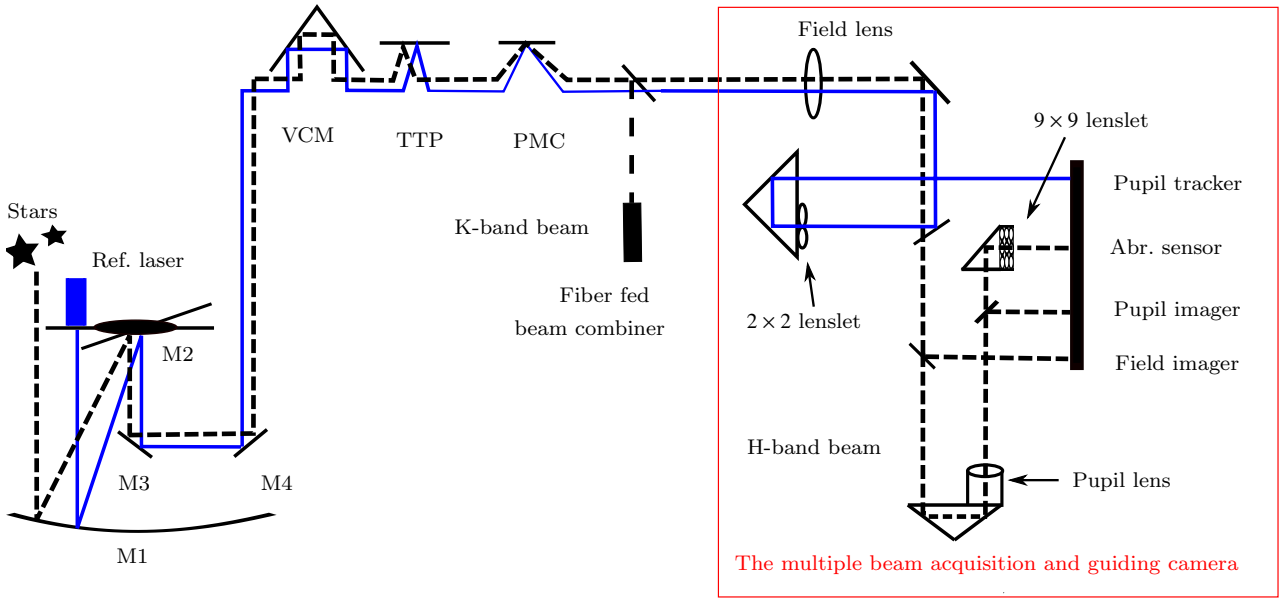

Figure 3. The multiple beam acquisition and guiding camera conceptual scheme. For simplicity, only one telescope beam case is presented. Only the H-band (dashed line) and 1.2 μm wavelength (solid line) are used for beam analysis. The K-band (not indicated) is used for interferometric observations. A dichroic mirror splits the incoming telescope beam and sends H-band and 1.2 μm wavelength beams to the multiple beam acquisition and guiding camera (red box in the Figure). The optical functions: a) pupil tracker; b) aberration; c) pupil imager; and d) field imager. The extracted parameters are used to stabilize the beams and to inject the K-band beam into the fibres using the VCM, TTP and PMC actuators.

2 THE BEAM GUIDING INSTRUMENT OPTICAL FUNCTIONS

2.1 Overall optical layout

The multiple beam acquisition and guiding camera, is a subsystem of GRAVITY. It has two sub-units: a) the external folding optics; and b) the core beam analyser. The folding optics has four optical entrance channels, accepts four 18 mm sized near infrared beams and redirects them into the beam analyser. The beam analyser is the core of the multiple beam acquisition and guiding camera. It implements four important optical functions (cf. Figure 3): a) pupil tracker – measures the telescope pupil shifts; b) aberration sensor – measures quasi-static wavefront aberrations; c) pupil imager – images the telescope pupil; and d) field imager – images the field and measures slow field drifts.

The multiple beam acquisition and guiding camera images are used to stabilize the telescope beams using tip-tilt and piston systems (TTPs), pupil motion controllers (PMCs, Pfuhl et al. 2014) and variable curvature mirrors (VCMs, Ferrari et al. 2003). The tip-tilt and piston systems are actuated mirror controllers placed in the pupil plane of the optical train where incoming beams are propagated. These are used to correct the field drifts. The pupil motion controllers are the pupil lateral shift mirrors located in a field plane of the optical train. They are used to correct the lateral pupil offsets. The variable curvature mirrors are focus/defocus mirrors placed at the image plane in the VLTI delay lines (Derie 2000). These are used to adjust the position of pupil longitudinally (pupil focus correction).

The specifications of the multiple beam acquisition and guiding camera have been defined as a trade-off between the beam guiding requirements (see Table 1) for the key Galactic Centre astrometry program of GRAVITY and the technical constraints (Amorim et al. 2012). The camera is designed to work in H-band wavelengths (1.45-1.85 μm) for the following reasons: a) the Galactic Centre is situated behind $\sim$30 magnitudes of visible extinction (Genzel et al. 2010) and is brighter in the near infrared; b) the VLTI throughput is optimized in the infrared as most of the visible light is fed into the visible wavefront sensors at the transmitted Coudé focus (Arsenault et al. 2003); c) the H-band is as close as possible to the science wavelengths (K-band). To increase stability and to reduce thermally emitted backgrounds, the camera operates at cryogenic temperatures (the detector at 80 K, the beam analyser at $\sim$ 110 K, the external folding optics at 240 K). The core optical functions of the camera are manufactured with a single optical material (fused silica, coefficient of thermal expansion $\sim$ $10^{-6}\,^{\circ}\mathrm{C}^{-1}$) to minimize stresses when it is cooled down to the cryogenic temperature. The optical functions are imaged on a 2048 × 2048 pixel Hawaii-2RG detector (Finger et al. 2008; Mehrgan et al. 2016). The detector is operated in correlated double sampling readout mode with the frame rate of 0.7 s and the readout noise of $13\,\mathrm{e}^{-}\,\mathrm{pix}^{-1}$ RMS error. The optical functions of the beam analyser are detailed in the following sections.

2.2 Pupil tracker

The VLTI pupils are re-imaged via delay lines in the GRAVITY beam combiner instrument. In between the telescope pupil and the GRAVITY fibre-fed beam combiner there exist several optical pupils including the delay lines. The pupils move laterally and longitudinally, due to the

Table 1. UT beam guiding requirements for a m_H = 13 mag star.

Parameter	Value (RMS)
Lateral pupil guiding	≤ 40 mm
Longitudinal pupil guiding	≤ 30 km
Field guiding	≤ 10 mas
Wavefront accuracy	≤ 80 nm

Table 2. Pupil tracker specifications for the UTs.

Parameter	Value
Wavelength	1.2 μm
2 × 2 lenslet	on 2.03 × 2.03 mm
Focal length (f_{PT})	14 mm
Reference beacons separation	1.6 m
Field of view	11.2 m
Pixel scale	59.86 mm pixel^{-1}
Detector pixel size (d_p)	18 μm
Field stop	2″ × 2″

optical train vibrations, while tracking the object of interest. The GRAVITY beam combiner obtains the effective pupil, i.e. the barycentric mean of all these randomly positioned pupil apertures in the whole optical train from the telescope to the beam combiner. The effective pupil is different from the telescope pupil. The typical maximum lateral pupil error is around ~ 5% of the pupil (~ 0.4 m for an 8 m pupil), much larger than the 40 mm required to achieve 10 μas astrometry (see Table 1).

While equalizing the optical paths of the telescopes with the delay lines, the longitudinal pupil position (or pupil defocus) has to be adjusted constantly using the delay line variable curvature mirrors to preserve the field of the VLTI (2″ × 2″, Ferrari et al. 2003). The variable curvature mirror corrects the longitudinal pupil positions (pupil defocus) by adjusting its curvature based on a calibration pointing model. Limitations in the pointing model introduce residual longitudinal pupil drifts. The typical maximum longitudinal pupil error is around 30 km at the UT. Whereas the requirement for the 10 μas astrometry is 10 km (see Table 1). In order to measure these pupil shifts, the pupil tracker was designed (Pfuhl et al. 2012; Amorim et al. 2012).

To detect the pupil motions, the telescope pupil is imaged by a 2 × 2 lenslet. Telescope pupil reference laser beacons (1.2 μm) are used. For each telescope, four beacons are mounted on the four symmetric spider arms (cf. left of Figure 6). The barycentre of these four laser beacon positions gives the centre of the pupil. These telescope pupil reference laser beacons are separated by 1.6 m and 0.4 m diagonally on the UTs and ATs, respectively (cf. Table 2).

Figure 4 (a) and (b) illustrate a case of a laterally shifted pupil, i.e., the 2 × 2 lenslet formed spots are laterally shifted from the reference telescope pupil formed spots. Figure 4 (c) and (d) illustrate a case of longitudinally shifted pupil, i.e., the lenslet formed spots have either converged (L_z < 0) or diverged (L_z > 0) with respect to the reference spots depending on the direction of the longitudinal displacement.

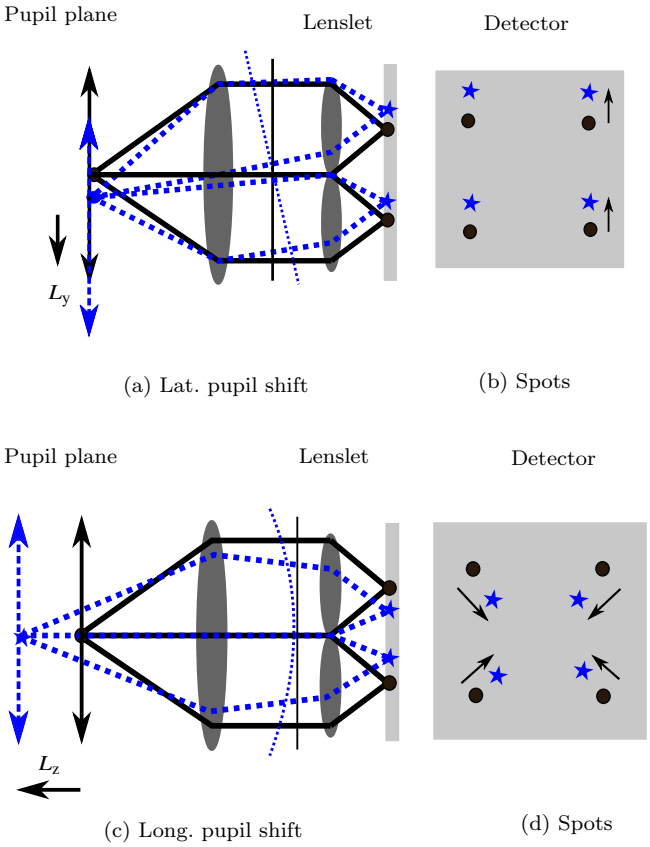

Figure 4. Pupil tracker working principle. The reference telescope pupil and corresponding laser beacon spots are represented by the solid lines in black and filled circles respectively. The shifted pupil and corresponding telescope pupil reference laser beacon spots are represented by dashed lines in blue and star symbols respectively. A typical lateral shifted pupil is presented in panels of (a) and (b). A typical longitudinal shifted pupil is presented in panels of (c) and (d).

Table 3. Pupil imager specifications for the UTs.

Parameter	Value
Wavelength	H-band (1.45-1.85 μm)
Field of view	11.2 m
Pixel scale	54 mm pixel^{-1}
Flux for m_H = 13 mag	1.8×10^4 e$^-$ s^{-1} image^{-1}
Field stop	2″ × 2″

2.3 Pupil imager

The pupil imager is designed to verify the pupil image quality visually (e.g. to identify pupil vignetting or pupil shifts). It is used to align GRAVITY with the VLTI during the commissioning/installation and visually monitor the telescope pupil during observations. It images the telescope pupils using telecentric lenses. Its specifications are presented in Table 3.

Table 4. Field imager specifications for the UTs.

Parameter	Value
Wavelength	H-band (1.45-1.85 μm)
Field of view	$4'' \times 4''$
Pixel scale	17.78 mas pixel^{-1}
Flux for $m_{\rm H}$ = 13 mag star	4.8×10^4 e$^-$ s^{-1}

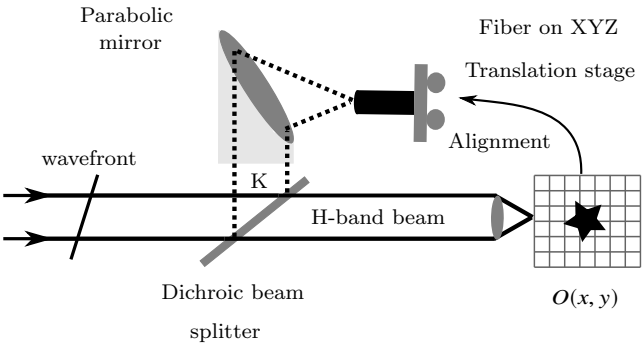

Figure 5. Star light injection into a single-mode fibre.

2.4 Field imager

The UTs are equipped with near infrared wavefront sensors based adaptive optics (CIAO, Scheithauer et al. 2016). The ATs, currently are only equipped with tip-tilt sensors and they will have adaptive optics modules in the near future (NAOMI, Gonté et al. 2016). In both cases, GRAVITY experiences slow field drifts greater than 10 mas due to its correction residuals and the VLTI tunnel seeing effects. The field imager aims to track these slow field motions. Its specifications are presented Table 4. The slow field tracking (with a frequency of 1 Hz) is to be complemented by a fast tip-tilt monitoring system. This system works by injecting the visible tip-tilt laser beacon beams before the VLTI tunnel and by imaging them inside GRAVITY, using the position sensitive diodes (Pfuhl et al. 2014). It will measure the field motions between the telescopes and GRAVITY.

In GRAVITY, single-mode fibres feed light into the integrated optics (Jocou et al. 2014; GRAVITY collaboration et al. 2017A), which implements the actual beams combination. The light injection into these fibres is stabilized by using the field imager measured field drifts (cf. Figure 5). The accurate position of star $O(x, y)$ is detected by the field imager using the H-band beam. Using this position, the single-mode fibre is aligned to the parabola focus with the fibre positioner (Pfuhl et al. 2014). Also using this position, the star light injection into the single-mode fibre is stabilized using the tip-tilt mirror located in front of the incoming beam.

2.5 Aberration sensor

The aberration sensor is designed to detect the quasi-static residuals of the UTs adaptive optics system (Scheithauer et al. 2016). For the ATs, it measures the telescope static aberrations as the ATs are not equipped with the adaptive optics yet. The measured quasi-static aberrations are used, once in a while, to focus the ATs or to correct the non-common path aberrations between the UTs adaptive optics system and GRAVITY. It consists of four Shack-Hartmann sensors, each with 9×9 sub-apertures. Its specifications are presented in Table 5.

Table 5. Aberration sensor specifications for the UTs.

Parameter	Value
Wavelength	H-band (1.45-1.85 μm)
Lenslet	9×9
Field of view per sub-aperture	$4''$
Pixel scale	250 mas pixel^{-1}
Sub-aperture size	16×16 pixel^2
Maximum Zernike order measured	28
Sub-aperture flux for an $m_{\rm H}$ = 13 mag star	760 e$^-$ s^{-1}
Field stop	$2'' \times 2''$

The pixel scale magnification in the field between the UTs and the ATs is 8/1.8 = 4.44, i.e. the field imager 17.78 mas/pixel scale at the UTs becomes 79 mas for the ATs. The pixel scale de-magnification in between the UTs and ATs for the lateral pupil and longitudinal pupil is 1.8/8 = 1/4.44 and $(1.8/8)^2 = 1/4.44^2$, respectively.

3 METHODS FOR BEAM GUIDING PARAMETERS EXTRACTION

3.1 Image acquisition and analysis software

A dedicated real-time software extracts the beams stabilization parameters from the detector images. The software is implemented within the ESO control software framework. It is written in C and C++ using mainly the ESO standard Common Library for Image Processing (CLIP, Ballester et al. 2008) and Common Pipeline Library (CPL, McKay et al. 2004) and installed in the VLT common software. It works on a Linux operating system based instrument workstation and does the image analysis in three steps. Firstly, every 0.7 s it integrates the multiple beam acquisition and guiding camera detector image and stores it in the instrument workstation shared memory. Secondly, it copies the detector image from the instrument shared memory and by analysing the input detector image it evaluates beams tip-tilts, pupil shifts and beam aberrations. These parameters are written to the instrument database and used for the beam stabilization in the closed loop. The multiple beam acquisition and guiding are carried out in real-time on the instrument in parallel to the observations, for all four telescopes.

3.2 Pupil tracking

The lateral and longitudinal shifts of the telescope pupils are translated as tip-tilt and defocus aberrations when imaged on the 2×2 lenslet. The pupil shifts are evaluated by analysing the pupil tracker image in three steps. First, the reference 2×2 sub-aperture spots are generated by illuminating an internal reference laser source, which is implemented by the calibration unit (Blind et al. 2014).

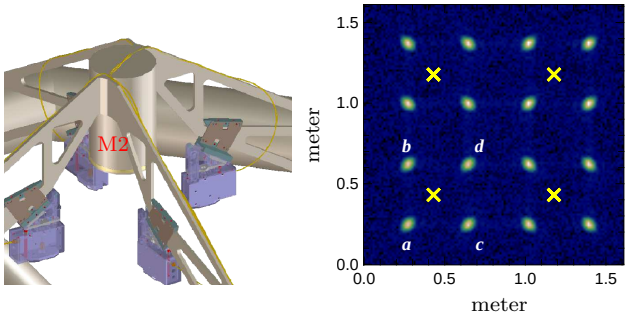

Figure 6. Left: external pupil reference beacons (blue boxes) installed on the telescope secondary mirror M2 spiders. These telescope pupil reference beacons are fed by a common laser diode via multi-mode fibres. Right: A numerically simulated pupil tracker image. The *a*-*b*-*c*-*d* spots are the pupil reference beacons for a sub-aperture. The cross-marks × in the middle are the centres of the lenslet sub-apertures.

Next, each sub-aperture j position $(R_j^{x,y})$ is computed by applying Gaussian fits. Second, the telescope pupil reference laser beacons spots in the detector image (see Figure 6) are identified using a flux threshold ($\sim 5\sigma$ above background) and their full-width-half-maximum (FWHM) thresholds. Next, their positions are computed. From the spot positions, the centre of each sub-aperture $(C_j^{x,y})$ is determined by taking the average of the telescope reference laser beacon positions. Finally, the spot shifts $(S_j^{x,y})$ are computed by comparing them with the internal reference sub-aperture positions $(R_j^{x,y})$

$$S_j^{x,y} = C_j^{x,y} - R_j^{x,y}.$$

The telescope lateral pupil shifts are evaluated by taking the average of these spot shifts along the X and Y directions

$$L_{x,y} = \frac{1}{4}\sum_{j=1}^{4} S_j^{x,y}, \tag{2}$$

The longitudinal pupil shifts are evaluated by computing the amount of convergence or divergence (in radians) of the spot shifts (Eq. 3, Salas-Peimbert et al. 2005)

$$L_z = \frac{d_p}{f_{PT}} \frac{(S_2^x + S_3^x) - (S_1^x + S_4^x) + (S_1^y + S_2^y) - (S_4^y + S_3^y)}{8}, \tag{3}$$

where f_{PT} is the focal length of the 2×2 lenslet and d_p the detector pixel size (cf. Table 2).

3.3 Pupil imaging

The pupil imager is used to visually monitor the telescope pupils for their quality during the preparation for observations and also while observing. However, it can also be used, in future, for the lateral pupil tracking in the presence of a bright astrophysical source. A cross-correlation algorithm (Poyneer 2003) allows computing the pupil shift from a shifted pupil image by correlating it with the reference pupil image.[4]

3.4 Object tracking with the field tracker

The field imager measures these field drifts by tracking the brightest object in the user-specified region (window) of interest. Windowing is important in crowded regions such as the Galactic Centre. The position of the brightest object is computed in two steps. Firstly, stars in the field are scanned using a 5σ flux threshold above background and a predetermined FWHM. Next, the detected stars are sorted in decreasing flux order. Secondly, the accurate position of the brightest object $O(x, y)$ is computed with a Gaussian fit in a window size of 8×8 pixel^2 centred on the object. To track binaries where both stars are of comparable magnitude, the position of the second brightest object within the window is also measured, the tracking reference is chosen by the instrument operator.

The atmospheric differential refraction effects are of relevance because the H-band photo-centre is used to estimate the fibre coordinates to inject the K-band beam into the fibre. The shift (ΔR) caused by the atmospheric differential refraction (e.g. Roe 2002) is

$$\Delta R \simeq 206265'' \left(\frac{n_{\lambda_K}^2 - 1}{2n_{\lambda_K}^2} - \frac{n_{\lambda_{FI}}^2 - 1}{2n_{\lambda_{FI}}^2} \right) \tan\zeta, \tag{4}$$

with λ_{FI} and λ_K the field imager (H-band) and the fibre (K-band) accepting wavelengths, $n_{\lambda_{FI}}$ and n_{λ_K} the corresponding refractive indices and ζ is the object zenith distance. The refractive index for a given wavelength and in function of the observing conditions (temperature, pressure and humidity) is computed using Eq. 1 in Roe (2002).

Since the effective wavelength of the field imager, λ_{FI}, changes with the colour of the object, its value is modelled (Stone 2002) as a function of the H-K colour considering the atmospheric transmission and the instrument transmission[5].

The atmospheric differential refraction object offset (ΔR) correction is applied in real time given the H-K object colour inserted by the observer in the observing block.

3.5 Beam wavefront sensing with the aberration sensor

The reconstruction of the aberrated wavefront is done by comparing the reference Shack-Hartmann spot locations with the aberrated spot locations. The reference spots were obtained as part of the calibration procedure using a collimated beam. During the observations, the spots of incoming telescope beams are acquired. The centroids of these spots are computed by applying Gaussian fits. When an extended scene is observed, the centroids are computed using a cross-correlation algorithm (Poyneer 2003). Slopes

[4] The reference pupil image is the pupil image where one wants to lock the pupil during observations. It can be a long exposure image of the telescope pupil.

[5] Product of all filters transmission, reflection of mirrors and efficiency of the detector as a function wavelength.

Table 6. End-to-end simulation of the guiding parameters accuracy and comparison with the requirements.

Parameter	Requirement (RMS)	Simulation (RMS)
Lateral pupil guiding	40 mm	4 mm
Longitudinal pupil guiding	30 km	200 m
Field guiding	10 mas	2 mas
Wavefront measurement	80 nm	70 nm

of the spots are computed by taking differences between the target to the reference spot positions and these are normalized by the focal length of the lenslet. Using these slopes, higher order aberrations of the input beams are evaluated in terms of Noll's Zernike coefficients (Dai 1996) up to 28 in number.

3.6 End-to-end simulations

A meticulous numerical modelling of the multiple beam acquisition and guiding camera is carried out to verify the beam analysing methods. These simulations are implemented in the `Yorick` [6] programming language for easy interpretation, debugging and plotting. The LightPipes (Vdovin et al. 1997) ANSI C library was ported to `Yorick` and the adaptive optics `yao` (Rigaut et al. 2013) library was used.

The multiple beam acquisition and guiding camera detector images are generated using the optomechanical model parameters (in Zemax, Amorim et al. 2012) and by applying the VLTI laboratory experimentally measured field motions, pupil motions (lateral and longitudinal) and higher order wavefront aberrations. Finally, the input beam aberrations are reconstructed back and characterised the multiple beam acquisition and guiding camera performance in terms of accuracy in the presence of adverse imaging conditions and sensitivity towards the faint stars. Table 6 presents the numerical analysis of the accuracy of the multiple beam acquisition and guiding camera.

4 LABORATORY CHARACTERIZATION

The multiple beam acquisition and guiding camera is characterized using the GRAVITY calibration unit in the MPE laboratory (Blind et al. 2014). The calibration unit simulates an artificial launch telescope designed by a parabolic mirror and two artificial stars with 95% Strehl ratio by illuminating two single-mode fibres. The four telescope pupil reference laser beacon beams are generated by four multi-mode fibres inserted in a pupil plane. Figure 7 presents the imaging modes of the camera, for one telescope, when illuminated by the calibration unit.

The field of view (FoV) of the pupil tracker, pupil imager and aberration sensor are estimated by scanning (applying tilts) a star target over their field of view. During the scanning, the flux and position of the target are recorded in each window. Figure 8 presents the flux in the pupil

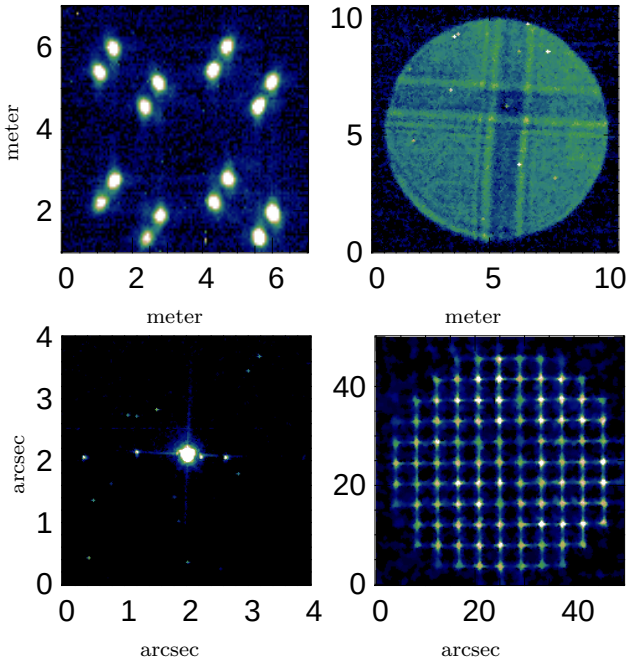

Figure 7. Optical imaging modes of the camera at the laboratory, scaled to the UT magnification. The top panel is the pupil tracker and pupil imager from left to right, respectively. The bottom panel is the field imager and aberration sensor imager from left to right, respectively. The complex structure in the pupil image is laboratory specific (Blind et al. 2014).

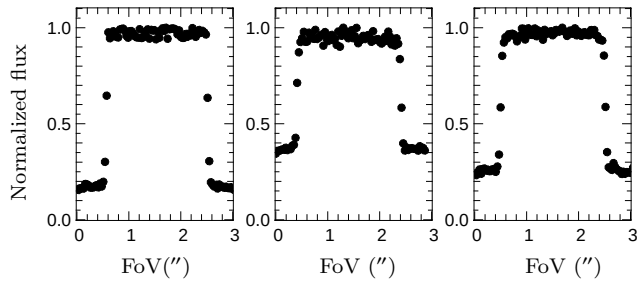

Figure 8. Target normalized flux in function of position for the pupil tracker, pupil imager and aberration sensor windows (from left to right).

tracker, pupil imager and aberration sensor windows as a function of star target position. The field stop of each optical function is apparent in the width of the curves in Figure 8, being $\simeq 2''$. The field stops as built matched the design values (cf. Tables 2,3 and 5).

4.1 Pupil tracking performance

The pupil tracker pixel scale is measured by equating the separation of telescope pupil reference laser beacons observed on the detector to the separation of those beacons installed on the telescope of the calibration unit. The measured value is within 5% of the design value of (Table 2).

The lateral pupil tracking performance is characterized in the laboratory by manipulating the pupil lateral correcting actuators. This experiment is carried out in two steps. First, known lateral pupil shifts are applied to the

[6] http://yorick.sourceforge.net/

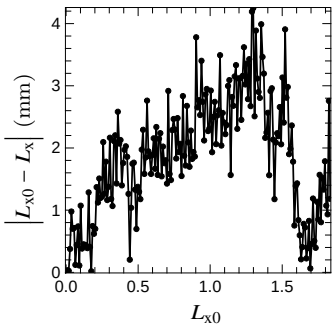

Figure 9. Absolute error in the lateral pupil position measurement (UT beam) as a function of input lateral pupil shift in the laboratory.

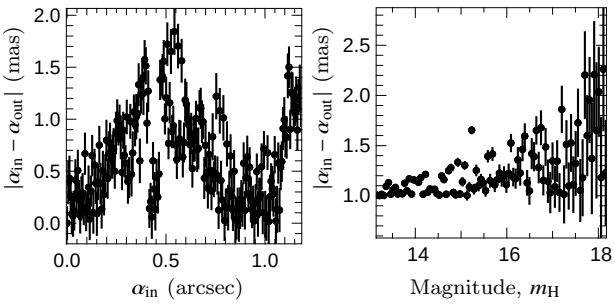

Figure 10. Performance of the field tracker in the laboratory for UT setup. Left: The absolute error as function of true object position. The observed shape is due to the mechanical instability of the tip-tilt correcting system. Right: The absolute error of object tracking as a function of star magnitude, m_H.

incoming beams by actuating the pupil lateral correcting actuators. Second, the input pupil shifts are estimated from the pupil tracker images as explained in Section 3.2. Figure 9 shows that the lateral pupil position measurement performance is in agreement with the end-to-end simulations and 10× better than the requirement. The longitudinal pupil tracking performance could not be characterised at the laboratory, only on-sky (cf. Section 5).

4.2 Field tracking performance

To characterize the performance of the field tracker, a known tip-tilts values α_{in} are applied to the incoming beams and measured them back α_{out} using the field tracker as explained in Section 3.4. The tip-tilts to the incoming beams are applied using the tip-tilt actuators. Figure 10 left panel presents the absolute error of the object position as a function of a known input tilt. The error is less than 2 mas. These measurements are done at high signal-to-noise conditions, i.e., negligible readout noise centroid error contribution. Figure 10 right panel presents the absolute RMS error as a function of the magnitude of a star. An absolute RMS error of 1 mas is observed for the equivalent of a $m_H = 13$ mag star.

Injection performance Figure 11 shows how the injection of star light into the fibre drops with unwanted tilts. From the figure it can also be seen that the size of the fibre core is around 60 mas. Using the field tracker enabled field

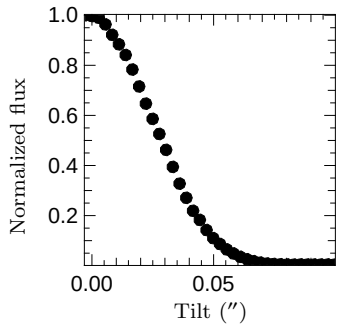

Figure 11. Fibre injection performance at the laboratory.

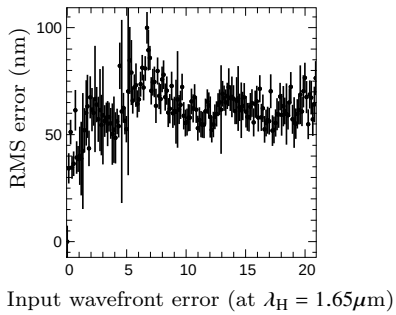

Figure 12. The RMS wavefront error as a function of an input wavefront applied at the laboratory (UT beam).

stabilization the coupling efficiency of the fibre is maintained around 75%.

Atmospheric differential refraction The atmospheric differential refraction offset ΔR (Eq. 4) importance can be computed using the effective wavelengths and a zenith angle $\zeta = 30°$. It is ~ 22 mas (which corresponds ~ 1.23 pixel shift) and corresponds to a ~ 20% loss of injection of light into the fibre.

4.3 Beam aberration sensing and performance

The aberration sensor wavefront estimation performance test is carried out in two steps. First, the focal lengths of the Shack-Hartmann lenslet are calibrated by applying series of tilts to the incoming plane wavefront (Kumar et al. 2013). Second, to measure the accuracy of the aberration sensor, known tip-tilt and defocus wavefront aberrations are applied to the incoming beams and measured them back using the aberration sensor function as explained in Section 3.5. Figure 12 presents the RMS wavefront error observed as a function of an input wavefront (tip, tilt and defocus RMS errors). It can be seen that the wavefront accuracy is $\approx \lambda/20$ at the UT scale. In this experiment a sub-aperture flux equivalent to a $m_H = 11$ mag star (~ 2500 ADU s^{-1}) is used.

5 ON-SKY CHARACTERIZATION

5.1 Image quality characterisation

Based on verification tests at MPE, the GRAVITY instrument passed Preliminary Acceptance Europe (PAE) in May 2015. The instrument was then deployed at the Paranal

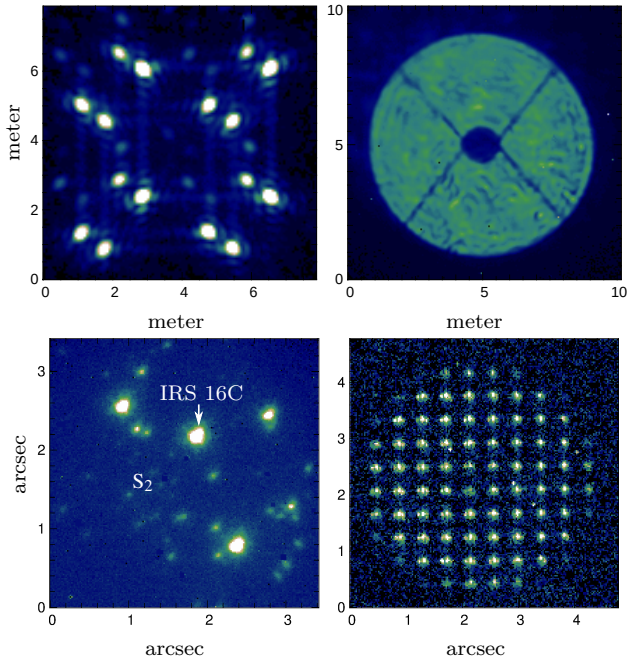

Figure 13. Imaging modes of camera observed on-sky with the UTs. Top (left to right): the pupil tracker and the pupil imager. The low intensity cross stripes visible in the pupil imager are the secondary mirror holding spiders. Bottom (left to right): the field tracker and the aberration sensor. The astrophysical target is the Galactic Centre. The aberration sensor image is rotated counter clockwise to the field image due to a mirror reflection (π phase).

Table 7. The field imager Strehl ratio, FWHM and pixel scales as built (at the UT scale).

Telescope arm	Strehl ratio lab	FWHM at lab (pixel)	Pixel scale at lab (mas pixel^{-1})	Pixel scale on-sky (mas pixel^{-1})
T1	0.90	2.65	18.23	17.77
T2	0.85	3.12	18.51	18.00
T3	0.70	3.18	18.20	17.64
T4	0.63	3.51	18.76	19.53

Observatory, Chile and got its first light in November 2015. Figure 13 presents the multiple beam acquisition and guiding camera detector image acquired on-sky with the UTs. Table 7 presents the Strehl ratio and the star FWHM at the camera, when it was illuminated using the calibration unit. Also, the pixel scale which is measured, at the laboratory and at the Paranal Observatory on-sky, are presented.

The sky field of view of the camera is larger than the nominal VLTI field of view ($2'' \times 2''$). This is confirmed by imaging (long exposures) the sky on the field imager and by moving the VLTI star separator tip-tilt mirrors (FSM, Delplancke et al. 2004) in several steps. Figure 14 presents the VLTI field of view and is around $3.6'' \times 3.6''$ at the UTs. This value is less than the design value $4'' \times 4''$ (cf. Table 4).

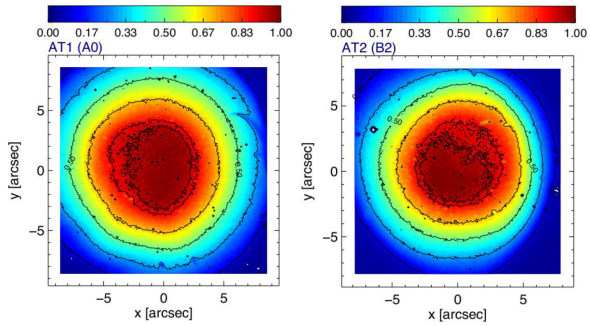

Figure 14. Representative fields of view of the field imager measured at two AT stations. The colour represents the normalised flux.

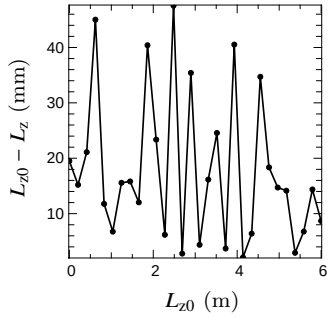

Figure 15. The longitudinal pupil shift residuals as a function of input longitudinal pupil shift (L_{z0}) at the VLTI, for an UT beam.

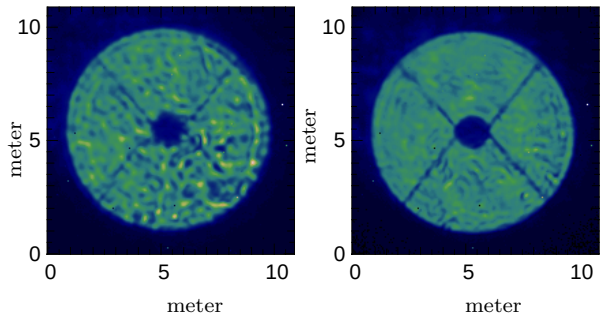

Figure 16. UT pupil images are obtained before (left) and after (right) closing the pupil guiding loop.

5.2 The pupil tracker characterisation

Longitudinal pupil tracking performance is characterized at the VLTI by manipulating the VLTI variable curvature positions (see Figure 15). Known longitudinal pupil shifts (L_{z0}) are applied to the beam by moving the variable curvature mirror and the input shifts are measured back (L_z) using the pupil tracker function as explained in Section 3.2. The longitudinal pupil accuracy is better than 400 m (i.e., 10^4 magnification between the 8 m telescope and 80 mm beam inside the lab). Figure 16 presents the UT pupil, before and after closing the pupil guiding loop. After closing the pupil guiding loop, an improvement of pupil focus can be seen.

Bright target performance The pupil tracker experiences high backgrounds from bright astrophysical

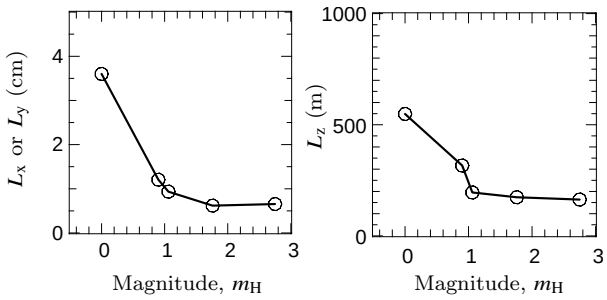

Figure 17. Pupil tracker performance (scaled to the UTs) as a function of the magnitude of several target stars. Left to right panels are the lateral pupil residuals along X or Y directions and the longitudinal pupil residuals.

targets observed in the J and H-bands due to: a) the closeness of the operating wavelengths of the pupil tracker (1.2 μm) and the field imager; b) because of no adequate filter is available for the pupil tracker. The best operation of the pupil guiding is possible when: a) the flux of the telescope pupil reference laser beacons is high; b) imaging a lower magnitude or red coloured astrophysical target (with low flux at 1.2 μm). The background problem is solved to a certain extent on two fronts: a) using the neutral density attenuation filters[7]; b) using the BLINK mode. This mode removes the background by taking two frames with the laser beacons on and off. The exposure with the beacons on is subtracted by an exposure with the beacons off. This efficiently removes the background caused by the astrophysical target. With this mode, the performance of the pupil guiding is improved additionally by 2 magnitudes. The performance of the pupil guiding as a function of target magnitude is presented in Figure 17. The pupil tracker performance degrades significantly for targets brighter than m_H = 1 mag.

5.3 The pupil imager

The pupil imager is, currently, used to visually monitor the telescope pupils for their quality during the preparation for observations and also while observing. However, it can also be used for the lateral pupil tracking in the presence of a bright astrophysical source to complement the problem of the pupil tracker (see Section 3.3).

5.4 The aberration sensor focus calibration

The aberration sensor is used for the focus correction for ATs. Figure 18 shows the aberration sensor focus measurement calibration as a function of the secondary mirror (M2) position (in arbitrary units). The right panel presents the corresponding star FWHM measured in the field imager.

[7] In order to not saturate the camera detector in bright astrophysical targets, GRAVITY is equipped with H-band neutral density attenuation filters (10 and 5 magnitudes) in front of the camera.

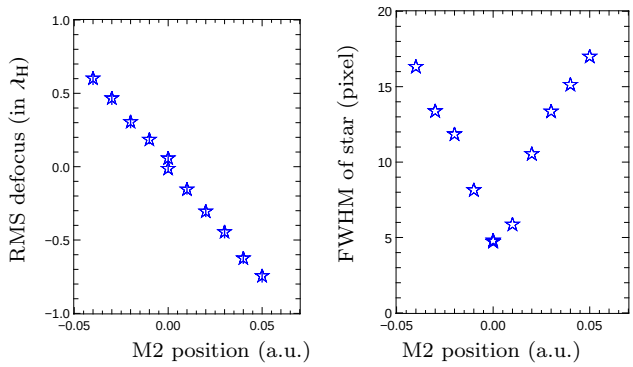

Figure 18. Focusing calibration of the ATs with the aberration sensor. Left: Zernicke defocus coefficient RMS versus M2 focus position (in arbitrary units – a.u.). Right: The corresponding FWHM of a star observed in the field imager.

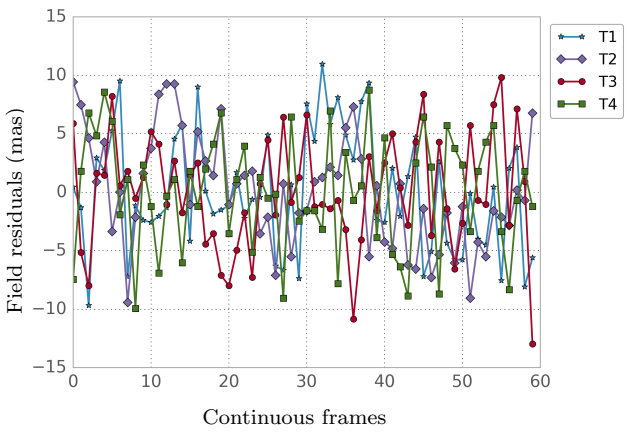

Figure 19. The field guiding residuals for object HD 141742 (m_H = 6.17) when observed with the UTs on 15th September 2016. A neutral density filter of 5 magnitudes was used.

5.5 The field and pupil guiding residuals

The field and pupil beam stabilizations are achieved with two types of actuators. The smaller field and pupil offsets occurring during interferometric observations are corrected in the closed loop using the GRAVITY internal actuators for speed and accuracy. Larger field and pupil offsets, which usually occur during the initial alignment of GRAVITY, are corrected using the VLTI based star separator actuators and delay line variable curvature mirror. If when operating in closed loop the offsets are larger than internal actuators range, they are offloaded to the VLTI star separator actuators.

Often, GRAVITY experiences optical misalignments with the VLTI, in the worst case, the field offsets of ~ 60 mas RMS and lateral pupil offsets of ~5% (0.4 m RMS) in the UT pupil. With the multiple beam acquisition and guiding camera enabled beam guiding, the field, lateral pupil and longitudinal pupil guiding are implemented with standard deviation residuals smaller than ±0.5 pixels RMS (10 mas RMS), ±0.2 pixels RMS (12 mm RMS) and ±400 m RMS at the UT respectively. Figures 19 and 20 present the field and pupil guiding residuals.

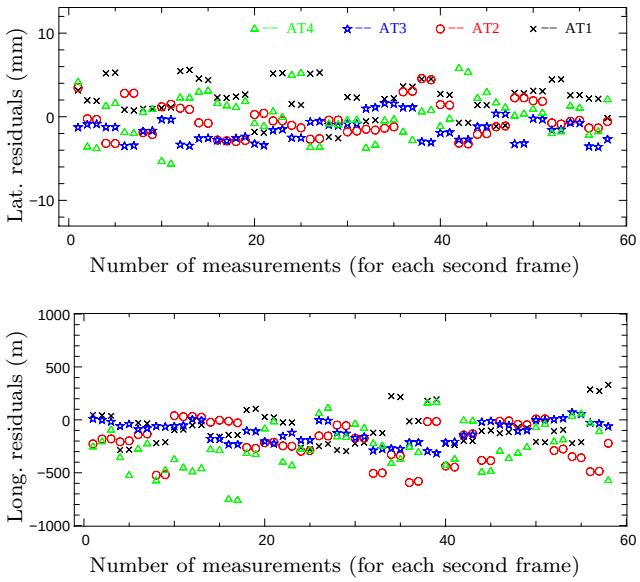

Figure 20. Pupil guiding residuals observed for the ATs, for 60 frames on 19th March 2016. The measured pupil shifts are scaled to the UT scale. The astrophysical target has $m_H = 1.74$. The pupil tracker is operated in the BLINK mode during this experiment.

Table 8. Astrometric error at the UT due to field and pupil residuals.

	Residual errors	One telescope	Four telescopes
Without beam guiding residuals	$\Delta\alpha \leq 60$ mas $\Delta L_x \leq 0.4$ m $\Delta L_z \leq 30$ km	316.6 μas $\delta OPD \leq 153.5$ nm	$\leq 633.3\,\mu$as
Beam guiding requirements	$\Delta\alpha \leq 10$ mas $\Delta L_x \leq 40$ mm $\Delta L_z \leq 10$ km	4 μas $\delta OPD \leq 1.95$ nm	$\leq 8\,\mu$as
Laboratory beam guiding residuals	$\Delta\alpha \leq 2$ mas $\Delta L_x \leq 4$ mm $\Delta L_z \leq 400$ m	–	–
On-sky beam guiding residuals	$\Delta\alpha \leq 10$ mas $\Delta L_x \leq 12$ mm $\Delta L_z \leq 400$ m	1.2 μas $\delta OPD \leq 0.58$ nm	$\leq 2.4\,\mu$as

5.6 Astrometric residuals study

The total astrometric error produced by the four telescopes (ref Eq. 1) adds to

$$\sigma_{4T} = \sqrt{\sum_{i=1}^{4} \sigma_{T,i}^2} \ . \tag{5}$$

The astrometric error caused by the field and the pupil motions is around 633.3 μas and 2.4 μas before and after closing the beam guiding loop, respectively, at the UT and for the baseline of 100 m. Table 8 gives summary of the guiding requirements and the achieved beam guiding is several conditions. The on-sky residuals are larger than the laboratory characterization (using the calibration unit generated beams) results because the multiple beam acquisition and guiding camera frame rate (0.7 s) is not quick enough to correct them.

A GRAVITY observation is described in detail in GRAVITY collaboration et al. (2017A). An animation of starlight tracing through the GRAVITY instrument is available elsewhere[8].

Operation of GRAVITY with the multiple beam acquisition and guiding camera started with the ATs in October 2016 and with the UTs in April 2017. GRAVITY first light and science verification results are published in, e.g., GRAVITY collaboration et al. (2017A,B,C,D); Le Bouquin et al. (2017); Kraus et al. (2017). The first verification of the narrow-angle astrometry of GRAVITY is done with a M-dwarf binary, GJ 65 and estimated the binary separation with residuals of 50 μas (GRAVITY collaboration et al. 2017A). However, the astrometric residual errors can be reduced further by computing the guiding residual errors carefully from the multiple beam acquisition and guiding camera images in off-line in the data reduction pipeline and inputting them into the astrometric calculations. There are also other possible error contributors in the GRAVITY measurements but they are out of the scope of this paper to describe in detail: a) uncertainty in the calibration of the narrow-angle astrometric baseline and wavelength; b) dispersion in the single-mode fibres and integrated optics.

6 SUMMARY AND CONCLUSIONS

Accurate beam acquisition and guiding camera methods for phase referencing optical/infrared interferometry are presented. These methods offer advances in near-infrared imaging and optical/infrared long-baseline interferometry: a) accurate and active pupil and field guiding required for sensitivity and astrometry; b) the characterization of the input telescope beams quality, the focus correction for the ATs and the possibility of correcting the non-common path aberration errors between the adaptive optics system and GRAVITY.

The beam acquisition and guiding camera performance is verified using laboratory generated telescope beams and on-sky at the VLTI. The characterization results show that it is able to analyse the telescope beams: a) field tracking in a crowded field with $\lesssim 10$ mas RMS residuals translates in an 75% coupling efficiency of near-infrared starlight into single-mode fibres b) lateral pupil tracking with residuals less than 12 mm RMS; c) longitudinal pupil tracking with residuals less than 400 m RMS; d) quasi-static higher order wavefront aberration measurements with 80 nm RMS. The multiple beam acquisition and guiding camera measured beam parameters are used in the stabilization of the field, pupil and the ATs focus correction. The pupil imager is used to visually monitor the telescope pupils for their quality during the preparation for observations and also while observing. In overall, the performance of the camera is in agreement with the requirements of the GRAVITY

[8] http://www.eso.org/public/videos/eso1622b/

science programs, although some work is still needed to push the residual errors further down by implementing the post-processing of the multiple beam acquisition and guiding camera images in the data reduction pipeline and also by correcting the non-common path aberration errors between adaptive optics and GRAVITY.

The adaptive optics assisted camera imaging is an asset for the GRAVITY science observations as it provides H-band images of the target using four different telescopes, simultaneously, in parallel to the interferometric observations in the K-band. This imaging can be useful in three ways: a) to extend wavelength coverage in the H-band (1.45-1.85 μm); b) to extend spatial resolution coverage (low resolution images from the field imager and the high resolution images from the interferometric large baselines); c) to solve the 2π interferometric phase wrapping ambiguity[9] using the multiple beam acquisition and guiding camera field images, provided that the camera is astrometrically calibrated (e.g. Yelda et al. 2010).

Although the multiple beam acquisition and guiding camera is a subsystem of GRAVITY, it can be used for other interferometric beam combiner instruments available at the VLTI (e.g. MATISSE, Lopez et al. 2014) for the purpose of an automated alignment with the VLTI and for closed loop tip-tilt guiding. Furthermore, the accurate pupil guiding developed here is of relevance: a) to high-contrast imaging as it requires pupil stabilization enabled extreme adaptive optics (e.g. SPHERE, Montagnier et al. 2007); b) to correct the misregistration of pupils in between the wavefront sensor and the deformable mirror, where they have moving optics in between[10]; c) to the accurate alignment of pupil mask to match the telescope pupil in order to limit the background radiation coming into the spectrographs (e.g. HARMONI, Hernandez et al. 2014). The pupil tracker allows both the telescope pupil rotation and the lateral shifts estimation accurately.

ACKNOWLEDGEMENTS

We thank the technical, administrative and scientific staff of the participating institutes and the observatory for their extraordinary support during the development, installation and commissioning of GRAVITY. Anugu acknowledges FCT and IDPASC-Portugal for his PhD grant SFRH/BD/52066/2012. The research leading to these results received funding from PTDC/CTE-AST/116561/2010, COMPETE FCOMP-01-0124-FEDER-019965, UID/FIS/00099/2013. This research was partially funded by European Commission Seventh Framework Programme, under Grant Agreements 226604 and 312430 (OPTICON Fizeau Programme).

[9] If the two stars separated more than λ/B, they suffer phase 2π wrapping ambiguity.

[10] e.g., the case where the deformable mirror placed at the telescope or the Coudé focus and the wavefront sensor placed inside the beam combiner laboratory

REFERENCES

Amorim A., Lima J., Anugu N., et al., 2012,Proc. SPIE, 8445, 844534, 2012
Arsenault R., et al., 2003, Proc. SPIE, 4839
Ballester P., et al., 2008,ADASS XVII, ASP Conference Series, 394
Benisty M., et al., 2009,A&A, 498, 2, 601-613
Blind N., et al., 2014, Proc. SPIE, 9146, 91461U
Colavita M. M., Wallace J. K., Hines B. E., et al., 1999, ApJ, 510, 1, 505-521
Colavita M. M., 2009, New Astronomy Reviews, 53, 344-352
Dai G. M., 1996, Journal of the Optical Society A, 13, 6, 1218-1225
Delplancke F., et al., 2004, Proc. SPIE, 5491, 1528
Derie F., 2000, Proc. SPIE, 4006, 25-31
Eisenhauer F., et al., 2014, The Messenger, 143, 16-24
Ferrari M., et al., 2003, Proc. SPIE, 4838
Finger G., et al., 2008, Proc. SPIE, 70210
Genzel R., Eisenhauer F., Gillessen S., 2010, Reviews of Modern Physics, 82, 4, 3121
Gonté, F. Y. J., et al., 2016, Proc. SPIE, 9907, 990720
GRAVITY collaboration, et al., 2017, A&A, 602, A94
GRAVITY collaboration, Lopez R. G., et al., 2017, A&A, arXiv preprint arXiv:1709.01348
GRAVITY collaboration, Petrucciet P.-O., et al., 2017, A&A, 602, L11
GRAVITY collaboration, Waisberg I., et al., 2017, ApJ, 844
Hernández E., et al., 2014, Proc. SPIE, 91513F, 9151.
Jocou L., et al., 2014, Proc. SPIE, 9146, 91461J
Kraus S., et al., 2017, ApJ, 835, 1, L5
Kumar M. S., Narayanamurthy C. S., Kumar AS. K., 2013, Optical Engineering, 52, 12
Lacour S., et al., 2014, A&A, 7
Le Bouquin J.-B., et al., 2017, A&A, 601, A34
Lippa M., et al., 2016, Proc. SPIE, 9907, 990722
Lopez B., et al., 2014, The Messenger, 157, 5
McKay D. J., et al., 2004, Proc. SPIE, 5493, 444-452
Mehrgan L. H., Finger. G., Eisenhauer F., Panduro J., 2016, Proc. SPIE, 9907, 99072F
Montagnier G., et al., 2007, Optics Express, 15, 23
Pfuhl O., et al., 2012, Proc. SPIE, 84451U, 8445
Pfuhl O., et al., 2014, Proc. SPIE, 9146, 914623
Poyneer L. A., 2003, Applied Optics, 42, 29, 5807-5815
Rigaut F., et al., 2013, Proc. AO4ELT 3, 2013
Roe H. G., 2002, PASP, 114, 794, 450-461
Salas-Peimbert D. P., et al., 2005 Appl. Opt., 44, 20, 4228-4238
Scheithauer S., et al., 2016, Proc. SPIE, 99092L , 99092L
Stone R., 2002, PASP, 114, 800, 1070-1086
Vdovin G., et al., 1997, Proc. SPIE, 3190, 1997
Yelda S., et al., 2010, ApJ, 725, 1, 331
Woillez J., Lacour S., 2013, ApJ, 764, 1, 109

This paper has been typeset from a TEX/LATEX file prepared by the author.

C.2 Submitted B

MONTHLY NOTICES of the Royal Astronomical Society

Peak-locking in Shack-Hartmann wavefront sensing

Journal:	*Monthly Notices of the Royal Astronomical Society*
Manuscript ID	MN-17-4049-MJ
Manuscript type:	Main Journal
Date Submitted by the Author:	18-Nov-2017
Complete List of Authors:	Anugu, Narsireddy; Universidade do Porto Faculdade de Engenharia, Engenharia Física; University of Exeter School of Physics and Astronomy, School of Physics, Astrophysics Group Garcia, Paulo; Universidade do Port, Faculdade de Engenharia Correia, Carlos; Laboratoire d'Astrophysique de Marseille, Université Aix-Marseille & CNRS
Keywords:	instrumentation: adaptive optics < Astronomical instrumentation, methods, and techniques, instrumentation: high angular resolution < Astronomical instrumentation, methods, and techniques, techniques: image processing < Astronomical instrumentation, methods, and techniques

SCHOLARONE™
Manuscripts

MNRAS **000**, 1–8 (2015) Preprint 18 November 2017 Compiled using MNRAS LATEX style file v3.0

Peak-locking in Shack-Hartmann wavefront sensing

Narsireddy Anugu,[1,2]★ Paulo J. V. Garcia,[1] Carlos M. Correia[3]
[1] *Faculdade de Engenharia, Universidade do Porto, rua Dr. Roberto Frias, 4200-465 Porto, Portugal; Centro Multidisciplinar de Astrofísica (CENTRA), Universidade de Lisboa, Portugal*
[2] *School of Physics, Astrophysics Group, University of Exeter, Stocker Road, Exeter EX4 4QL, UK*
[3] *Aix Marseille Univ, CNRS, LAM, Laboratoire d'Astrophysique de Marseille, Marseille, France.*

Accepted XXX. Received YYY; in original form ZZZ

ABSTRACT
Shack-Hartmann wavefront sensing relies on accurate spot centre measurement. Several algorithms were developed with this aim, mostly focused on precision, i.e. minimizing random errors. In the solar and extended scene community, the importance of the accuracy (bias error due to peak-locking) of the centroid determination was identified and solutions proposed. But these solutions are not practical, especially for real-time systems. To date, no systematic study of the bias error was conducted. This article bridges the gap by quantifying the bias error for different correlation peak-finding algorithms and types of sub-aperture images and by proposing a practical solution to minimize its effects. Four classes of sub-aperture images (point source, elongated laser guide star, crowded field and solar extended scene) together with five types of peak-finding algorithms (1D parabola, the centre of gravity, Gaussian, 2D quadratic polynomial and pyramid) are considered, in a variety of signal-to-noise conditions. The best performing peak-finding algorithm depends on the sub-aperture image type, but none is satisfactory to both bias and random errors. A practical solution is proposed that relies on the anti-symmetric response of the bias to the sub-pixel position of the true centre. The solution decreases the bias by a factor of ~ 7 to values of $\lesssim 0.02$ pix. The computational cost is typically twice of current cross-correlation algorithms.

Key words: Instrumentation: adaptive optics – Techniques: high angular resolution – Techniques: image processing

1 INTRODUCTION

The Shack-Hartmann wavefront sensor is commonly used to measure the wavefront aberrations in astronomical adaptive optics (Tyson 2015), optical testing (Malacara 2007), ophthalmology (Burns et al. 2014) or microscopy (Booth 2014). It consists of a two dimensional (2D) array of micro lenses. For a plane wavefront incidence, the spots are focused on the optical axis of the each micro lens – the reference centres. For an aberrated wavefront, the imaged spots are displaced from the reference centres. The estimation of the spot displacements between the aberrated and the reference spots allows one to retrieve the incident aberrated wavefront profile (Dai 1996)

Correlation algorithms are used to estimate spot displacements when extended sources are present (cf. Rais et al. (2016) for a recent review). The cross-correlation: a) is optimal at lower signal-to-noise ratios (Vijaya Kumar et al. 1992) and; b) is fast and of simple implementation over other methods such as maximum likelihood (Gratadour et al. 2005) and iterative gradient-based shift estimators (Rais et al. 2016); c) has unitary gain (Gratadour et al. 2010). Cross-correlation is applied to measure image displacements for solar adaptive optics (Wöger & Rimmele 2009; Löfdahl 2010; Townson et al. 2015), laser guide star elongated spots (Thomas et al. 2008; Basden et al. 2014) and to extended scene wavefront sensing (Poyneer 2003; Robert et al. 2012). The image displacement is computed by cross-correlating a reference[1] image to the target aberrated sub-aperture image. The correlation algorithm can be implemented either in spatial domain (Löfdahl 2010) or in the Fourier domain (Poyneer 2003; Sidick 2013). In both domains, the image displacement is measured in two steps. In the first step, the cross-correlation between the reference and the target image is computed. In the second step, a sub-pixel peak-finding algorithm is applied to the correlation image (Poyneer 2003). Commonly used peak-finding algorithms in image registration are 1D parabola fitting (Poyneer 2003; Thomas et al.

★ E-mail: narsireddy.anugu@fe.up.pt

© 2015 The Authors

[1] Cf. Basden et al. (2014) for several approaches for reference image generation.

2006; Robert et al. 2012), Gauss fitting (Nobach & Honkanen 2005), centre of gravity, pyramid fitting (Bailey 2003) and 2D quadratic polynomial fitting (Löfdahl 2010). These will be addressed further in the article (cf. Table 1).

Sub-pixel peak-finding in the correlation image is biased towards integer pixels. In adaptive optics, these errors are often referred as systematic bias errors. Methods for their correction are modelling and a posteriori correction (Wöger & Rimmele 2009; Löfdahl 2010; Sidick 2013). These approaches are limited because the bias errors depend on: a) modelling; b) the sub-aperture image characteristics; c) the noise level; d) the combination of correlation and the peak-finding algorithms; making it difficult to model – especially in low signal-to-noise conditions.

In the following, the bias problem of centroid algorithms is addressed. In Sec. 2 the methods used are presented, including a novel algorithm for bias error reduction. The results on the bias performance of several peak-finding algorithms are presented in Sec. 3.1. It is found that no algorithm is simultaneously satisfactory for both bias and random errors. The results on the proposed solution to the bias error are presented and discussed in Sec. 3.2. In Sec. 4 we conclude by recalling the main ideas.

2 METHODS

2.1 Current peak-finding methods

Consider the reference (I_0) and sub-aperture (I_S) images, with size $N \times N\,\mathrm{pix}^2$. The cross-correlation in the image domain (C), is given by

$$C[m,n] = \sum_{i=1}^{N}\sum_{j=1}^{N} I_S[i+m, j+n]\; I_0[i,j], \tag{1}$$

The image displacement in integer pixels is determined from the correlation maximum location, which is at the pixel (x_0, y_0). The sub-pixel image displacement $(s'_x,\, s'_y)$ is estimated by applying 2D centroid algorithms (cf. Table 1 and Sec. 1) to the correlation map $C[m,n]$. In most algorithms only five pixels are used: (x_0, y_0), (x_0-1, y_0) , (x_0+1, y_0) , (x_0, y_0-1) and (x_0, y_0+1). For the 2D quadratic polynomial fit nine pixels instead of five are required for the estimation of the six coefficients. The estimation of s'_y is analogous to s'_x.

The measured displacement s' (in a given direction x or y) by the centroid algorithms is related to the real displacement s by

$$s' = s + \beta + \sigma, \tag{2}$$

where β is the bias error and σ the noise error. As referred in the Introduction these algorithms have systematic errors, the bias error β exhibits a "sinusoidal" variation with an exact shape depending on σ, image and centroid algorithm. In Fig. 1 an example of this bias is presented, in the absence of noise, for a commonly used algorithm. The origin of the bias is well known in the strain measurement community, it is due to the transfer function of the centroid algorithm (e.g. Schreier et al. 2000). For example, the transfer function of the linear interpolation is not unitary but a complex number. Its module and phase changes with interpolation position.

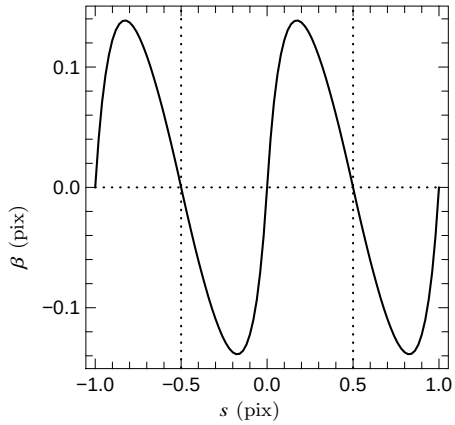

Figure 1. Bias error for a point source with centre of gravity centroid algorithm versus s_x. The shift vector is $\vec{s} = [s, s]^T$, i.e. $s_x = s$.

Therefore a bias in intensity and shift when an interpolation is made (cf. Schreier et al. 2000, for details).

In the presence of noise σ, the bias error β in Eq. 2 is estimated by taking the average of a large number of realizations. The noise error is then significantly reduced and Eq. 2 becomes

$$\langle s' \rangle \simeq s + \beta, \tag{3}$$

where the $\langle\rangle$ denotes average.

The noise error σ is estimated by the square of the standard deviation of the random sample of realizations

$$\sigma^2 \simeq \frac{1}{n-1}\sum_{i=1}^{n}\left(s' - \langle s' \rangle\right)^2, \tag{4}$$

with n the number of realizations.

2.2 Window shift peak-finding algorithm

In the standard approach, the sub-pixel peak centre is determined by directly applying a peak-finding algorithm of Table 1. In this work, a method to reduce the bias error in the peak-finding is proposed. A similar method was previously applied in the context of particle image velocimetry (Gui & Wereley 2002), but to our knowledge, it is presented for the first time in the context of adaptive optics.

It is a two-step method: a) coarse search; b) fine search. In Algorithm 1 the pseudo-code of the method is presented. In the first step (coarse search, lines 2 to 4) the integer pixel maximum location (x_0, y_0) is found. In the second step, (fine search, lines 5 to 19) an image region of interest (I_{ROI}, cf. line 15) is interpolated from the sub-aperture image I_S. The interpolation is made with the same sampling as the original image. At each iteration, the interpolation is done at changing fractional initial positions δ (cf. line 7). Then the correlation between the reference I_0 and each I_{ROI} is computed (cf. line 13). The sub-pixel displacements s' are then obtained using the peak-finding algorithms of Table 1 (cf. line 16). These sub-pixel displacements are then corrected by the step δ introduced during the interpolation (cf. line 17). This process is repeated K times, with varying δ (cf.

Table 1. Sub-pixel (s'_x, s'_y) peak-finding algorithms.

Algorithm
1D Parabola fit (PF): $s'_x = x_0 + 0.5 \times \frac{C[x_0-1, y_0] - C[x_0+1, y_0]}{C[x_0-1, y_0] + C[x_0+1, y_0] - 2C[x_0, y_0]}$
Gaussian fit (GF): $s'_x = x_0 + 0.5 \times \frac{\ln(C[x_0-1, y_0]) - \ln(C[x_0+1, y_0])}{\ln(C[x_0-1, y_0]) + \ln(C[x_0+1, y_0]) - 2\ln(C[x_0, y_0])}$
Pyramid (PYF): $s'_x = x_0 + 0.5 \times \frac{C[x_0-1, y_0] - C[x_0+1, y_0]}{\min\left(C[x_0-1, y_0], C[x_0+1, y_0]\right) - C[x_0, y_0]}$
2D Quadratic polynomial fit (QPF) $(s'_x, s'_y) = \left(x_0 + \frac{2a_1a_5 - a_2a_4}{a_4^2 - 4a_3a_5}, y_0 + \frac{2a_2a_3 - a_1a_4}{a_4^2 - 4a_3a_5}\right)$ with polynomial $f(x) = a_0 + a_1x + a_2y + a_3x^2 + a_4xy + a_5y^2$.
Centre of Gravity (CoG) $s'_x = x_0 + \frac{C[x_0-1, y_0] - C[x_0+1, y_0]}{3\min\left(C[x_0-1, y_0], C[x_0+1, y_0]\right) - \left(C[x_0, y_0] + C[x_0+1, y_0] + C[x_0-1, y_0]\right)}$

line 7). Because K correlations took place, s' is a vector of K elements. The individual displacements $s'[k]$ are affected by the bias β. This bias is "sinusoidal" and anti-symmetric, with period 1 pix, as referred in Fig. 1. The algorithm then takes the average of all K displacements (cf. line 19), which approximately cancels out the bias.

For computational efficiency the cross-correlation C is not computed in all pixels but only for a sub-image of size $5 \times 5\,\mathrm{pix}^2$ centred in the maximum, generating a cropped version of the cross correlation: C_5. Simulations show that the centroid algorithms behave similarly for C and C_5.

The combination of the original pixel grid based conventional correlation (in a large field of view) and a sub-image grid correlation within a small field of view, warrants a high dynamic range shift determination to the algorithm.

2.3 Synthetic sub-aperture images

Four types of sub-aperture image models of relevance for astronomical adaptive optics were used: a) a point source diffracted spot; b) a laser guide star elongated spot (Schreiber et al. 2009); c) a crowded field image; d) a solar photosphere image (Löfdahl 2010). The simulation of the point source and the laser guide star are realized using 2D Gaussian profiles (circular $2 \times 2\,\mathrm{pix}^2$ and elliptical $3 \times 6\,\mathrm{pix}^2$ with a 45° rotation angle, respectively). The crowded field sub-aperture images are obtained by shifting and adding circular Gaussian profiles of varying intensity. To model the sub-aperture solar photosphere image, a Swedish Solar Telescope solar granulation image is used[2]. All the sub-aperture images are Nyquist sampled and have a size of $16 \times 16\,\mathrm{pix}^2$. The synthetic sub-aperture images are presented in Fig. 2.

[2] http://www.isf.astro.su.se/gallery/

The synthetic image shifts (s) due to atmospheric tilts are generated as follows. For the point source, laser guide star and crowed field the shifts s are directly applied to the Gaussian profiles. The original solar image has a factor of 10 larger sampling than the one used for the sub-aperture images. The original image is shifted and blurred to the target Nyquist resolution by convolving it with a PSF. The resulting image is binned to generate a $16 \times 16\,\mathrm{pix}^2$.

Due to the extended and low contrast nature of the solar image, the cross-correlation algorithm is slightly adapted. The mean intensity is subtracted from the reference and sub-aperture solar images because their linear intensity trend (low contrast) can shift the correlation centre from its correct position (Löfdahl 2010).

Noise is added to the synthetic sub-aperture images. For all images a Gaussian read-out-noise (σ_R) of $1\,\mathrm{e}^-\,\mathrm{pix}^{-1}$ is assumed, in line with new generation detectors (Finger et al. 2014; Feautrier et al. 2016). Each synthetic image was generated with counts in each pixel following Poisson statistics. The total image signal-to-noise ratio (SNR) is calculated as

$$\mathrm{SNR} = \frac{N_\mathrm{e}}{\sqrt{N_\mathrm{e} + \sigma_\mathrm{R}^2 N_\mathrm{P}}}, \tag{5}$$

where N_e and N_P are the total number of electrons and pixels in the sub-aperture image. For reference, $N_\mathrm{e} = 5\times10^3\,\mathrm{e}^-$, corresponds to a 9.5 magnitude H-band star with integration time of 10^{-2} s, when a 9×9 lenslet and a 8 m class telescope considered. For the solar image case $N_\mathrm{e} = 5 \times 10^4\,\mathrm{e}^-$ corresponds to a SNR = 104.

Data: Reference image I_0; sub-aperture image I_S; sub-sampling scale K.
Result: Unbiased sub-pixel shift $\langle s' \rangle$.

```
begin
    Coarse search;
    C[x, y] = Correlation(I_S; I_0);
    (x_0, y_0) = FindCentreInteger(C);
    Fine search;
    for k = 1 to K do
        δ = (k − 1)/K;
        for i = x_0 − 2 to x_0 + 2 do
            x = Range2D(i − N/2 + 1 + δ; i + N/2 + δ; N);
            for j = y_0 − 2 to y_0 + 2 do
                y = Range2D(j − N/2 + 1 + δ; j + N/2 + δ; N);
                I_ROI = Interpolate2D(I_S; x; y);
                C_5[i, j] = Correlation(I_ROI; I_0);
            end
        end
        s' = FindCentre(C_5);
        s'[k] = s' − δ //remove input shift applied to I_ROI at interpolation step;
    end
    ⟨s'⟩ = Average(s'[k]);
end
```

Algorithm 1: Window shift peak-finding algorithm. The function `FindCentre` is one of the peak-finding algorithms presented in Tab. 1. The function `Range2D`(a, b, N) creates a square 2D mesh from (a, a) to (b, b), with N^2 pixels. Other functions are self-explanatory. In Section 2.2 the algorithm is explained in detail. The I_{ROI} has image dimensions as I_0.

3 RESULTS AND DISCUSSION

3.1 Performance of current peak-finding method

3.1.1 No noise case

To study the bias, synthetic sub-aperture images displaced horizontally at known positions s are generated. In this section, the sub-aperture images have no noise. The positions s varied from -1 pix to 1 pix, in steps of 0.05 pix. For each synthetic image, the correlation centres s' are computed with the conventional cross-correlation as described in Sec. 2.1. Then the peak-finding algorithms of Table 1 are applied to estimate the position s'. The biases are then simply $\beta = s' - s$. For completeness, the bias is also presented for the determination of s' with the centre of gravity algorithm directly (i.e. without the correlation) in the sub-aperture images point source and elongated laser guide star. The results are presented in Fig. 3, for the four types of sub-aperture images.

It is found that the bias are anti-symmetric ($\beta(-x) = -\beta(x)$) for all sub-aperture images as expected. It is periodic for the point source, laser guide star and crowded field images. But not periodic for the solar image. This non-periodicity is due to the extended scene nature of the image. When a shift is applied different parts of the image enter the field of view of the sub-aperture. Therefore the solar image does not have $\beta = 0$ pix at $s = \pm 0.5$ pix. The exact shape of the bias curve depends on the centroid algorithm and also on the nature of the image. In the $[-0.5, 0.5]$ pix interval the bias extreme values are located approximately at $s = \pm 0.25$ pix for all images except the laser guide star[3].

Sharp transitions are observed for extended sub-aperture images at pixel positions $s = \pm 0.5$ pix. This is due to the shift vector being diagonal: $\vec{s} = [s, s]^T$, which translates in the peak of the correlation being "split" into two diagonal pixels. When the shift s is, e.g. 0.4 pix, the brighter pixel is in the lower left one and the bias is negative. When the shift is e.g. 0.6 pix, the brighter pixel is the top right and the bias is positive.

The best performing centroid algorithm depends on the image: a) for the point source and crowded field, it is the Gaussian fit; b) for the solar image it is 2D quadratic polynomial; c) for the laser guide star it is the centre of gravity. The reason for this behaviour is the matching of the algorithm to the actual shape of each image correlation centre (e.g. point source and crowded field are generated with circular Gaussians).

3.1.2 Varying signal-to-noise ratio

The centroid algorithms' performance was tested in varying SNR conditions. For each SNR, 500 random realizations are generated at an input shift vector $\vec{s} = [s_{\max}, s_{\max}]^T$ where the bias is approximately maximum: a) $s_{\max} = 0.25$ pix for the point, crowded field and solar images; b) $s_{\max} = 0.4$ pix for the laser guide star image. Note that the exact maximum location depends on the algorithm and therefore $s_{\max}$ is approximate. The input shifts are measured by applying the conventional cross-correlation (Eq. 1) and centroid algorithm (cf. Table 1). The bias and SNR are computed using Eq. 3 and Eq. 4, respectively. The SNR is varied via N_{P} in the sub-aperture images.

The results are presented in Fig. 4. The first column presents the RMS centroid error (σ). It is computed by the RMS of s'. It decreases with SNR as expected. The direct image centre determination via the Centre of Gravity algorithm has a worse behaviour for the point source and laser guide star than the correlation algorithms. The superiority of the correlation with respect to σ is well known in the literature (e.g. Thomas et al. 2006). Intuitively it is expected because of the noise smoothing and shape matching. All correlation algorithms have a similar behaviour.

The centre column of Fig. 4 shows that $|\langle s' \rangle - s|$ increases to an asymptotic value, the bias error β. $|\langle s' \rangle - s|$ is not constant because at low SNR the effective image shape changes. Intuitively the low value of $|\langle s' \rangle - s|$ at low SNR can be explained by a pure noise image, for which the bias is expected to be zero. The large values of $|\langle s' \rangle - s|$ for the low SNR of the solar image (centre column, bottom row of Fig. 4) are due to the large variance of $|\langle s' \rangle - s|$ for this sub-aperture image. The large bias for the laser guide star

[3] The shape of the β curve for the laser guide star is due to applying shift $\vec{s} = [s, s]^T$ along the diagonal of the image. For a horizontal shift, it would have a similar shape as the point source and crowded field.

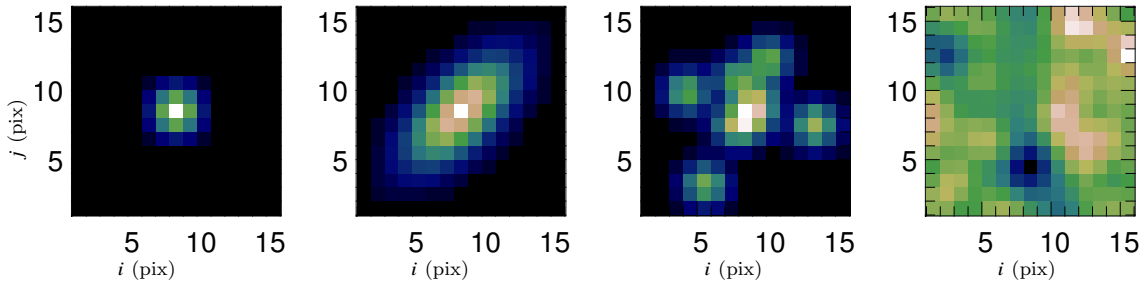

Figure 2. Synthetic Shack-Hartmann sub-aperture images. From left to right: a) the point source; b) the elongated laser guide star (LGS); c) the crowded field; d) the solar photosphere.

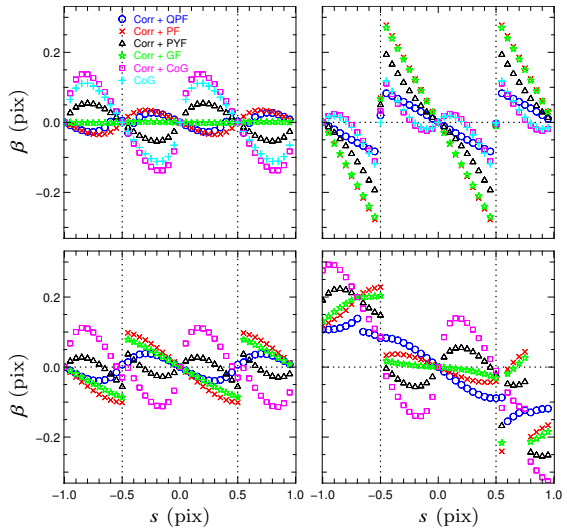

Figure 3. Bias errors for various peak-finding algorithms and sub-aperture images. The algorithm colour/symbol legend is presented at the top left panel, cf. Table 1 for abbreviations translation. The "Corr +" label is used when the algorithm is applied to the correlation image. Sub-aperture images are: point source (top left); laser guide star (top right); crowded field (bottom left); and solar photosphere (bottom right). The shift vector is $\vec{s} = [s, s]^T$. The top left (point source) and right (laser guide star) images also include the results for direct application of the Centre of Gravity algorithm to the sub-aperture images, plus signs labelled "CoG".

in comparison to others is caused by the shape of the correlation peak, which is elongated and oriented 45° rotation angle.

The right column of Fig. 4 plots $|\langle s' \rangle - s|$ versus σ. The dashed line is the imaginary curve $|\langle s' \rangle - s| = \sigma$. Points above the curve show a bias error larger than the centroid error. Typically the bias error is larger than the noise error for SNR larger than 10, except for the solar case where it becomes important for SNR larger than 200.

3.2 Performance of the window shift method

In this section the performance of the algorithm introduced in Section 2.2 is presented, initially for a fixed SNR and then for a varying SNR.

3.2.1 *Fixed signal-to-noise ratio*

Fig. 5 shows the comparison of the window shift method with the conventional cross-correlation algorithm. One of the worst performing centroid algorithms – the centre of gravity – was used. The SNR conditions are the same as in Section 3.1.1. The sampling factor is $K = 5$. The window shift method drastically reduces the bias. For the solar image the final bias is larger, because the shift will include pixels from the edge of the image that are not present in the reference image.

3.2.2 *Varying signal-to-noise ratio*

The performance of the window shift method as a function of SNR is presented in Fig. 6. The same setup as the one presented in Section 3.1.2 is used (e.g. s position). The sampling factor is $K = 5$. The residual errors are well below 0.05 pix for all SNR and sub-aperture image type.

The performance is similar to the windowed, adaptive thresholding centre of the mass method of Townson et al. (2015)[4].

3.2.3 *Varying sampling factor K*

The effect of the sampling factor K in reducing the bias β of the centroid algorithm is presented in Fig.7. The setup is the same as Section 3.2.1, except for the sampling factor K, which varied. The centre of gravity algorithm was used considering its better performance against lower SNR for point, crowded field and solar images.

The bias β strongly decreases with the sampling factor K. It approximately follows a $\propto K^{-1}$ relation. For sampling factors $K > 5$–6 no significant improvement is observed. This behaviour is similar to the one observed by Gui & Wereley (2002) in a different context.

3.2.4 *Computational efficiency*

Several number of factors can influence the total execution time of the algorithm, importantly, the sub-aperture window size, the efficiency of programming, the performance

[4] Note that a different SNR metric is used in Townson et al. (2015), i.e. in their Figure 7 a SNR of 20 corresponds to an SNR ~ 100 in our Figure 6.

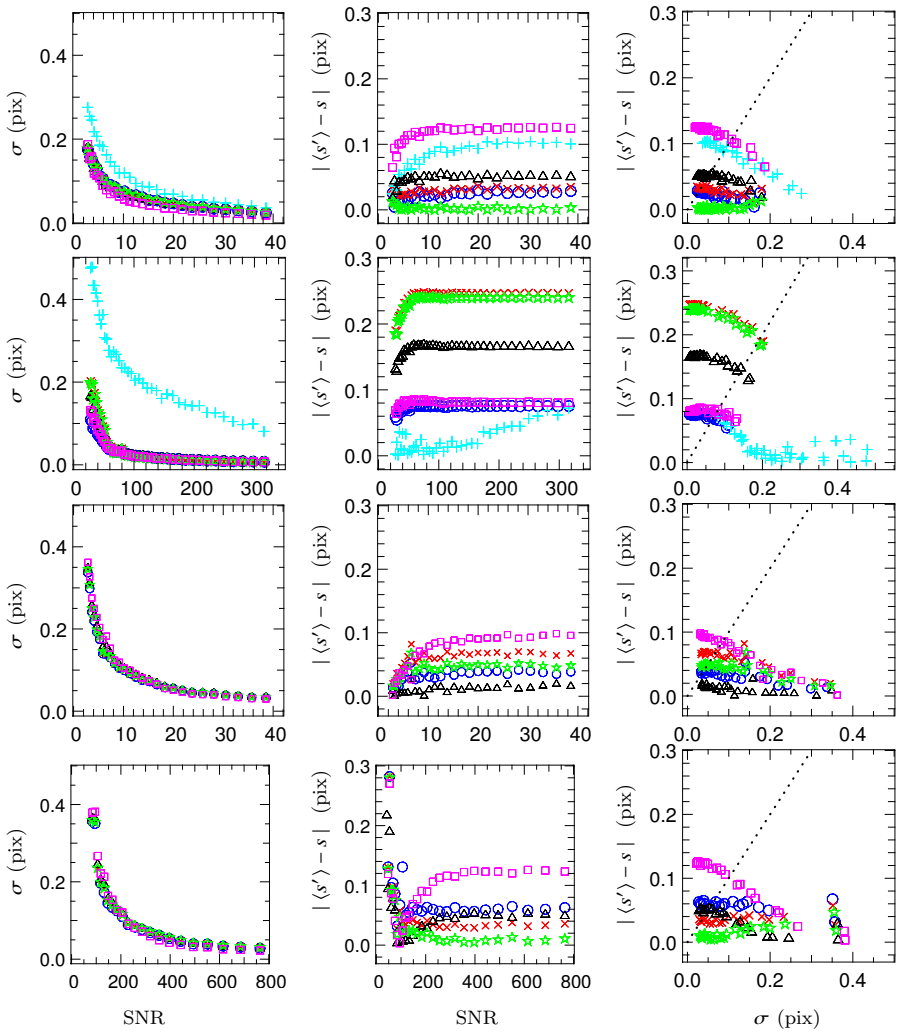

Figure 4. Performance of centroid algorithms with SNR. Left column: RMS centroid error σ; centre column: $|\langle s' \rangle - s|$, which coverages to bias error β at high SNR; right column $\langle s' \rangle - s$ versus σ. The dotted line in the right column traces $\langle s' \rangle - s = \sigma$. The algorithm colour/symbol legend is the same as presented in the top left panel of Fig. 3. The rows from top to bottom are: point source, laser guide star, crowded field, solar image, respectively. The dotted line in the last column is where bias error and random error is equal. The data points above this dotted line indicate bias error domination over random error.

of hardware and the programming language. Therefore only the relative the computational efficiency was computed. It was found that the proposed window shift method is 2.5 times slower in comparison to the conventional algorithm for $K = 3$. For the large sub-apertures, the computational time ratio is reduced because the window shift method uses a fixed and small correlation sub-image C_5. If the sub-aperture size is increased from $16 \times 16\,\text{pix}^2$ to $32 \times 32\,\text{pix}^2$ the window shift method is only 1.4 times slower.

4 CONCLUSIONS

A systematic study of the bias error in conventional centroid algorithms used for slope measurement in Shack-Hartmann wave-front sensors is presented for the first time. It is found that the bias can be of the same order of magnitude of the centroid error, especially at moderate and high signal-to-noise ratios. No centroid algorithm is good enough for reducing both the bias and the RMS centroid error in conventional correlation methods. A window shift method is proposed based on the anti-symmetric nature of the bias. It works by sampling K times the sub-aperture image, at the same resolution, but shifted by a sub-pixel step, with size function of K. The obtained K shifts are then averaged out, significantly cancelling the bias. The window shift method is studied in function of image type, centroid algorithm, SNR and K sampling factor. It is found that it robustly reduces the bias to percent level of a pixel. The computational cost of the algorithm is optimized by obtaining the correlation in a small region C_5, being roughly twice of conventional approaches.

The window shift method can be applied to other algo-

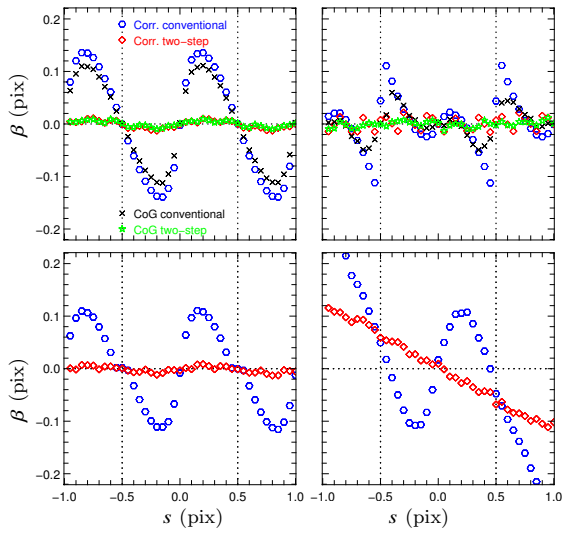

Figure 5. Bias errors of the window shift method in comparison with the conventional approach. The algorithm legend is presented at the top left panel. Sub-aperture images are: point source (top left); laser guide star (top right); crowded field (bottom left); and solar photosphere (bottom right). The shift vector is $\vec{s} = [s, s]^T$. The top row also includes the performance for direct sub-aperture images (labelled CoG).

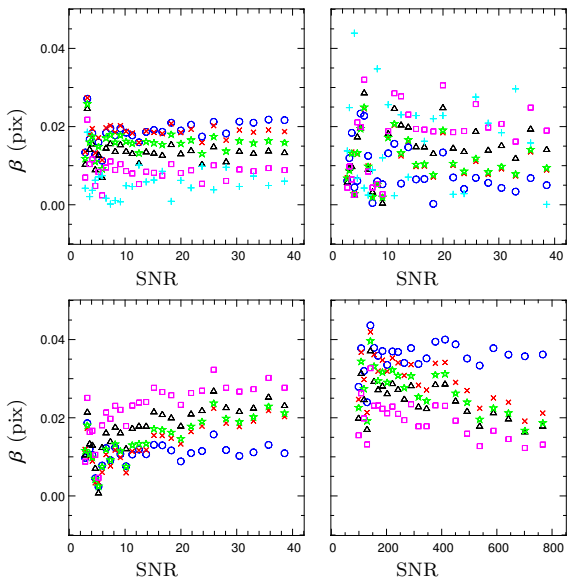

Figure 6. Residual bias errors for window shift method as a function of SNR: point source (top left); laser guide star (top right); crowded field (bottom left); and solar photosphere (bottom right). The algorithm colour/symbol legend is same as in Fig. 3.

rithms which work similar to the cross-correlation algorithm such as square difference function, absolute difference function and square of the absolute difference function (Löfdahl 2010). The square difference function is especially important for the solar type of images as it gives a significantly smaller random error and more anti-symmetric pattern of systematic error (Löfdahl 2010). However, the systematic error values are larger in a comparison to the cross-correlation. The proposed method would be of relevance for the square difference function to reduce its systematic error by using its nice anti-symmetric pattern.

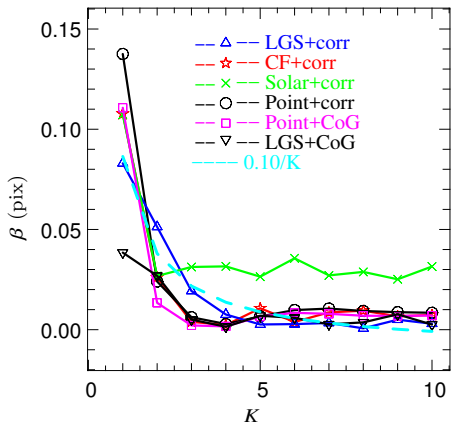

Figure 7. Performance of the window shift method as a function sampling factor K. The curves are for: point source, laser guide star (LGS), crowded field (CF) and solar image. The dashed curve depicts the function $\beta(K) = 0.1/K$.

Further developments are the study of the window shift algorithm for sub-aperture images that have a sampling smaller than the critical sampling and for Shack-Hartmann devices with a small number of apertures, such as those used for fast tip-tilt correction or pupil tracking.

ACKNOWLEDGEMENTS

We are grateful to Lancelot, J. P and Akondi, V for commenting and proof reading of the manuscript. Fundação para a Ciência e a Tecnologia (FCT) (SFRH/BD/52066/2012; PTDC/CTE-AST/116561/2010) and the European Commission (EC) (Grant Agreement 312430). CMC wishes to acknowledge A*MIDEX project (no. ANR-11-IDEX-0001-02) funded by the French Government programme "Investissements d'Avenir", managed by the French National Research Agency (ANR).

REFERENCES

Akondi, V. & Vohnsen, B. 2013, Ophthalmic and Physiological Optics, 33, 434-443

Bailey, D. G. 2003, in Proceeding of Image and Vision Computing New Zealand, 414-419

Basden, A. G., Chemla, F., Dipper, N., et al. 2014, MNRAS, 439, 968

Booth, M. J. 2014, Light: Science & Applications, 3, e165

Burns, S. A., Elsner, A. E., Chui, T. Y., et al. 2014, Biomedical Optics Express, 5, 961

Dai, G.-M. 1996, Journal of the Optical Society of America A, 13, 1218

Feautrier, P., Gach, J.-L., & Bério, P. 2016, Proc. SPIE, 9907, 990715

Finger, G., Baker, I., Alvarez, D., et al. 2014, Proc. SPIE, 9148, 914817

Gratadour, D., Mugnier, L. M., & Rouan, D. 2005, A&A, 443, 357
Gratadour, D., Gendron, E. & Rousset, G. 2010, J. Opt. Soc. Am. A 27, A171
Gui, L., & Wereley, S. T. 2002, Experiments in Fluids, 32, 506
Löfdahl, M. G. 2010, A&A, 524, A90
Malacara, D. 2007, Optical shop testing (John Wiley)
Nobach, H. & Honkanen, M. 2005, Experiments in Fluids, 38, 511
Poyneer, L. A. 2003, Appl. Opt., 42, 5807
Rais, M., Morel, J. M., Thiebaut, C., Delvit, J. M.& Facciolo, G. 2016, In Journal of Physics: Conference Series, 756, 1
Rigaut, F. & Van Dam, M. 2013, Third AO4ELT Conference - Adaptive Optics for Extremely Large Telescopes, 13173
Robert, C., Michau, V., Fleury, B., Magli, S., & Vial, L. 2012, Optics Express, 20, 14, 15636
Schreiber, L., Foppiani, I., Robert, C., et al. 2009, MNRAS, 396, 3, 1513
Schreier, H. W., Braasch, J. R., & Sutton, M. A. 2000, Optical Engineering, 39, 11
Sidick, E. 2013, Appl. Opt., 52, 26, 6487
Thomas, S., Fusco, T., Tokovinin, A., et al. 2006, MNRAS, 371, 1, 323
Thomas, S. J., Adkins, S., Gavel, D., Fusco, T., & Michau, V. 2008,MNRAS, 387, 173
Townson, M. J., Kellerer, A., & Saunter, C. D. 2015, MNRAS, 452, 4022
Tyson, R. K. 2015, Principles of adaptive optics, 4th Edition, CRC Press
Vijaya Kumar, B. V. K., Dickey, F. M., & Delaurentis, J. M. 1992, Journal of the Optical Society of America A, 9, 5, 678
Wöger, F. & Rimmele, T. 2009, Appl. Opt., 48,1, A35

This paper has been typeset from a TEX/LATEX file prepared by the author.

U.Porto Journal of Engineering, 1:2 (2015) 45-51
ISSN 2183-6493

Received: 28 January, 2015
Accepted: 9 March, 2015
Published: 1 December, 2015

C.3 UPJE2015

A low cost auto-filling and refrigeration rate regulated liquid nitrogen controller for near infrared instruments

Narsireddy Anugu[1], Antonio Amorim[2], Paulo Garcia[1], Paulo Gordo[2], Tiago Frederico[2], Jorge Abreu[2]

[1]SIM-Faculdade de Engenharia da Universidade do Porto, 4200-465 Portugal; [2]SIM-Faculdade de Ciências da Universidade de Lisboa, 1749-016, Portugal; (narsireddy.anugu@fe.up.pt)

Abstract

Liquid Nitrogen is one of the key refrigerating elements in cooling near infrared science instruments to reduce the dark, readout noises and thermal emissions in the near infrared originated from the instrument structure. Usually, a small liquid nitrogen tank connected to the near infrared instrument is auto filled from a large Dewar in order to maintain required low temperatures during the experiment for several hours. The detectors used in these instruments are quite expensive and they need to be cooled down steadily (< 2K/min) to avoid mechanical damage. The steady state cooling of the detector is the key requirement to be considered while cooling down the detector. In this paper, a controller is developed to auto-fill the liquid nitrogen tank and also to keep the refrigeration rate of the detector below 2K/min. A systematic survey of auto-filling controllers is studied. The auto-filling of liquid nitrogen from Dewar to tank is implemented with a standard on-off controller. To address the critical refrigeration rate of the detector, two approaches are studied: a) by fixed time pumping; b) by feedback the detector cooling rate. In this work we have used inexpensive equipment to develop this controller. It is very successfully used for GRAVITY acquisition camera, a near infrared instrument for European Southern Observatory. This controller has been stable and efficient for our experiment. This low cost controller can be used for any student laboratory and research.

Subject Headings. Thermodynamics, Astronomy, Optics, Electronics.
Author Keywords. Liquid Nitrogen, Liquid Level Controllers, Refrigeration Rate, Beam Analyzing, Near Infrared Astronomy.

1. Introduction

Liquid Nitrogen (LN_2) is one of the most common cooling agents in near infrared astronomical instruments. For example, acquisition camera (Gordo et al. 2014) is a multiple telescope's near infrared beams analyzing instrument which is refrigerated with LN_2. The advantages of keeping near infrared instruments at low temperatures are to minimize detector's readout and dark noises and it also reduces thermal emissions in the near infrared originated from the instrument structure. The acquisition camera, a sub instrument of GRAVITY(Eisenhauer et al. 2011), is designed to operate at LN_2 temperatures. GRAVITY is a beam combiner instrument, which combines four very large telescopes (8 m) beams of European Southern Observatory (ESO) and delivers very precise astrometric measurements of stars positions in the vicinity of Milky Way Galactic Center supermassive Black Hole (Gordo et al. 2014). The acquisition camera instrument has been built (optical alignment and assembly) at room temperature. However, before it integrating within GRAVITY instrument, it requires a refrigeration system to validate its optical performance at LN_2 temperature.

The acquisition camera optical performance evaluating experiments at LN_2 temperatures are usually carried out for a few days (Gordo et al. 2014). The optical experiments consist of mainly measuring how well the optics is focused and characterization of the system performance. During the course of the experiment, the instrument must be maintained at LN_2 temperatures. It can be achieved by having a thermal connection between the acquisition camera to a cold finger of a LN_2 tank within a cryostat (Carvas 2012). In order to reduce time and effort of filling the LN_2 tank manually, it is automatically filled from large a LN_2 Dewar. Detectors (ex: Hawaii 2RG) used for the infrared instruments are usually expensive and those need to be refrigerated steadily (< 2K/min rate) in order to ensure their safety. It is the critical requirement that needs to be taken care of while filling automatically the LN_2 tank.

A lot of research has been reported on reliable and efficient auto-filling (Landis, Madden, and Goulding 1986; Gamblin, Goldberg, and Scag 1959; Murray and Atkinson 2004; Shuhua Ma et al. 2010; Morrell and Manning 1996; Zhao Yiding and Song Zengfeng 2010). Landis et al., Gamblin et al., Murray et al. and Morrel et al. describes an on-off control method, and Shuhua et al. & Zhao et al. reports a proportional-integral-derivative (PID) based control method for auto-filling. The standard auto-filling controllers do not address the detector refrigeration rate (R, R < 2K/min) during the cooling down process. However, commercially available Lakeshore cryogenic temperature controller (model 350) offers solution to the steady state refrigeration of the detector. This controller is equipped with heaters to warm the detector in order to keep the detector refrigeration rate below its critical limit. But these controllers are relatively expensive.

In this context, it was motivated to develop a low cost controller which can automatically fill LN_2 tank efficiently by taking care of the detector refrigeration rate under control during cooling down process. As far as we know, a low cost detector refrigeration rate regulated auto filling system has not yet reported elsewhere, hence reported here.

The content of this paper is organized in three main sections. The Sec. 2 briefly summarizes the controller's concept and design. The designed controller hardware and software implementations are presented in Sec. 3 and 4.

2. Control operation and design (auto-filled + detector refrigeration rate regulated)

To auto-fill the LN_2 tank, a standard on-off controller (Morrell and Manning 1996) is chosen for its low cost and easy implementation. In the on-off control method, LN_2 is pumped for a time and stopped abruptly for another time. When pressure is applied to the Dewar, the liquid stored in it is transferred into the LN_2 tank which is placed inside the cryostat via a LN_2 delivery pipe. The flow is usually controlled by a solenoid valve (S). The on-off controller time periods are coded in a processor and the valve is opened and closed based on that processor signal. The operation of the on-off controller system is shown in Fig. 1 left panel.

The liquid level in the tank can be detected by mounting two temperature sensors within it. One is at the bottom (A_0) of the tank and second one is at its inlet (A_1) as shown in Fig. 1. The temperature controller issues "ON" signal when a temperature sensor detects the temperature of LN_2 (set point 77K). That is when it is fully submerged within LN_2, otherwise it gives a zero voltage "OFF" signal. Utilizing these two sensor signals (ON/OFF states), liquid level in the tank can be estimated. Based on that, instructions are sent to the solenoid valve to transfer LN_2 from Dewar to the tank. LN_2 transfer flow chart is presented in Table. 1. In the filling process, the liquid is allowed to flow until the inlet (A_1) sensor is submerged in LN_2.

In other words, when the valve is open and if the tank is fully filled, the control valve is automatically shut.

In order to keep the critical detector refrigeration rate under control (< 2K/min) during the cooling down process, it is studied in two ways. Firstly, the detector refrigeration rate is calculated for every 1 s and feedback to the solenoid valve control. Secondly, the control valve is opened and closed for a fixed interval of time to fill the tank, in cycles, as a step function. The time period is chosen such that the detector refrigeration rate is always below 2K/min during the cooling down process.

Sensor A_0	Sensor A_1	LN_2 level	Filling state
OFF	OFF	empty	fill
ON	OFF	partially filled	fill
ON	ON	full	don't fill

Table 1: The on-off control opens the solenoid valve to fill when the liquid level falls below the inlet sensor (A_1)

The time period is mainly dependent on pressure applied to Dewar in order to flow LN_2, amount of liquid in the tank, diameter of the LN_2 delivery pipe and the cold finger. The fixed time value can be measured in two ways. Firstly, it can be estimated using empirical calculation. The empirical time period calculation involves considering the specific heats of the material used in the system and liquid pumping flow rate (lit/s). Secondly, the fixed time can be calibrated from a cool down experiment. The calibration involves experimenting different time periods to obtain an optimized value. Once the time period is chosen, the hardware cannot be altered.

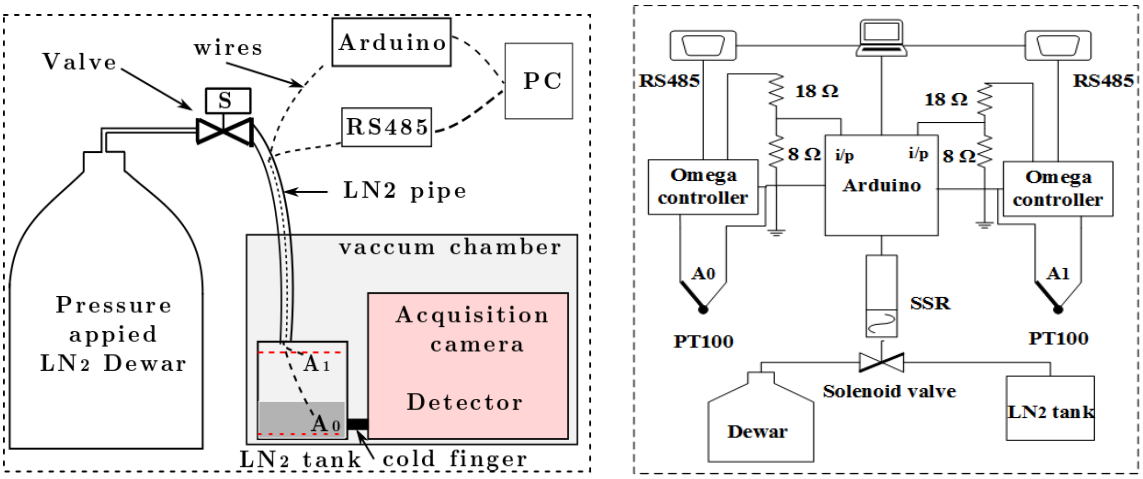

(a) (b)

Figure 1: (a) LN_2 auto filling from Dewar to tank is transferred via solenoid valve. (b) The circuit diagram of the controller. The valve is controlled by an Arduino by utilizing level detection sensors signals

The detector refrigeration rate controller performance is dependent on choosing appropriate fixed time period (T) or refrigeration rate limit (R) properly, in the above mentioned algorithms. The refrigeration rate does not go to zero immediately when the valve is closed but it takes time to reach it. The reason is cooling inertia. Taking this effect into count, a fixed time period and a refrigeration rate limit parameters are essential to be appropriately employed in the control process. In this work, the fixed time period is evaluated from the calibration experiment as shown in Figure 2. The detector refrigeration rate limit is taken as 1.5 K/min.

3. Control Hardware

The on-off controller hardware consists of a Dewar, a valve, a liquid carrying pipe, LN_2 level detecting sensors in the tank, a solid state relay and a processor as indicated in Morrell and Manning 1996 and shown in Fig. 1 right panel. While choosing the hardware, preference is given for a simple circuit and for a low cost solution.

The acquisition camera vacuum cryostat is built in-house (Carvas 2012). A Dewar of 100 liters of capacity is already available was used. Two LN_2 level detecting temperature sensors (PT100) are mounted in the LN_2 tank. These sensors are connected to Omega controllers (CN7800) using LN_2 insulated wires. The sensor temperatures are read by the Omega controller. The Omega controller delivers ON/OFF voltages to a processor (an Arduino UNO) after comparing the temperature detected inside the tank to a user input set point temperature (77 K). The Arduino utilizes these two level detecting sensor inputs and estimates the liquid filling valve state (open/close). The Arduino estimated valve state is fed to a solenoid valve with the aid of solid state relay (Crydom DC60S7). When the valve is open, it transfers the LN_2 into the tank as shown in Figure 1.

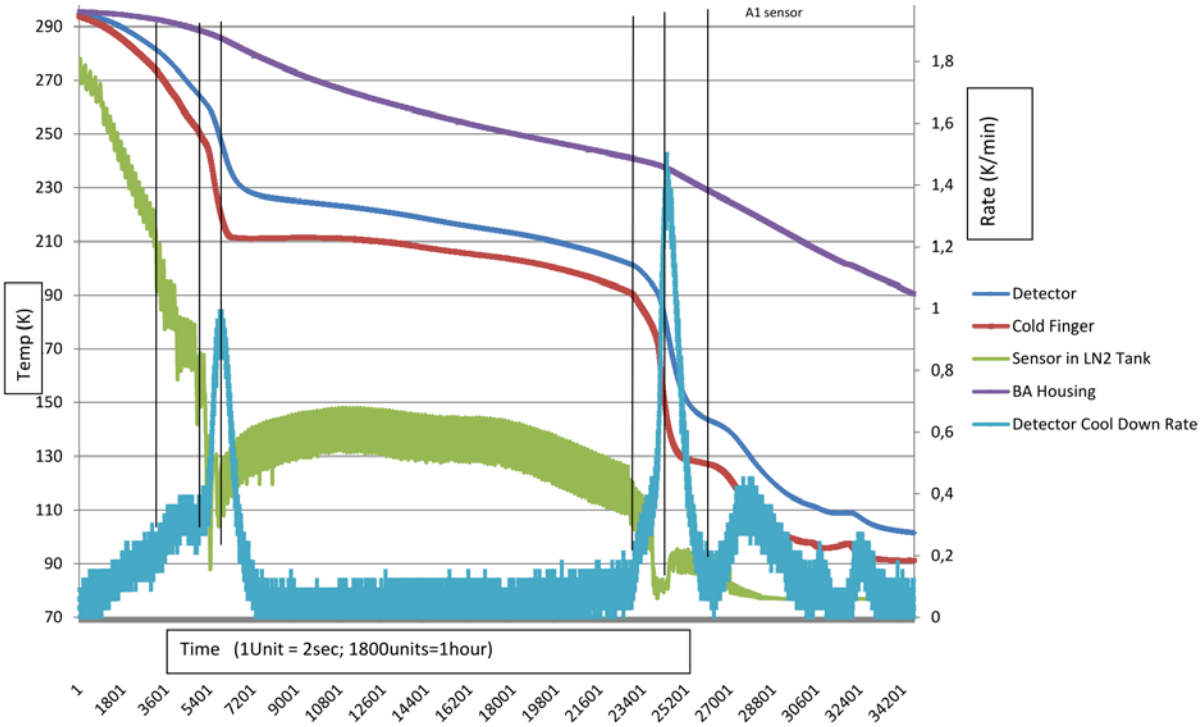

Figure 2: The temperatures of sensors attached at detector, cold finger, inside the LN_2 tank and BA housing are presented. BA housing represents the core optics of acquisition camera. The detector cooled down/refrigeration rate is controlled to 2K/min limit

The detector temperatures are monitored using the ESO delivered Lakeshore cryogenic temperature monitor (model 224). This model only senses detector's temperature and it does not equip with heaters. Utilizing the Omega controller RS485 serial port communication, the liquid level detection sensors (A_0 and A_1) and instrument temperatures are logged on a PC by using a FTDI device (USB-COM485-PLUS4).

4. Control Software

A Tcl-Tk and C combined software is written to read the temperatures of the level detection sensors (A_0 and A_1) and detector's temperature for every 1 s. The level detection sensors temperatures and detector temperature are acquired using Omega controller RS485 serial port communication and using a Lakeshore temperature monitor respectively.

Using detector temperature for every 1 s, the detector refrigeration rate (K/s) is computed and plugged into the Arduino software environment. Utilizing the both detector refrigeration rate and level detection sensors inputs, the Arduino software evaluates the final valve filling state.

In other approach, the valve is opened for 1 min and closed for 4 minutes to steadily refrigerate the detector by keeping refrigeration rate below 2K/min. These two time periods are empirically calculated from a cooling down calibration as shown in Fig. 2. In this experiment different possibilities of time periods are kept under verification. From this, found out that 1 min opening and 4 min closing of valve are the best possibilities to auto fill the LN_2 tank by maintaining the detector refrigeration rate below 2K/min. While this fixed time period filling process is running, the tank is maintained without overflow. When the tank is full, the filling process is delayed to the next iteration of filling.

The software also handles the controller of failure cases. In case of the Dewar is run out of the LN_2, the software detects it by evaluating the inlet temperature sensor (A_1) signals. Because the liquid level in the tank is being dropped down for every 1 second. In this case, the filling process is automatically terminated after checking 5 minutes of no liquid filling. The same case is repeated if any temperature sensors are broken for any reason.

In order to understand the system behavior in case of system malfunction and to quantify the instrument experimental performance at a desired temperature, the liquid level detection sensors delivered temperatures, the detector cooling rate, and liquid filling enabled instructions are logged and monitored for every 1 s. These parameters are displayed in the lab using a graphical user interface as shown in Fig. 3. The instrument temperatures and detector cooling rate are plotted using Zabbix software and accessed remotely using a simple browser.

5. Discussion

The temperature controller developed in this work has successfully auto-filled and maintained the level of LN_2 in between upper and lower limits as previously reported by Morrell and Manning 1996 and Murray and Atkinson 2004. Along with this, controller kept the detector refrigerate rate under control (< 2K/min) during the cooling down process which is the critical requirement. It is the main and key outcome of the work and it is achieved with a low cost. So far, it is satisfactory with the performance in comparison to expensive commercially available controllers (example, Lakeshore model 350). This controller is successfully used for the acquisition camera optical performance validating experiments (Gordo et al. 2014) of GRAVITY project.

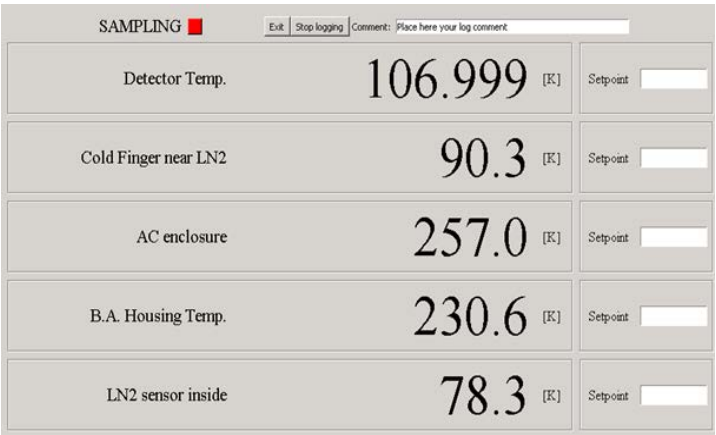

Figure 3: A graphical user interface (GUI) is developed to monitor the temperatures of different parts of the instrument during the cooling down process

The fixed time and detector refrigeration rate limit are the critical parameters that need to be employed properly in order to refrigerate the system in a steady state and by keeping the detector refrigeration rate under control. The detector cooling rate feedback based controller is more efficient in performance in comparison to the fixed time period based controller. Reasons are the following: The rate of liquid transfer via valve is dependent on the pressure (0.5 bar) applied to the tank and the amount of liquid stored in it. When the fixed time period opening based controller is in operation, the liquid is pumped in large amounts in the beginning. But as the time goes on, the rate of liquid transferred by the valve is kept reduced and as a result the system gets warmer which is not desirable. Furthermore, the fixed time period controller requires a few calibration cool down experiments in the begging in order to choose the optimized fixed time value.

Some improvements can be developed to the current design. Currently the fixed time period is programmed in the beginning of control process. In order to address a uniform pumping rate during the cooling down process, it is envisaged to develop software which can accept flexible different fixed on-off timing lengths in the middle of the control process.

6. Conclusions

The developed controller is able to auto-fill the LN_2 tank and also keeps the detector refrigeration rate under control during the cooling down process. This controller has withstood a large number of temperature cycles and it is reliable and efficient for our experiment. This controller is developed with a reasonable simple circuit and at low cost. It can be easily adaptable to research and student laboratory experiments.

Anugu acknowledges FCT for his PhD grant SFRH/BD/52066/2012. Thanks to J. Lima, J. Castanheira and A. Dias help in the laboratory. Special thanks to P. Carvas for helpful discussions. Authors would like to extend thanks to the anonymous reviewers for their valuable comments and suggestions to improve the manuscript.

References

Carvas, Pedro. 2012. “A Infra-Estrutura de Teste Da Câmara Multi-Telescópio Do GRAVITY.” http://repositorio.ul.pt/handle/10451/9109.

Eisenhauer, F., G. Perrin, W. Brandner, C. Straubmeier, K. Perraut, A. Amorim, M. Schöller, et al. 2011. “GRAVITY: Observing the Universe in Motion.” *The Messenger* 143: 16–24. http://adsabs.harvard.edu/abs/2011Msngr.143...16E.

Gamblin, Rodger L., Ernest Goldberg, and Dane T. Scag. 1959. “Liquid Nitrogen Liquid Level Controller.” *Review of Scientific Instruments* 30 (5). AIP Publishing: 371. DOI: 10.1063/1.1716629.

Gordo, Paulo, Antonio Amorim, Jorge Abreu, Frank Eisenhauer, Narsireddy Anugu, Paulo Garcia, Oliver Pfuhl, et al. 2014. “Integration and Testing of the GRAVITY Infrared Camera for Multiple Telescope Optical Beam Analysis.” In *SPIE Astronomical Telescopes + Instrumentation*, edited by Jayadev K. Rajagopal, Michelle J. Creech-Eakman, and Fabien Malbet, 91461V. International Society for Optics and Photonics. DOI: 10.1117/12.2056572.

Landis, D. A., N. W. Madden, and F. S. Goulding. 1986. “A Reliable Automatic Liquid Nitrogen Filling System.” *IEEE Transactions on Nuclear Science* 33 (1). IEEE: 399–402. DOI: 10.1109/TNS.1986.4337129.

Morrell, C., and P.P. Manning. 1996. "An Automatic Liquid-Nitrogen Filling System for Use with Solid-State X-Ray Detectors." *Nuclear Instruments and Methods in Physics Research Section A: Accelerators, Spectrometers, Detectors and Associated Equipment* 381 (2-3): 560–66. DOI: 10.1016/S0168-9002(96)00741-3.

Murray, Andrew J, and Steven Atkinson. 2004. "An Automatic Controller for Filling and Maintaining Liquid Nitrogen Levels in Dewars." *Measurement Science and Technology* 15 (5): N31–34. DOI: 10.1088/0957-0233/15/5/N01.

Shuhua Ma, Junjie Wang, Jinkuan Wang, Cheng Cui, and Yiding Zhao. 2010. "Research on the LN2 Auto-Filling System for Dewar Vessel Based on Bang-Bang + PID Control." In *2010 Chinese Control and Decision Conference*, 2937–40. IEEE. DOI: 10.1109/CCDC.2010.5498670.

Zhao Yiding, and Song Zengfeng. 2010. "The Intelligent Controller of Filling Liquid Nitrogen Based on the Grey Prediction Theory." In *2010 International Conference On Computer Design and Applications*, 3:V3–274 – V3–277. IEEE. DOI: 10.1109/ICCDA.2010.5540748.

C.4 SPIE2016

PROCEEDINGS OF SPIE

SPIEDigitalLibrary.org/conference-proceedings-of-spie

GRAVITY acquisition camera: characterization results

Narsireddy Anugu, Paulo Garcia, Antonio Amorim, Erich Wiezorrek, Ekkehard Wieprecht, et al.

Narsireddy Anugu, Paulo Garcia, Antonio Amorim, Erich Wiezorrek, Ekkehard Wieprecht, Frank Eisenhauer, Thomas Ott, Oliver Pfuhl, Paulo Gordo, Guy Perrin, Wolfgang Brandner, Christian Straubmeier, Karine Perraut, "GRAVITY acquisition camera: characterization results," Proc. SPIE 9907, Optical and Infrared Interferometry and Imaging V, 990727 (4 August 2016); doi: 10.1117/12.2233315

Event: SPIE Astronomical Telescopes + Instrumentation, 2016, Edinburgh, United Kingdom

SPIE.

GRAVITY acquisition camera: characterization results

Narsireddy Anugu*[a], Paulo Garcia[a], Antonio Amorim[b], Erich Wiezorrek[c], Ekkehard Wieprecht[c], Frank Eisenhauer[c], Thomas Ott[c], Oliver Pfuhl[c], Paulo Gordo[b], Guy Perrin[d], Wolfgang Brandner[e], Christian Straubmeier[f] and Karine Perraut[g]

[a]Universidade do Porto, Faculdade de Engenharia, Unidade FCT CENTRA, Rua Dr. Roberto Frias, s/n, P-4200-465 Porto, Portugal; [b]CENTRA-SIM and FCUL - Edificio C8, Campo Grande, P1749016 Lisboa, Portugal;
[c]Max Planck Institute for extraterrestrial Physics, PO Box 1312, Giessenbachstr., 85741 Garching, Germany;
[d]Observatoire de Paris Meudon, Paris, France;
[e]MaxPlanck-Institut fur Astronomie, Heidelberg, Germany;
[f]Universität zu Köln Germany;
[g]Institut de Planétologie et d´Astrophysique de Grenoble (IPAG), Grenoble, France

ABSTRACT

GRAVITY acquisition camera implements four optical functions to track multiple beams of Very Large Telescope Interferometer (VLTI): a) pupil tracker: a 2×2 lenslet images four pupil reference lasers mounted on the spiders of telescope secondary mirror; b) field tracker: images science object; c) pupil imager: reimages telescope pupil; d) aberration tracker: images a Shack-Hartmann. The estimation of beam stabilization parameters from the acquisition camera detector image is carried out, for every 0.7 s, with a dedicated data reduction software. The measured parameters are used in: a) alignment of GRAVITY with the VLTI; b) active pupil and field stabilization; c) defocus correction and engineering purposes. The instrument is now successfully operational on-sky in closed loop. The relevant data reduction and on-sky characterization results are reported.

Keywords: optical and infrared interferometry, GRAVITY, wavefront sensing, adaptive optics, pupil tracking

1. INTRODUCTION

GRAVITY is a high precision narrow angle astrometry and interferometric imaging instrument.[1] It has been built for the Very Large Telescope Interferometer (VLTI) of the European Southern Observatory and was born with the goal of monitoring the stellar sources in the vicinity of the Galactic Center super massive black hole and the actual emission of the black hole close environment environment. It combines four beams (in the K-band) coherently of either Unit Telescopes (UTs) or Auxiliary Telescopes (ATs), delivering an astrometry of ~ 10 micro-arcseconds (μas) and a angular resolution of around ~ 4 milli-arcseconds (mas).

The main error sources for the GRAVITY astrometric measurements are the atmospheric turbulence and the error in the baseline length (B) between any two telescopes. The GRAVITY-Coudé Infrared Adaptive Optics (CIAO) measures and corrects wavefront aberrations induced by the atmospheric turbulence in the light path from the sky to the Coudé laboratory.[2] However the CIAO corrections do not include the VLTI tunnel seeing induced fast moving tip-tilts. These are tracked by launching external lasers at the telescopes (at the star separator) and imaging them in the GRAVITY beam combiner.[3] The measured tip-tilts are corrected by dedicated tip-tilt-piston mirrors. But the above corrections involve tip-tilt residuals of more than 10 mas. These tip-tilt errors limit the performance of GRAVITY in two ways:[4] a) efficiency of star light injection into the single mode fibers which are used to transport the light to the integrated optics[5] to make the beam combination; b) unwanted tip-tilt error causes additional astrometric error.

The factor limiting the precision in measuring the accurate baseline (RMS error of a few mm for a ~ 100 m baseline) length between two telescopes is pupil position errors. These errors are mainly due to the misalignments

*narsireddy.anugu@fe.up.pt

Optical and Infrared Interferometry and Imaging V, edited by Fabien Malbet, Michelle J. Creech-Eakman, Peter G. Tuthill, Proc. of SPIE Vol. 9907, 990727
© 2016 SPIE · CCC code: 0277-786X/16/$18 · doi: 10.1117/12.2233315

Downloaded From: https://www.spiedigitallibrary.org/conference-proceedings-of-spie on 12/14/2017 Terms of Use: https://www.spiedigitallibrary.org/terms-of-use

and temperature gradients. In between the telescope pupil and the fiber-fed beam combiner, there exists several optical pupils that are under motion due to the optical train vibrations while tracking the object of interest. The typical lateral and longitudinal pupil position errors experienced by the VLTI are around 5% in the pupil diameter and 1 m, respectively, for the 80 mm beam. Eq. 1 gives the astrometric error[6] associated with the given tip-tilt error ($\Delta\alpha$) and pupil lateral position (ΔL) errors. For example, for 10 mas tip-tilt error and 0.4 m (5% of 8 m pupil) lateral pupil position error, the astrometric error becomes 40 μas for a single beam combiner

$$\sigma = \frac{\Delta\alpha \times \Delta L}{B}. \tag{1}$$

The CIAO measures and corrects the incoming distorted wavefronts with respect to a flat wavefront generated in the Coudé laboratory. However, there are many optics and tunnel seeing in between the CIAO and the GRAVITY beam combiner. They will also introduce additional wavefront aberrations to the incoming beam. The quasi-static wavefront aberrations and the non-common path errors that exist between the CIAO and the GRAVITY beam combiner also contribute to the astrometric error.[4]

Therefore a beam stabilization system is required to address the above issues. The GRAVITY acquisition camera has been built to image and analyze the VLTI beams and to: a) enable the stabilization of star light injection into the single mode fibers; b) minimize the astrometric errors induced by the field and the pupil errors.

2. ACQUISITION CAMERA

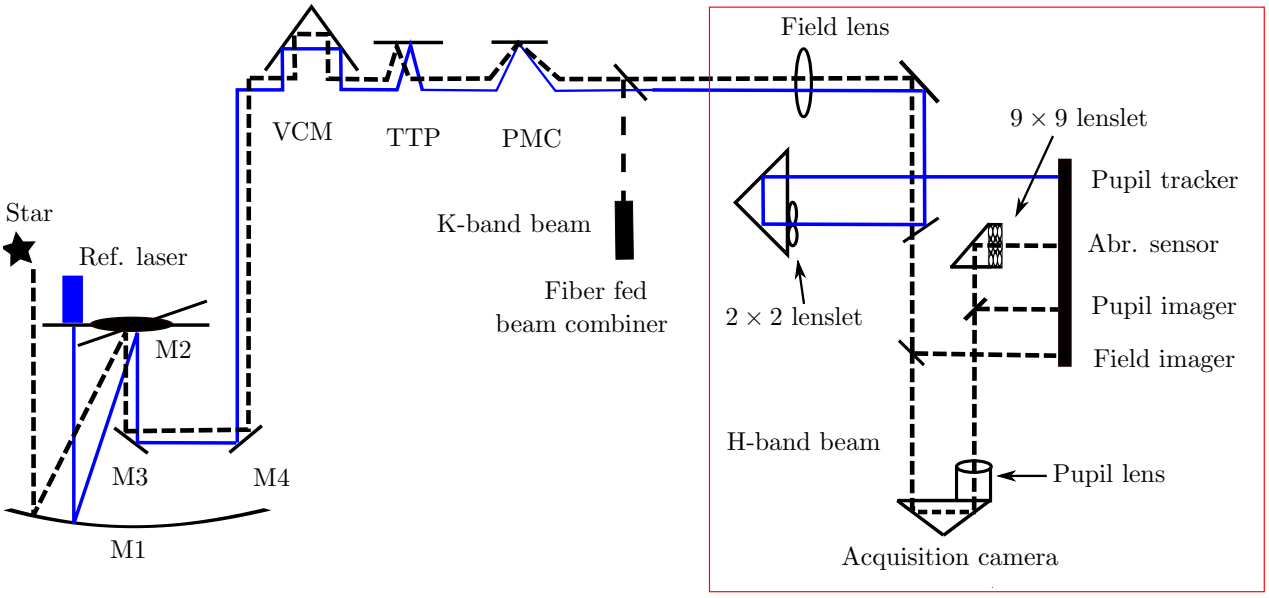

Figure 1: The acquisition camera working principle and optical layout (for clarity only one telescope beam case is shown). The astrophysical target's K-band beam is used for science measurements and the H-band beam is used for beam stabilization. The H-band beam feeds the three imaging modes of the acquisition camera: aberration sensor, pupil imager, field imager. The pupil tracker images external pupil reference laser light (1.2 µm). The box in red color encloses the acquisition camera optics.

Figure 1 presents the optical layout of the acquisition camera for one telescope beam. The acquisition camera provides four optical imaging modes: a) field imager – images and tracks the field (tip-tilt) of input beams; b) pupil tracker – tracks the telescope pupil motions by imaging four pupil beacons that are installed on the spiders of secondary mirror (M2) of the telescope; c) aberration sensor – implements four 9 × 9 lenslets to sense the

Downloaded From: https://www.spiedigitallibrary.org/conference-proceedings-of-spie on 12/14/2017 Terms of Use: https://www.spiedigitallibrary.org/terms-of-use

incoming distorted wavefronts; d) pupil imager – images telescope pupil, which is used for monitoring the pupil visually during the observations. Pupil tracker images four pupil guiding laser beacons of 1.2 µm wavelength with a 2×2 lenslet. The other three imaging modes image astrophysical targets in the H-band. The acquisition camera uses a 2048×2048 pixel Hawaii-2RG detector to image all four input telescope beams. The optical design of the camera[7] and its optical alignment and integration[8] are presented in the previous SPIE proceedings.

To extract the beam stabilization parameters from the detector images, a dedicated software has been developed based on the image analysis methods presented in Anugu et al. (2014).[9] The software was written in C and C++ using CLIP library[10] and integrated in the GRAVITY observational software.[11] This software works on the instrument workstation and does the image analysis in two steps. First, it reads the acquisition camera detector image from the instrument shared memory for every 0.7 s (detector frame rate). Second, it evaluates the beam's tip-tilts, pupil shifts and the wavefront aberrations by analyzing the input detector image. The evaluated parameters are written to the instrument database. They feed the beam stabilization which uses: a) the tip-tilt and piston (TTP); b)the pupil motion controller (PMC)[3] and; c) the Variable Curvature Mirror (VCM).[12] By stabilizing the field, it enables the injection of the K-band light of the astrophysical targets into single mode fibers which transport the beams towards the interferometric beam combiner. The image acquisition, analysis and beam correction are carried out on-line in the instrument workstation in parallel to the observations for all four telescopes.

3. CHARACTERIZATION RESULTS

GRAVITY passed Preliminary Verification Europe tests (PAE) in early 2015 and was moved in August 2015 to the Paranal Observatory where it got its first light in November 2015. Fig. 2 presents the acquisition camera detector image acquired on-sky with the ATs.

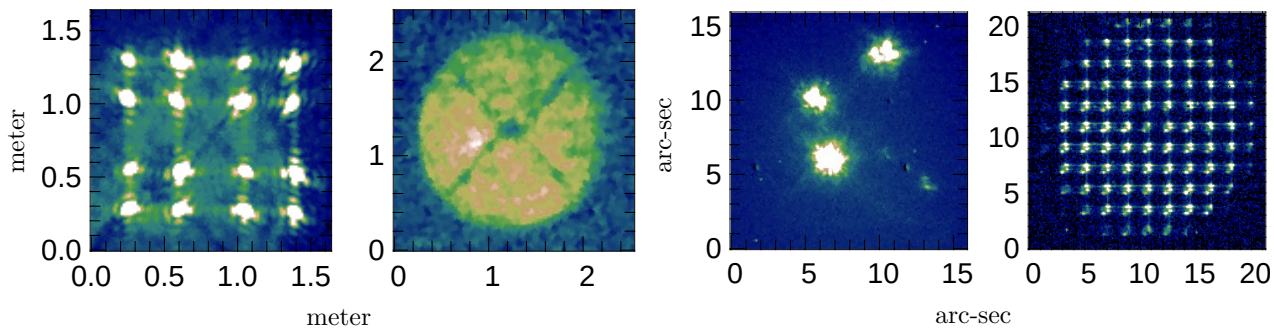

Figure 2: On-sky measurements of the acquisition camera imaging modes (left to right): pupil tracker, pupil imager, field tracker and aberration sensor. The astrophysical target is θ^1 Ori A (North up and East on right). The aberration sensor image is rotated counter clockwise to the field image due to the mirror reflection.

3.1 Characterization for PAE

During the PAE, the acquisition camera was characterized using the GRAVITY calibration unit.[13] The calibration unit is a GRAVITY subsystem which provides laboratory beams and artificial stars to test GRAVITY functionalities. It generates two artificial stars and four pupil guiding reference beams to test the acquisition camera imaging modes.

3.1.1 Field tracking

Characterization of the field tracker is accomplished in three fronts: a) RMS and absolute tracking accuracy; b) RMS accuracy as a function of target magnitude; c) target flux injection into the fibers. To characterize the absolute accuracy of the field tracker, known tip-tilts ($\theta_{\rm i}$) are applied to the incoming beams by manipulating the TTP device and measured backm ($\theta_{\rm o}$), using the field tracker function.

Downloaded From: https://www.spiedigitallibrary.org/conference-proceedings-of-spie on 12/14/2017 Terms of Use: https://www.spiedigitallibrary.org/terms-of-use

Figure 3 (left panel) presents the absolute tracking accuracy and is around ~ 2 mas and the RMS error is ~ 1 mas. These measurements are carried out with a "star" with an H-band magnitude of 15. Figure 3 (middle panel) presents the RMS error of the field tracker as a function of "star" magnitude. These "stars" are realized by the Calibration Unit and by varying the voltage of the lamp. Figure 3 (right panel) presents how the flux injection in the fiber is reduced. By enabling the field stabilization, the coupling efficiency of the fiber is maintained around 80%.

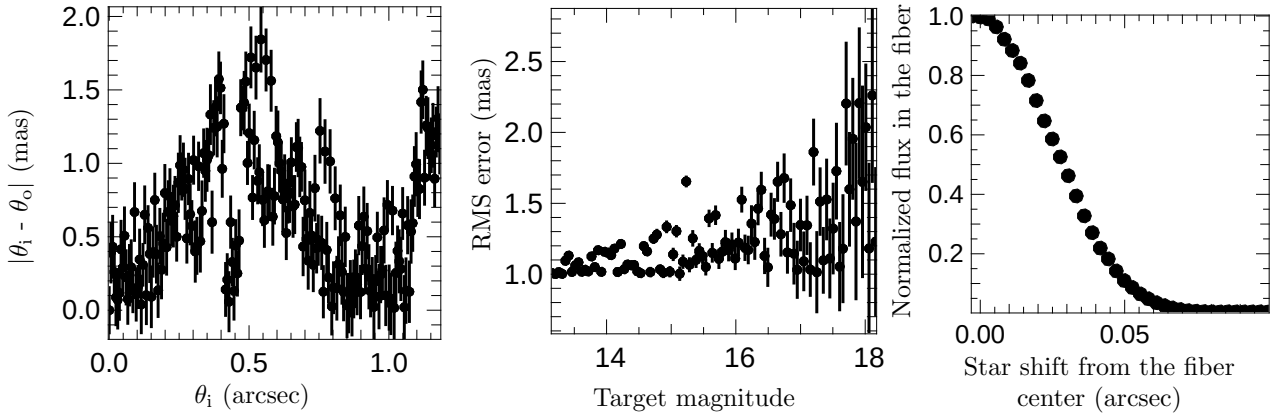

Figure 3: Performance of the field tracker in the laboratory. Left: the absolute field tracking error $|\theta_i - \theta_o|$ as a function of true object position θ_i. Middle: the RMS error of the field tracking as a function of target magnitude. Right: Normalized star's flux injection into the fiber as function of tip-tilt/star shift from the fiber center.

3.1.2 Lateral pupil tracking

The lateral pupil tracking accuracy tests are implemented in two steps by manipulating the PMC actuators. First, known lateral pupil shifts (L_{x_0}) are applied to the incoming beams by actuating the PMCs. Second, the input pupil shifts are sensed (say, L_x) using the pupil tracker function. Figure 4 presents the lateral pupil tracking accuracy as a function of the input pupil shifts. The lateral pupil tracking absolute accuracy is better than 4 mm at the UT beam magnification (0.05% of the UT diameter) and the RMS error is 2 mm.

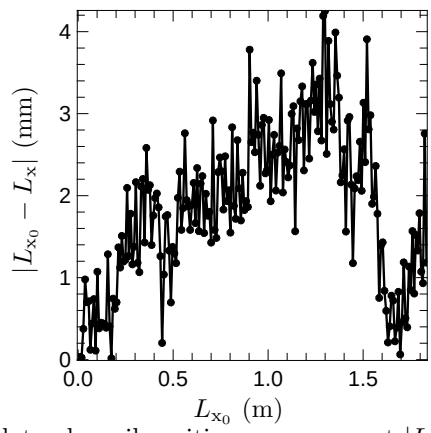

Figure 4: The absolute error in the lateral pupil position measurement $|L_x - L_{x_0}|$ as a function of input lateral pupil shift L_{x_0}. The measurements are in the UT scale and where obtained in the laboratory.

3.1.3 Longitudinal pupil tracking

Longitudinal pupil tracking precision is characterized by manipulating the VCM positions. In this experiment, known longitudinal pupil shifts are applied to the beam by moving the VCM and those are measured back by

Downloaded From: https://www.spiedigitallibrary.org/conference-proceedings-of-spie on 12/14/2017 Terms of Use: https://www.spiedigitallibrary.org/terms-of-use

the pupil tracker. Fig.5 (left panel) presents the longitudinal pupil characterization results and it can be seen that the accuracy is better than 40 mm for the 80 mm beam. The middle and right panel present, respectively, the UT pupil before and after closing the pupil guiding loop.

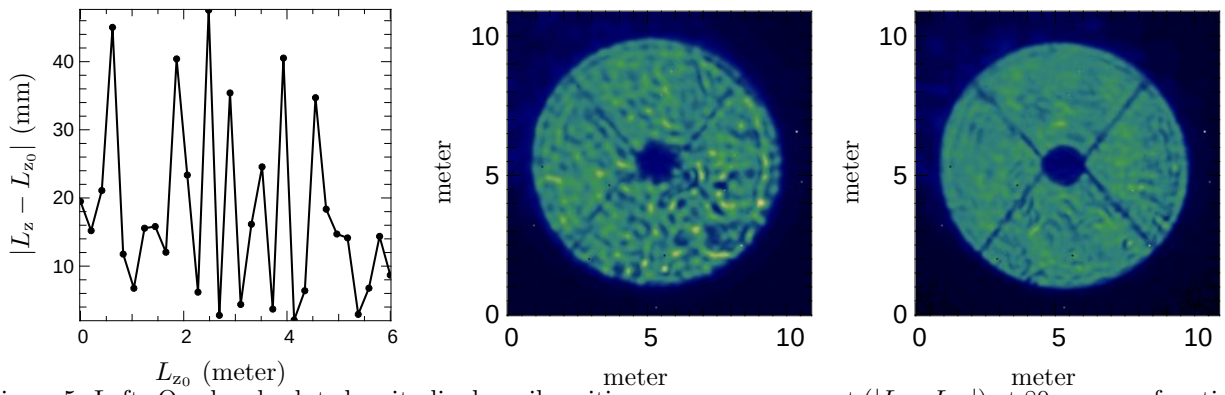

Figure 5: Left: On-sky absolute longitudinal pupil position error measurement ($|L_z - L_{z_0}|$) at 80 mm as a function of input longitudinal pupil position L_{z_0}. Center, right: On-sky pupil images obtained before and after closing the pupil guiding closed loop.

3.2 On-sky beam guiding performance

The acquisition camera beam guiding has been tested for the ATs and for the UTs. The guiding difference between the ATs and the UTs is that the ATs are not corrected by CIAO. For this reason, the field imager is used to measure slow (tunnel) atmospheric tip-tilts. Whereas for the UTs, the field imager is used to measure the residual tip-tilts of the CIAO. The ATs telescope focus correction is implemented by tracking the focus using the aberration sensor and correcting it with their M2 mirrors.

As stated previously, the GRAVITY field and pupil offset corrections are achieved using two types of actuators: a) the VLTI star separator actuators[14] and the delay line VCM; b) GRAVITY internal field (TTP) and pupil (PMC) actuators. The VLTI star separator has a field selector mirror and a pupil position mirror (M14, laterally and longitudinally movable). Small field and pupil corrections occurring during interferometric observations are corrected in closed loop using GRAVITY internal actuators for the speed and accuracy. Large field and pupil offsets (which usually take place during the initial alignment of GRAVITY with the VLTI) are corrected using star separator actuators. While operating with GRAVITY internal actuators in the closed loop, when the offsets are larger than GRAVITY internal actuators range, they are offloaded to the VLTI actuators.

During the installation, verification and commissioning phases, the guiding loops of the field, the pupil were extensively tested. Characterization of the field guiding is realized by observing several dual-field stars and checking the stability of injection of star's light into single mode fibers. Characterization of the pupil guiding is implemented by applying known pupil shifts with pupil correcting actuators and checking their stability over an hour. The pupil tracker experiences high backgrounds from bright astrophysical targets due to the closeness of: a) the operating wavelengths of the pupil tracker (operating at 1.2 μm) and the field tracker (operates at H-band – 1.65 μm) and; b) no adequate dichroic filter for the pupil tracker. The operation of the pupil guiding for an interferometric observation depends on two factors: a) the flux of the pupil guiding laser beacons; b) the magnitude of the astrophysical target. To remove the astrophysical target background, a new software mode, BLINK, is implemented. The basic idea of this mode is to remove the background by switching OFF and ON the pupil beacons. During the turn OFF period, the background is stored and the is subtracted from the subsequent frame. The performance of the pupil guiding is improved by 2 magnitudes when using this BLINK mode. Currently it can operate up to magnitude 1 for the ATs.

The non-common path errors between the CIAO and GRAVITY are calibrated by inputting known wavefronts to the GRAVITY beams that are generated by manipulating the MACAO deformable mirror[15] and measuring the input wavefront aberrations using the aberration sensor. The offsets are then taken into account by CIAO to compensate the non-common path aberrations.

Downloaded From: https://www.spiedigitallibrary.org/conference-proceedings-of-spie on 12/14/2017 Terms of Use: https://www.spiedigitallibrary.org/terms-of-use

The following summarizes the current on-sky performance of the acquisition camera:

- **Pupil guiding residuals:** The standard deviation of the lateral and the longitudinal pupil guiding residuals are remain smaller than ± 0.2 pixels RMS on the detector (i.e., 12 mm at the UTs) and the 50 mm for 80 beam size respectively in the presence of faint astrophysical target.
- **Field guiding residuals:** The standard deviation of the field guiding residuals are smaller than ± 0.36 pixels (6.4 mas). When the tests of the field guiding for the ATs (not equipped with the CIAO) took place, the laser based tunnel seeing tip-tilt tracking system was not installed. That is why the residuals are large.
- **Focus guiding** The standard deviation of the focus guiding residuals for the ATs are within ± $\lambda/8$ RMS.

4. DISCUSSION AND CONCLUSIONS

The GRAVITY acquisition camera was installed at the Very Large Telescope Interferometer during the last months of 2015. Since then it has been successfully working in the closed loop to stabilize the slow (tunnel) atmospheric turbulence field motions and the pupil motions.

The camera is characterized using laboratory generated telescope beams at MPE and on-sky at the Paranal Observatory. The characterization results revealed that it is able to analyze the telescope beams with the accuracy required by 10 μas astrometry, namely: a) field tracking with 2 mas RMS; b) lateral pupil tracking with 4 mm RMS (at the UT scale); c) longitudinal pupil tracking with 50 mm RMS (at 80 mm beam scale); and d) quasi-static higher order wavefront aberration measurements with 80 nm RMS.

The acquisition camera measured beam parameters are used in the stabilization of the field, the pupil and the focus correction. With the stabilization of the field, the star's light injection into single mode fibers is improved. The quasi-static higher order aberrations measurements are used for the non-common path errors corrections between the CIAO and GRAVITY. The pupil imager is used for visual monitoring. By stabilizing the telescope beams, the astrometric error induced by the field (accuracy of 2 mas RMS, cf. Section 3.1.1) and the pupil errors (accuracy of 12 mm RMS) is minimized to 0.34 μas).

Acknowledgments

Anugu acknowledges FCT-Portugal grant SFRH/BD/52066/2012. The research leading to these results was partially supported by FCT-Portugal grant PTDC/CTE-AST/116561/2010 and the European Community's Seventh Framework Programme under Grant Agreement 312430.

REFERENCES

[1] Eisenhauer, F., Brandner, W., Straubmeier, C., Perraut, K., Gillessen, S., Lima, J., Henning, T., Garcia, P., Kellner, S., Avila, G., Perrin, G., Brandner, W., Straubmeier, C., Perraut, K., Amorim, A., Schöller, M., Gillessen, S., Kervella, P., Benisty, M., Araujo-Hauck, C., Jocou, L., Lima, J., Jakob, G., Haug, M., Clénet, Y., Henning, T., Eckart, A., Berger, J.-P., Garcia, P., Abuter, R., Kellner, S., Paumard, T., Hippler, S., Fischer, S., Moulin, T., Villate, J., Avila, G., Gräter, A., Lacour, S., Huber, A., Wiest, M., Nolot, A., Carvas, P., Dorn, R., Pfuhl, O., Gendron, E., Kendrew, S., Yazici, S., Anton, S., Jung, Y., Thiel, M., Choquet, É., Klein, R., Teixeira, P., Gitton, P., Moch, D., Vincent, F., Kudryavtseva, N., Ströbele, S., Sturm, S., Fédou, P., Lenzen, R., Jolley, P., Kister, C., Lapeyrère, V., Naranjo, V., Lucuix, C., Hofmann, R., Chapron, F., Neumann, U., Mehrgan, L., Hans, O., Rousset, G., Ramos, J., Suarez, M., Lederer, R., Reess, J.-M., Rohloff, R.-R., Haguenauer, P., Bartko, H., Sevin, A., Wagner, K., Lizon, J.-L., Rabien, S., Collin, C., Finger, G., Davies, R., Rouan, D., Wittkowski, M., Dodds-Eden, K., Ziegler, D., Cassaing, F., Bonnet, H., Casali, M., Genzel, R., and Lena, P., "GRAVITY: Observing the Universe in Motion," *The Messenger* **143**(March), 16–24 (2011).

[2] Kendrew, S., Hippler, S., Brandner, W., Clénet, Y., Deen, C., Gendron, E., Huber, A., Klein, R., Laun, W., Lenzen, R., Naranjo, V., Neumann, U., Ramos, J., Rohloff, R.-R., Yang, P., Eisenhauer, F., Fedrigo, E., Suarez-Valles, M., Amorim, A., Perraut, K., Perrin, G., and Straubmeier, C., "The GRAVITY Coude Infrared Adaptive Optics (CIAO) system for the VLT Interferometer," *eprint arXiv:1207.2945* (2012).

Downloaded From: https://www.spiedigitallibrary.org/conference-proceedings-of-spie on 12/14/2017 Terms of Use: https://www.spiedigitallibrary.org/terms-of-use

[3] Pfuhl, O., Haug, M., Eisenhauer, F., Kellner, S., Haussmann, F., Perrin, G., Gillessen, S., Straubmeier, C., Ott, T., Rousselet-Perraut, K., Amorim, A., Lippa, M., Janssen, A., Brandner, W., Kok, Y., Blind, N., Burtscher, L., Sturm, E., Wieprecht, E., Schoeller, M., Weber, J., Hans, O., and Huber, S., "The fiber coupler and beam stabilization system of the GRAVITY interferometer," in [*SPIE Astronomical Telescopes + Instrumentation*], Rajagopal, J. K., Creech-Eakman, M. J., and Malbet, F., eds., 914623, International Society for Optics and Photonics (jul 2014).

[4] Lacour, S., Eisenhauer, F., Gillessen, S., Pfuhl, O., Woillez, J., Bonnet, H., Perrin, G., Lazareff, B., Rabien, S., Lapeyrere, V., Clenet, Y., Kervella, P., and Kok, Y., "Reaching micro-arcsecond astrometry with long baseline optical interferometry; application to the GRAVITY instrument," *Astronomy & Astrophysics* (apr 2014).

[5] Jocou, L., Perraut, K., Nolot, A., Berger, J. P., Moulin, T., Labeye, P., Lacour, S., Perrin, G., Lebouquin, J. B., Bartko, H., Thiel, M., and Eisenhauer, F., "The GRAVITY integrated optics beam combination," in [*Optical and Infrared Interferometry II. Edited by Danchi*], **7734**, 773430–773430–12 (2010).

[6] Lacour, S. and Bonnet, H., "GRAVITY Astrometric Error Budget," *VLT-TRE-GRA-15882-3201* (2011).

[7] Amorim, A., Lima, J., Anugu, N., Eisenhauer, F., Graeter, A., Haug, M., Ott, T., Pfuhl, O., Thiel, M., Wieprecht, E., Carvas, P., Garcia, P., Perrin, G., Brandner, W., Straubmeier, C., and Perraut, K., "The final design of the GRAVITY acquisition camera and associated VLTI beam monitoring strategy," in [*Optical and Infrared Interferometry III. Proceedings of the SPIE, Volume 8445, article id. 844534, 14 pp. (2012).*], Delplancke, F., Rajagopal, J. K., and Malbet, F., eds., **8445**, 844534 (sep 2012).

[8] Gordo, P., Amorim, A., Abreu, J., Eisenhauer, F., Anugu, N., Garcia, P., Pfuhl, O., Haug, M., Sturm, E., Wieprecht, E., Perrin, G., Brandner, W., Straubmeier, C., Perraut, K., Naia, M. D., and Guimarães, M., "Integration and testing of the GRAVITY infrared camera for multiple telescope optical beam analysis," in [*Proceedings of the SPIE, Volume 9146, id. 91461V 8 pp. (2014).*], Rajagopal, J. K., Creech-Eakman, M. J., and Malbet, F., eds., **9146**, 91461V (jul 2014).

[9] Anugu, N., Garcia, P. J. V., Wieprecht, E., Amorim, A., Burtscher, L., Ott, T., Gordo, P., Eisenhauer, F., Perrin, G., Brandner, W., Straubmeier, C., and Perraut, K., "The GRAVITY/VLTI acquisition camera software," in [*Proceedings of the SPIE, Volume 9146, id. 91462C 13 pp. (2014).*], Rajagopal, J. K., Creech-Eakman, M. J., and Malbet, F., eds., **9146**, 91462C (jul 2014).

[10] Ballester, P., Biereichel, P., Kaufer, A., Kiekebusch, M., and Lorch, H., "CLIP: Bridging Pipelines to Instrument Control Software," *Astronomical Data Analysis Software and Systems ASP Conference Series* **394** (2008).

[11] Burtscher, L., Wieprecht, E., Ott, T., Kok, Y., Yazici, S., Anugu, N., Dembet, R., Fedou, P., Lacour, S., Ott, J., Others, Paumard, T., Lapeyrere, V., Kervella, P., Abuter, R., Pozna, E., Eisenhauer, F., Blind, N., Genzel, R., Gillessen, S., Hans, O., Haug, M., Haussmann, F., Kellner, S., Lippa, M., Pfuhl, O., Sturm, E., Weber, J., Amorim, A., Brandner, W., Rousselet-Perraut, K., Perrin, G. S., Straubmeier, C., and Schöller, M., "The GRAVITY instrument software/high-level software," in [*SPIE Astronomical Telescopes+ Instrumentation*], Rajagopal, J. K., Creech-Eakman, M. J., and Malbet, F., eds., 91462B—-91462B, International Society for Optics and Photonics, International Society for Optics and Photonics (jul 2014).

[12] Ferrari, M., Lemaitre, G. R., Mazzanti, S. P., Derie, F., Huxley, A., Lemerrer, J., Lanzoni, P., Dargent, P., and Wallander, A., "Variable curvature mirrors: implementation in the VLTI delay-lines for field compensation," in [*Interferometry for Optical Astronomy II*], **4838**, 1155–1162 (2003).

[13] Blind, N., Eisenhauer, F., Haug, M., Gillessen, S., Lippa, M., Burtscher, L., Hans, O., Haussmann, F., Huber, S., Janssen, A., Kellner, S., Kok, Y., Ott, T., Pfuhl, O., Sturm, E., Weber, J., Wieprecht, E., Amorim, A., Brandner, W., Perrin, G., Perraut, K., and Straubmeier, C., "GRAVITY: the Calibration Unit," *Optical and Infrared Interferometry IV* **9146**, 12 (jul 2014).

[14] Nijenhuis, J., Visser, H., de Man, H., Dekker, B., Mekking, J., and Kamphues, F., "Simultaneous observation of two stars using the PRIMA Star Separator," in [*Optical and Infrared Interferometry*], **7013**, 70133F (jul 2008).

[15] Arsenault, R., Alonso, J., Bonnet, H., Brynnel, J., Delabre, B., Donaldson, R., Dupuy, C., Fedrigo, E., Spyromilio, J., Erm, T., Farinato, J., Hubin, N., Ivanescu, L., Kasper, M., Oberti, S., Paufique, J., Rossi, S., Tordo, S., Stroebele, S., Lizon, J.-L., Gigan, P., Pouplard, F., Delplancke, F., Silber, A., Quattri, M.,

Downloaded From: https://www.spiedigitallibrary.org/conference-proceedings-of-spie on 12/14/2017 Terms of Use: https://www.spiedigitallibrary.org/terms-of-use

and Reiss, R., "MACAO-VLTI first light: adaptive optics at the service of interferometry," *The Messenger (ISSN 0722-6691)* (2003).

Downloaded From: https://www.spiedigitallibrary.org/conference-proceedings-of-spie on 12/14/2017 Terms of Use: https://www.spiedigitallibrary.org/terms-of-use

C.5 SPIE2014a

PROCEEDINGS OF SPIE

SPIEDigitalLibrary.org/conference-proceedings-of-spie

The GRAVITY/VLTI acquisition camera software

Narsireddy Anugu, Paulo J. V. Garcia, Ekkehard Wieprecht, Antonio Amorim, Leonard Burtscher, et al.

Narsireddy Anugu, Paulo J. V. Garcia, Ekkehard Wieprecht, Antonio Amorim, Leonard Burtscher, Thomas Ott, Paulo Gordo, Frank Eisenhauer, Guy Perrin, Wolfgang Brandner, Christian Straubmeier, Karine Perraut, "The GRAVITY/VLTI acquisition camera software," Proc. SPIE 9146, Optical and Infrared Interferometry IV, 91462C (24 July 2014); doi: 10.1117/12.2055831

Event: SPIE Astronomical Telescopes + Instrumentation, 2014, Montréal, Quebec, Canada

SPIE.

The GRAVITY/VLTI acquisition camera software

Narsireddy Anugu[*a], Paulo Garcia[a], Ekkehard Wieprecht[b], Antonio Amorim[c], Leonard Burtscher[b], Thomas Ott[b], Paulo Gordo[c], Frank Eisenhauer[b], Guy Perrin[d], Wolfgang Brandner[e], Christian Straubmeier[f] and Karine Perraut[g]

[a]Universidade do Porto, Faculdade de Engenharia, Laboratório SIM Unidade FCT no 4006, Rua Dr. Roberto Frias, s/n, 4200-465 Porto, Portugal; [b]Max Planck Institute for extraterrestrial Physics, PO Box 1312, Giessenbachstr., 85741 Garching, Germany; [c]SIM and FCUL - Edificio C8, Campo Grande, P1749016 Lisboa, Portugal; [d]Observatoire de Paris Meudon, Paris, France; [e]MaxPlanck-Institut fur Astronomie, Heidelberg, Germany; [f]Universität zu Köln Germany; [g]Institut de Planétologie et d´Astrophysique de Grenoble (IPAG), Grenoble, France

ABSTRACT

The acquisition camera for the GRAVITY/VLTI instrument implements four functions: a) field imager: science field imaging, tip-tilt; b) pupil tracker: telescope pupil lateral and longitudinal positions; c) pupil imager: telescope pupil imaging and d) aberration sensor: The VLTI beam higher order aberrations measurement.

We present the dedicated algorithms that simulate the GRAVITY acquisition camera detector measurements considering the realistic imaging conditions, complemented by the pipeline used to extract the data. The data reduction procedure was tested with real aberrations at the VLTI lab and reconstructed back accurately.

The acquisition camera software undertakes the measurements simultaneously for all four AT/UTs in 1 s. The measured parameters are updated in the instrument online database. The data reduction software uses the ESO Common Library for Image Processing (CLIP), integrated in to the ESO VLT software environment.

Keywords: optical and infrared interferometry, GRAVITY, VLTI, adaptive optics, pupil tracking

1. INTRODUCTION

The GRAVITY is a VLTI/ESO instrument, the main goal of the instrument is to detect the highly relativistic motions of a flare surrounding the supermassive black hole at the center of Galactic Center, and therefore probe physics of the Galactic Center black hole. Other astrophysical aims are to study mass accretion, intermediate black holes, young planets, star clusters and active galactic nuclei and including imaging.[1] It operates in the K-band and combines the four AT or UT beams to produce interferograms from six baselines simultaneously. It offers an unprecedented astronomical accuracy of around 10 μas between two objects.

The GRAVITY instrument consists of five major components namely wavefront sensors, beam stabilization system,[2,3] fring-tracker, fiber-fed integrated optics,[4] and laser metrology. The wavefront sensors sense the four beams wavefronts using a reference star (IRS7) picked with the PRIMA star separator. The corrections are implemented with a deformable mirror. The residual wavefront errors, telescope tunnel seeing induced errors and telescope pupil position shifts are detected and corrected by the beam stabilization system. The fiber coupler[2] separates the fringe tracker object, the science object. Also it feed them to the fringe-tracker and the integrated optics using single-mode fibers respectively. The fringe-tracker detects the atmospheric piston error to stabilize the fringes. The instrument internal differential optical path difference between the two objects is measured with a dedicated laser metrology system. The interference pattern of the four stabilized beams is implemented with an integrated optics. Having all these facilities, the GRAVITY provides the accurate astrometry.

The VLT beams analysis has been carried out with the sub systems namely the acquisition camera and the tip-tilt guiding system.[2] The tip-tilt guiding system detects fast tip-tilts using tip-tilt guided lasers operating at 0.655 μm and while the acquisition camera implements four following important detections

*narsireddy.anugu@fe.up.pt

Optical and Infrared Interferometry IV, edited by Jayadev K. Rajagopal, Michelle J. Creech-Eakman, Fabien Malbet, Proc. of SPIE Vol. 9146, 91462C • © 2014 SPIE • CCC code: 0277-786X/14/$18
doi: 10.1117/12.2055831

Downloaded From: https://www.spiedigitallibrary.org/conference-proceedings-of-spie on 12/17/2017 Terms of Use: https://www.spiedigitallibrary.org/terms-of-use

- Pupil tracker: tracks the telescope pupil lateral and longitudinal positions using pupil guiding laser beacons
- Field imager: slow tip-tilt tracking using a science field reference star
- Pupil imager: re-imaging AT/UT telescope pupil
- Aberration sensor: senses the VLTI beam wavefront aberrations using the science field

Pupil tracker works with 1.2 μm pupil guiding laser beams. The remaining functions of the acquisition camera uses the H-band sky light. The full description of the acquisition camera optical design and mechanical design can be found at Amorim et al. (2012).[3]

The telescope beam parameter measurements can be accomplished basically in two steps: a) one is the detection of the beam offset parameters by using the acquisition camera optics; b) reconstruction of beam offset parameters by using a software.

In this paper we present an overview of the concepts and the simulations of the optical functions of the acquisition camera. Furthermore we summarize the methods involved in reconstructing of the VLTI beam offset parameters. Finally we outline the acquisition camera software architecture and the operational scenarios.

2. NUMERICAL SIMULATION OF THE ACQUISITION CAMERA

A meticulous numerical simulation of the acquisition camera is a prerequisite for designing methods or algorithms to verify their accuracy and validation. These numerical simulations of the acquisition camera has been implemented mainly using LIGHTPIPES[5] and YAO.[6]

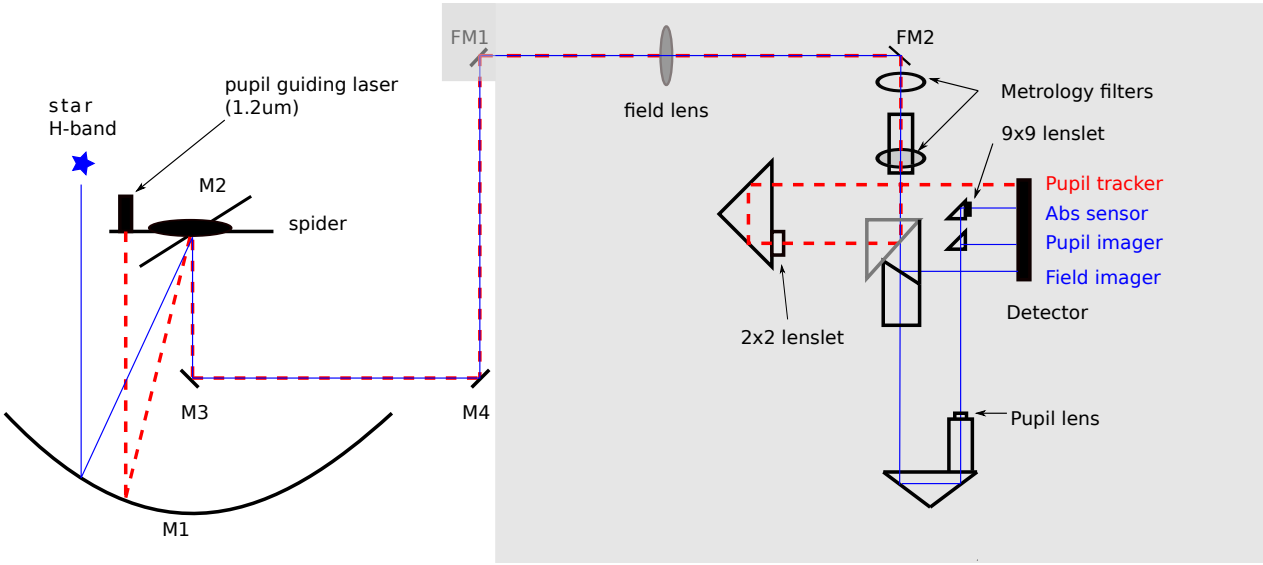

Figure 1. The optical layout of the acquisition camera. The telescope light (pupil guiding laser + H-band) propagation into the acquisition camera optics is presented. In this cartoon, only a single pupil guiding laser beacon (red color dashed ray line) has been shown out of 4 lasers mounted on a single telescope. The H-band sky (black solid ray line) light has been used by the field imager, the aberration sensor and the pupil imager. The FM1 is a mirror, and also the first optical element of the acquisition camera. The FM1, the field lens and the FM2 are the optical elements which used to fold the light into the optical functions. The dichoric splits the light into the 1.2 μm and the H-band light. The 1.2 μm beam guided to the pupil tracker. The two beam splitters present in the figure are used to distribute the H-band light to the field imager, the pupil imager and the aberration sensor.

Downloaded From: https://www.spiedigitallibrary.org/conference-proceedings-of-spie on 12/17/2017 Terms of Use: https://www.spiedigitallibrary.org/terms-of-use

2.1 VLT beam aberrations

The telescope beam which is fed to the acquisition camera consists of wavefront residual errors from the adaptive optics system of the GRAVITY, the VLTI tunnel seeing induced tip-tilts and the higher order aberrations and also the important telescope pupil positions jitter. The tunnel induced tip-tilts contribute 90% of the wavefront error to the beam. The pupil position tracking is important since the imaging baselines can introduce astrometric errors when the telescope pupil and the field plane are mismatched.[7] The main source for the pupil position jitter is the movements of the delay line carriages during the observations.

The higher order aberrations induced by the tunnel seeing and the optical aberrations induced by the movements of delay line carriages were experimentally measured using a Shack-Hartmann at the VLTI lab.[8,9] A phase emulating these referred beam aberrations is simulated using the experimentally measured Zernike coefficients. The phase is expressed as a linear combination of Zernike polynomials.[10]

2.2 Field imager

The field imager is the critical function of the acquisition camera. It images the $4'' \times 4''$ Galactic Center/science field and also tracks the tip-tilts of a star. These tip-tilts are used to improve coupling efficiency of the light injection of the star light into the fiber-fed beam combiner.

In order to check the validity and accuracy of the field imager, simulated the field imager image using all appropriate sources of noises. These are telescope tunnel seeing, chromatic aberrations and atmospheric differential refraction.[11] Among them the atmospheric differential refraction is the critical parameter in this instrument for two reasons. The acquisition camera has considerable amount of unwanted illumination from the J-band (we call it as blue leaks) whereas the central operating wavelength is at H-band. Furthermore the field imager measures the reference object position at this central wavelength but the science instrument works at K-band. With the atmospheric differential refraction effects the star gets elongated along the zenith direction. With the tunnel seeing the image becomes tilted and gets bigger in size.

In order to numerically simulate the field imager with possible real conditions, we obtained a NACO Galactic Center image from the ESO archive and re-sampled the image to match the field imager pixel sampling. The resulting image has the tunnel seeing effects. Applied the atmospheric differential refraction effects considering the field imager throughput and the object color spectrum.

The atmospheric differential refraction is defined through the refractive index profile of the atmosphere which is dependent on the telescope operating temperature, altitude and wavelength of the optical/infrared beam. The atmospheric differential effected image has been simulated using

$$I_{\text{eff}} = \int_{\lambda_{\min}}^{\lambda_{\max}} I(\lambda, x(\lambda), y(\lambda)) T(\lambda)\, \mathrm{d}\lambda \tag{1}$$

Where I_{eff} is the intensity distribution of the star induced by the atmospheric differential refraction shifts. The $T(\lambda)$ represents effective transmission of field imager throughput, atmospheric transmission, filter transparency, and detector efficiency. The $I(\lambda, x(\lambda), y(\lambda))$ is the star profile at a particular wavelength. For each wavelength, flux of the object changes with its spectrum and its shape changes with the atmospheric differential refraction. The amount of the object shape elongates along the zenith is related to the how big the difference between the reference wavelength (H-band) and the leaking wavelength (λ) for a given zenith angle. Furthermore at a particular wavelength the elongation is dependent on the zenith angle. Starting from 1.0 μm to 2.0 μm wavelength, for each step size ($d\lambda$) of 2 nm, integrated the image $I(\lambda, x, y)$.

2.3 Pupil tracking

The imaging baselines can introduce astrometric errors when the telescope pupil and the field plane are not stabilized.[7] These pupil motions are monitored simultaneously during the observations by the pupil tracker. In order to actively monitor the four AT/UT telescope pupil motions simultaneously, four pupil guiding laser beacons (1.2 μm) are mounted on each telescope secondary mirror spiders. These laser beams are feed to the acquisition camera pupil tracker. They are imaged by a 2×2 lenslet for each telescope laser beams as shown

Downloaded From: https://www.spiedigitallibrary.org/conference-proceedings-of-spie on 12/17/2017 Terms of Use: https://www.spiedigitallibrary.org/terms-of-use

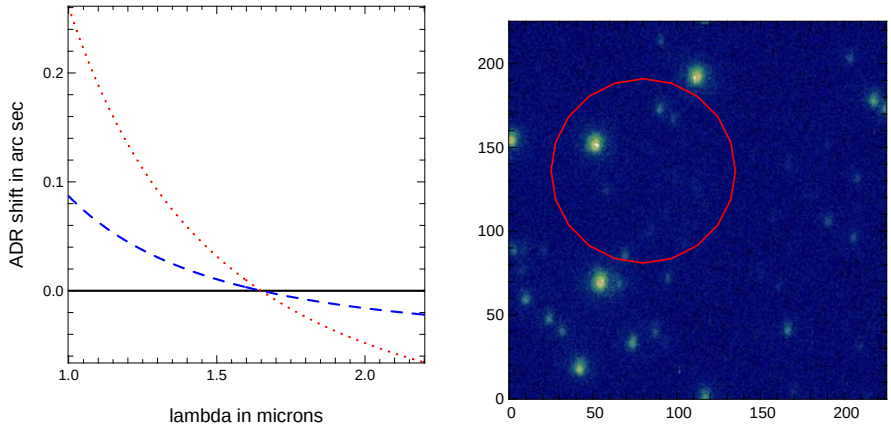

Figure 2. (Left) The left plot indicates the atmospheric differential refraction shift in pixels for three different zenith angles 0 (black solid line), 30 (blue dashed) and 60 (red dotted). (Right) The simulated field imager image. The circle indicates the 2 arc sec science field in which the Sgr A* and the reference object available.

in Fig. 1. The reconstruction of the pupil position shifts are implemented with the pupil tracker software as explained in Sec. 3.3.

The simulation procedure for the pupil tracker is explained in blocks as shown in Fig. 3 for each of the single laser beam. First, the begin function forms initial data structures for plane wavefront. Second, the outcome of the begin field is aberrated using tip-tilt and defocus aberrations using Zernike polynomials (for lateral and longitudinal pupil shifts case), next it was filtered out through a circular aperture. In order to accomplish a pupil guiding laser position on the telescope with respect to the lenslet, the incoming field was tilted appropriately. In the next step, the lenslet function filters the incoming wavefront field through positive lens. Then, the wavefront field was propagated to the focal length distance of lenslet with Fresnel diffraction. The illuminated image has 4 Airy spots, for a single laser beacon. Applied the same procedure to generate the lenslet images of the remaining laser beacons. Next combine all the four illuminated field uncoherently. Finally, applied the $12e$ readout and the photon noise to the image using the Gaussian and the Poisson statistics.

Figure 3. Simulation blocks of illuminating a pupil guiding laser through the lenslet.

The lateral and longitudinal pupil shifts are measured with respect to the fiber coupler reference position. In order to measure any existed mechanical drifts between the fiber coupler and the acquisition camera, a reference laser has been mounted inside the fiber coupler. This laser beam is imaged by the same pupil tracker lenslet. The fiber coupler laser illuminated spots can be seen as the labels C1 to C4 in the Fig. 4.

Another key idea needs attention in the simulation is the field de-rotation, implemented in the instrument. Because of this the pupil tracker spots rotates with the field de-rotator.

The pupil tracker simulated images are shown in Figs. 4 and 5. The pupil guiding laser beacons illuminated spots have been represented with numbers 1-4 respectively. The fiber coupler reference spots are represented with C1 to C4. In the Fig. 4 the pupil tracker spots rotation is presented. The spot labels 1-2-3-4 represent the four pupil guiding lasers which rotate around the fiber coupler reference spot center with the same angle as the de-rotator. In the Fig. 5 the pupil motions (left-lateral pupil shift; right-longitudinal pupil shift) are demonstrated. A barycenter is defined as the average position of the 1-2-3-4 pupil guiding lasers which situated around the fiber coupler spot. It can also seen that the barycenter of the corner spots (1-2-3-4) is not matching well with the fiber coupler reference spots due to the pupil shifts. The pattern (4 star marks), shifted vertically in

Downloaded From: https://www.spiedigitallibrary.org/conference-proceedings-of-spie on 12/17/2017 Terms of Use: https://www.spiedigitallibrary.org/terms-of-use

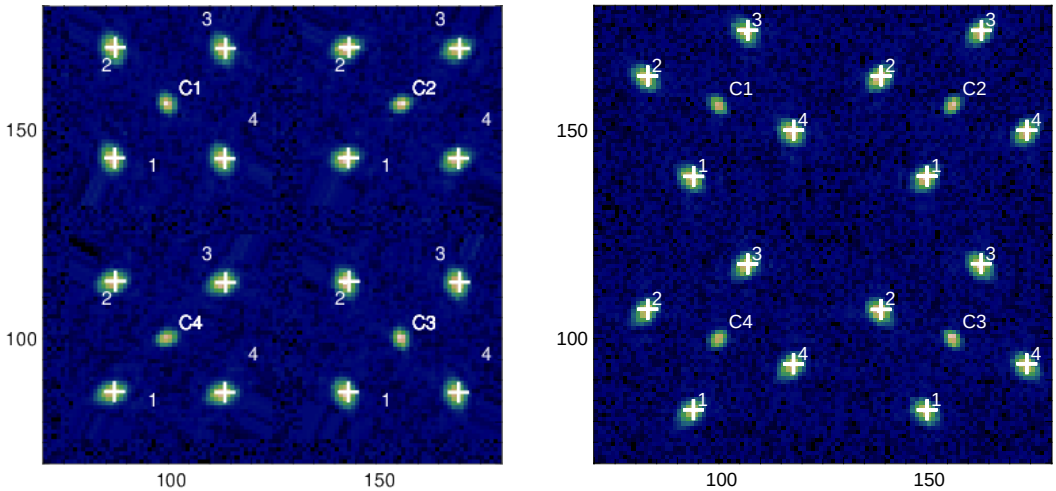

Figure 4. The synthetic image of the pupil tracker. The right image is rotated 25^0 degrees in anti-clockwise with respect to the left image. The C1-C4 represents the fiber coupler reference spots illuminated by the fiber coupler laser. The spots around the C1 which labeled as 1-2-3-4 are the pupil guiding laser illuminated spots imaged by a single sub-aperture lenslet. In this image the barycenter of the four corner spots (labeled as 1-2-3-4) is matching with the fiber coupler reference spot. The + mark is the label where the aberration free spots positions are expected.

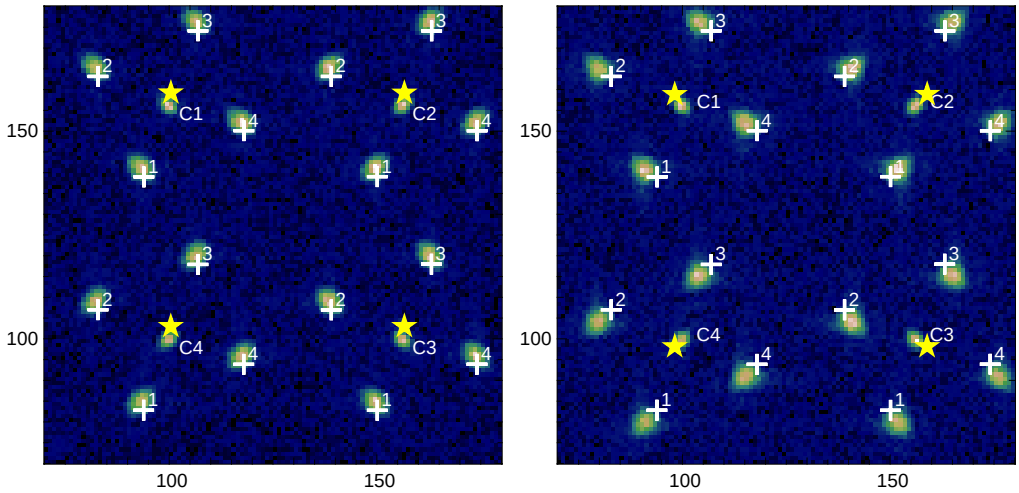

Figure 5. The pupil tracker images for the case of lateral (left image) and longitudinal (right image) pupil shifts. The + mark noted here is the expected position of spots when the aberration free beam is inputted (pupil shifts are zero). It is only indicated for visual inspection purpose. The star mark indicates the barycenter position of the four corner spots (labeled as 1-2-3-4). It is clear that barycenter position (star mark) is not matching with the fiber coupler reference spot.

the left image and diverged in the right image with respect to the fiber coupler reference spots. In the left image, the pupil shifted laterally in y-direction is demonstrated. In the right image the pupil shifting longitudinally is demonstrated. If there is only a pupil lateral shift to exist, the distance between the barycenters is equal to the distance between the fiber coupler reference spots. In case the longitudinal pupil shift to exist, the distance between the barycenters is not equal to the distance between the fiber coupler reference spots.

2.4 Aberration sensing

The aberration sensor is the important function used to characterize the telescope beam quality and also plays a key role in the improvement of the throughput of the fiber-fed beam combiner. To measure the higher order aberrations in the four VLTI beams, the aberration sensor implements a 9×9 Shack-Hartmann sensors one

Downloaded From: https://www.spiedigitallibrary.org/conference-proceedings-of-spie on 12/17/2017 Terms of Use: https://www.spiedigitallibrary.org/terms-of-use

for each one telescope. It images the 4" × 4" Galactic Center/science image. The higher order aberration reconstruction has been implemented with aberration sensor software presented in Sec. 3.4.

In order to validate the software to quantify whether it fits in the GRAVITY specifications, the aberration sensor images were simulated with the VLTI tunnel induced seeing using YAO with version 5.3.[6] A realistic model of the aberration sensor is simulated considering the VLT aberrations as explained in [Anugu et al. 2014].[12]

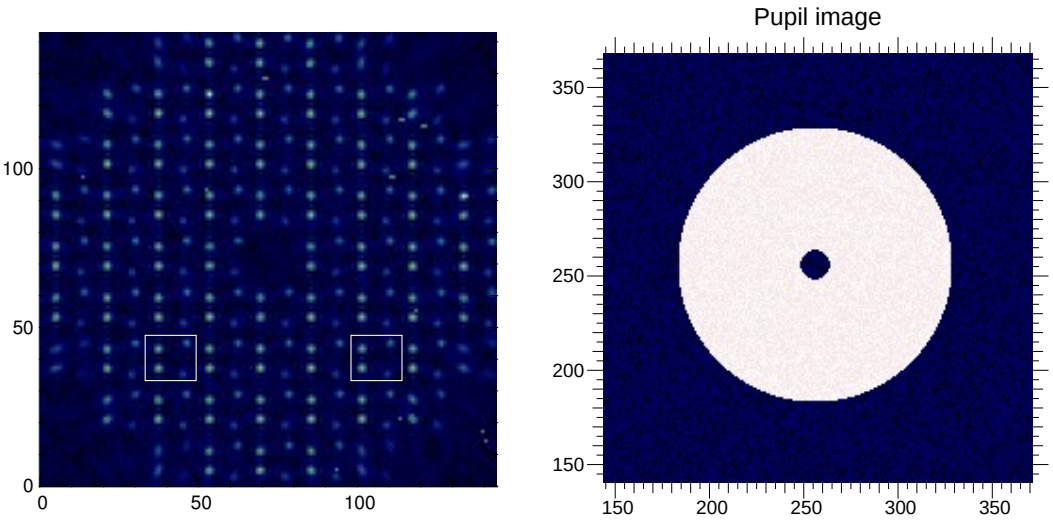

Figure 6. (left) The aberration sensor image. The white box represents the 16×16 pixel window. (Right) A synthetic image of a pupil imager.

2.5 Pupil imaging

It images the telescope pupils. The purpose of the pupil imager is to verify the pupil alignment during observations and as part of the instrument installation. Furthermore the pupil tracker working strategy can be monitored. The pupil imager uses a 8 mm diameter lens to re-image the telescope pupil. To simulate the synthetic pupil image we did convolution of pupil shape with the Airy point spread function (PSF) of the 8 mm diameter aperture. A typical image is presented in the Fig. 6.

In the following section we describe the methods of the reconstruction of the VLTI beam parameters algorithms.

3. METHODS OF ESTIMATING THE VLTI BEAM PARAMETERS

3.1 Preprocessing

Before executing the main data reduction algorithms, the detector image is processed for its background, flat-field correction and bad pixel correction to enhance the accuracy of estimating the telescope beam parameters. The flat-field correction operation consists of dividing the intensities in the image to be processed by the master flat image. The simplest background removal (sky subtraction) can be done by subtracting the master sky frame from the acquisition camera detector image. The master sky was prepared by taking several sky frames at different positions. Then these frames were median combined, to make appropriate scaling to the same sky level and to eliminate the contribution of objects in the field. The bad pixels were interpolated from the good pixels among the 8 nearest.

3.2 Field imager

The aim of the field imager is to track the object position (x_T, y_T) accurately which is dynamically altered by the tunnel seeing tip-tilts. Due to the atmospheric differential refraction, the object shape is dictated by a large number of atmospheric factors derived from the refractive index, temperature, operating wavelength and

Downloaded From: https://www.spiedigitallibrary.org/conference-proceedings-of-spie on 12/17/2017 Terms of Use: https://www.spiedigitallibrary.org/terms-of-use

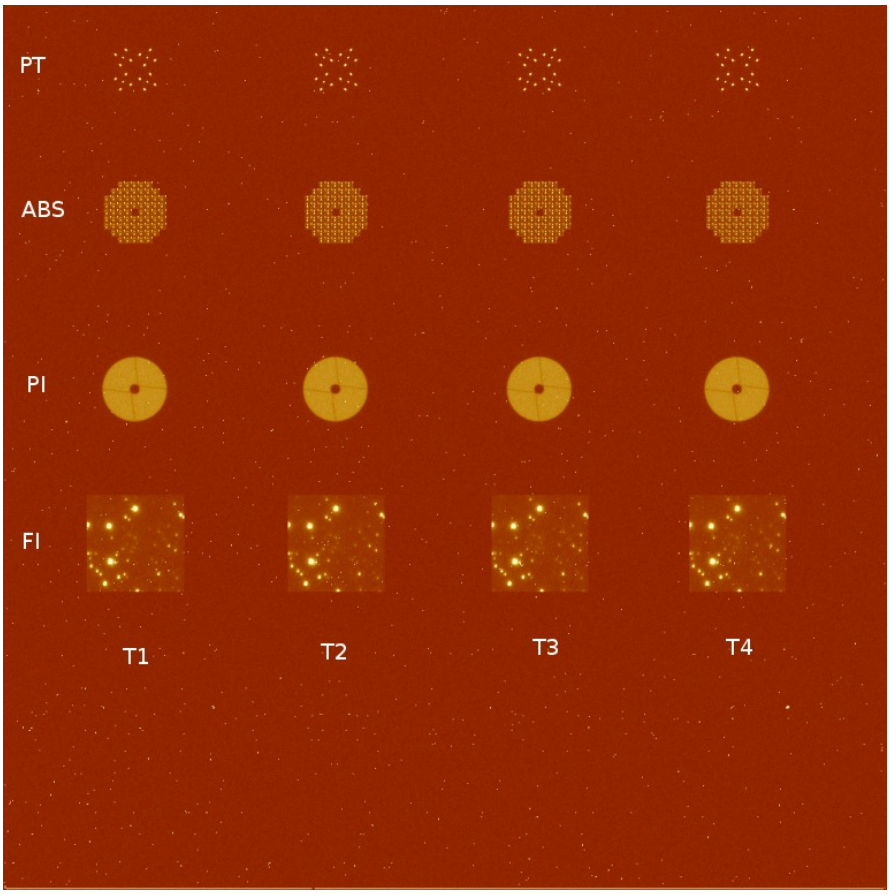

Figure 7. The final detector image. All four telescope beams are imaged on 2048×2048 pixel detector in a column wise. Each row indicates a particular imaging function of all four telescopes. The PT, ABS, PI, FI abbreviates to the pupil tracker, the aberration sensor, the pupil imager and the field imager.

reference wavelength, and zenith angle of the star. The goal of the field imager algorithm is to compute the position altered by the tip-tilts by offsetting the atmospheric differential refraction effects.

An important parameter in calculating the atmospheric differential refraction effects is the effective wavelength. Generated the atmospheric differential induced images for zenith angle starting from zero to 60 degrees. For each such image, measured the atmospheric biased centroid error. The centroid error is presented in the Fig. 8 with representation of black solid line with error bars. From this plot, best fit effective wavelength has been found (blue line) which predicts the same centroid biased shifts.

For our convenience the true object position, the tilted object position and the atmospheric differential refraction effected object position are represented as (x_0, y_0), $(x_{\mathrm{T}}, y_{\mathrm{T}})$ and $(x_{\mathrm{A}}, y_{\mathrm{A}})$ respectively. The software has three important tasks to compute to find the true object position which is altered by the tunnel seeing: a) scans for objects in a given science field, if found, estimates the brightest object position roughly; b) computes the accurate center of the brightest object using 2d Gaussian fit based on rough estimate; 3) Offset the atmospheric differential refraction effects on the measured centroids as explained below

As presented in Fig. 2, the circle indicates the $2'' \times 2''$ diameter of the search field. As a starting step the software filter out the hot pixels, cosmic rays using a threshold minimum and a threshold maximum. Also this step concludes if there is no object data found. If the object data is available, it extracts the objects in the image using aperture photometry. Then the objects were sorted out using the flux order. By knowing the brightest object rough position, computes a two dimensional Gaussian fit on the object. Due to the atmospheric differential effects the Gaussian fit centroid position is biased. The centroid position has the both tip-tilts and

Downloaded From: https://www.spiedigitallibrary.org/conference-proceedings-of-spie on 12/17/2017 Terms of Use: https://www.spiedigitallibrary.org/terms-of-use

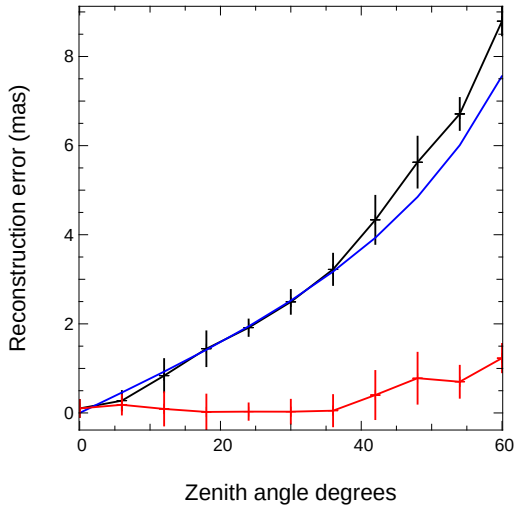

Figure 8. The black line with error bars indicates the atmospheric differential refraction biased centroid error $(y_{\mathrm{A}} - y_0)$ for a given zenith angle. The blue line is the predicted atmospheric differential centroid shift using the effective wavelength. The red line indicates the absolute reconstruction error of the true centroid of the object which is altered by the tip-tilt after offsetting the atmospheric differential refraction effects.

atmosphere differential effects $(x_{\mathrm{T+A}}, y_{\mathrm{T+A}})$. The atmospheric differential refraction bias was corrected using the effective wavelength predicted shift. Which gives the centroid position of the object $(x_{\mathrm{T}}, y_{\mathrm{T}})$ only altered by the tip-tilt. The flow chart of the software is presented in Fig. 9.

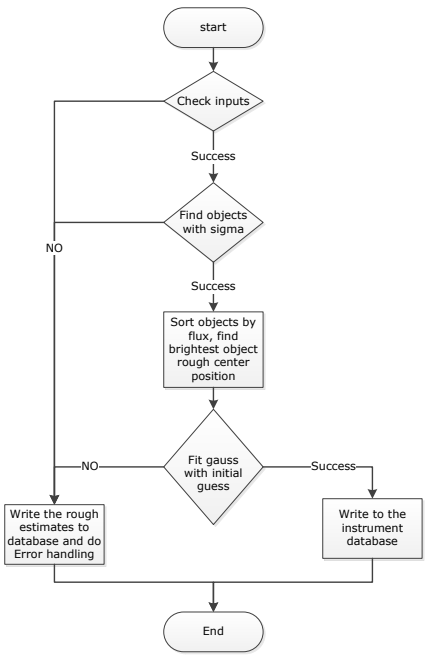

Figure 9. The field imager pipeline flow chart.

We investigated the atmospheric differential refraction effects on a 13 magnitude H-band Galactic Center object. The atmospheric differential refraction Galactic Center image was constructed. On this image applied the known tip-tilts. The inputted tip-tilts were reconstructed using the above explained procedure. The results are presented in Fig. 8. The red line indicates the absolute difference between the input tip-tilt and measured tip-tilt.

Downloaded From: https://www.spiedigitallibrary.org/conference-proceedings-of-spie on 12/17/2017 Terms of Use: https://www.spiedigitallibrary.org/terms-of-use

The measured tip-tilt measurements are used to feed the light efficiently into a single mode fibers such that it delivers the light into the integrated optics to carry the four beams interferometry.

3.3 Pupil tracking

3.3.1 Reconstruction algorithm

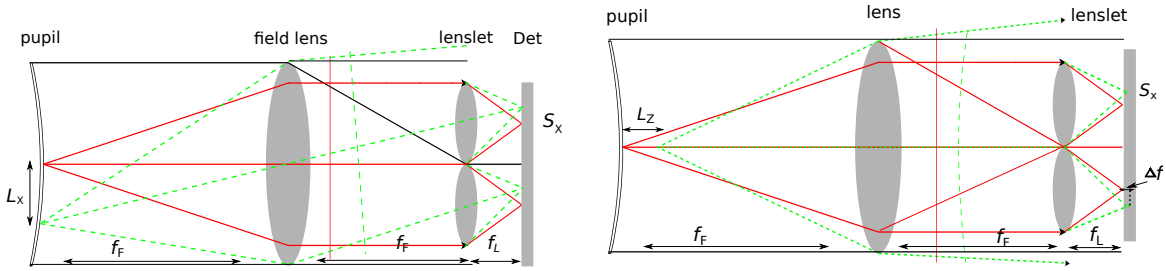

Figure 10. The left and right cartoon stands for the lateral and longitudinal pupil shifts paraxial models of the pupil tracker respectively. The f_F, f_L are the focal lengths of the field lens and the lenslet. The S_x is the spot shift resulted by the lateral (L_x) and longitudinal (L_z) pupil shifted beams. The Δf is the longitudinal defocus error.

The paraxial model of the pupil tracker is shown in Fig. 10. The pupil shifts have been demonstrated as the tilted ray (dashed line in green) with respect to the reference ray (solid line in red). By observing the spots pattern (see Fig. 5) one can estimate the telescope pupil motions instantaneously. When the telescope pupil shifted laterally, inputted beam appears as the tip-tilt beam to the lenslet. The spots formed by the lenslet are horizontally or vertically shift effective depending on the pupil shift direction. When the telescope pupil shifted longitudinally, the inputted beam to the lenslet appears as either a diverging or a converging wavefront. In a result, the lenslet forms a diverging or a converging spot pattern with respect to the shift free beam formed spots.

A typical pupil tracker image with the 4 pupil guiding lasers is presented in Fig. 5. When a pupil shift free beam falls on the lenslet, the barycenter positions are very well match with the fiber coupler reference positions. In case of a laterally shifted beam falls on the lenslet, the barycenter positions are either shifted in horizontal or vertical direction with respect to the fiber coupler reference spots. On the other hand if the pupil is longitudinally shifted, the barycenter positions are either diverged or converged with respect to the fiber coupler spots.

The pupil position shifts measurements were carried out in 2 steps: a) computes the tip, tilt and defocus aberration errors; b) The lateral pupil positions can be related to the tip-tilt aberration coefficients and while the longitudinal pupil position related to the defocus coefficient. By comparing the barycenter positions with the fiber coupler reference spots position, slopes can be computed. Using the slopes, evaluated the first three aberration coefficients (excluding piston).[12] From the Fig. 10, the tilt angle of the beam with respect to the optical axis of the lenslet is equal to beam angle subtends with the field lens optical axis

$$L_{\mathrm{x}} = \frac{S_{\mathrm{x}}}{f_{\mathrm{L}}} f_{\mathrm{F}}, \qquad L_{\mathrm{y}} = \frac{S_{\mathrm{y}}}{f_{\mathrm{L}}} f_{\mathrm{F}} \tag{2}$$

Where L_{x}, L_{x} are the lateral pupil shifts in X-Y directions.

When the defocus beam (converging or diverging) incident on the lenslet, longitudinal defocus error (Δf) is occurs (see, Fig. 10). The longitudinal defocus error results from the image formed by the lenslet being observed not at the focus of the lenslet (f_L), but at a point longitudinally displaced from it. The collimated beam resulted reference image sphere is centered at focus (f_L), and the defocussed resulted sphere located differed from f_L. The distance between the defocussed resulted sphere location to the lenslet pupil is $I_L = f_L \pm \Delta f$. The longitudinal pupil shift (L_z) is positive when the Δf is positive and vice versa. This calculations are applicable for the conventions mentioned in the Fig. 10.

The longitudinal defocus (Δf) is related to the defocus aberration coefficient (A_d) by Mahajan (1991)[13]

Downloaded From: https://www.spiedigitallibrary.org/conference-proceedings-of-spie on 12/17/2017 Terms of Use: https://www.spiedigitallibrary.org/terms-of-use

$$\Delta f = 8F_{\#}^2 A_d \tag{3}$$

The $F_{\#}$ is the ratio of the focal length of the lenslet (f_L) to the diameter (D) of lenslet.

The longitudinal pupil shift can be measured combining the above equations

$$L_z = \frac{f_F^2 \Delta f}{f_L I_L} \tag{4}$$

The acquisition camera works with a 18 mm beam (AT). We can rewrite the lateral and longitudinal shifts for the 80 mm (UT) as 4.44 [L_{x}, L_{y}, L_{z}]. The numerical factor 4.44 is the magnification between UT and AT beam sizes.

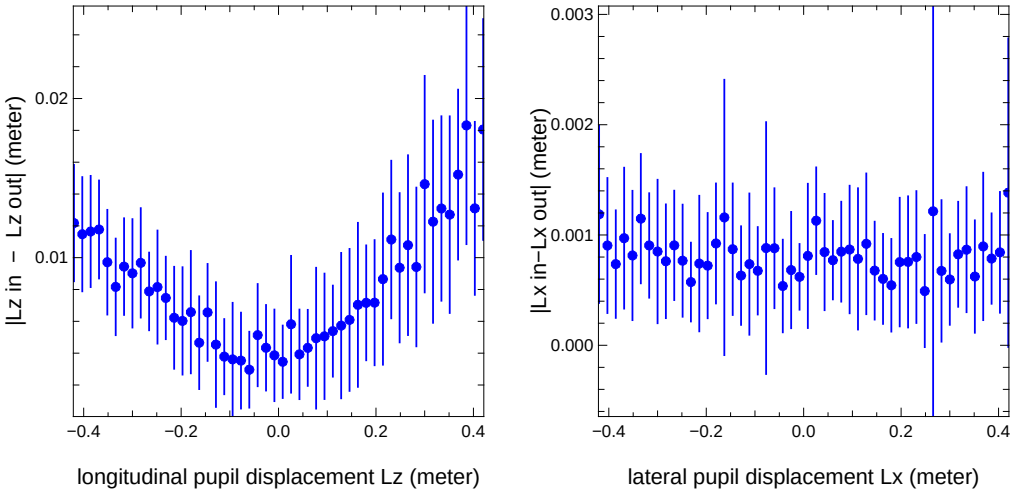

Figure 11. Pupil position reconstruction measurement accuracy for a given input pupil position displacements.

The investigation of the pupil shifts measurement accuracy has been carried out in this work. Simulated 100 pupil tracker images for known shifts with the flux of 5×10^3 photons per sub-aperture. The flux of the lasers can be tuned accordingly to fulfill above flux requirements. At each iteration, the pupil shifts were inputted compared to the measured shifts. The difference between the actual input and the measured pupil shifts is to determine the absolute pupil shift error. The Fig. 11 presents the mean and rms of the pupil shifts absolute error for the 80 mm beam (UT). The lateral and longitudinal pupil shifts were measured with the VLTI lab aberrations with an accuracy of less than 3 mm and 25 mm respectively for the UT.

The operational scenario of the pupil tracker software is presented in the Fig. 12. The flow chart consists in: a) reading the fiber coupler (reference) guess window positions from the instrument database; b) making the guess window positions for the telescope guiding laser illuminated spot positions using the reference spots and the K-mirror rotation angles; c) fitting the 2d Gaussian on each spot and evaluate the spot shifts. From them measure the tip, tilt and defocus coefficients and relate them to the pupil shifts; d) finally updates the instrument database with the pupil shifts.

These lateral pupil shifts are corrected with fiber coupler pupil guiding device. It has a flat mirror mounted on a piezo actuator to control lateral pupil motion. The longitudinal pupil shifts are corrected via variable curvature mirror of the VLTI.

3.4 Aberration sensing

3.4.1 Reconstruction algorithm

The aberration sensor evaluates the slow wavefront aberrations in the form of Zernike polynomials. The aberration sensor function carries out two important calculations: a) measurement of wavefront slopes. The wavefront

Downloaded From: https://www.spiedigitallibrary.org/conference-proceedings-of-spie on 12/17/2017 Terms of Use: https://www.spiedigitallibrary.org/terms-of-use

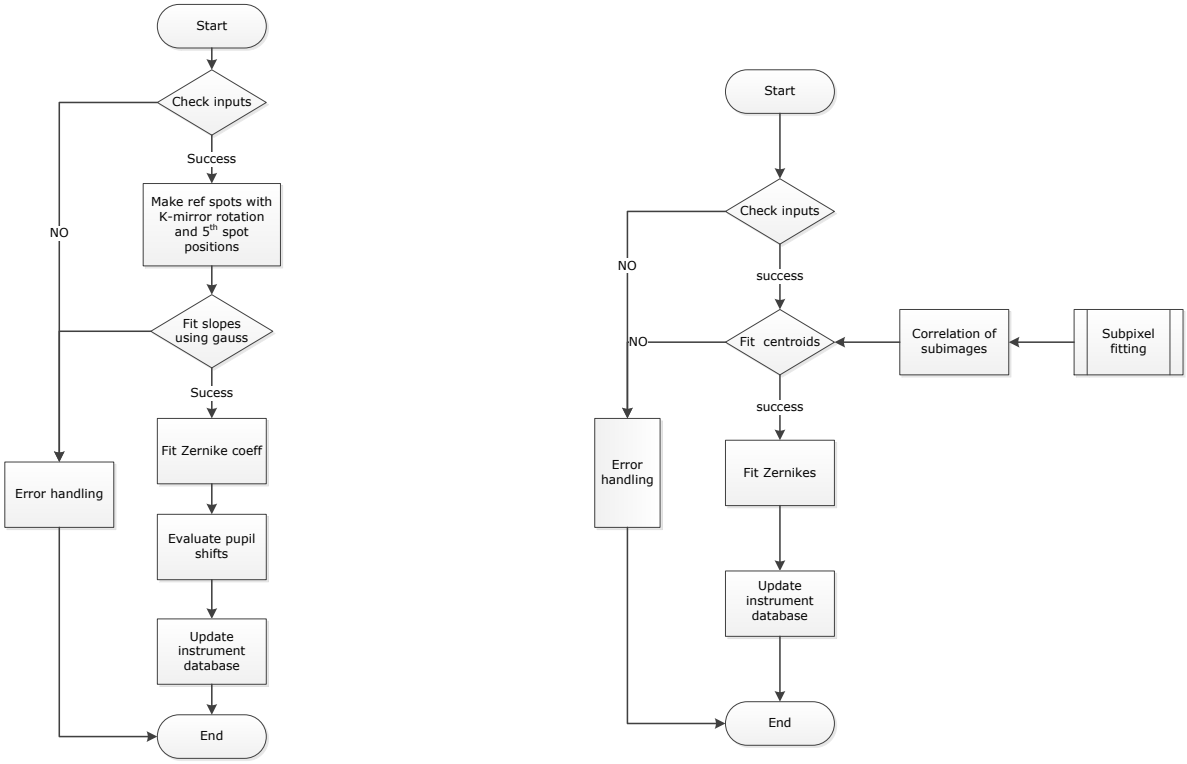

Figure 12. The pupil tracking and aberration sensing operational scenario algorithms.

slopes were calculated from the Galactic Center image using the sum of squared differences correlation (SSD) algorithm; b)relate the slopes to the Zernike polynomials. The wavefront is represented as a linear combination of Zernike polynomials (until 6th order). The full details of the wavefront reconstruction available at Anugu et al. (2014).[12]

The aberration sensor operational scenario is presented in the Fig. 12. The software starts with reading the reference window positions of the aberration sensor image grid for all four telescopes. These reference positions were automatically calibrated by a calibration software by feeding a point source light. Using the reference positions grid, extracted 16×16 pixel window Galactic Center sub-aperture images. A reference image has been generated using the available sub apertures images of the aberration sensor.[12] Using the SSD algorithm computed the image shifts between the reference image and the live aberration sensor image. The Zernike polynomial coefficients were fitted from the computed image shifts.

The Zernikes measured are used to characterize the VLTI beams quality and also plays a vital role in improving the light injection coupling efficiency of the fiber-fed beam combiner.

3.5 Pupil imaging

The pupil imager image the telescope pupils to check the pupil tracking strategy by displaying the full pupil and confirms the centering of the fiber tilt at the pupil injector. For this particular imaging function, data reduction software is not required.

4. SOFTWARE DEVELOPMENT AND OPERATIONAL SCENARIOS

All the acquisition camera software developed on the VLT2011 instrument workstation. The Common Library for Image Processing procedures are used mainly for image data reduction (CLIP).[14] This software is integrated

Downloaded From: https://www.spiedigitallibrary.org/conference-proceedings-of-spie on 12/17/2017 Terms of Use: https://www.spiedigitallibrary.org/terms-of-use

in the GRAVITY software[15].[16]

With 1 Hz rate, the acquisition camera software triggers automatic callbacks to new image events. With this, the detector acquires a new image for each callback and stores the image buffer into the shared memory. Then the acquisition camera software is provided with the image pointer. The top level procedure of the software calls its low level functions namely the field imager, the pupil tracker and the aberration sensor. The estimated parameters are then stored in the instrument database and will be used to apply the correction for the pupil position shifts, to make the efficient light coupling scheme and to characterize the telescope beam quality. These routines works online on the instrument parallel to the observations simultaneously for all telescope beams.

Each individual function of the acquisition camera software can be called at any time during the observation. The pupil imager performs at any time. The pupil tracking can be executed when the pupil guiding lasers are switched on. The field imager and aberration sensor to be used during the science observations.

5. CONCLUSIONS AND DISCUSSIONS

Presented numerical simulation of the full acquisition camera with all possible aberrations and the procedures to extract the beam aberration parameters. The input beam aberration parameters inputted during the simulation were reconstructed back accurately. As presented in Fig. 8, the field imager measures the tip-tilts with an accuracy better than 2 mas at the 1s integrated image. The pupil tracker data reduction results are presented in Fig. 11. It measures the lateral and longitudinal pupil shifts at an accuracy better than 3 mm and 25 mm respectively. The aberration sensor measures the absolute wavefront error less than 100 nm at the 2s integrated image. The pupil imager requirements are met. The accuracy measurements are within the GRAVITY specifications. Furthermore the operational scenarios of the software are presented. Presently the work presented here is now being adapted to the real instrument data.

Acknowledgments

Anugu acknowledges FCT for his PhD grant SFRH/BD/52066/2012. The research leading to these results have received funding from projects "Instrumentation second generation Very Large Telescope Interferometer" PTDC/CTE-AST/116561/2010, COMPETE FCOMP-01-0124-FEDER-019965 with grant number 226604 and the European Community's Seventh Framework Programme under Grant Agreement 312430.

REFERENCES

[1] Eisenhauer, F., Perrin, G. S., Brandner, W., Christian, Perraut, Rousselet-Perraut, K., Amorim, A., Roberto, A., Genzel, R., Kervella, P., Bohm, A., Eckart, A., Garcia, Paulo, Accardo, M., Pfuhl, O., Paumard, T., Deen, C. P., Wank, I., Gordo, P. R., Delplancke-Stroebele, F., Gillessen, S., Lacour, S., Henning, T. F., Wiest, M., Magnard, Y., Anugu, N., Finger, G., Blind, N., Clenet, Y., Hippler, S., Yazici, S., Ventura, N., Lima, J., Garcia, C., Burtscher, L., Gendron, E., Huber, A., Lazareff, B., Gitton, P., Kok, Y., Rousset, G., Klein, R., Monin, J.-L., Jakob, G. H., Sturm, E., Habois, X., Laun, W., Benisty, M., Jochum, L., Haug, M., Fedou, P., Lenzen, R., Kern, L., Kellner, S., Lapeyrere, V., Neumann, U., Lizon, J.-L., Wieprecht, E., Chapron, F., Panduro, J., Mehrgan, L. H., Ott, T., Dembet, R., Ramos, J. R., Scholler, M., Lippa, M., Sevin, A., Rohloff, R.-R., Stroebele, S., Weber, J., Collin, C., Salzinger, A., Valles, M. S., Haussmann, F., Ziegler, D., Scheithauer, S., Wittkowski, M., Hans, O., Azouaoui, N., and Yang, P., "GRAVITY: getting ready for ESO's VLT Interferometer," in [*Society of Photo-Optical Instrumentation Engineers (SPIE) Conference Series*], **9146** (2014).

[2] Pfuhl, O., Haug, M., Eisenhauer, F., Penka, D., Amorim, A., Kellner, S., Gillessen, S., Ott, T., Wieprecht, E., Sturm, E., Hauß mann, F., Huber, S., Lippa, M., Burtscher, L., Rousselet-Perraut, K., Straubmeier, C., Perrin, G., and Brandner, W., "GRAVITY: beam stabilization and light injection subsystems," in [*Optical and Infrared Interferometry III. Proceedings of the SPIE*], Delplancke, F., Rajagopal, J. K., and Malbet, F., eds., **8445**, 84451U (Sept. 2012).

Downloaded From: https://www.spiedigitallibrary.org/conference-proceedings-of-spie on 12/17/2017 Terms of Use: https://www.spiedigitallibrary.org/terms-of-use

[3] Amorim, A., Lima, J., Anugu, N., Eisenhauer, F., Graeter, A., Haug, M., Ott, T., Pfuhl, O., Thiel, M., Wieprecht, E., Carvas, P., Garcia, P., Perrin, G., Brandner, W., Straubmeier, C., and Perraut, K., "The final design of the GRAVITY acquisition camera and associated VLTI beam monitoring strategy," in [*Society of Photo-Optical Instrumentation Engineers (SPIE) Conference Series*], Delplancke, F., Rajagopal, J. K., and Malbet, F., eds., **8445**, 844534–844534–14 (Sept. 2012).

[4] Jocou, L., Perraut, K., Nolot, A., Moulin, T., Magnard, Y., Labeye, P., Lapras, V., Eisenhauer, F., Perrin, G., Amorim, A., Brandner, W., and Straubmeier, C., "The integrated optics beam combiner assembly of the GRAVITY/VLTI instrument," in [*Optical and Infrared Interferometry III. Proceedings of the SPIE*], Delplancke, F., Rajagopal, J. K., and Malbet, F., eds., **8445**, 84452X (Sept. 2012).

[5] Vdovin, G., van Brug, H., and van Goor, F., "LightPipes: software for education in coherent optics," in [*Fifth International Topical Meeting on Education and Training in Optics*], SPIE, Volume 3190, Delft, Netherlands (1997).

[6] Rigaut, F. and Van Dam, M., "Simulating Astronomical Adaptive Optics Systems Using Yao," *Proceedings of the Third AO4ELT Conference. Firenze* (2013).

[7] Lacour, S., Eisenhauer, F., Gillessen, S., Pfuhl, O., Woillez, J., Bonnet, H., Perrin, G., Lazareff, B., Rabien, S., Lapeyrere, V., Clenet, Y., and Kok, Y., "The baseline paradox of optical interferometry. Application to the GRAVITY astrometric error budget," *arXiv:1404.1014v2* , 13 (Apr. 2014).

[8] Pfuhl, O., "Quasi-static aberrations of the VLTI, VLT-TRE-GRA-15880-7103," tech. rep., GRAVITY/VLT (2011).

[9] Pfuhl, O., "Characterization of the VLTI pupil stability, VLT-TRE-GRA-15880-7102," tech. rep., GRAVITY/VLT (2011).

[10] Noll, R. J., "Zernike polynomials and atmospheric turbulence," *Optical Society of America* **66**, 207–211 (1976).

[11] Roe, H. G., "Implications of Atmospheric Differential Refraction for Adaptive Optics Observations," *Publications of the Astronomical Society of the Pacific* **114**, 450–461 (Apr. 2002).

[12] Anugu, N., Garcia, P., Amorim, A., Gordo, P., Eisenhauer, F., Perrin, G., Brandner, W., Straubmeier, C., and Perraut, K., "Near-infrared aberration tracking using a correlation algorithm on the Galactic Center," in [*Society of Photo-Optical Instrumentation Engineers (SPIE) Conference Series*], **9148** (2014).

[13] Mahajan, V. N., "Aberration theory made simple," *Tutorial Texts in Optical Engineering* (1991).

[14] Ballester,P., Biereichel,P., Kaufer,A., Kiekebusch,M., and Lorch,H., "CLIP: Bridging Pipelines to Instrument Control Software," *Astronomical Data Analysis Software and Systems ASP Conference Series* **394** (2008).

[15] Burtscher, L., Wieprecht, E., Ott, T., Kok, Y., Yazici, S., Anugu, N., Dembet, R., Fedou, P., Lacour, S., Ott, J., Eisenhauer, F., Blind, N., Genzel, R., Gillessen, S., Hans, O., Haug, Marcus, Haussmann, F., Huber, S., Janssen, A., Kellner, S., Lippa, M., Pfuhl, O., Sturm, E., Weber, J., Amorim, A., Brandner, W., Perrin, G., Straubmeier, C., Perraut, K., Schller, M., Abuter, and Roberto, "The GRAVITY instrument software/high-level software," in [*Society of Photo-Optical Instrumentation Engineers (SPIE) Conference Series*], **9146** (2014).

[16] Ott, T., Wieprecht, E., Burtscher, L., Kok, Y., Yazici, S., Anugu, N., Dembet, R., Fedou, P., Lacour, S., Ott, J., Eisenhauer, F., Blind, N., Genzel, R., Gillessen, S., Hans, O., Haug, Marcus, Haussmann, F., Huber, S., Janssen, A., Kellner, S., Lippa, M., Pfuhl, O., Sturm, E., Weber, J., Amorim, A., Brandner, W., Perrin, G., Straubmeier, C., Perraut, K., Schller, M., Abuter, and Roberto, "The GRAVITY instrument software/hardware related aspects," in [*Society of Photo-Optical Instrumentation Engineers (SPIE) Conference Series*], **9146** (2014).

Downloaded From: https://www.spiedigitallibrary.org/conference-proceedings-of-spie on 12/17/2017 Terms of Use: https://www.spiedigitallibrary.org/terms-of-use

C.6 SPIE2014b

PROCEEDINGS OF SPIE

SPIEDigitalLibrary.org/conference-proceedings-of-spie

Near-infrared aberration tracking using a correlation algorithm on the Galactic Center

Narsireddy Anugu, Paulo Garcia, Antonio Amorim, Paulo Gordo, Frank Eisenhauer, et al.

Narsireddy Anugu, Paulo Garcia, Antonio Amorim, Paulo Gordo, Frank Eisenhauer, Guy Perrin, Wolfgang Brandner, Christian Straubmeier, Karine Perraut, "Near-infrared aberration tracking using a correlation algorithm on the Galactic Center," Proc. SPIE 9148, Adaptive Optics Systems IV, 91485B (21 July 2014); doi: 10.1117/12.2055869

Event: SPIE Astronomical Telescopes + Instrumentation, 2014, Montréal, Quebec, Canada

SPIE.

Near-infrared aberration tracking using a correlation algorithm on the Galactic Center

Narsireddy Anugu[*a], Paulo Garcia[a], Antonio Amorim[c], Paulo Gordo[c], Frank Eisenhauer[b], Guy Perrin[d], Wolfgang Brandner[e], Christian Straubmeier[f] and Karine Perraut[g]

[a]Universidade do Porto, Faculdade de Engenharia, Laboratório SIM Unidade FCT no 4006, Rua Dr. Roberto Frias, s/n, 4200-465 Porto, Portugal; [b]Max Planck Institute for extraterrestrial Physics, PO Box 1312, Giessenbachstr., 85741 Garching, Germany; [c]SIM and FCUL - Edificio C8, Campo Grande, P1749016 Lisboa, Portugal; [d]Observatoire de Paris Meudon, Paris, France; [e]MaxPlanck-Institut fur Astronomie, Heidelberg, Germany; [f] Universität zu Köln Germany; [g] Institut de Planétologie et d´Astrophysique de Grenoble (IPAG), Grenoble, France

ABSTRACT

The GRAVITY acquisition camera has four 9x9 Shack-Hartmann sensors operating in the near-infrared. It measures the slow variations of a quasi-distorted wavefront of four telescope beams simultaneously, by imaging the Galactic Center field.

The Shack-Hartmann lenslet images of the Galactic Center are generated. Since the lenslet array images are filled with the crowded Galactic Center stellar field, an extended object, the local shifts of the distorted wavefront have to be estimated with a correlation algorithm. In this paper we report on the accuracy of six existing centroid algorithms for the Galactic Center stellar field. We show the VLTI tunnel atmospheric turbulence phases are reconstructed back with a precision of 100 nm at 2 s integration.

Keywords: adaptive optics, correlation algorithm, aberration sensing, wavefront sensing, optical and infrared interferometry, GRAVITY, VLTI

1. INTRODUCTION

GRAVITY is a VLTI instrument, it aims at observing the motions of sources orbiting in the vicinity of the Sgr A*, the Galactic Center Black Hole, with an astrometric accuracy of 10 micro-arc seconds. The tracking of the sources allow it to probe the physics of the Galactic Center gravitational field and general relativity effects.[1] It combines all the four Auxiliary Telescope or Unit Telescope beams with a novel integrated optics chip. The real time atmospheric turbulence aberrations are corrected with an adaptive optics system, the piston jitter is sensed by a fringe tracker to stabilize the fringes, the VLT tunnel atmospheric jitter and the pupil position motions are stabilized by a beam stabilization system and the instrument internal differential optical path difference is measured with a dedicated laser metrology. Having all these facilities, GRAVITY provides an astrometric precision of the order 10 micro-arc seconds and imaging resolution of 4 milli-arc seconds.

The acquisition camera is a subsystem of the beam stabilization system.[2,3] It is partially responsible for measuring the parameters of telescope pupil shifts induced by the VLTI delay lines, variable curvature mirrors and telescope vibrations, while taking observations. It also measures the slow wavefront residuals of atmospheric turbulence, slow variations of the wavefront induced by the tunnel seeing and the slow vibrations of the optical elements. These measurements are used to characterize the telescope beams quality and also crucial for star light injection into a fiber and to meet the accurate astrometric requirements.[3,4] The acquisition camera implements 4 optical functions. They are pupil tracking, field and pupil imaging, tip-tilt tracking and the higher order aberration measurements. The detail concepts of the acquisition camera pupil tracking and tip-tilt tracking and pupil imaging are available in Amorim et al. (2012)[2] and Anugu et al. (2014).[5]

*narsireddy.anugu@fe.up.pt

Adaptive Optics Systems IV, edited by Enrico Marchetti, Laird M. Close, Jean-Pierre Véran, Proc. of SPIE Vol. 9148, 91485B · © 2014 SPIE
CCC code: 0277-786X/14/$18 · doi: 10.1117/12.2055869

Downloaded From: https://www.spiedigitallibrary.org/conference-proceedings-of-spie on 12/17/2017 Terms of Use: https://www.spiedigitallibrary.org/terms-of-use

The aberration sensor is feed with the H-band 4" × 4" Galactic Center stellar field. It is imaged by a 9 × 9 Shack-Hartmann sensor for each telescope beam. The reconstruction of the wavefront aberrations is carried out by measuring the image shifts or slopes. The aberration sensor records an image for every 1 s.

Correlation algorithms have been used extensively in the adaptive optics community to measure the image mismatch between two images.[6–11] There are different correlation algorithms in currently in use. In this paper we investigate the performance of some of the correlation algorithms for a synthetic aberration sensor image data illuminated by the Galactic Center stellar field. The generation of synthetic data is presented in Sec.2. We investigate the accuracy of the algorithms in Sect.3, by testing them on identical images with known shifts, as well as the influence of noise and variations in intensity level. In Sect.4 we use the wavefront reconstruction methods to reconstruct the incoming distorted wavefront and study the performance of the aberration sensor.

2. SYNTHETIC GALACTIC CENTER ABERRATION SENSOR DATA

Realistic simulation of the aberration sensor synthetic data is essential to validate the accuracy and the feasibility of the reconstruction of the wavefront aberrations. The accurate generation of the aberration sensor image data involves considering the Galactic Center, VLTI tunnel atmosphere, vibrations induced by the delay line carriages and the atmospheric differential refraction effects.

The simulation of the aberration sensor data has been accomplished out in two fronts. Generated a point source illuminated Shack-Hartmann sensor image. In the second, we investigate the modeling of the Galactic Center illuminated Shack-Hartmann sensor.

2.1 VLT quasi-static aberrations

The GRAVITY system has four wavefront sensors to sense the fast wavefront aberrations of the four 4 telescope beams. The aberration sensor measures the remain quasi-static aberrations including the GRAVITY adaptive optics residuals, the slow wavefront aberrations induced by the VLTI tunnel atmosphere and the wavefront aberrations induced by instrument vibrations. To validate the aberration sensor wavefront measurement accuracy in the presence of above specified wavefront error, a phase map has been simulated with the experimentally measured aberrations. These tunnel seeing and optical vibrations induced aberrations were measured by a Shack-Hartmann sensor at the VLTI laboratory.[12] In Fig. 1, the wavefront aberrations which were reconstructed in the form of Zernike coefficients are presented. The Zernike coefficients (rms wavefront error) are in lambda (633 nm) units. Using these coefficients a phase has been generated.[13]

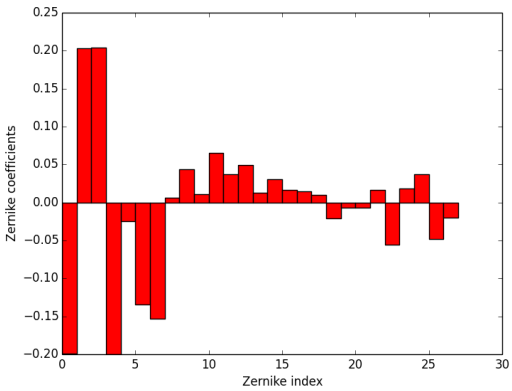

Figure 1. Typical Zernike coefficients measured at the VLTI laboratory.

Downloaded From: https://www.spiedigitallibrary.org/conference-proceedings-of-spie on 12/17/2017 Terms of Use: https://www.spiedigitallibrary.org/terms-of-use

Table 1. The aberration sensor specifications

Eff. number of sub-apertures	9×9
Full pupil size	144 × 144 pixels
Beam diameter	18 mm
Sub-aperture size pixels	16 × 16
Pixel size	250 mas
Operating wavelength	1.65 μm

2.2 Quasi-point source illuminated aberration sensor

The simulations of the quasi-plane wavefront illuminated aberration sensor have been carried out using the YAO 5.3 version.[14] The main parameters adapted in the YAO parameter file are presented in the Table. 1. In Fig. 2, a simulated Shack-Hartmann array spots which is illuminated by a point source is presented. By applying a weighted centroid algorithm on each of the shifted spots we can determine its centroids. In the same figure the wavefront slopes are presented.

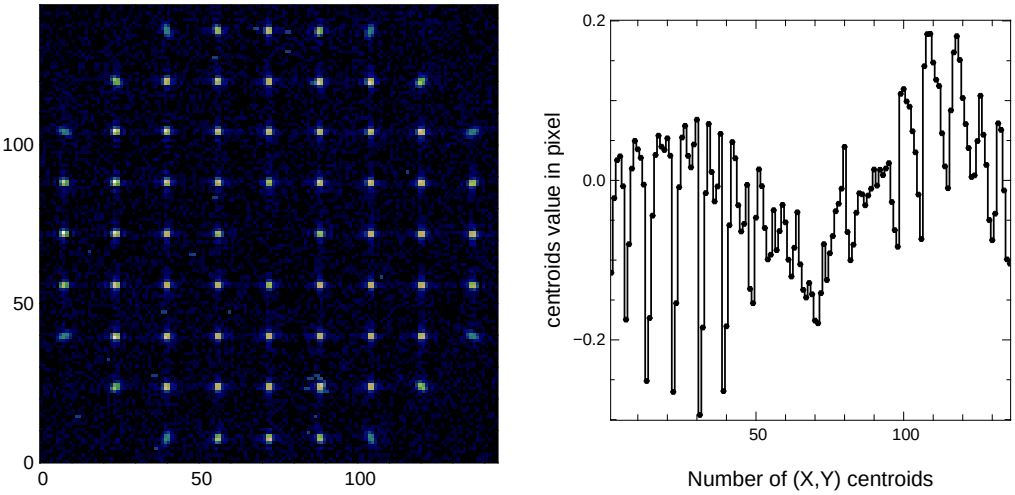

Figure 2. (left) Typical point source illuminated Shack-Hartman spots. This image is mapped into 144 × 144 pixels with a pixel scale of 250 mas. (Right) The slopes evaluated from this image which were induced by the VLT aberrations.

2.3 The Galactic Center illuminated aberration sensor

To model the Galactic center illuminated aberration sensor data, a NACO Galactic Center image was obtained from the ESO archive. The Galactic Center image was first interpolated to the aberration sensor pixel scale and then convolved with the point spread function of the sub-aperture. This image was projected on the Shack-Hartmann lenslet grid. This image represents the VLT aberrations free aberration sensor image.

A set of 100 images are simulated with different readout noise, photon noise and the VLT aberrations. The readout and photon noise are introduced using the Gaussian and Poisson statistics. With regards to the VLT aberrations, it is applied on the aberration sensor image with the following methods explained below.

2.3.1 Fourier transform shifting

The Galactic Center illuminated aberration sensor imagelet was generated by applying the VLT aberrations in the Fourier plane of the Galactic Center image. The VLT aberrations (Fig. 3) projected on the lenslet, was divided into several pieces equal to the sub-aperture size. Each piece of the phase $\phi(u, v)$ applied on the sub-aperture Galactic Center using Eq. 1. Finally the photon and read out noise synthetic images are generated. The aliasing was taken care by the zero padding.

$$s_2(x, y) = FT^{-1}\Big\{FT\big[s_1(x, y)\big]\exp(-i\phi(u, v))\Big\} \tag{1}$$

Downloaded From: https://www.spiedigitallibrary.org/conference-proceedings-of-spie on 12/17/2017 Terms of Use: https://www.spiedigitallibrary.org/terms-of-use

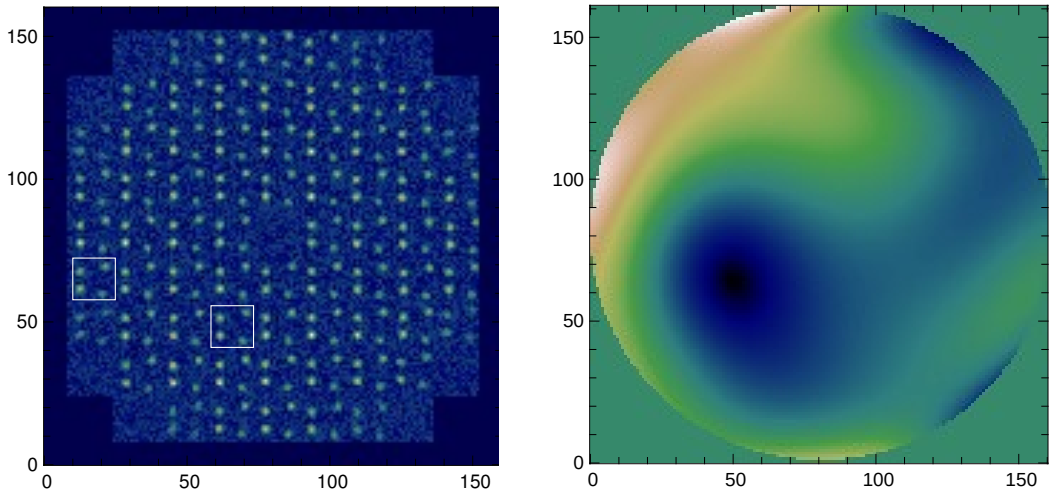

Figure 3. (left) Typical Galactic Center aberration sensor image. The square window indicates a sub-aperture image. The pixel scale is 250 mas. (Right) Numerically simulated VLT phase map.

Where $s_1(x, y)$ and $s_2(x, y)$ are the sub-aperture Galactic Center and its distorted version respectively.

2.3.2 Using point source slopes

The second technique uses the point source evaluated slopes, to apply the aberration shifts on the Galactic Center aberration sensor images. The point source shifts adapted here need to be evaluated very accurately, otherwise the shift estimation error introduces additional error to the Galactic Center imagelet. These point source resulted shifts were generated only with the aberrations. Utilizing the point source shifts (Δx, Δy) corresponding to each sub-aperture generated Galactic Center imagelets using Eq. 2. The aberration sensor images pixels were corrupted using the Poisson and Gaussian statistics.

$$s_2(x, y) = s_1(x + \Delta x, y + \Delta y) \longleftrightarrow S_2(u, v) = S_1(u, v)e^{-2\pi(u\Delta x + v\Delta y)} \tag{2}$$

Where $S_1(u, v)$ and $S_2(u, v)$ are the Fourier plane images of the sub-aperture Galactic Center and its distorted version respectively.

2.3.3 Shift-and-add method

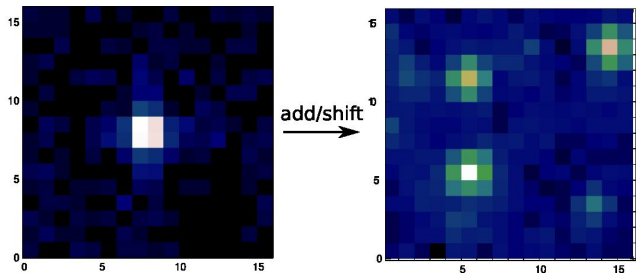

Figure 4. Shift and add method. In this method a point source was used to generate the crowded stellar field by shifting and adding.

A further technique that can be used to obtain a Galactic Center illuminated imagelet is by shifting and adding the point source lenslet spots. In general the Galactic Center image is the sum of scattered point sources. First of all the point like sources positions and fluxes in the Galactic Center image are computed. By knowing the point like sources position and their flux, generated artificial Galactic Center image using the point source illuminated

Downloaded From: https://www.spiedigitallibrary.org/conference-proceedings-of-spie on 12/17/2017 Terms of Use: https://www.spiedigitallibrary.org/terms-of-use

lenslet spot. The VLT aberrations introduced to the point source lenslet spots are also preserved in the Galactic Center aberration sensor. Finally the aberration sensor image pixels include the Poisson and Gaussian statistics.

The aberration sensor image simulated using the above three methods are compared for the wavefront reconstruction in the Sec. 4.

3. CORRELATION ALGORITHMS

3.1 Generation of reference image

The centroid estimate of the aberration sensor is computed by finding the mismatch between a reference and the live aberration sensor image. A critical aspect in estimating the image shift accurately is choosing the best reference image. Normally one can pick a reference sub-aperture image from the available sub-aperture images. But the centroid measurement introduces additional error if the random reference window is not centered (locally tilt). This problem can be solved by the long exposure, where the image is centered and tilt free.

Generation of a reference image starts with selecting a set of good signal-to-noise ratio sub-aperture images available within a single frame of the aberration sensor. Using these images, a long exposure reference image can be constructed by using the following procedure. For each image the position of the bright spot is computed. It is centered by shifting the bright spot to the position corresponding to zero pixel. The centering has been implemented to a sub-pixel precision. Finally, all sub-aperture images were averaged to compute the long exposure image.

3.2 Algorithms

The centroid measurement is the critical part of the reconstruction of the aberrated wavefront. Different correlation algorithms have been referred in the literature based on the performance and computational load. The solar physics adaptive optics community has been extensively using these correlation algorithms to track the solar granules.[9–11] Some of the algorithms have been listed in Table 2.

Table 2. Correlation algorithms, I_0, I_L reference and live images, * is complex conjugation, $\bar{I}_0$ is the mean intensity of I_0.

Name	Correlation coefficient
Cross correlation, image domain (CCI)	$\sum I_L(x \pm \Delta x, y \pm \Delta y) \times I_0(x, y)$
Cross correlation, Fourier domain (CCF)	$FT^{-1}\{FT[I_L(x \pm \Delta x, y \pm \Delta y)] \times FT^*[I_0(x, y)]\}$
Sum of square difference (SSD)	$\sum \left[I_L(x \pm \Delta x, y \pm \Delta y) - I_0(x, y)\right]^2$
Zero mean sum of square difference (ZSSD)	$\sum \left[\left(I_L(x \pm \Delta x, y \pm \Delta y) - \bar{I_L}\right) - (I_0(x, y) - \bar{I_0})\right]^2$
Sum of absolute difference function (SAD)	$\sum \left\lvert I_L(x \pm \Delta x, y \pm \Delta y) - I_0(x, y)\right\rvert$
Zero mean sum of absolute difference (ZSAD)	$\sum \left\lvert \left[I_L(x \pm \Delta x, y \pm \Delta y - \bar{I_L}\right] - \left[I_0(x, y) - \bar{I_0}\right]\right\rvert$
Sum of absolute difference squared (SADS)	$\left[\sum \lvert I_L(x \pm \Delta x, y \pm \Delta y) - I_0(x, y)\rvert\right]^2$

The image shifts are measured by evaluating the mismatch measurement between the live window I_L and the reference window (I_0). Before the mismatch search process begins, the live window is zero padded (cf. Fig.5). The live window and the reference window have the pixel sampling of $M \times M$ and $N \times N$ respectively after the zero padding. During the correlation search process, for each iteration the search window is extracted from the live window in the integer pixel increments. The search window size is equal to the reference window size. For each such integer pixel increment step evaluated the correlation coefficient between the search and the reference window. The resulted correlation coefficient is placed in a two dimensional array (r, c). For the CCI, CCF the best matched center position situated at the correlation coefficient maxima. On the other hand the SSD, ZSSD, SAD, ZSAD, and SADS algorithms score the best matching position where the coefficient is minimum. The center of the correlation image peak or valley can be evaluated to sub-pixel precision level using a parabola fit with 5 pixels around the maxima or the minima.[8] The Fig. 5, shows the search window, zero padded live image and the reference window.

Downloaded From: https://www.spiedigitallibrary.org/conference-proceedings-of-spie on 12/17/2017 Terms of Use: https://www.spiedigitallibrary.org/terms-of-use

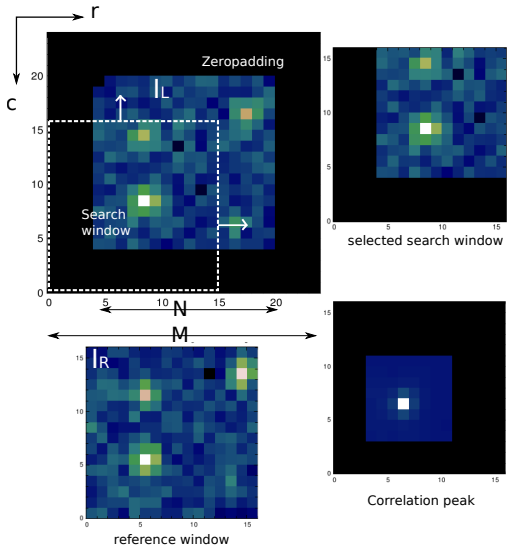

Figure 5. Implementation of the centroid computation using a correlation algorithm. The live image is zero padded. A search window is selected from the zero padded live image (top left). The dashed window shows the first selection of the search window. For each iteration the selection of the images is carried out with an increment of a pixel in horizontal direction followed by the vertical direction. For each such increment the correlation coefficient between the search window and the reference window is computed (bottom right). The correlation coefficient value is stored in an array. A typical correlation peak has been shown for the CCI algorithm.

In order to minimize the computational cost in the SSD and the SAD type algorithms, clipping of the rows and the columns of the search window and the reference window are implemented. This not only saves the computational load but also cuts out any noise information present in the edges of the windows. In the case of the CCF it is necessary to zero-pad the sub-aperture images before calculation of the image correlation to avoid aliasing in the Fourier transform.[15]

Lofdahl et al.[9] reviewed the SSD, CCI, CCF, SAD algorithms with an artificial data and pointed out that the SSD and SAD are the best in performance with the others. However, his work computes the similarity between the live window and the reference window by moving the search window in the integer pixel increments. This integer pixel increment limits the accuracy of the shift measurement. We propose a dub-pixel precision movement of the search window to improve the accuracy of the shift measurement at the expense of computational load.

3.2.1 Sub-pixel increments

In order to perform the image with a sub-pixel, the search window was interpolated. We reviewed the interpolation algorithms, in particular, the linear, the cubic splines and the Akima interpolation methods studying the performance of the accurate re-sampling of the live window. The interpolation algorithms have been implemented using the YORICK and GNU scientic libraries. The study reveals that the cubic splines are very accurate at the presence of smooth data. On the other hand when data got hot pixels the cubic splines oscillates badly. Throughout this work we chose the cubic splines as the bad pixels are corrected by the pre-processing software.

In Fig. 6, the integer pixel increment algorithm is presented. In the Fig. 7 the sub-pixel increment algorithm is presented. It can be see that the sub-pixel algorithm performs better than the former.

3.3 Comparative analysis with the Galactic Center image

Comparison of the correlation algorithms was performed by giving input shifts (x_0, y_0) to the Galactic Center image and measuring back the input shifts (x_c, y_c). The aberration sensor image was integrated for 2s, which counts to 2000 photos per sub aperture. The image was corrupted by the Poisson and readout noise. The Figs.

Downloaded From: https://www.spiedigitallibrary.org/conference-proceedings-of-spie on 12/17/2017 Terms of Use: https://www.spiedigitallibrary.org/terms-of-use

6, 7 present an absolute error in the measurement for the case of integer pixel increment algorithm and sub-pixel increment algorithm. The absolute centroid error (ACE) is defined as

$$ACE = \sqrt{(x_0 - x_c)^2 + (y_0 - y_c)^2} \tag{3}$$

In this simulation, the absolute centroid error was evaluated from the mean of a set of 100 realizations.

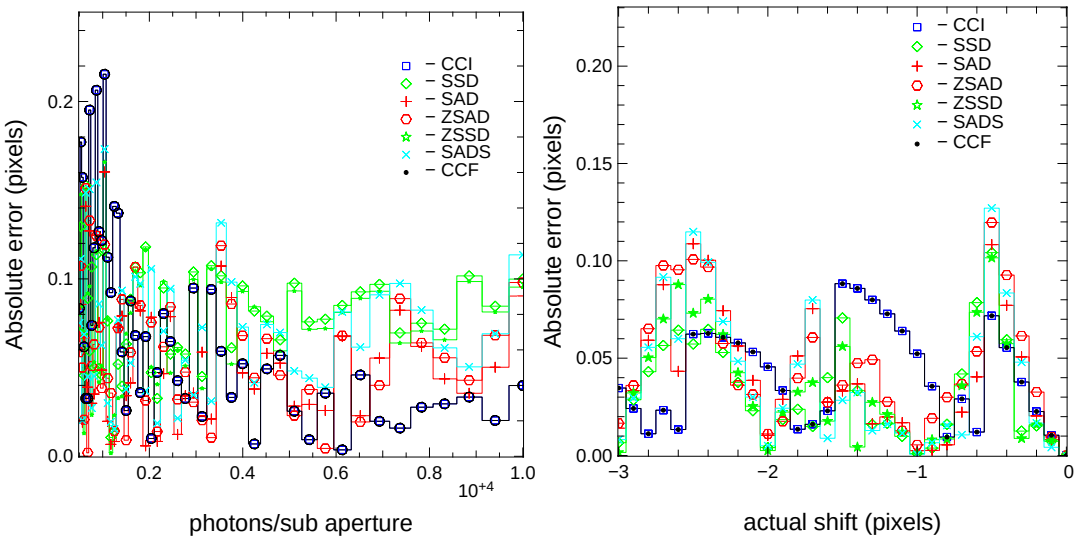

Figure 6. The integer pixel increment of the search window algorithm. (Left) The correlation algorithms compared on the Galactic Center image at the different photons per sub-aperture. (Right) The absolute centroid error for the true input shifts. The CCI, CCF, SSD, ZSSD, SAD, ZSAD and SADS algorithms are represented with a square, solid circle, diamond, star, circle, plus and cross mark symbols respectively.

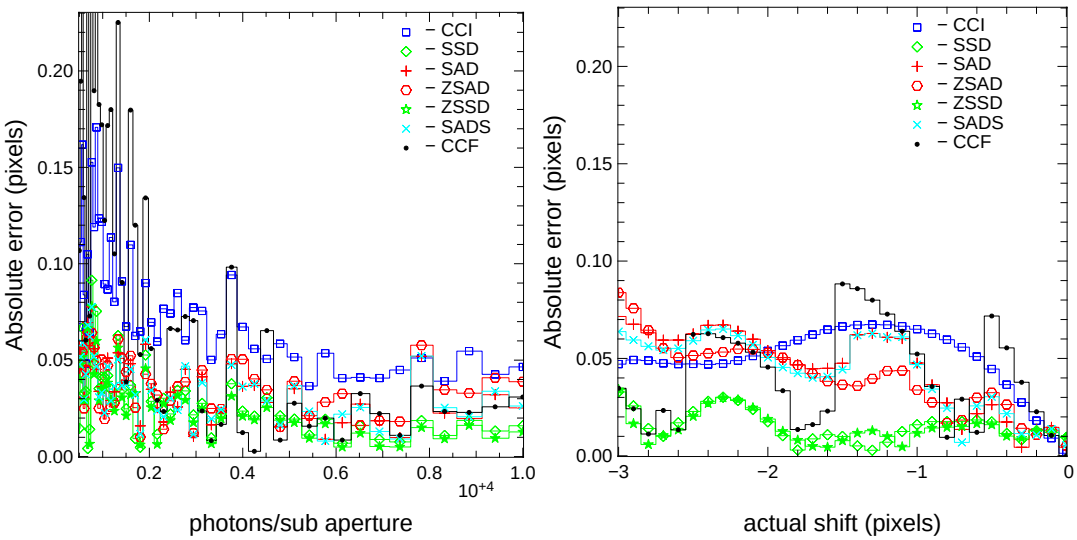

Figure 7. The sub-pixel increment of the search window applied for all algorithms except the CCF.

We investigated the correlation algorithms accuracy with a number of photons available for each sub-aperture. From the Fig. 7, it can be seen that centroid measurement error is minimum when the flux increases for all given algorithms. Also it can be seen that the ZSSD and SSD algorithms are giving less centroid error. The algorithm pairs SSD, ZSSD and SAD, ZSAD and SSD, SAD are in the tight correlation. The ZSSD algorithm

Downloaded From: https://www.spiedigitallibrary.org/conference-proceedings-of-spie on 12/17/2017 Terms of Use: https://www.spiedigitallibrary.org/terms-of-use

requires more computational load with respect to the SSD. So we chose SSD correlation algorithm to compute the centroids.

3.3.1 Investigation of atmospheric differential refraction

The wavelength dependency of the refraction index of the atmosphere causes the star beam to be smear.[16] The aberration sensor has considerable unwanted illumination from J-band where as the central operating wavelength is at H-band. Due to the atmospheric differential refraction, a star shifted around 0.07 arc sec, 17 arc sec in the sky at a wavelengths of 2.25 and 1.0 μm respectively. The elongation causes the aberration sensor image to be spread out, resulting in a decrease in the signal-to-noise ratio, in turn, leads to an increase in centroid measurement error.

In order to account this error, atmospheric differential refraction affected aberration sensor image were constructed considering the 13th H-band magnitude star, using the Paranal observatory conditions and the optical throughput for the aberration sensor. We studied that the atmospheric differential refraction induced absolute centroid error, that is less than 0.01 px.

4. ESTIMATING THE ABERRATION COEFFICIENTS

To determine the wavefront aberrations at the lenslet plane, one requires two sets of image centroid positions. One set is obtained from the reference image, and the other from the live image. The reference image centers are measured with a point source in the lab. The live image centers are measured online by using the cross correlation algorithm. By comparing the reference center positions with the live center ones, we can obtain an array of the shifts $(\Delta x, \Delta y)$. Each element of this array is the local slope of the wavefront at the corresponding lenslet position. The local slopes allow reconstructing the complete wavefront error by a model wavefront reconstruction method.

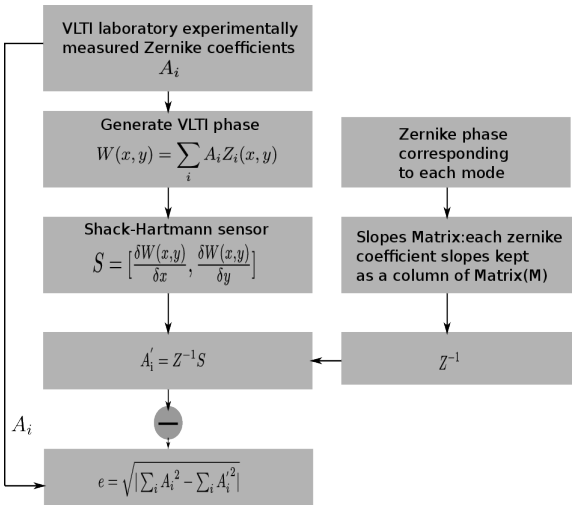

Figure 8. The absolute wavefront error reconstruction method.

The shifts corresponding to the tunnel seeing are computed between each sub-aperture image by performing the SSD cross correlation algorithm using the reference window.

In order to validate the wavefront aberrations measurement characterization, the Galactic Center illuminated image was corrupted by the VLT aberrations, the Poisson and readout noise. For each set of parameters, a Monte-Carlo simulation included 100 random realizations. At each iteration, the true wavefront inputted was compared to the measured wavefront. The difference between the actual input and the measured wavefront allow it to determine the absolute wavefront error. In Fig. 8, the absolute wavefront error computational procedure is presented. In the Fig. 9, a typical Zernike coefficients measured from the aberration sensor image are presented.

A comparison of the wavefront absolute error computed for the extended object generation methods is presented in the Fig. 10. The measured absolute wavefront error for the "shift-and-add" and the "point source slopes"

Downloaded From: https://www.spiedigitallibrary.org/conference-proceedings-of-spie on 12/17/2017 Terms of Use: https://www.spiedigitallibrary.org/terms-of-use

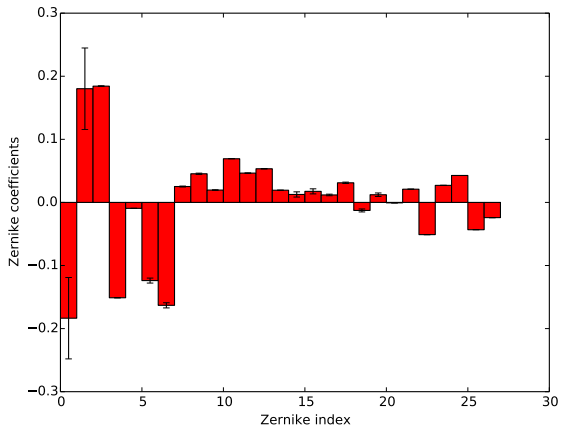

Figure 9. The Zernike coefficients measured from the aberration sensor image. This image was distorted with the VLT aberrations.

methods are in good correlation with the point source wavefront error. The "point source slopes" method uses the generated slopes or shifts information from the point source algorithm. These slopes have intrinsic centroid computation error. When these slopes or shifts are used the absolute wavefront error measured has additional error. That is why the "point source slopes" method absolute wavefront error is slightly above the "shift-and-add" method. It can be see that the absolute wavefront error is less than 100 nm at 2000 photons per sub-aperture.

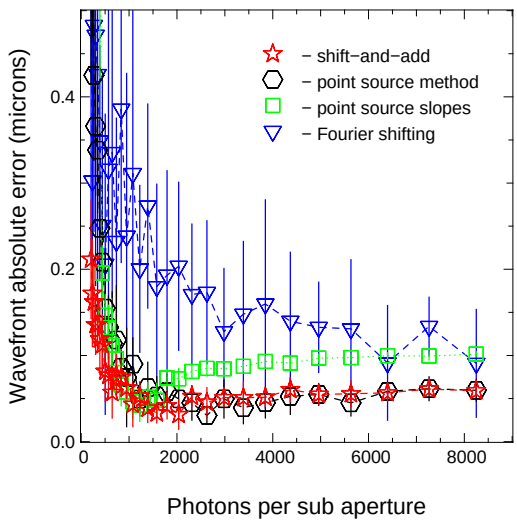

Figure 10. The absolute wavefront error for the algorithms. The square, the star and the down triangle represents the Galactic Center aberration simulation algorithms namely the "point source slopes", the "shift-and-add" and the "the direct Fourier shifting method using direct phase" algorithms respectively. The polygon represents the point source illuminated aberration sensor.

The aberration sensor software has been implemented on the VLT2011 instrument workstation using the Common library for Image Processing library. When the aberration sensor function is called, the software extracts the four aberration sensor images for the four telescopes from the acquisition camera detector image. On each telescope aberration sensor image applies the SSD algorithm to find the image shifts. Using the image shifts information constructs the Zernike polynomials up to the 6th order. The evaluated parameters are stored in the database for further usage. Full details of the software operational scenario can be found at Anugu et al. (2014).[5]

Downloaded From: https://www.spiedigitallibrary.org/conference-proceedings-of-spie on 12/17/2017 Terms of Use: https://www.spiedigitallibrary.org/terms-of-use

5. DISCUSSIONS AND CONCLUSIONS

A simulation of the Galactic Center aberration sensor is reported. A comparative study of the different correlation algorithms is presented. From the shift measurement and the flux analysis study using the Galactic Center image reveals that the ZSSD and SSD are the best in comparison with the others (cf. Fig. 7). According to the results shown in the Fig. 10, we can see that the wavefront error is less than 100 nm for the point and extended source at 2000 photons per sub-aperture (2s integration) by considering the acquisition camera noise sources. Furthermore the point source algorithm is within the GRAVITY specifications. The extended case accuracy results are slightly above the requirements. The work presented here is now being adapted to the real aberration sensor instrument data. A two star field aberration sensor data has been acquired at the MPE laboratory. The VLT aberrations are implemented in the laboratory using the phase screens. This data allows studying more elaborately the feasibility of the code.

6. ACKNOWLEDGMENTS

Anugu acknowledges FCT for his PhD grant SFRH/BD/52066/2012. The research leading to these results have received funding from projects "Instrumentation second generation Very Large Telescope Interferometer" PTDC/CTE-AST/116561/2010, COMPETE FCOMP-01-0124-FEDER-019965, with grant number 226604 and the European Community's Seventh Framework Programme under Grant Agreement 312430.

REFERENCES

[1] Eisenhauer, F., Perrin, G. S., Brandner, W., Christian, Perraut, Rousselet-Perraut, K., Amorim, A., Roberto, A., Genzel, R., Kervella, P., Bohm, A., Eckart, A., Garcia, Paulo, Accardo, M., Pfuhl, O., Paumard, T., Deen, C. P., Wank, I., Gordo, P. R., Delplancke-Stroebele, F., Gillessen, S., Lacour, S., Henning, T. F., Wiest, M., Magnard, Y., Anugu, N., Finger, G., Blind, N., Clenet, Y., Hippler, S., Yazici, S., Ventura, N., Lima, J., Garcia, C., Burtscher, L., Gendron, E., Huber, A., Lazareff, B., Gitton, P., Kok, Y., Rousset, G., Klein, R., Monin, J.-L., Jakob, G. H., Sturm, E., Habois, X., Laun, W., Benisty, M., Jochum, L., Haug, M., Fedou, P., Lenzen, R., Kern, L., Kellner, S., Lapeyrere, V., Neumann, U., Lizon, J.-L., Wieprecht, E., Chapron, F., Panduro, J., Mehrgan, L. H., Ott, T., Dembet, R., Ramos, J. R., Scholler, M., Lippa, M., Sevin, A., Rohloff, R.-R., Stroebele, S., Weber, J., Collin, C., Salzinger, A., Valles, M. S., Haussmann, F., Ziegler, D., Scheithauer, S., Wittkowski, M., Hans, O., Azouaoui, N., and Yang, P., "GRAVITY: getting ready for ESO's VLT Interferometer," in [*Society of Photo-Optical Instrumentation Engineers (SPIE) Conference Series*], **9146** (2014).

[2] Amorim, A., Lima, J., Anugu, N., Eisenhauer, F., Graeter, A., Haug, M., Ott, T., Pfuhl, O., Thiel, M., Wieprecht, E., Carvas, P., Garcia, P., Perrin, G., Brandner, W., Straubmeier, C., and Perraut, K., "The final design of the GRAVITY acquisition camera and associated VLTI beam monitoring strategy," in [*Society of Photo-Optical Instrumentation Engineers (SPIE) Conference Series*], Delplancke, F., Rajagopal, J. K., and Malbet, F., eds., **8445**, 844534–844534–14 (Sept. 2012).

[3] Pfuhl, O., Haug, M., Eisenhauer, F., Penka, D., Amorim, A., Kellner, S., Gillessen, S., Ott, T., Wieprecht, E., Sturm, E., Hauß mann, F., Huber, S., Lippa, M., Burtscher, L., Rousselet-Perraut, K., Straubmeier, C., Perrin, G., and Brandner, W., "GRAVITY: beam stabilization and light injection subsystems," in [*Optical and Infrared Interferometry III. Proceedings of the SPIE*], Delplancke, F., Rajagopal, J. K., and Malbet, F., eds., **8445**, 84451U (Sept. 2012).

[4] Lacour, S., Eisenhauer, F., Gillessen, S., Pfuhl, O., Woillez, J., Bonnet, H., Perrin, G., Lazareff, B., Rabien, S., Lapeyrere, V., Clenet, Y., and Kok, Y., "The baseline paradox of optical interferometry. Application to the GRAVITY astrometric error budget," *arXiv:1404.1014v2* , 13 (Apr. 2014).

[5] Anugu, N., Garcia, P., Wieprecht, E., Burtscher, L., Ott, T., Antonio, A., Gordo, P., Eisenhauer, F., Perrin, G., Brandner, W., Straubmeier, C., and Perraut, K., "The GRAVITY/VLTI acquisition camera software," in [*Society of Photo-Optical Instrumentation Engineers (SPIE) Conference Series*], **9146** (2014).

[6] Rimmele, T. R. and Radick, R. R., "Solar adaptive optics at the National Solar Observatory," *Proc. SPIE Vol. 3353* **3353**, 72–81 (1998).

Downloaded From: https://www.spiedigitallibrary.org/conference-proceedings-of-spie on 12/17/2017 Terms of Use: https://www.spiedigitallibrary.org/terms-of-use

[7] Scharmer, G. B., Dettori, P. M., Lofdahl, M. G., and Shand, M., "Adaptive optics system for the new Swedish solar telescope," *Innovative Telescopes and Instrumentation for Solar Astrophysics. Edited by Stephen L. Keil* **4853**, 370–380 (2003).

[8] Poyneer, L. A., La Fortune, K., and Chan, C., "Scene-based wavefront sensing for remote imaging," in [*Advanced Wavefront Control: Methods*], Gonglewski, J. D., Vorontsov, M. A., and Gruneisen, M. T., eds., **5162**, 91–102 (Dec. 2003).

[9] Löfdahl, M. G., "Evaluation of image-shift measurement algorithms for solar Shack-Hartmann wavefront sensors," *Astronomy & Astrophysics* **524**, A90 (Nov. 2010).

[10] Martin, J. and Crowley, J. L., "Experimental comparison of correlation techniques," in [*IAS-4, International Conference on Intelligent Autonomous Systems*], (1995).

[11] Rimmele, T. R. and Marino, J., "Solar Adaptive Optics," *Living Reviews in Solar Physics* **8** (2011).

[12] Pfuhl, O., "Quasi-static aberrations of the VLTI, VLT-TRE-GRA-15880-7103," tech. rep., GRAVITY/VLT (2011).

[13] Noll, R. J., "Zernike polynomials and atmospheric turbulence," *Optical Society of America* **66**, 207–211 (1976).

[14] Rigaut, F. and Van Dam, M., "Simulating Astronomical Adaptive Optics Systems Using Yao," *Proceedings of the Third AO4ELT Conference. Firenze* (2013).

[15] Press, W. H., Teukolsky, S. A., Vetterling, W. T., and Flannery, B. P., [*Numerical Recipes 3rd Edition: The Art of Scientific Computing*], Cambridge University Press (2009).

[16] Roe, H. G., "Implications of Atmospheric Differential Refraction for Adaptive Optics Observations," *Publications of the Astronomical Society of the Pacific* **114**, 450–461 (Apr. 2002).

Downloaded From: https://www.spiedigitallibrary.org/conference-proceedings-of-spie on 12/17/2017 Terms of Use: https://www.spiedigitallibrary.org/terms-of-use

Appendix D

Co-author publications

D.1 Peer-reviewed

- GRAVITY collaboration et al. [including N. Anugu], "First light for GRAVITY: Phase referencing optical interferometry for the Very Large Telescope Interferometer", **A&A, 602, A94 (2017)**, https://doi.org/10.1051/0004-6361/201730838.

- GRAVITY collaboration et al. [including N. Anugu], "Submilliarcsecond Optical Interferometry of the High-mass X-Ray Binary BP Cru with VLTI/GRAVITY", **APJ, 844, 1 (2017)**, http://iopscience.iop.org/article/10.3847/1538-4357/aa79f1/meta.

- GRAVITY collaboration et al. [including N. Anugu], "Accretion-ejection morphology of the microquasar SS 433 resolved at sub-au scale", **A&A, 602, L11 (2017)**, https://doi.org/10.1051/0004-6361/201731038.

- GRAVITY collaboration et al. [including N. Anugu], "The wind and the magnetospheric accretion onto the T Tauri star S Coronae Australis at sub-au resolution", **A&A (2017)**, https://doi.org/10.1051/0004-6361/201731058.

- S. Kraus et al. [including N. Anugu], "A High-mass Protobinary System with Spatially Resolved Circumstellar Accretion Disks and Circumbinary Disk", **APJL, 835, 1 (2017)**, http://iopscience.iop.org/article/10.3847/2041-8213/835/1/L5/meta.

D.2 Conference proceedings

- P. Gordo, A. Amorim, J. Abreu et al., "Integration and testing of the GRAVITY infrared camera for multiple telescope optical beam analysis," **Proc. SPIE, 9146, 91461V (2014)**, http://dx.doi.org/10.1117/12.2056572.

- L. Burtscher, E. Wieprecht, T. Ott et al., "The GRAVITY instrument software/high-level software", **Proc. SPIE, 9146, 91462B (2014)**, http://dx.doi.org/10.1117/12.2055928.

- T. Ott, E. Wieprecht, L. Burtscher et al., "The GRAVITY instrument software/hardware related aspects", **Proc. SPIE, 9146, 91462A (2014)**, http://dx.doi.org/10.1117/12.2055927.
- A. Amorim, J. Lima, N. Anugu et al., “The final design of the GRAVITY acquisition camera and associated VLTI beam monitoring strategy,” **Proc. SPIE, 8445, 844534 (2012)**, http://dx.doi.org/10.1117/12.925993.

Appendix E

Acquisition camera test report, VLT-TRE-GRA-15885-6305

VLTI

GRAVITY

Phase D

Acquisition camera test report

Doc. No.: VLT-TRE-GRA-15885-6305

Issue: 1.05

Date: 23.03.2015

Author(s): Narsireddy Anugu

Name Date Signature

Paulo Gordo

Name Date Signature

Proj. Manager: A. Amorim .....

Name Date Signature

Proj. Responsible F. Eisenhauer .....

Name Date Signature

TABLE OF CONTENTS

1 Scope 3
1.1 Applicable documents 3
1.2 Reference documents 3
1.3 Acronyms 4
2 Test Purpose and test objectives 5
2.1 Definitions 5
3 Telescope beam analyzer 6
3.1 Field tracker 6
3.2 Pupil tracker 13
3.3 Aberration sensor 18
3.4 Pupil imager 22
4 Control loop performance 26
4.1 Stability of field tracking and correction 26
4.2 Stability of pupil tracking and correction 26
4.3 Stability of aberration sensing 26
5 Annex I – Support notes for AC occlusion focusing test 27
6 Annex II-Shack-Hartmann slopes 29

1 Scope

The scope of this report is to check if the acquisition camera is compliant with requirements. In this report, an attempt made to verify the acquisition camera hardware and software. Ultimately the instrument shall pass in order to certify that the instrument has completed the implementation phase and is ready for commissioning.

1.1 Applicable documents

The following applicable documents (AD) of the exact issue form part of the present document to the extent specified herein.

AD Nr	Doc. Nr	Doc. Title	Issue	Date
AD1	VLT-SOW-ESO-15880-4854	GRAVITY - Statement of Work	1.0	07.07.2011
AD2	VLT-SPE-ESO-15880-4853	GRAVITY - Technical Specifications	1.0	07.07.2011

Table 1: Applicable documents.

1.2 Reference documents

The following reference documents (RD) contain useful information relevant to the subject of the present document.

RD Nr	Doc. Nr	Doc .Title	Issue	Date
RD1	VLT-PLA-GRA-15885-6301	The acquisition camera	4.0	01.03.2015
RD2	VLT-PLA-GRA-15882-9502	Calibration Plan	3.0	31.7.2011
RD3	VLT-TRE-GRA-15880-3101	GRAVITY - Beam Combiner Instrument System Design	4.0	01.03.2015
RD4	VLT-TRE-GRA-15882-3201	GRAVITY - Astrometric ErrorBudget	3.1	15.01.2012

Table 2: Reference documents.

1.3 Acronyms

AO	Adaptive Optics
AT	Auxiliary Telescope
CAN	Controller Area Network
CCL	Combined Coudé Lab
DDL	Differential Delay Line
ESO	European Southern Observatory
FoV	Field of View
HW	Hardware
ICD	Interface Control Document
I/F	Interface
IR	Infrared
LAN	Local Area Network
LCU	Local Control Unit
MAIT	Manufacture, Assembly, Integration & Testing
MPE	Max-Planck-Institut für extraterrestrische Physik (Garching)
OPD	Optical Path Difference
PAE	Preliminary Acceptance Europe
PDR	Preliminary Design Review
RTC	Real Time Computer
SCP	Service Connection Point
TBD	To Be Defined
TBC	To Be Confirmed
S/W	Software
UT	Unit Telescope
VLT	Very Large Telescope
VLTI	Very Large Telescope Interferometer
WFS	Wave Front Sensor

2 Test Purpose and test objectives

This document attempts to provide the acquisition camera performance characterisation details. It consists of preliminary results obtained during the MAIT phase.

2.1 Definitions

The acquisition camera performance accuracy is expressed in absolute, relative and rms errors.

Absolute error is defined as the difference between the measured value of a quantity and its actual value. Here the actual value is obtained from the calibration.

In this report, acquisition camera performance parameters presented are computed with respect to M1 unless otherwise specified.

Acquisition camera tests are carried out by illuminating calibration unit stars and pupil guiding lasers beams. The acquisition camera image data took with 5th magnitude neutral density filter. The performance results presented here are computed with 5th magnitude neutral density filter unless otherwise stated.

3 Telescope beam analyzer

3.1 Field tracker

3.1.1 Field tracking accuracy with input tip-tilts

Goal: Object position measurement accuracy for input tip-tilts applied

Requisites: Calibration unit lamps, tip-tilt and piston (TTP) controller

Experiment: Acquisition camera images are obtained by moving the tip-tilt device. With tip-tilt device motions, star in the field is drifted from its original.

Output: Analyzed the image data using field tracker software:

1. Calibration of TTP device voltage to field tracker pixel scale (cf. Table 3).

Table 3: Shift of a star in pixels (error ± 0.1 px) when one volt applied to the tip-tilt system

TTP: 12.olt	Tel.1 (px)	Tel.2 (px)	Tel.3 (px)	Tel.4 (px)	Detector
Y- axis	-16.85	-17.38	-17.97	-16.96	X
X– axis	15.15	15.75	15.74	15.57	Y

For the TTP device, when x volt is applied it moves field star along y-axis on the detector plane. When y voltage is applied to TTP, it moves star along negative x-direction on the detector. These values are obtained by moving the TTP for 200 steps (0.02 step size) and calculated its slope (voltage/px).

3. For each voltage step (0.02 V) applied to the TTP device (from reference [-0.84 V, -3.37 V]), an image is acquired and the star position measured in pixels coordinates. The star position in pixels is converted to M1 sky coordinates using the design 17.78 mas pixel scale. FWHM of diffraction limited star is 2.4 pixels. In a next step, the absolute and relative errors are computed using the measured value and actual value. The actual value is predicted from the calibration of voltage to pixel scale (cf. Table. 3). The tip-tilt voltages are calibrated; those are 0.302 ± 0.001 as/volt and 0.277 ± 0.001 as/volt respectively.

Fig. 1 presents the performance of finding the star position when voltage applied to TTP along the y-direction. Fig. 2 presents the performance of finding the star position when voltage applied to TTP along x-direction.

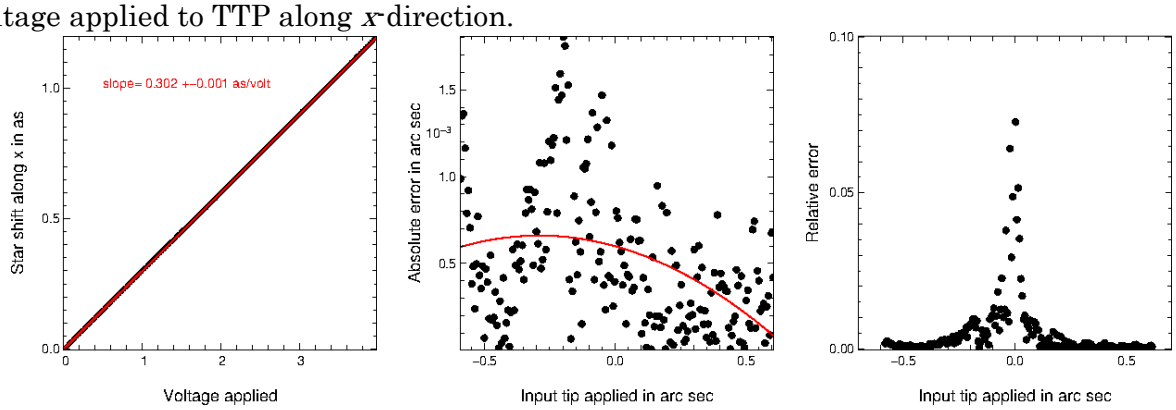

Fig.1: L*eft panel* is the calibration of voltage applied to the shift of star in arc sec (absolute value) along x-axis. *Middle panel* and *right panels* indicates the absolute error and relative error of star position measurement.

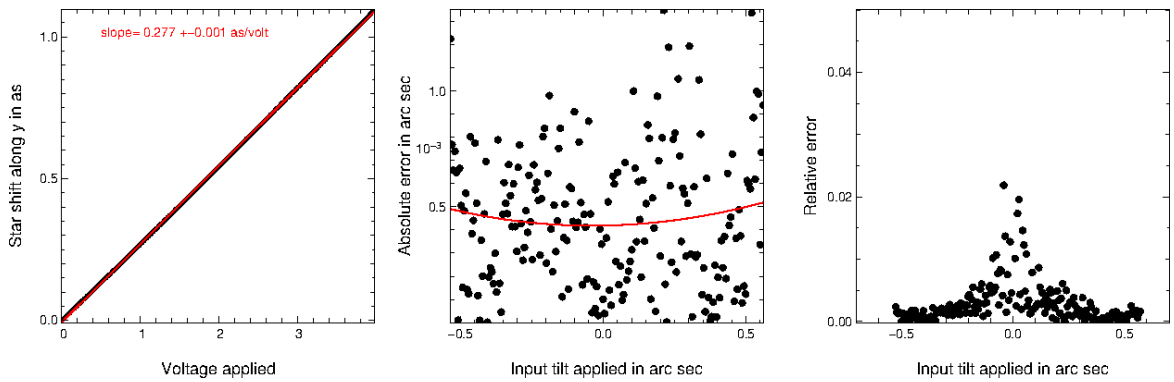

Fig. 2: L*eft panel* is the calibration of voltage applied to the shift of star in arc sec (absolute value) along y-axis. *Middle panel* and *right panels* indicates the absolute error and relative error of star position measurement.

Outcome: The object position absolute and rms errors are 1.2 mas and 1 mas respectively. These data is acquired when the star is at 7.5 equivalent magnitudes in H-band, i.e. the star magnitude that would reproduce the results with the 5 magnitude filter on. The field imager is able to measure large tip-tilts which are more than 1 arc sec, if required.

Notes: Here atmospheric differential refraction errors are not included.

3.1.2 Star magnitude vs lamp voltage

Goal: Magnitude of star for a given lamp voltage

Requisites: Calibration unit lamp

Experiment: Obtained acquisition camera image data by varying voltage of lamp, with the 5th magnitude filter on.

Output: Fig. 3 presents calibration of lamp voltage with star magnitude.

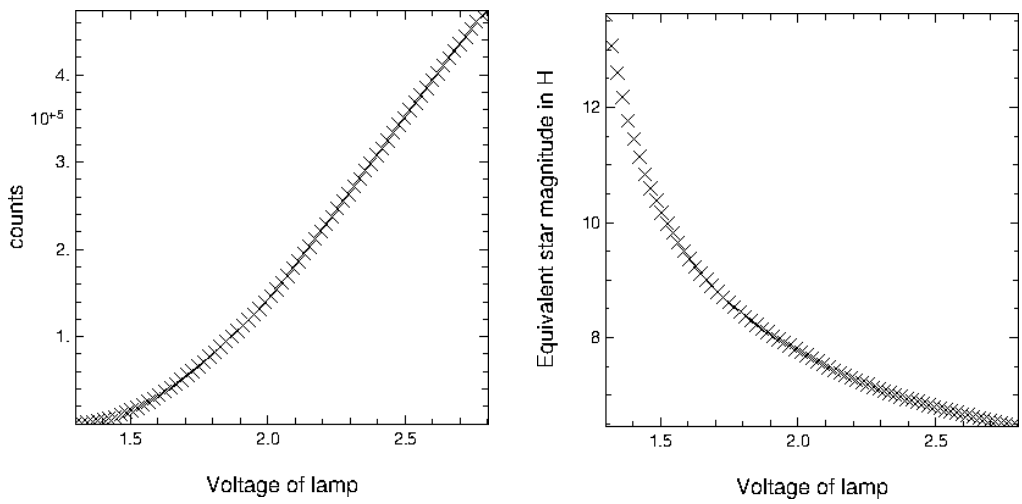

Fig. 3: The calibration of lamp voltage is presented. *Left panel* presents the counts observed on the detector with varying the lamp voltage. *Right panel* presents the voltage of lamp 4 (intensity 1) which is scaled to equivalent star magnitude in H band, i.e. the star magnitude that would reproduce the results with the 5th magnitude filter on.

3.1.3 Field tracking limiting magnitude

Goal: To find field star position tracking accuracy with its magnitude

Requisites: Calibration unit lamps

Experiment: Field imager data is obtained with equivalent star magnitude of 13th magnitude in H band.

Output: The position of effective 13th mH star can be found within 1 mas and 1.0 mas of absolute and rms error.

Notes: Here atmospheric differential refraction errors are not included.

3.1.4 Image quality

Goal: To find image quality of the field imager in Strehl units

Requisites: calibration unit lamp

Experiment: Acquisition camera image with a field star (lamp 4, intensity 1)

Output: Table. 4, presents the Strehl ratio for each telescope.

Image quality is computed in terms of Strehl ratio for four telescopes beams (cf. Fig. 4).

```
./strehl -p 8.0 -d 0 -l '1.65 0.001' -s 0.0178  -r 0.1 -R '0.1 1' -S 32 -P '64 64' star.fits

use: ./strehl [options] <cubes...>

options are:

               -p size      M1 size in meters
               -d size      M2 size in meters (incl. obs. ratio)
               -l 'l0 dl'   Central wavelength and width in microns
               -s scale     Pixel scale in arcsec/pix
               -r radius    Star radius in arcsec
               -R 'r1 r2'   Background radii in arcsec
               -b value     Background known value
               -S size      Size of generated PSF image
               -P 'x y'     Specify star position in pixels
               -g           Save PSF as 'psf_strehl.fits'
               -T name      Get default settings for a telescope
                            name can be '3.60' or 'ut4'
```

Fig. 4: A typical field imager detector image is presented. Here please ignore the position of stars in detector plane as the TTP is randomly positioned.

Table 4: Strehl ratio of stars computed

Measurement	Tel.1	Tel.2	Tel.3	Tel.4
Strehl	0.53	0.7	0.85	0.9

Outcome: The Strehl ratio requirement is 0.8. The field imager imaging quality is partially compliant. Future focus adjusting activities will allow the improvement of Strehl rations.

3.1.5 Field imager field centers

Goal: To find field imager field centers for software and monitoring purpose.

Requisites: calibration unit, 1550 nm laser, TTP device

Experiment: Field star is scanned across its FOV by applying tip-tilts. When the star is shifted, depending on the field stop size, the flux over the pupil imager and aberration sensor window will be changed accordingly. For this image data acquisition, a 1550 nm wavelength laser is illuminated from the side of calibration unit.

Output: Scanning the star in the FOV of field imager allows us to find the centre. During this scanning, flux observed in the aberration sensor window (180 x 180 pixels) is like a step function (cf. Fig. 5 and 6) as the star moved from one side to the other side of FOV (in *x* and *y* directions). It can be also seen that the aberration sensor field stop is in centre while taking the data.

The size of field stop of the aberration sensor can be measured as the width of pixels where the maximum in the step function. That is computed as 2.02 arc sec. Figs. 6 and 7 present the variation flux over the aberration sensor window when the star is scanned in *x* and *y* directions.

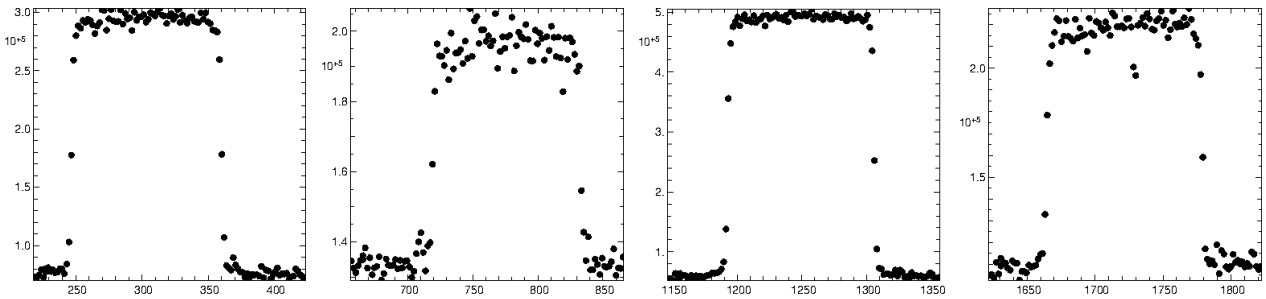

Fig. 5: The ordinate represents the measured flux over aberration sensor window (180 pixels diameter). Abcissa presents the field star position a long x-axis.

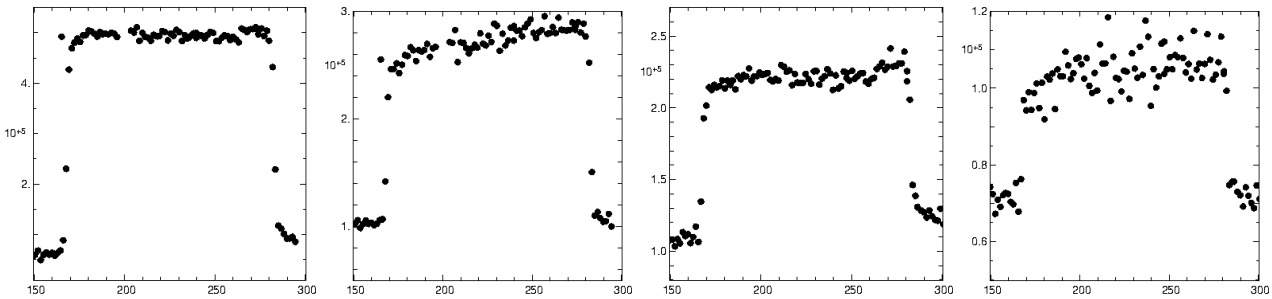

Fig. 6: The ordinate represents the measured flux over aberration sensor window. Abcissa presents the field star position a long y-axis.

Table 5: Field imager centers

centre	T1	T2	T3	T4
X	302	777	1249	1721
Y	225	225	226	225

3.1.6 Pixel scale

Goal: To find pixel scale of the field imager

Requisites: Calibration unit, binary stars

Experiment: Obtained acquisition camera image data having binary stars in the field.

Output: The accurate positions of stars can be computed using Gaussian fit for two stars (cf. Fig. 87. The position difference between two stars allows us to compute the separation between them in pixels (cf. Table 6). By knowing actual stars separation in calibration unit (1.54 arc sec, 4% error in measurement); one can compute pixel scale of field imager as given in Table 7.

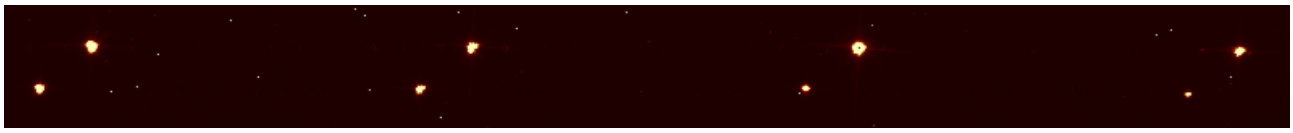

Fig. 7: Field imager for four telescopes.

Table 6: Stars separation in pixels (error ± 0.05 pixel)

measurement	Tel.1	Tel.2	Tel.3	Tel.4
Stars separation (px)	82.1	82.14	82.24	82.22

Pixel scale = separation of stars in design (arc sec) / number of pixels separated in Det.

Table 7: Pixel scale computation for 4 telescopes

measurement	Tel.1	Tel.2	Tel.3	Tel.4
Pixel scale mas	18.76	18.74	18.72	18.73

Outcome: Measured pixel scales are within 5% error with designed values. This error is arrives from binary star separation measurement in the calibration unit.

3.1.7 Defocus measurement

Goal: Acquisition camera focusing performance is measured in order to characterize the acquisition camera focusing status so that during next warm up the improvement of focusing is performed.

Requisites: 1550 nm wavelength star from telescope, filter slider

Experiment: Obtained acquisition camera image data by obstructing the pupil. The pupil is obstructed by moving the neutral density filter slider. Depending on the level of defocus, effectively, the star in the field moves when filter is moved from positions “open” to “pos 1” and “pos 2”.

Output: Table 8 presents the focal length shifts. Fig. 8 presents the field star shifts when filter is moved top to bottom.

Table 8: Focus analysis by using pupil obstruction method (top down filter movement), in pixel coordinates. See Annex 1 for details on the un-focusing distances calculations.

	T1. x	T1. y	T2. x	T2. y	T3.x	T3.y	T4.x	T4.y
Filter open	307.5	253.7	786.0	245.1	1216.6	254.9	1691.4	258.6
Top blocked (shift from ref)	0.010162	-1.294	-0.7064	-1.756	-0.4403	-2.696	-0.3727	-1.394
Bottom blocked (shift from ref)	-0.6217	3.224	0.8396	1.3715	-0.365	1.08866	-0.16954	0.4746
Top-bottom difference	0.63	-4.52	-1.55	-3.13	-0.075	-3.79	0.2	-1.87
	Detector is Before focus Lens have to increase distance (i.e lens have to go down)		Detector is Before focus Lens have to increase distance (i.e lens have to go down)		Detector is Before focus Lens have to increase distance (i.e lens have to go down)		Detector is Before focus Lens have to increase distance (i.e lens have to go down)	
Unfocused by [mm]		-5.4		-3.4		-4.3		-1.5

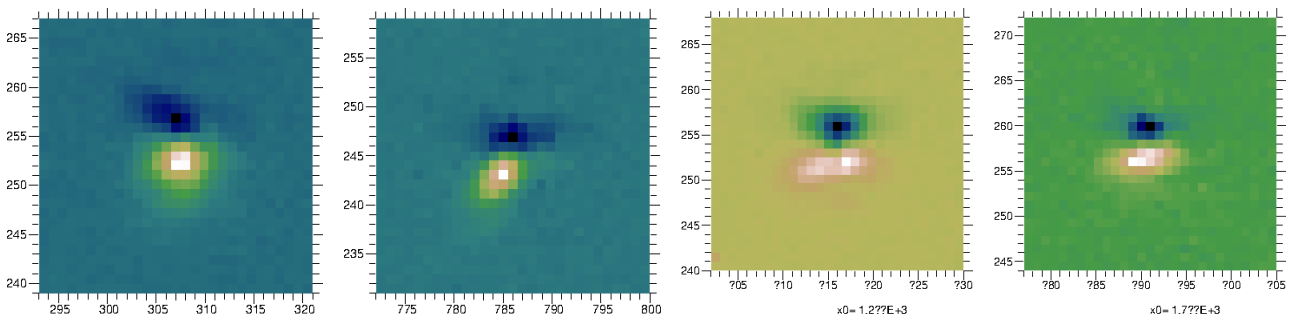

Fig. 8: Top- down difference of images for Tel. 1 to Tel. 4 from left to right respectively.

Since the Strehl ratio for telescope 4 (cf. Table 4) is approximately 0.9. It is considered that telescope 4 channel is focused. Therefore we have considered that our un-focusing measurements have a -1.5 mm offset. Table 9 presents the number of millimetres that needs to be moved in order to make focus the Tel. 1 and 2. The Tel. 3 and 4 are within requirements (i.e. compliant with Strehl ratio).

Table 9: Optical alignment proposed for next iteration

	T1	T2	T3	T4
Unfocused by [mm]	-3.9	-1.9	compliant	compliant
Lens has to down	19.5	9.5		

[in number of turns of kinematic mount]				

3.1.8 Blueshifts in the lamp for increasing voltage

Goal: To find blueshifts in the lamp for increasing voltage

Requisites: Calibration unit, pupil actuator, pupil guiding laser

Experiment: By increasing the voltage of lamp (increasing of intensity), acquisition camera image data is obtained.

Output: It is observed that while changing the voltage of lamp, the star position computed for four telescopes is drifted (around 0.6 pixel or10 mas) as shown in Fig. 8 and 9. The lamp being used to generate the stars is Quartz-Tungsten Halogen lamp from B&W Tek (model BPS101). It has blueshift intensity for high powers applied to the lamp.

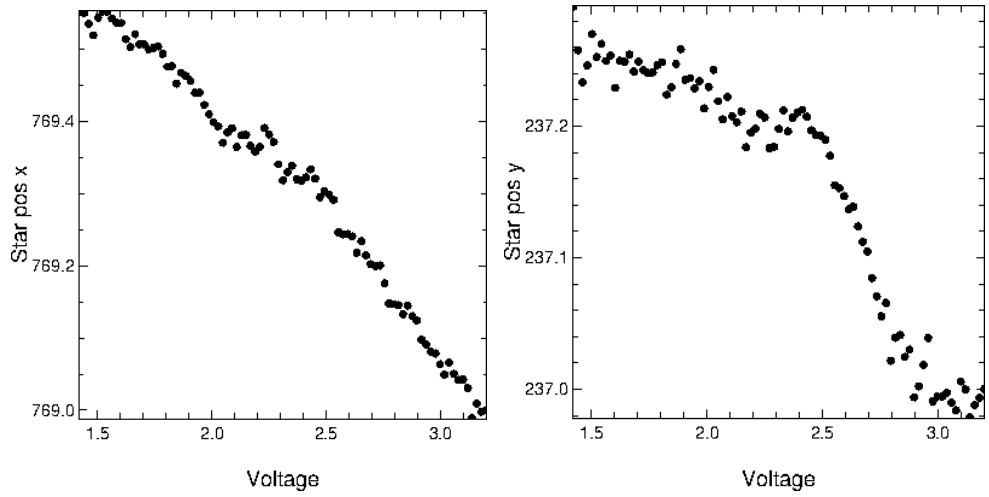

Fig 9. a: The position of star while chaning the voltage of lamp. Oberserved for telescope 2.

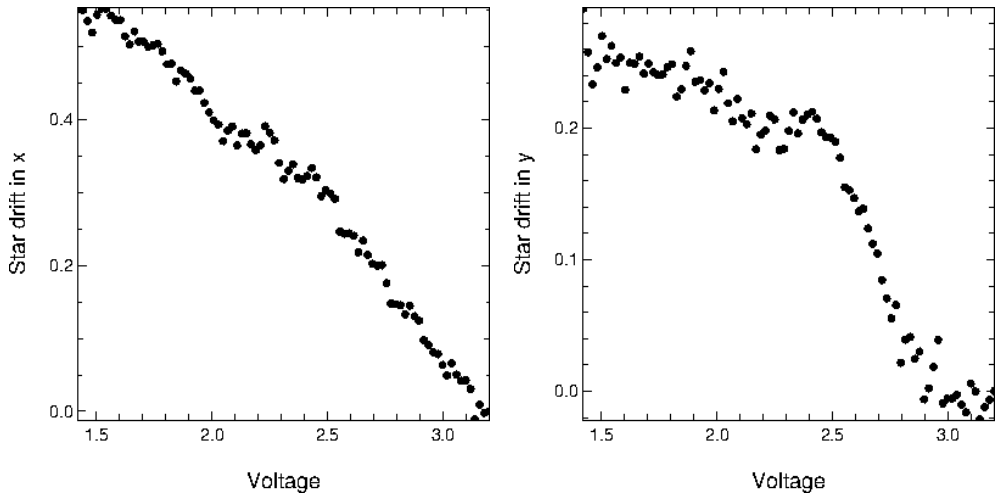

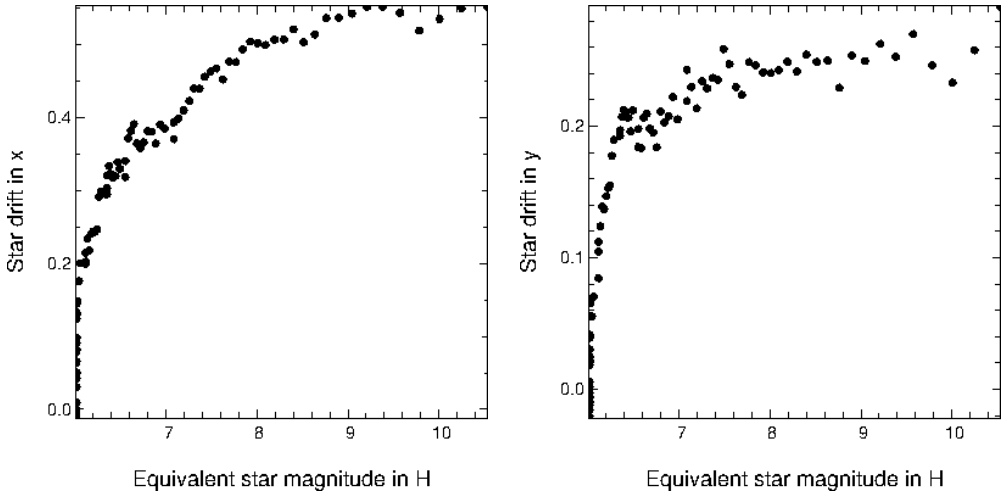

Fig. 9.b: The star drift in pixels w.r.t to the bright star (high voltage). The top panel represents the drift in voltage scale and the bottom panel represents the star drift scaled to equivalent star magnitude in H, with 5th magnitude filter on.

3.2 Pupil tracker

3.2.1 Lateral pupil position measurement accuracy

Goal: To find lateral pupil position measurement accuracy

Requisites: Calibration unit, pupil actuator, pupil guiding laser

Experiment: Pupil tracker image data is obtained by moving the pupil actuator with 1.2 µm pupil guiding laser beams are turned ON.

Output: The accuracy of the lateral pupil position is measured with the acquired data. Results are presented in the following Figs. 10 and 11. The pupil tracker pixel scale considered here is 59.8598 mm. The lateral pupil shift with PMC device is calibrated. For one volt applied to it, it moves the pupil around 3.0 pixels on the detector or 0.185 m at M1 (see Table 10).

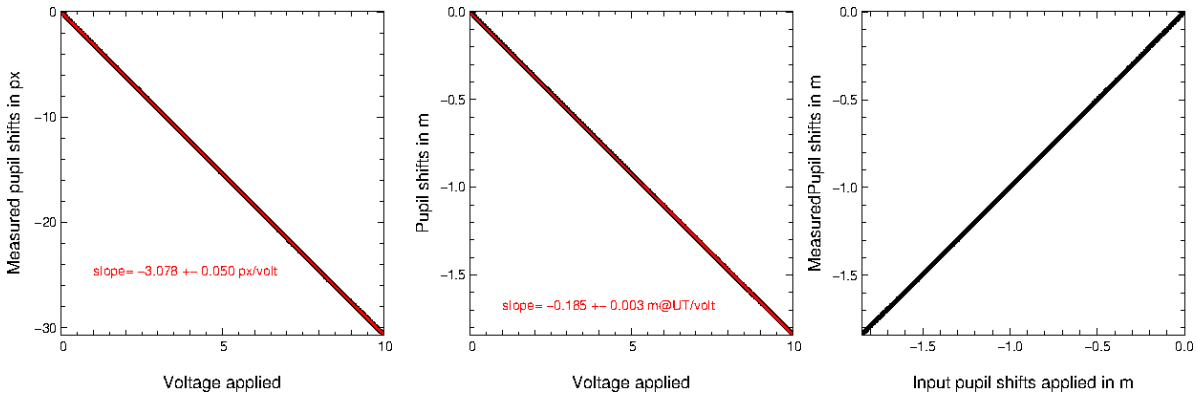

Fig. 10: Lateral pupil position measured for input lateral pupil shifts applied. *Left panel* presents voltage applied to the PMC along *x* direction and measured pupil positions in pixels. *Middle panel* presents pupil shifts which are calibrated for applied voltages. *Right panel* presents re-scaling the pupil shifts from pixels to meters at M1.

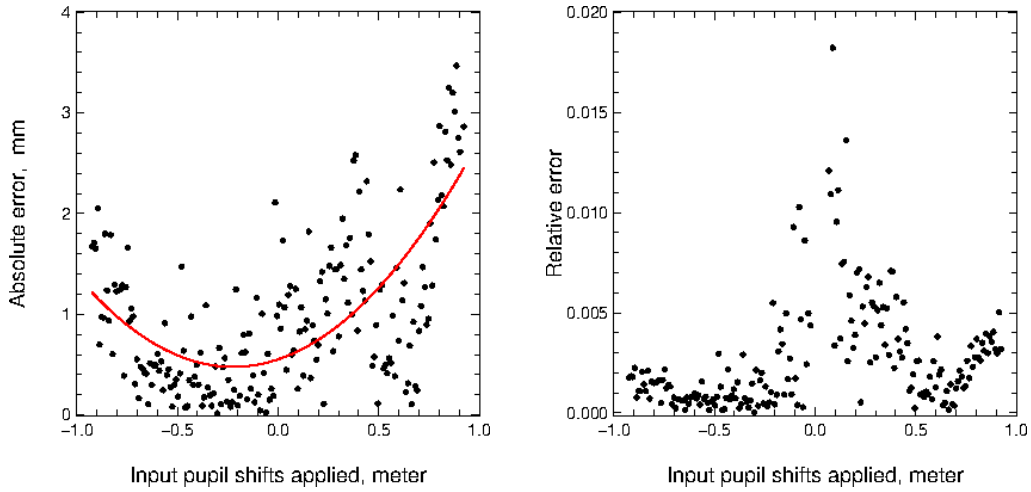

Fig. 11: Lateral pupil position measurement absolute and relative errors for input pupil shifts applied at M1.

Table 10: lateral pupil voltage to pixel scale

	T1 (x, y)	T2 (x, y)	T3 (x, y)	T4 (x, y)
PMC x	-3.078	-3.16149	-3.04691	-3.02691
PMC y	2.90937	2.93181	2.92529	2.94100

Outcome: The pupil tracker until now measured a maximum shift of 1.8 m at M1. That is 22.5 percentage of M1. The absolute and rms errors of the lateral pupil measurements accuracies are around 3.5 mm and 1 mm respectively at M1. These fall within GRAVITY requirement of 4 mm rms at M1.

3.2.2 Longitudinal pupil position measurement accuracy

Goal: To find longitudinal pupil position measurement accuracy

Requisites: Calibration unit, pupil guiding laser and delay lines movement

Experiment: Acquisition camera images are acquired by moving the delay lines (d11, d12, d13 and d14) from 0 to 1.8e6 steps (i.e., shift of 25 mm). For this longitudinal pupil analysis, the zero step is considered as the reference position, and the longitudinal pupil shifts are computed with respect it.

Output: The longitudinal pupil shifts measurement accuracy has been validated by moving the calibration unit delay lines. Using the pupil spots divergence (in this case), the longitudinal pupil shifts are measured. This calculation involves three steps. First, defocus aberration coefficient is computed using the pupil tracker spots divergence/convergence nature in comparison to reference. Secondly, using the defocus coefficient, longitudinal defocus shift of pupil tracker lenslet is computed using Eq. 1-3c of Mahajan (1991). Finally, longitudinal pupil shift is computed using the longitudinal defocus shift. Then, the delay line steps are scaled in millimetres (1.8e6 is 25 mm). The measured longitudinal pupil shift is plotted against input pupil shifts (cf. Fig. 12).

When the spots are diverged, defocus aberration coefficient measured as positive. The longitudinal pupil shift measured from it is towards the acquisition camera instrument from the reference position. In this measurement, the CU delay line is moved by 25mm (from zero steps to 1.8e6 steps). Therefore, the pupil measured is shifted towards the acquisition camera.

The 18 mm beam measurements are converted to 80 mm beam with 4.44^2 magnification factor. The absolute error is calculated in between input and output. The middle and right panels of Fig. 12 presents longitudinal pupil measurement accuracy in terms of absolute and relative errors.

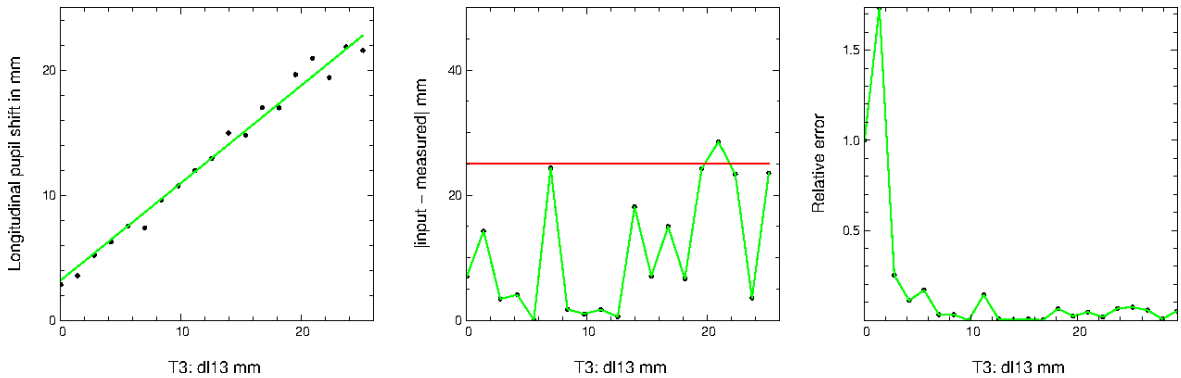

Fig. 12: *Left panel* presents measured longitudinal pupil shift against input pupil shifts (at 18 mm beam). *Middle* and *right panel* presents the absolute and relative errors computed at 80 mm beam. The red line is the 25 mm line.

Outcome: The maximum absolute and rms errors of the measurements are better than 45 mm and 15 mm respectively for an 80 mm beam. These measured results are very close to GRAVITY requirement 25 mm rms at 80 mm beam.

3.2.3 Characterization of pupil tracker limiting magnitude

Goal: Determine the pupil tracker performance in the presence of bright stars in the field-of-view (Problem: the star adds background light to the pupil tracker images)

Requisites: calibration unit, lamp 4 and pupil guiding lasers

Experiment: While varying the field star flux, the pupil guiding lasers are turned ON and OFF.

Output: Pupil tracker is facing background problem from the H-band star (field imager). Here a software solution (BLINK mode) is proposed, that is each pupil tracker image is subtracted by a background caused by the field star with same detector integration.

Fig. 13 presents calibration of lamp voltage with observed star magnitude (lamp 4, intensity 1). In this computation considered $116e^3$ photons/sec/star for a 13 mH star at detector. The Fig. 14 presents pupil tracker background observed for varying star magnitude.

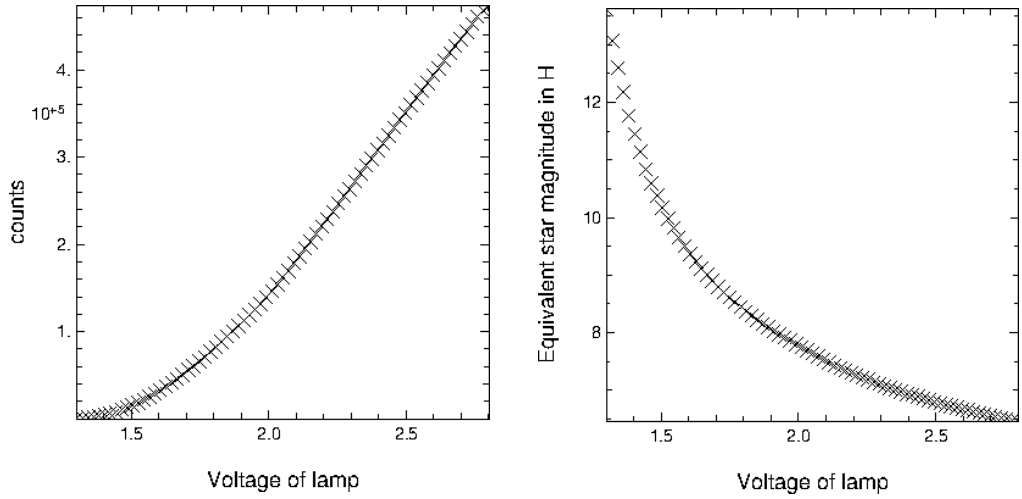

Fig. 13: Calibration of lamp counts with voltage applied to it. This figure is the replication of Fig. 3.

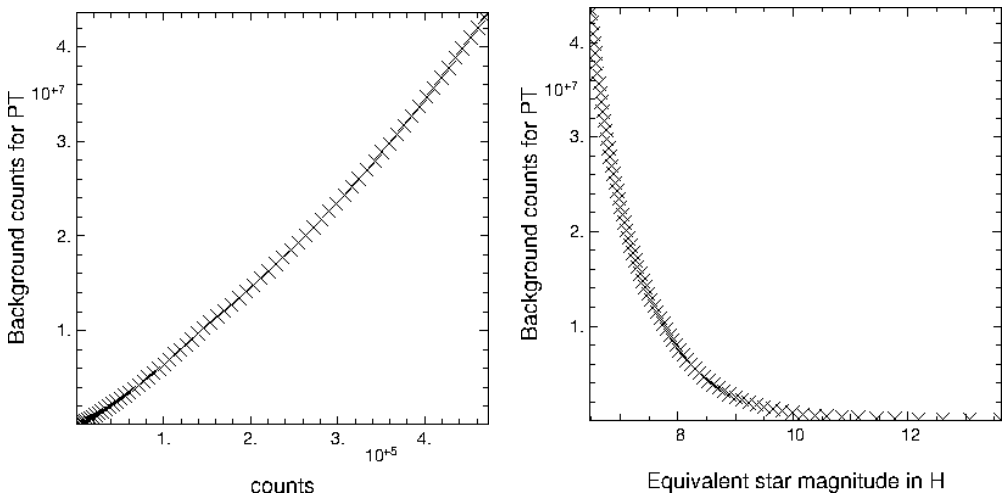

Fig. 14: Pupil tracker window(160 x 160 pixels) background detector counts, with 5 magnitude filter on. The field star position is computed by using a Gauss fit and the pupil tracker window background is computed by summing all intensities in 160x160 pixels window.

The pupil tracker background is dependent on the field star light and the star position in the field of view. When the closed loop tip-tilt system is off (field star position is constant), the pupil tracker is able to detect input pupil motions until the lamp voltage 2.5 V using the BLINK mode. BLINK mode is separate calling routine to correct the pupil tracker background. In which, for every pupil tracker frame, the pupil tracker image is subtracted by star background. The star background is taken by switching off the pupil tracker lasers.

But when the closed loop tip-tilt system is ON, the pupil tracker background is changing rapidly as the high speed TTP actuators are working in a loop. When both tip-tilt and pupil tracking loops are running, the performance of pupil tracker reduces from 2.5 V to 1.75 V of lamp voltage using the BLINK mode. The 1.75 lamp voltage corresponds to 8th magnitude of star as shown in Fig. 13.

Please note that while changing the voltage of lamp, from lower to higher, the lamp light is blueshifted (Fig. 9). It means that for each increment of lamp voltage the pupil tracker is

getting extra 'bluer colour' background counts into its pass band in addition to star light background. This effect is not considered here.

This limiting star magnitude can be improved as if the pupil tracker flux is increased. An increment of 10 times from the current peak of the pupil tracker spots in the detector (100-200 counts) would gain a factor of 2.5 more magnitudes.

Outcome: The pupil tracker is able to work until 8th star magnitude.

3.2.4 Pixel scale of pupil tracker

Goal: To find pupil tracker pixel scale

Requisites: Calibration unit

Experiment: Obtained acquisition camera image having pupil tracker guiding lasers ON.

Output: Measured the distance between two diagonal laser spots (cf. Fig. 15). By knowing the distance between the pupil guiding lasers, we can measure the pixel scale.

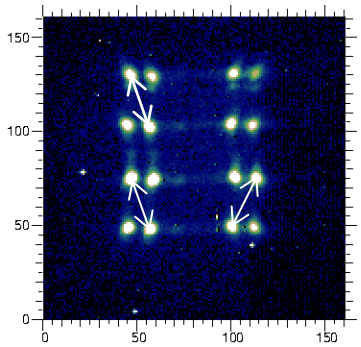

Fig. 15: A typical pupil tracker image. Diagonal spots allow us to measure the pixel scale of the pupil tracker. Image of lasers (1.2 µm)

In the calibration unit, two diagonal pupil tracker lasers are separated by 0.65 mm that corresponds to 1.6 m on the UT. These two lasers are separated on the detector as 27.1 pixels. That scales to 58.0 mm per pixel at M1 and 24 µm per pixel at calibration unit.

The pupil tracker image is spanned for 110 pixels (spots separation between extreme bottom left and extreme up and right). Field of view of a lenslet is 111 pixels/2 lenslets *x* 58 mm/ pixel = 3.19 m at UT.

Outcome: The measured pixel scale and field of view are within 3 percentage error with design values 59.8598 mm and 3.3 m respectively.

3.2.5 Image quality

Goal: To find image quality of pupil tracker

Requisites: calibration unit

Experiment: Obtained a pupil tracker image with 1.2 µm source on date 2015-01-29.

Output: The Strehl ratio of the pupil tracker spots is measured as give below.

./strehl -p 8.0 -d 0 -l '1.2 0.001' -s 0.08 -r 0.13 -R '0.13 1' -S 8 -P '129 129' PT.fits

The FWHM of a typical pupil tracker spot is (5.0, 4.5) pixels with flux around 5e3 counts/spot at detector. The Strehl measured with following script gives around 0.53.

Outcome: The measured Strehl is not compliant with GRAVITY specification of 80%. It is expected since the camera is not in perfect focus and already planned to correct this in the next iteration (ref sec. 3.1.7).

3.2.6 Pupil tracker field stop size

Goal: To find the pupil tracker field stop size in arc sec

Requisites: Calibration unit lamp

Experiment: Obtained acquisition camera images with scanning field star in the field imager FOV. While the star is scanning in the field imager FOV, the detector counts measured in the pupil tracker window (160 *x* 160) is plotted against the field star position. The width of the step function (width of counts over 1.5e5 in Fig. 16) allows measuring the pupil tracker field stop size.

Output: Fig 16 presents the pupil tracker window flux observed while scanning the star in the FOV of field imager. The measured width of the pixels is 111. Therefore, the size is 1.973 arc sec (1 px = 17.78 mas/px).

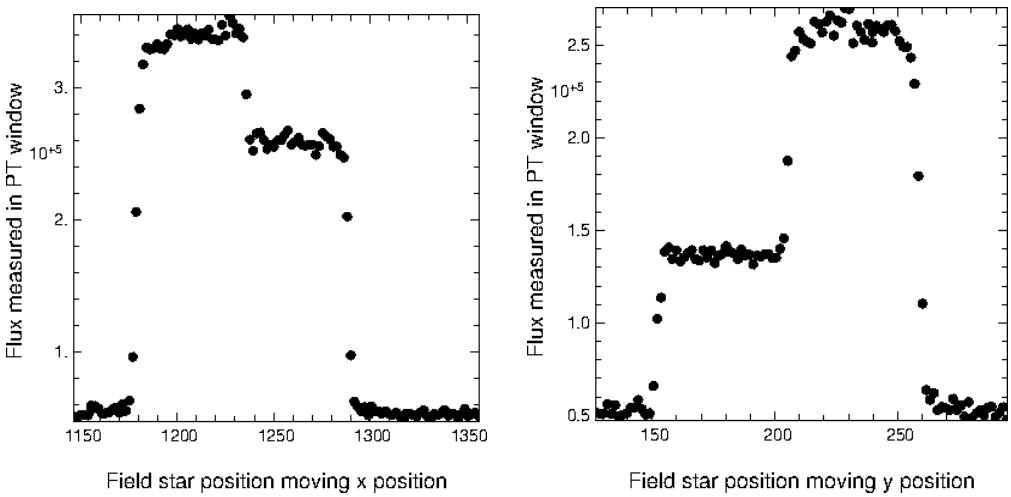

Fig. 16: The ordinate represents the measured flux over pupil tracker window (180 pixels diameter). Abcissa presents the field star position a long x-axis.

Outcome: The pupil tracker field stop size is 1.973 ± 0.05 arc sec.

3.3 Aberration sensor

3.3.1 Calibration of aberration sensor shifts with voltage

Goal: Quasi-static aberrations sensing accuracy

Requisites: Calibration unit lamp, TTP device

Experiment: Tip-tilts are applied to the incoming beams using TTP device. For each tip and tilt applied to the beam (step size 0.02, from reference [-0.84 v, -3.37 v]), obtained aberration sensor images.

Output: Calibration of aberration sensor shifts with applied voltages is shown in Fig. 17. This calculation made it for telescope 1. For each volt step applied to TTP device in both directions, it moves absolutely 1.111, 0.985 pixels in *x* and *y* directions respectively. The design pixel

scale and the diffraction limited FWHM lenslet spot of aberration sensor is 0.25 arc sec and 1.5 pixels (0.375 arc sec) respectively. Each lenslet sub-aperture images the Galactic Center field stars in 16 pixels.

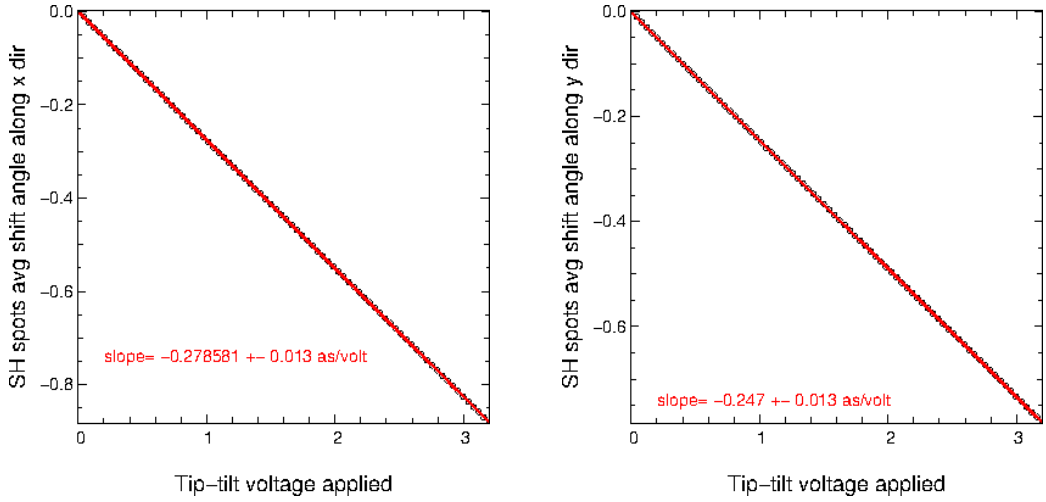

Fig. 17: *Left panel* present the measured Shack-Hartmann angular global shifts (arc sec) in x-direction for applied tip-tilt voltages. *Right panel* present the measured Shack-Hartmann angular global shifts (arc sec) in y-direction for applied tip-tilt voltages. The data presented here for telescope 1. One arc sec angular shift corresponds to 4 pixels shift on the detector.

The calibration of Shack-Hartmann slopes (arc sec/voltage) is equal to field imager calibrated star slope (arc sec/voltage) within 5 percentage error.

3.3.2 Quasi-static aberrations sensing accuracy

Goal: Quasi-static aberrations sensing accuracy
Requisites: Calibration unit lamp, TTP device
Experiment: Tip-tilts are applied to the incoming beams using TTP device. For each tip and tilt applied to the beam (step size 0.02, from reference [-0.84 v, -3.37 v]), obtained aberration sensor images.
Output: For each step, lenslet spot shifts are computed with respect to the reference. Next the tip and tilts $T(x,y)$ at M1 are measured from the spot shifts $S(x,y)$ (see Annex II). Measured the applied tip-tilts at M1 and plotted its performance in Figs 18 and 19.

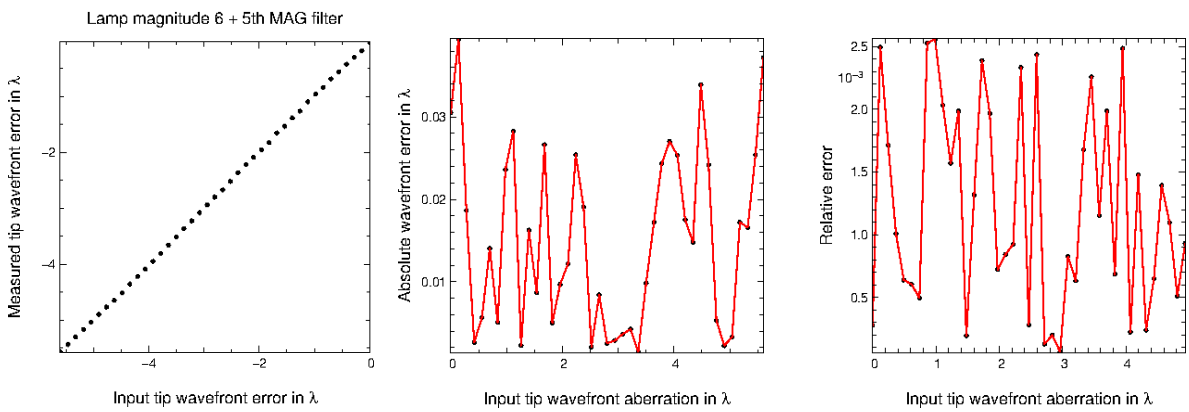

Fig. 18: *Left panel* presents the measured wavefront aberration against input wavefront aberration in λ units(@1.65 μm).. *Middle panel* presents the absolute tip

error measured in λ units (1.65 µm). *Right panel* presents relative error that occur in the measurement.

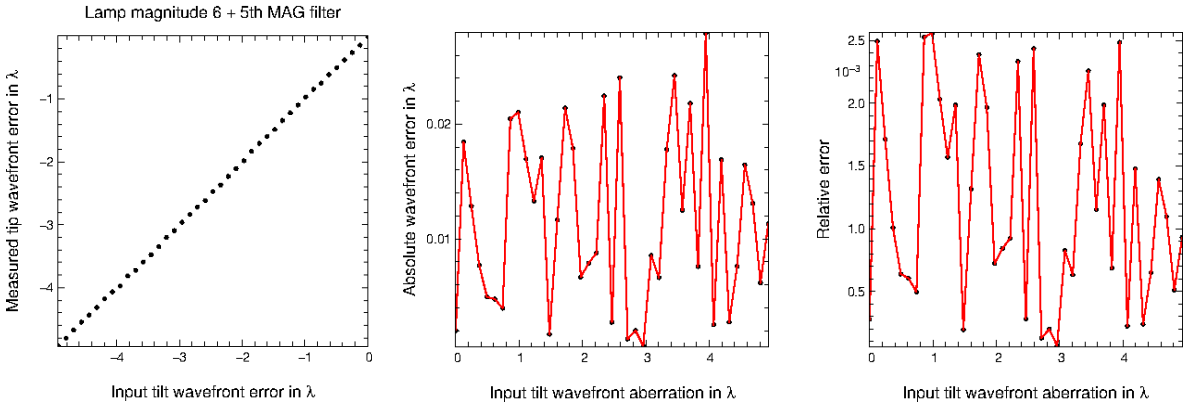

Fig. 19: *Left panel* presents the measured wavefront tilt aberration against input wavefront tilt aberration in λ units(@1.65 µm).. *Middle panel* presents the absolute tilt error measured in λ units (1.65 µm). *Right panel* presents relative error that occur in the measurement.

For the TTP device when x voltages are applied, it moves the lenslet spots along y-axis on the detector plane. When y voltage is applied to TTP, it moves lenslet spots along negative x-direction on the detector.

$$Wavefront\ error\ variance\ = \sum_{i=2}^{28} measured(a_i^2) - input\ (a_{tip}^2 + a_{tilt}^2)$$

Outcome: The total wavefront error occurred while measuring the input tip-tilt wavefront aberration is λ/30 or 54 nm rms at M1. The central wavelegth being considered is 1.65 µm. All measurements are made with equivalent 6th magnitude star, with 5th magnitude filter on.

3.3.3 Pixel scale and sub aperture field of view

Goal: To find pixel scale and sub aperture field of view

Requisites: Calibration unit lamp, lamps

Experiment: Acquisition camera image is obtained with illuminating binary stars in the field.

Output: The separation between imaged binary stars is found in the aberration sensor lenslet window (cf. Fig. 20).

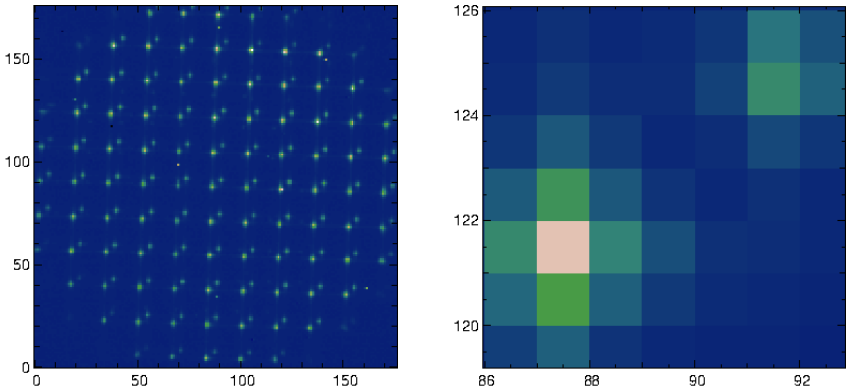

Fig. 20: Aberration sensor image with binary stars in its field of view. *Left panel* is the aberration sensor window for Tel. 1. *Right panel* is the same but zoomed to see binary stars.

Table.11: Two stars seperation in aberration sensor

Measurement	Tel.1	Tel.2	Tel.3	Tel.4
Stars separation (px)	5.54	5.70	5.57	5.59

$$Pixel\ scale\ = \frac{1.54\ as}{\sqrt{S_x^2 + S_y^2}}$$

Where, S_x and Sy are the separation of two stars in the detector (pixels). It is taken that two stars in the calibration unit are separated by 1.54 arc sec (with 5% error in measurement). Computed pixel scales are presented in Table 12.

Table 12: Pixel scale calculated for each telescope

Measurement	Tel.1	Tel.2	Tel.3	Tel.4
Pixel scale (mas)	278.5	270.1	276.5	275.5

The aberration sensor image occupied 192 pixels in diameter on the detector. The field of sub-aperture is192 pixels/12 lenslets x 275 mas/pixel (cf. Table 12) = 4.4 ± 0.05 arc sec.

The 9 x 9 lenslet of aberration sensor images M1 pupil. The image spanned on the detector is 149.4 ± 1 pixels or 2.69 mm (149.4 x 18μm detector pixel scale).

Outcome:

1) The measured pixel scale is 10% error with design pixel scale (250 mas). This error includes 4% error in measurement of star separation in the calibration unit and 5% error from the Gauss fit in finding the positions on the detector.

   Also the pixel scale of the aberration sensor is measured by applying series of tip-tilts. The voltage to arc sec calibration scale from field imager (0.302 arc sec/volt, sec. 3.1.1) and the voltage to pixel scale calibration from aberration sensor (1.11 pixel/volt, sec. 3.3.3) allow us to measure the aberration sensor pixel scale in arc sec.

   Pixel scale = (0.3 arc sec /volt) / (1.11 pixel/volt) = 270 ± 13 mas.

2) The field of sub aperture is 6% error with design value (4.14 arc sec).

3.3.4 Aberration sensor field stop

Goal: To find the aberration sensor field stop size and field centers

Requisites: Calibration unit lamp

Experiment: Obtained acquisition camera images with field star scanning in the field imager FOV. While the star is scanning in the field imager FOV, detector counts available in the aberration sensor window (160x160 pixels) is observed and plotted against the field star position. The width of the step function (cf. Figs 6 and 7) allows it measuring the aberration sensor field stop size. The centers of aberration sensor are also computed by using the center of width of step function.

Output: Table 13 presents the centers of the aberration sensor for each telescope.

Table 13: Aberration sensor centers

centre	T1	T2	T3	T4
X	306	778	1241	1704
Y	1067	1064	1068	1063

3.3.5 Aberration sensor image quality

Goal: To find image quality of aberration sensor

Requisites: calibration unit

Experiment: Obtained an aberration sensor image on date 2015-01-23.

Output: Measured Strehl ratio of the aberration sensor spots.

The Strehl measured with following script gives around 0.53.

./strehl -p 8.0 -d 0 -l '1.65 0.001' -s 0.250 -r 0.5 -R '1.0 2' -S 8 -P '129 112' -g ABS.fits

Outcome: The measured Strehl is not compliant with GRAVITY specification of 80%. It is expected since the camera is not in perfect focus and already planned to correct this in the next iteration (ref sec. 3.1.7).

3.4 Pupil imager

3.4.1 Image quality

Goal: Image quality

Requisites: Calibration unit lamp

Experiment: Obtained pupil imager images.

Output: Fig. 21 presents a typical pupil imager for four telescopes.

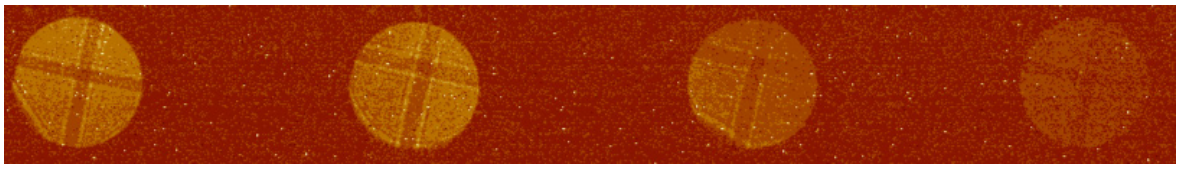

Fig. 21: A typical pupil imager

It is observed that flux obtained for four telescopes are not uniform as shown in Figs. 22 and 23. It is not clear why the flux is getting reduced from T1 to T4.

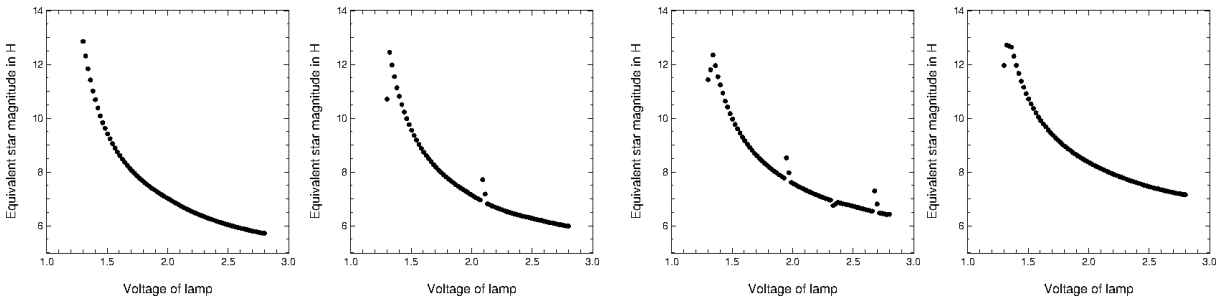

Fig. 22: Equivalent star magnitude in H against the voltage applied to lamp, 5 magnitude filter is on.

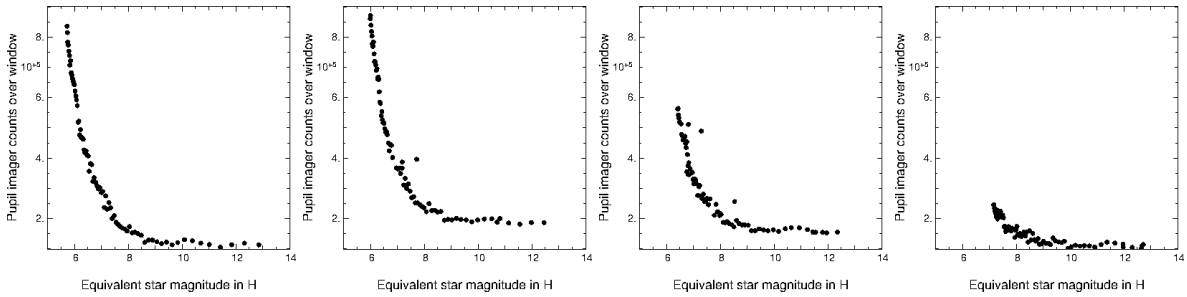

Fig. 23: Flux over the pupil imager window (180 pixels diameter) observed against the equivalent star magnitude in H, 5 magnitude filter is on.

The Strehl ratio of the pupil imager is not tested. This will be tested by injecting a pupil guiding laser into the pupil imager field and will measure the Strehl ratio of the imaged point source.

3.4.2 Pupil imager field stop

Goal: To find pupil imager field stop size and center positions

Requisites: calibration unit, 1550 nm laser, TTP device

Experiment: Field star is scanned across its FOV by applying tip-tilts to it. When the star is moving in the field imager FOV, depending on the pupil imager field stop size, the flux over the pupil imager window will be changed accordingly. For thisexperiment, a 1550 nm wavelength laser is used from the side of calibration unit to illuminate the acquisition camera.

Output: Scanning a star in the FOV of field imager allows us to find the centres of pupil imager and also to find its field stop size. During this scanning, the counts observed in the pupil imager window (180 x 180 pixels) is behaves like a step function (cf. Figs. 24 and 25) as the star moves from one side to the other side of FOV (in *x* and *y* directions).

The size of field stop can be measured from the width of the step function as shown in Fig. 24 and 25. That is resulted as 2 ± 0.05 arc sec. The centers of the pupil imager are found by taking the center position of the width of the step function. Table 14 presents the centers of the pupil imager for each telescope.

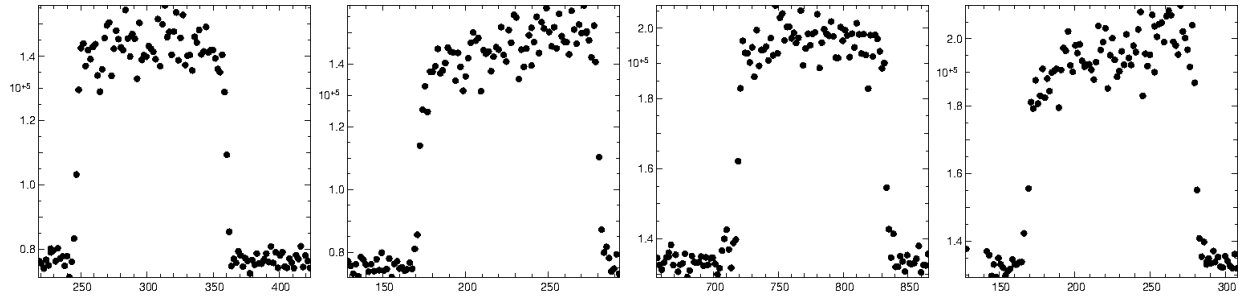

Fig. 24: The ordinate represents the measured flux over pupil imager window (180 pixels diameter). Abcissa presents the field star position a long x-axis.

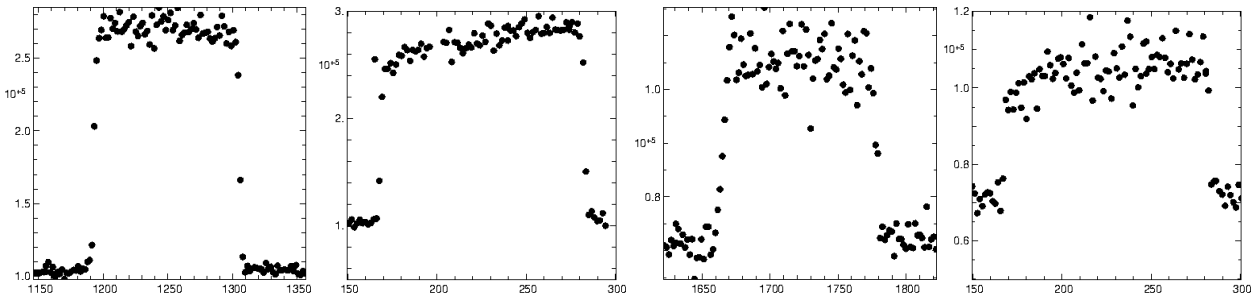

Fig. 25: The ordinate represents the measured flux over pupil imager window (180 pixels diameter). Abcissa presents the field star position a long y-axis.

Table 14: Pupil imager centers

centre	T1	T2	T3	T4
X	306	774	1243	1704
Y	654	650	651	654

Pupil imager images M1 pupil on the detector in 149.4 ± 1 pixels (cf. sec 3.3.3). The pixel scale of it is measured and that is 53.5 ± 0.3 mm/pixels (8 m/149.4 pixels).

3.4.3 Transmission in H band (1.45 μm to 1.85 μm)

Goal: Sum of transmission of field, pupil and aberration sensor

Requisites: Calibration unit lamp, filters transmission curves

Experiment: Manufacturer provided individual components of dichroic, filter and coating of the material transmissions are taken and calculated the transmission of acquisition camera.

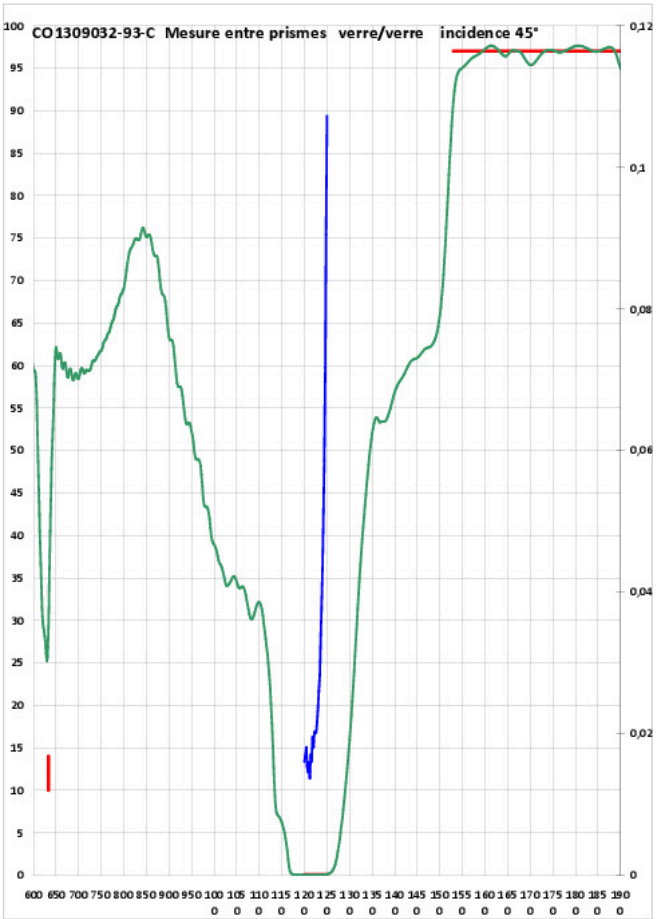

Fig. 26: Transmission curve of dichoric

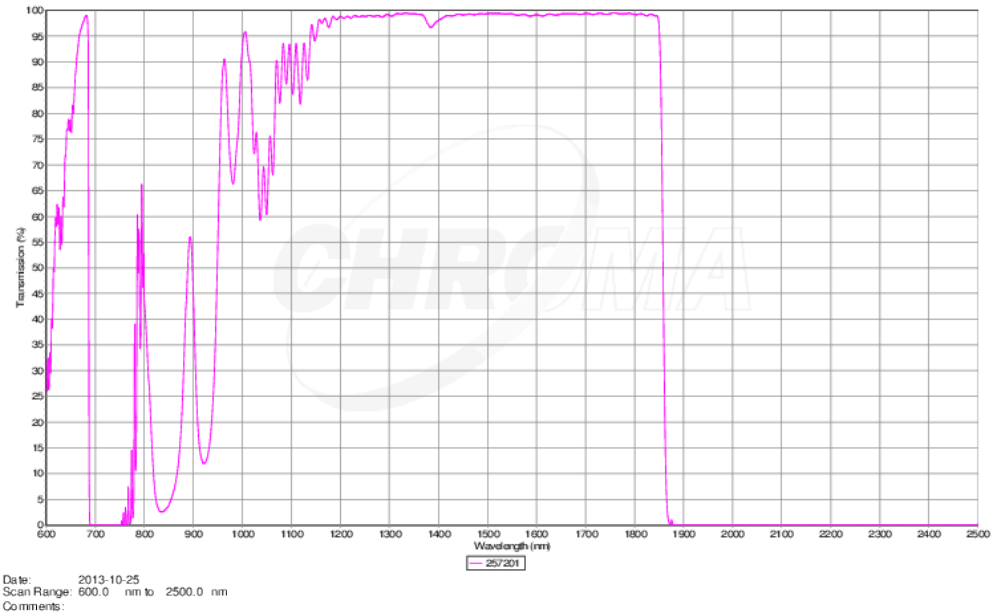

Fig. 27: Transmission curve of filter

Output: Coating of the material is 98.2 %. The sum of the transmission (in H-band) of the field, pupil and aberration is 87.96 %. Whereas the metrology wavelength (at 1.908 μm) transmission is 0.0028 %.

4 Control loop performance

4.1 Stability of field tracking and correction

Goal: Field tracking star limiting magnitude in closed loop

Requisites: Calibration unit lamp 4, TTP

Experiment: Observation of performance of gvttpControl with field tracker

Output: The gvttpControl loop can work with star magnitude of 13.

4.2 Stability of pupil tracking and correction

Goal: Pupil tracker performance characterisation in closed loop

Requisites: Calibration unit lamp 4, pupil guiding lasers, TTP, PMC, delay lines

Experiment: As mentioned in Sec. 3.3.2, the pupil tracker is facing backgrounds from the field star. To improve the pupil tracker performance in the presence of field star magnitude BLINK mode is implemented.

Output: The pupil tracker is able to measure the 22.5% lateral pupil shift at M1 with an accuracy of 3.5 mm. The input longitudinal pupil shifts are measured with absolute and rms accuracies with 45 mm and 15 mm respectively for 80 mm. Right now, the pupil tracker is working until 8th star magnitudes with BLINK mode in operation.

Please note that while changing the voltage of lamp, from lower to higher, the lamp light is blueshifted (Fig. 9). It means that for each increment of lamp voltage the pupil tracker is getting extra 'bluer colour' background counts into its pass band in addition to star light background. This effect is not considered here.

4.3 Stability of aberration sensing

Goal: Stability of aberration sensing

Requisites: Calibration unit lamp 4, TTP

Experiment: Obtained aberration sensor images for lamp voltage at 2.8 and studied the stability performance of it by moving the tip-tilt device.

Output: The measurement accuracy is presented in Sec. 3.3.2. It measures the input wavefront aberration until 10 λ with accuracy better than 80 nm (@1.65 μm). These measurements are made with 6th magnitude lamp plus 5th magnitude filter.

5 Annex I – Support notes for AC occlusion focusing test

The focusing of the field imager is tested by using partial pupil obscuration method. In general if the system is focused, the star image formed on the detector by the field imager does not change its position while pupil is under obstruction. However, when the system is unfocussed the star position is drifted during the pupil obstruction. Based on the direction of the star drifting, the sign of focal correction is measured. To understand it, a simple model is simulated in ZEMAX using physical propagation.

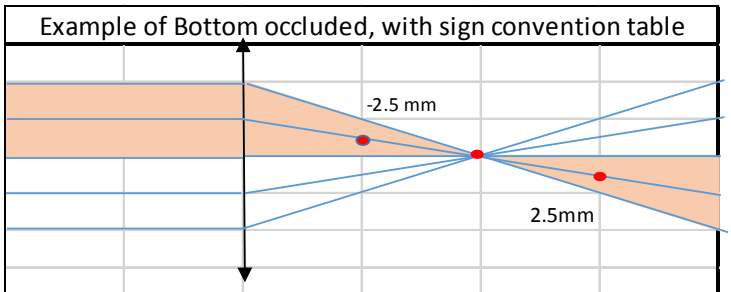

	before focus	After focus
top occlusion	spot goes down -	spot goes up +
bottom occlusion	spot goes up +	spot goes down -

Fig. 28: Occlusion sign convention

For a focused detector, upper and lower pupil obscuration, the Gaussian centroids shift distance is 0.4 pixels. If the detector is placed 2.5 mm before or after the focal plane, the shift in centroids becomes either -2.2 or 1.2 pixels, leading to a variation of 0.68 pixels per milli meter of focal distance. The figure below shows the normalized radiance at the stop surface plane with bottom and top obscuration.

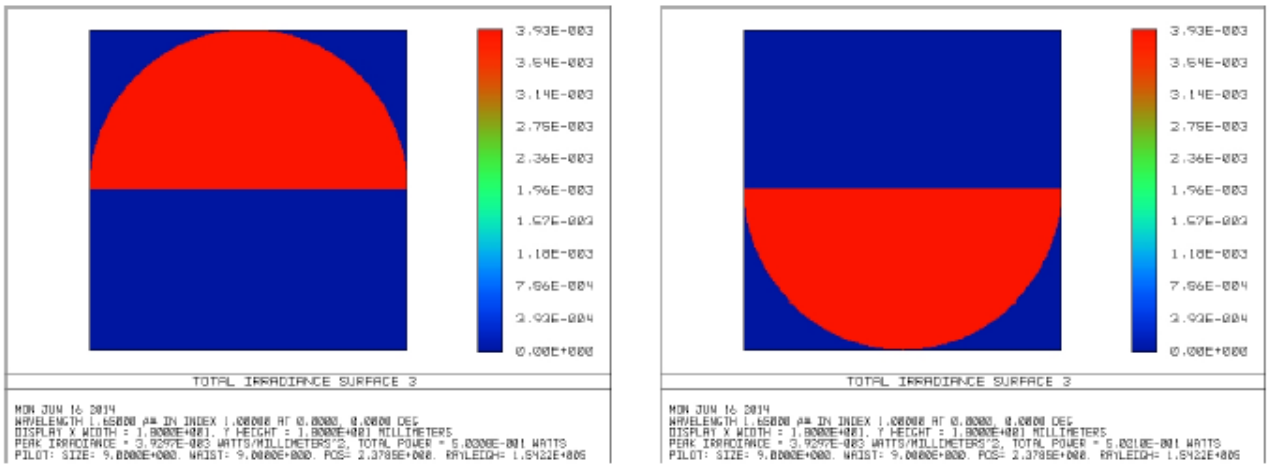

Fig. 29: The normalized radiance at the stop surface plane with bottom and top obscuration.

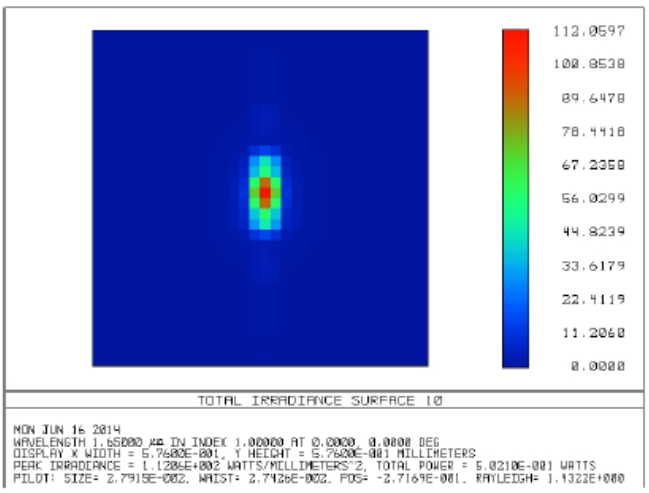

Fig. 30: The ZEMAX simulation of the _field for the bottom-blocked case. The pixel size is set to the detector pixel size of 18m.

The difference between the bottom-blocked and top-blocked images for a plane 2.5 mm after the focal plane is displayed in the next table 8.

Liner relation between un-focusing distance and centroid distance in pixels is given as *Y=mx+b*. Where Y is unfocused distance in milli-meters and x is the centroids distance in pixels. M and b values are 1.470588 and 0.7353 respectively.

Also the chromatic compensation (focal shift with wavelength) from 1.55 to 1.65 µm has to be taken in account (-0.51 mm).

6 Annex II-Shack-Hartmann slopes

Aberration sensor image of telescope 1 is shown in Fig. 31. It uses 9x9 Shack-Hartmann, the lenslet spots are shown in yellow circles. Each sub-aperture field is imaged in 16x16 pixels. Fig. 32 presents the counts/sub-aperture/sec. From these spots positions reference grid is computed. The lenslet spots centroids are computed using weighted center of gravity (WCoG, S. Thomas, MNRAS, 2006), with Gauss weights. The aberration sensor bad pixel map is updated and corrected of those bad pixels by averaging the four (good) neighbors. In Fig. 31 right panel shows the lenslet spots are indexed. Using this index a reference grid array is prepared that is [1 ..69 (*x*-pos), 70-138 (y-pos)]. For a test wavefront, a test lenslet array spots positions are computed and compared with reference array to measure spots shifts/slopes.

The lenslet sub-aperture focal lengths are calibrated by applying series of tip-tilts angles and measured the spots shifts (Fig. 33, 34). It allows us to see the uniformity of focal lengths of sub-apertures because for a given tip-tilt angle applied, the amount of spot shift depends on the focal length of sub-aperture.

The computed spot centroid slopes are multiplied with slopes2zernike matrix which produces Zernike coefficients (Fig. 18, 19 and 35). The slopes2zernike matrix is generated using yao (http://frigaut.github.io/yao/). In this experiment, the aberration sensor is simulated by inputting design specifications. For this, inputted 28 individual Zernike phases, and for each phase computed its slopes. Placed those slopes in a matrix as columns, with matrix size [138 (slopes measured for each individual phase) X 28 (Zernike phases applied)]. Then this matrix inverted that gives the slopes2zernike matrix.

Zernike coefficients = slopes2zernike [28 x 138] *X* slopes array [138 x 1].

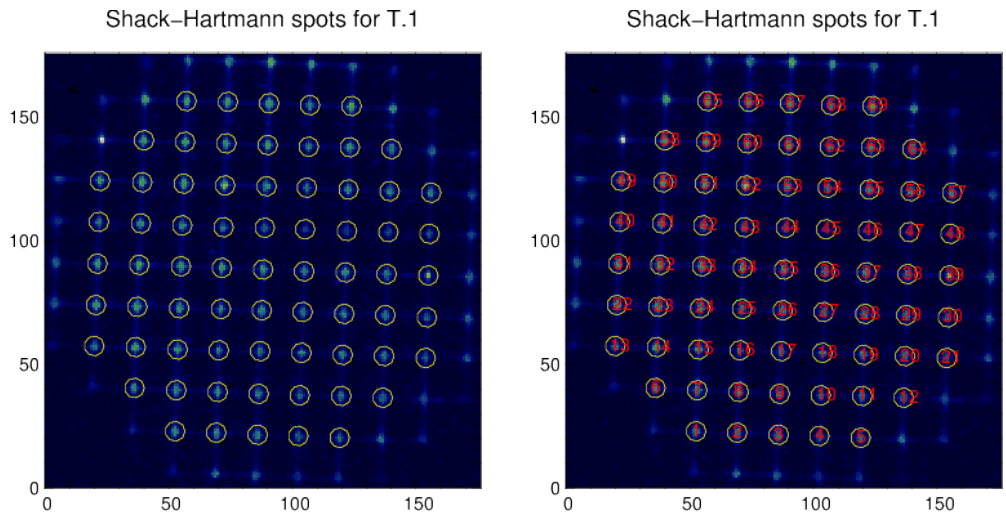

Fig. 31: The effective lenslet spots (69 in number) and their index which are used for the slopes measurement.

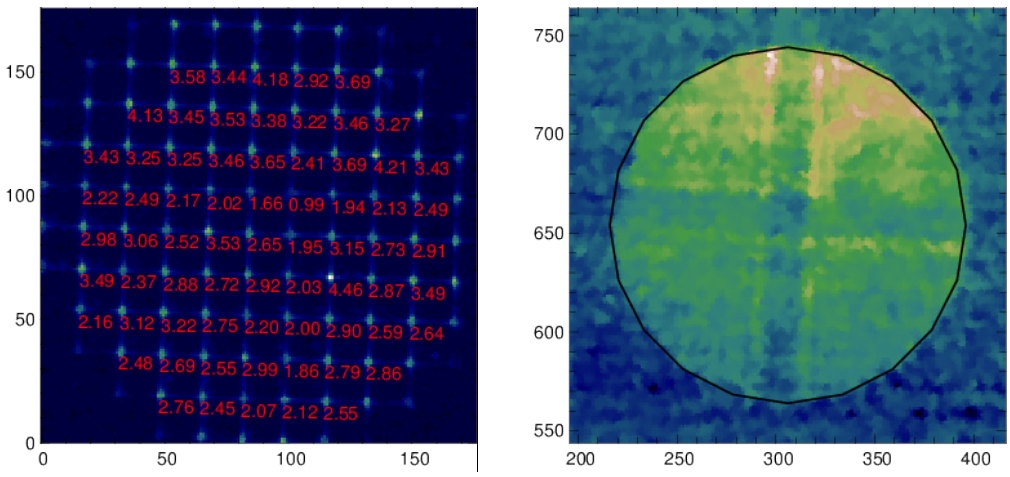

Fig. 32: The number of counts observed in Shack-Hartmann sub-apertures in kilos. The flux of spots where pupil spiders are located which is less in comparison to others. The counter part of the pupil imager where pupil spiders can be seen.

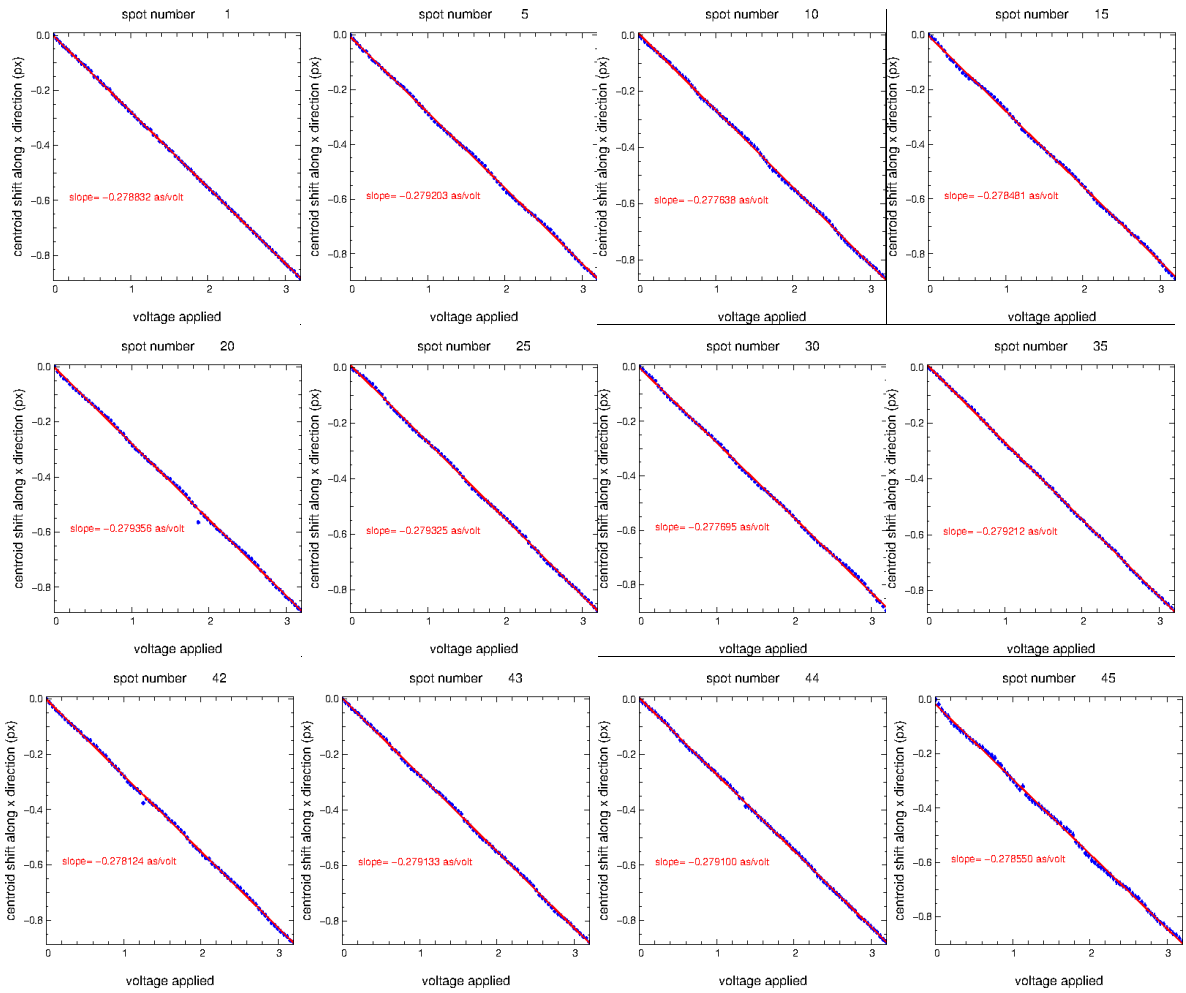

Fig. 33: The typical lenslet spot position is shifted in arc sec with the x-direction voltages applied. Once can see that there are wiggles in the measured centroid positions of spots that is because of low pixel sampling (FWHM of spot = 1.5 pixel).

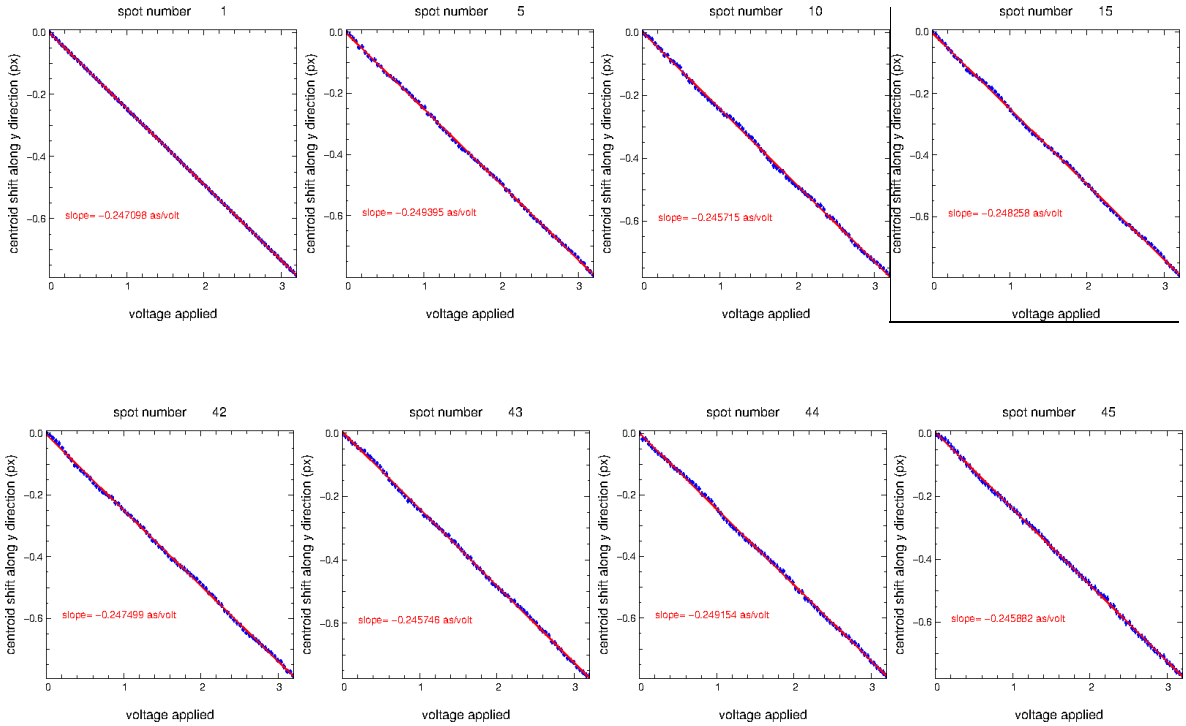

Fig. 34: The typical lenslet spot position is shifted in arc sec with the y-direction voltages applied.

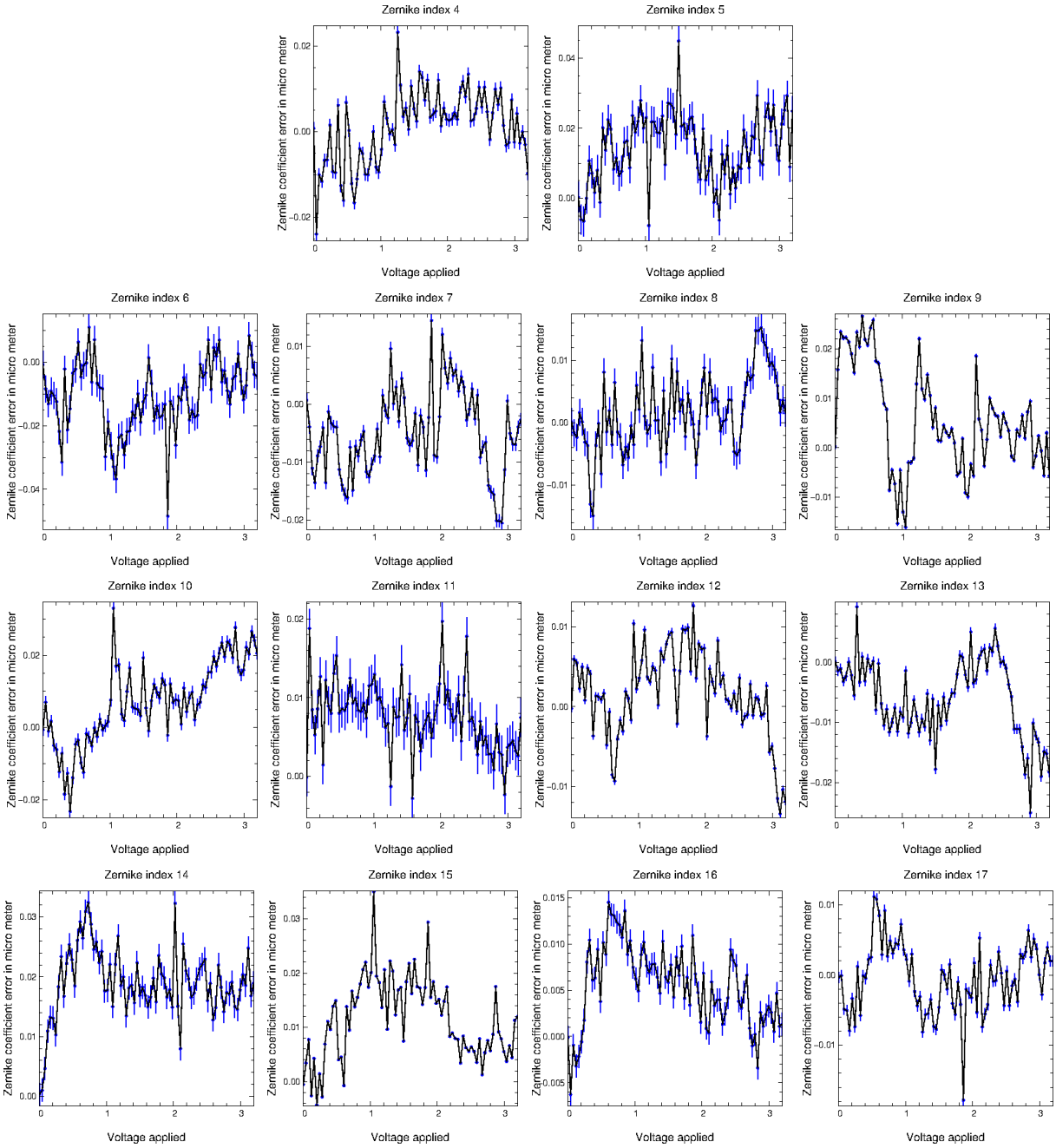

Fig. 35: The error distribution of the first Zernike coefficients measured in micro meters when tip-tilt voltages are applied along x and y directions. Presented here how the Zernike coefficients are varying for different voltages applied. These Zernike errors are coming from the centroid measurement error.

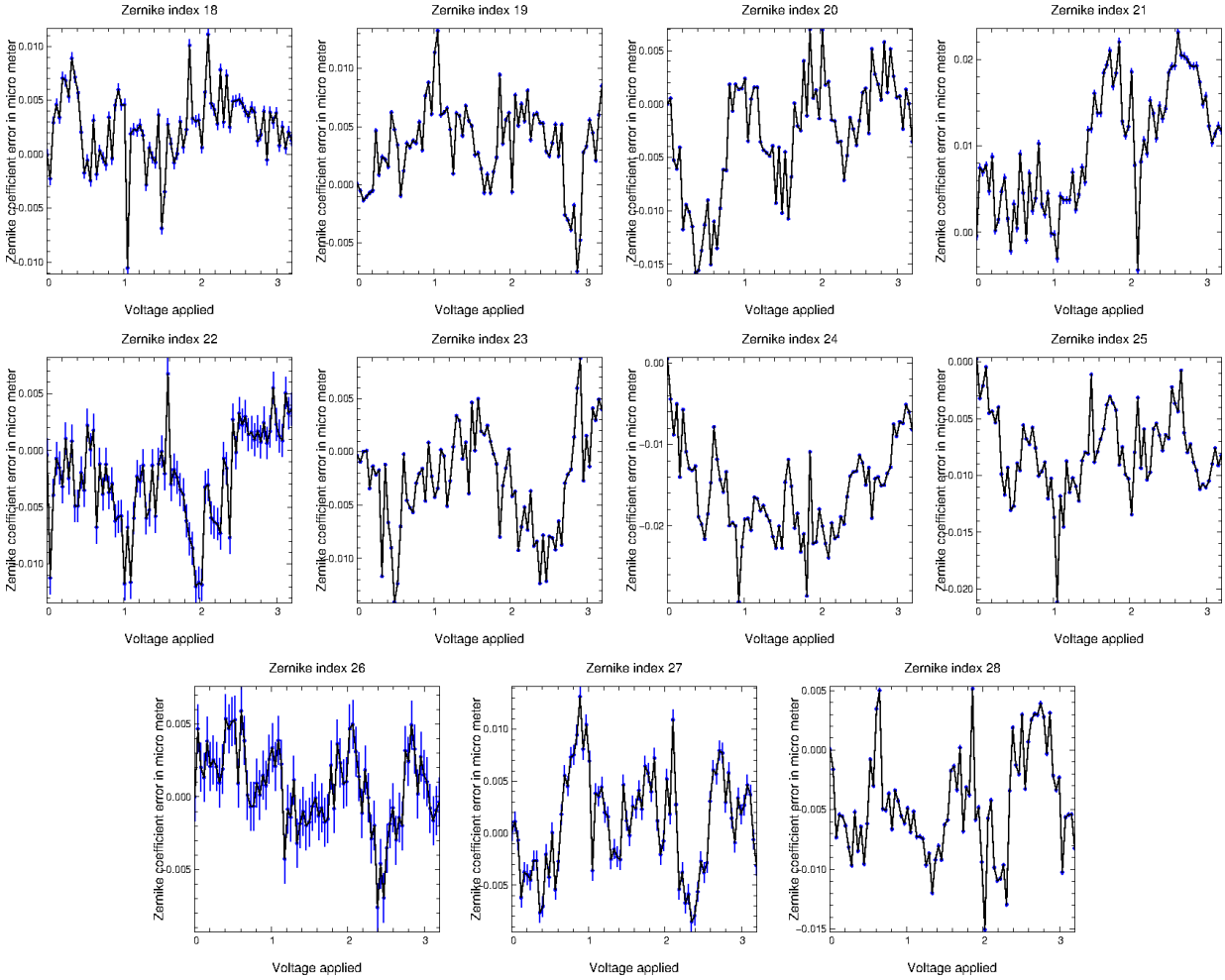

Fig. 36: The higher order Zernike coefficients measured in micro meters when tip-tilt voltages are applied along x and y directions. Presented here how the Zernike coefficients are varying for different voltages applied. These Zernike errors are coming from the centroid measurement error.

End of document